Modeling and simulations of dynamics and motility in active fluids

Giuseppe Negro

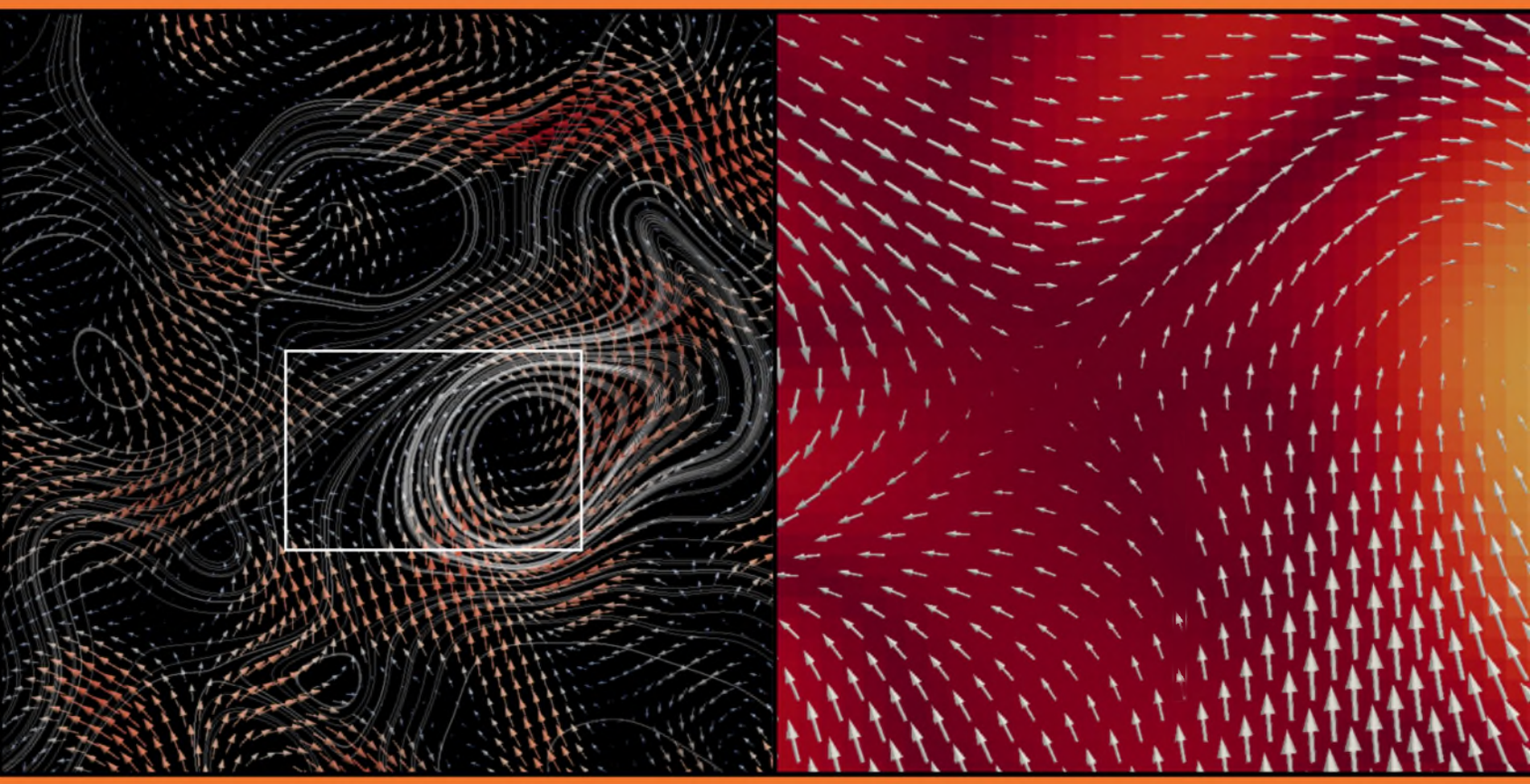

Dottorato in Fisica XXXII ciclo
Università degli studi di Bari "A. Moro"

Supervisor
Prof. Giuseppe Gonnella
Dr. Antonio Lamura

Modeling and simulations of dynamics and motility in active fluids

Dottorato in Fisica XXXII Ciclo
Università degli studi di Bari "A. Moro"

by

Giuseppe Negro

to obtain the degree of PhD

Project duration: November 1, 2016 – November 1, 2019
Supervisor

Prof. G. Gonnella	Dipartimento di Fisica "M. Merlin" Bari
Dr. A. Lamura	CNR, Bari

CONTENTS

ABSTRACT

This thesis deals with the description, at a continuum level, of active fluids. Examples of active fluids are suspensions of biological filaments, such as actomayosin microtubules bundles, activated with motor proteins and bacterial cultures. The constituents of these systems have the natural tendency to assemble and align, thus developing structures with typical polar or nematic order. Combination of this property with self-motility capacity is at the origin of a wealth of interesting phenomena, including spontaneous flow and unusual rheological properties. Some experimental evidence will be presented in Chapter 1.

In the last two decades much effort has been posed in understanding these properties with the declared aim to reproduce, control and exploit them. Here we mainly focus on self-propulsion and the rheology of active emulsions. To describe these phenomena we rely on a continuous description that makes use of vectorial or tensorial order parameters borrowed form liquid-crystal theory. The dynamical models used will be presented in Chapter 2. The dynamical equations are numerically solved using a well known Navier-Stokes solver, the Lattice Boltzmann Method, coupled with finite difference method. This numerical scheme and its MPI implementation will be described in Chapter 3.

In Chapter 4 and 5 we will present our numerical results. In particular in Chapter 4 we will focus on self-propulsion. First results concerning a scalar active model, to spot out the role of compressibility in cell propulsion, will be presented. Then in the second part of Chapter 4 we will present some mesmerizing results regarding the self-propulsions of an active cholesteric droplet. In Chapter 5 the morphology and rheology of an emulsion composed of an active and a passive phase will be analysed. Within our model it is possible to reproduce some rheological experiments regarding bacterial suspensions, and to explain the origin of the different flow regimes observed.

ACKNOWLEDGMENTS

First and foremost, I would like to thank Prof. Giuseppe Gonnella, my supervisor, for his invaluable guidance, infinite patience, and constant dedication to his job. I would also like to thank Dr. Antonio Lamura. Thanks to his helpful conversations and teachings, I've acquired much of the knowledge and the skills I needed to put this work together.

I thank Prof. D. Marenduzzo for sharing his endless inspiring views and for his caring guidance during the two periods I spent in Edinburgh. I am also very grateful to Dr. Adriano Tiribocchi, who started this work years ago, and never stopped providing support and new ideas to our group.

I am grateful to my colleague Livio Carenza, for making amazing this journey. Sharing working hours with him will be hardly forgettable, making this Ph.D. infinitely more valuable.

I am grateful to Alessia, who gave me shelter and offered me support, love and joy, through the good and the bad.

I am grateful to my family: my father Jimmy, my mother Tina, my brother Sabino, and my "sister" Francesca, for supporting me in pursuing my studies. I am also deeply grateful to my grandmother Janna who always motivated me.

For the third time in a thesis, I have to be grateful to Lino and Daniela. To me you have been, and still are, my extended family.

1

ACTIVE MATTER

Any physical isolated system evolves towards equilibrium. No matter which is its nature – a gas in a box, a system of electric charges or the whole universe – it will evolve to minimize some thermodynamic potential or free energy to end up in a state where no flow of any kind occurs, where all forces sum up to zero and temperature is uniform in space and constant in time. This is the *Heat Death of the Universe*. Despite thermodynamics predicts this as the inevitable end of any system, there is a huge number of situations where equilibrium is well far to be reached and there are net flows of matter, energy, *etc.*.

In thermodynamics, a system is said to be in equilibrium when no mass or energy flow occurs, and it minimizes some thermodynamic potential, or free energy; such states have a spatially uniform temperature, are mechanically at equilibrium - all the forces sum to zero - and no macroscopic change can be observed in time. In systems that are at a state of non-equilibrium there are, by contrast, net flows of matter or energy.

There are different classes of non-equilibrium systems. Among them driven systems are those forced out of equilibrium by some external forces – such as a gradient in the temperature or in some other chemical potential, and display non-equilibrium stationary states. A known example is represented by a Newtonian fluid – water, for instance - enclosed between two slabs at different temperatures. In this case a temperature gradient set up across the fluid, and if the gradient if enough pronounced, it would eventually give rise to rolling vortical flow. Such convection rolls will endure as long as the external force persists, and for some time after that, until dissipative effects will maximize the entropy of the system until equilibrium is reached again, that is when the temperature is uniform and net flows are extinguished. Active systems constitute a new class of non-equilibrium systems, in which driving is local. They are in fact forced out of equilibrium by the individual constituent particles themselves. These are inherently not in equilibrium, having some internal energy storage to draw from to perform all sorts of work, and eventually to move. This is, typically, the case of biological systems, which store large quantities of energy to be used for motion, growth, replication, chemical synthesis, and much more.

Living matter, such as collection of animals in the form of schools of fish, birds flocks or swimming bacteria, constitutes a humongous source of examples of systems evolv-

ing far from equilibrium. This vast class of non-equilibrium condensed matter systems has come to be known as *active matter*. Despite the nature of living systems may considerably differ, they still share common feature that can be described in a unified frame. Ordering is, for instance, one of the most important features on which life relies. The comprehension of this unique ability of living organisms to self-organize their constituents into functional ensembles is the declared central objective of active-matter physics.

This introductory chapter is devoted to the description of some active matter systems and to their peculiar behaviours that have no equivalent in their equilibrium counterpart. In particular I will present some experimental results regarding the two phenomena this thesis is most concerned about: self propulsion and unusual rheological response.

1.1. ORDER AND COLLECTIVE MOTION

Active constituents have the natural tendency to assemble and align, thus developing tendency to form patterns and display collective organized behaviour [25]. This property is a consequence of self-motility capacity, which is at the origin of many non-equilibrium properties that do not always find an equivalent in standard externally driven non-equilibrium systems; one of the key differences can be found in the injection of energy at small scales (i.e. the size of the active agents) rather than having a forcing that acts on the scales of the whole system. This leads in fluidic systems to developing hydrodynamic instabilities that for example generate turbulent-like behaviours even at small Reynolds numbers, where no classic turbulence can be accounted for [50, 107, 115, 167].

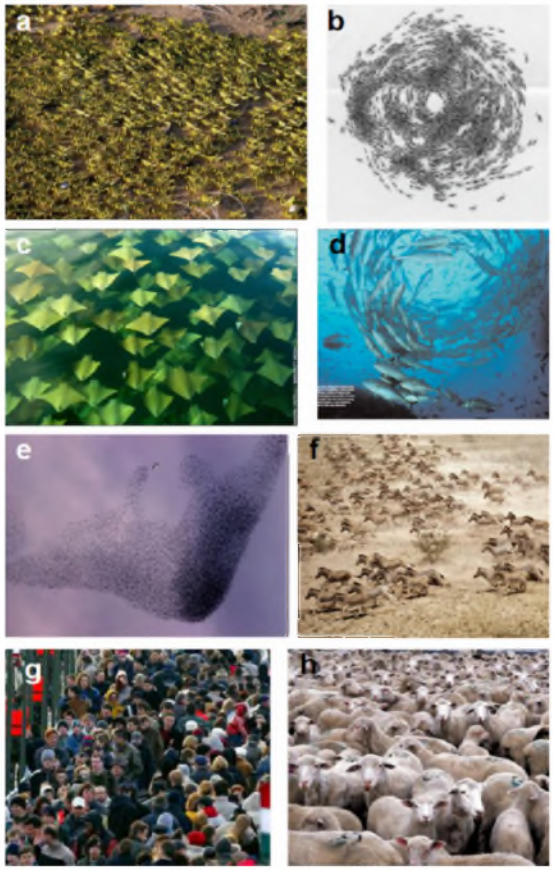

Figure 1.1: A gallery of images related to collective motion of different animal species. While the single organisms each have their individual orientation, different degrees of overall polar order can be observed from case to case, ranging from uniform motion in a single direction **(a,c,e,f)**, vortices **(b,d)**, to more disordered states in which the different orientations average to zero **(g,h)**. Adapted from [200].

Macroscopic systems, such as herds of horses, flock of birds or schools of fish, still exhibit this natural tendency to organize in ordered pattern and develop coherent motion. Numerical models of self-organized motion, inspired both by biology [5, 35, 156] and physics [18, 38, 76, 199], support the idea that simple rules of interaction among the individuals are sufficient

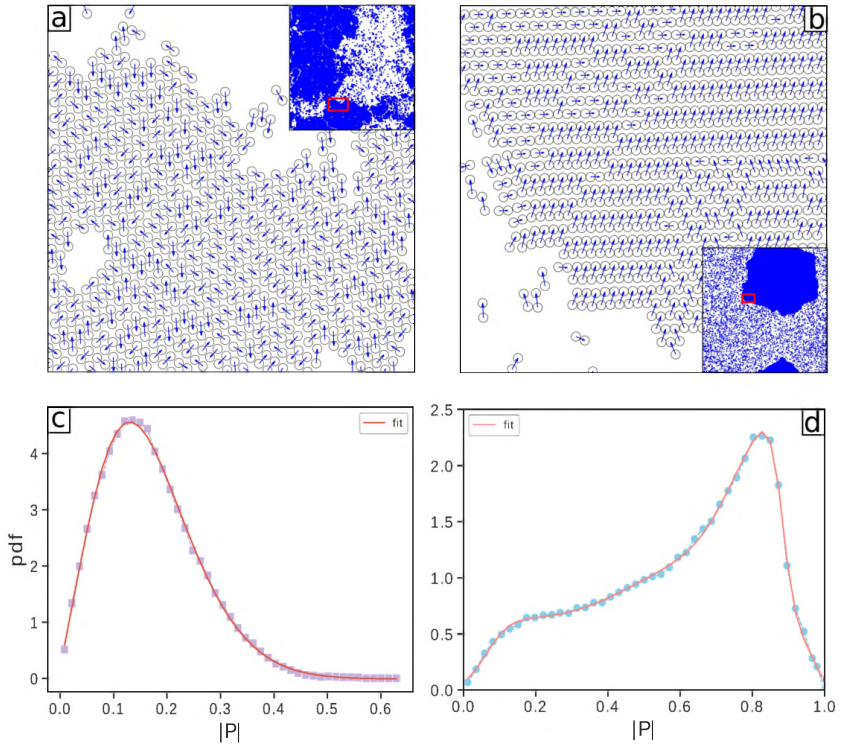

Figure 1.2: System of self-propelled Brownian dumbbells for total covered fraction area $\phi = 0.5$ and different values of the self-propulsion force corresponding to the Péclet number (parameter proportional to the intensity of the self-propulsion force) $Pe = 10$ and $Pe = 40$, in panels (a) and (b), respectively. For the definition of the model and detailed meaning of parameters see [37, 145]. Dumbbells have a tail and a head; the blue vectors represent the directions of self-propulsion of each dumbbell, related to the tail-head axis. The snapshots represent small portions (red boxes) of the larger systems shown in the insets. Both cases correspond to points in the phase diagram where a dilute and a more dense aggregated phase coexist. Note that for small Péclet number polar order is not present in the aggregated phase that only shows hexatic order, while for higher Péclet the hexatic phase is polarized. The probability distributions (*pdf*) of the local coarse-grained polarization field confirm this behaviour. At small Péclet the *pdf* (panel (c)) shows a maximum at a polarization magnitude $|P| \approx 0.15$ while at $Pe = 40$ the *pdf* (panel (d)) can be interpreted as taking contributions from two distributions with maxima at $|P| \approx 0.18$ and $|P| \approx 0.8$, respectively [145]. Figure adapted from [23].

to produce collective behaviour. Activity alone actually favours aggregation and can induce a phase transition, often called Motility Induced Phase Separation (MIPS) [26].

Recent researches [143] have also shed light on the mechanism at the base of motion in large groups of animals, where the leaders of the group – usually more experienced than other – tend to occupy a strategic position to govern the dynamic of the whole group. In macroscopic animal systems, the tendency to assemble in ordered patterns is exploited as a defensive mechanism. Here the environment in which the system evolves – air for the birds, water for fish, play a secondary role, since the interaction between different units is basically visual [108] so that such systems are usually addressed as *dry* to oppose to the case of microscopic systems – such as cytoskeletal or bacterial suspensions – where the hydrodynamics becomes important and strongly influences the overall motion. These are momentum conserving systems and for this reason they deserve the name of *wet systems*. In the following we will be concerned only with the latter.

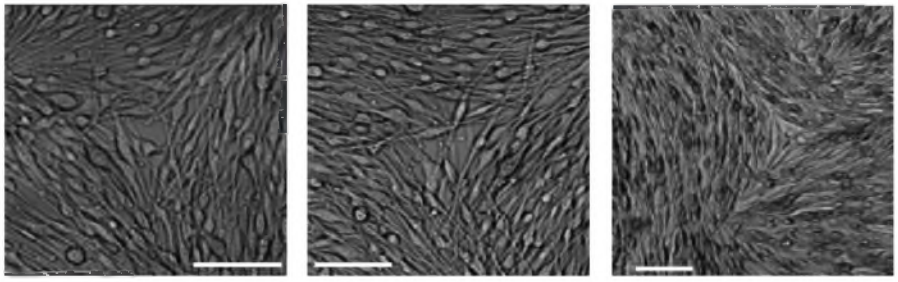

Figure 1.3: Three different examples of human melanocytes, melanin-producing cells, forming nematic structures [97].

Active constituents are in general anisotropic (such as an elongated structure). This sets a favoured direction for their self-propulsion or for the generation of forces. For this reason one of the most important feature of active systems is orientational order. This feature is pretty evident for the case of groups of animals, that usually orient their body in the direction they are moving towards, (Fig. 1.1); but this remains valid even at smaller scales, in systems of bacteria or polymerising eukaryotic cellular filaments – such as actin or microtubules – that exhibit asymmetric ends, dubbed 'head' and 'tail' [146].

Depending upon the symmetries of the microscopic agents and their reciprocal interactions, these active fluids generally fall into two wide subcategories. The first one is the active polar fluid composed of elongated self-propelled particles, characterized by a head and a tail, whose interactions have polar symmetry. Such systems may order in polar states, when all the particles are on average aligned along the same direction, as in the case of bacteria self-propelled along the direction of their head [47]. Nevertheless systems of intrinsic polar particles, such as actin filaments cross-linked with myosin [16, 189, 191, 192] or microtubule bundles coupled with kinesin motors [42, 160, 182], may still arrange in a nematic fashion, restoring head-tail symmetry, when interactions favour alignment regardless of the polarity of the individual particles. As an example Fig.1.2 shows the aggregated phase of a system of self-propelled Brownian polar dumbbells [37, 74, 179, 180] which, depending on the strength of the self-propulsion force, may arrange in a polar state (right) or in an isotropic state (left), a behaviour also found in bacterial colonies [43]. The second class includes head-tail symmetric, or *apolar*, particles that may move back and forth with no net motion, and order in nematic states. Examples of realizations in nature include *melanocytes* [97] – *i.e.* melanin-producing cells in human body (Fig.1.3 shows examples of melanocytes forming nematic structures) – and *fibroblasts* [49], that are cells that play a central role in wound healing. Both of them are spindle-shaped, with no head-tail distinction.

On the practical side, the complex features of active matter can be exploited to craft in vitro living materials with non-trivial topological properties, as in the experiment by Sanchez et al. [160]. Here, stiff polar filaments assembled from monomeric tubulin protein (Fig. 1.4 a), known as *microtubules*, were made *active* by the addition of kinesins (Fig. 1.4 b). This specialized type of protein can convert chemical fuel into mechanical energy, and functions by hydrolyzing ATP[1] and undergoing a conformational

[1]The Adenosine Triphosphate is a chemical exploited in any form of life to store energy coming from glycolysis. When reacting with water molecules it is turned into Adenosine Diphosphate (ADP) and

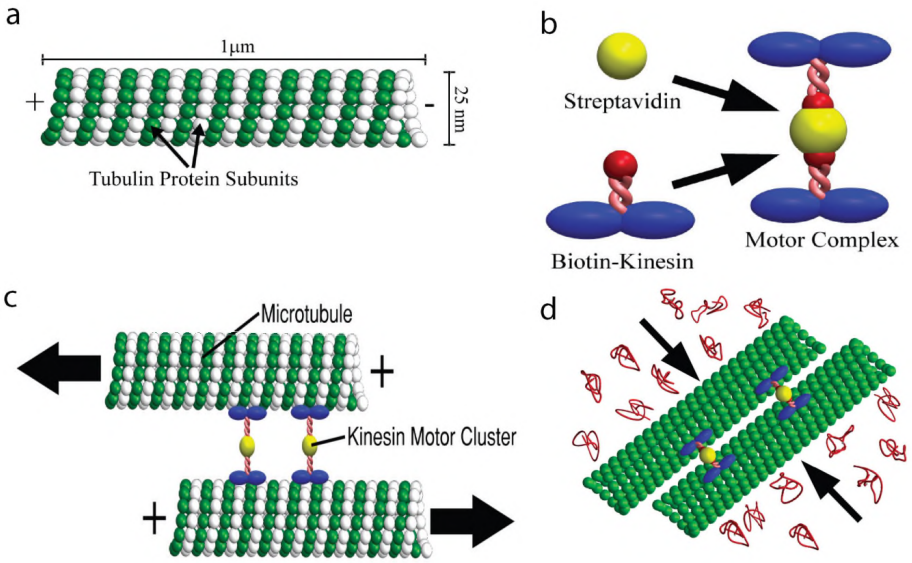

Figure 1.4: **(a)** Sketch of a microtubule assembled from monomeric tubulin protein. **(b)** Kinesin cluster obtained exploiting affinity of streptavidin protein and biotin. **(c-d)** Combining microtubules, kinesin motor crosslinkers, and depletion agent PEG (represented in red) results in the formation of microtubule bundles in which the motor clusters drive inter-filament sliding.

change which advances the motor along the microtubules substrate, thus allowing the motor to *walk* along the microtubule filament they are attached to. To generate activity at the microtubule, multiple kinesin motors are tied together into cluster and crosslinked to multiple microtubules, thus exerting forces between multiple filaments (Fig. 1.4 c). Moreover a non-absorbing polymer (poly-ethylene glycol or PEG) induces an effective attractive interaction between microtubule filaments. This 'bundling' mechanism is entropically driven but can also be thought of in terms of the PEG exerting an osmotic pressure on the microtubules. The combination of microtubules, kinesin motor crosslinkers, and depletion PEG agents (Fig.1.4 d), results in the formation of microtubule bundles in which the motor clusters drive inter-filament sliding, thus resulting in net extension of bundles.

For high filament concentrations, hydrodynamic instabilities driven by internally sustained flows could be observed; furthermore, the filament network displays a strong order. Like in nematic liquid crystal phases, no positional order is observed but constituents tend to point in the same direction. Topological defects, which are regions 'out of phase', are also observed (Fig.1.5), characterized by half-integer $\pm 1/2$ topological charge[2].

Self-organized patterns and sustained flows have been also observed in bacterial suspensions [47, 50]. Suspensions of *B. subtilis* can even exhibit chaotic flow patterns, as shown in Fig. 1.6, characterized by travelling *jets* of high collective velocities and surrounding vortices.

inorganic phosphate thus releasing energy that is ready to be exploited in many processes fundamental for the correct functioning of living cells and organisms.

[2]A rigorous definition of topological defects will be given in the next chapter.

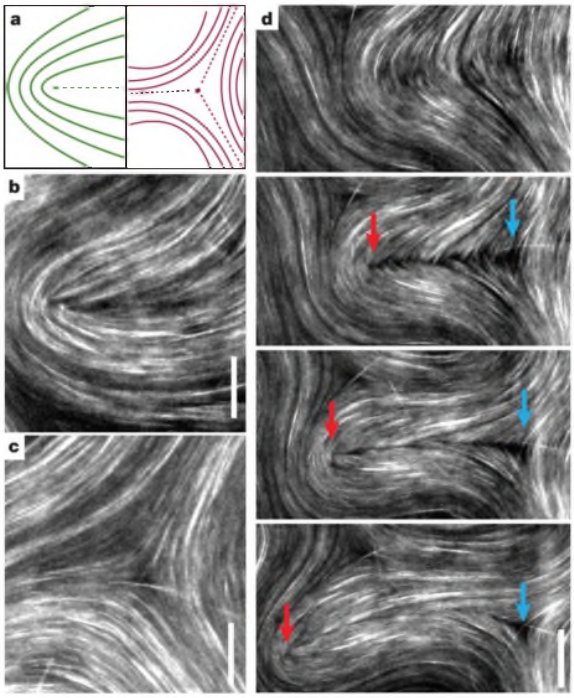

Figure 1.5: **(a)** Schematic illustration of nematic $+1/2$ and $-1/2$ disclination charges. A definition of topological defects and their role in active systems will be discussed in the next Chapter. **(b,c)** Microtubules under the effect of active stress from molecular motors (kinesins) exhibiting nematic order; **(d)** Sequence of images showing the generation of defect charges from an originally defect free nematic domain [160]. Here red arrows correspond to $+1/2$ defects, while blue ones to $-1/2$ disclinations.

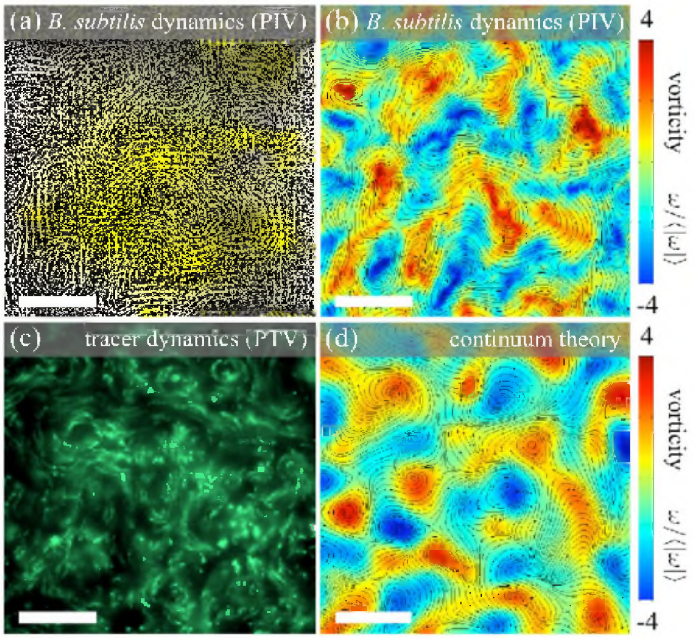

Figure 1.6: **(a)** Very dense homogeneous suspension of B. subtilis showing collective bacterial dynamics. Longest arrows correspond to velocity of 30 $\mu m/s$. **(b)** Streamlines and normalized vorticity field determined from PIV (particle image velocimetry) data in **(a)**. **(c)** Turbulent 'Lagrangian' flow of fluorescent tracer particles (false-color) in the same suspension, obtained by integrating emission signals over $1.5s$. **(d)** Partial snapshot of a 2D slice from a 3D simulation of the continuum model. Figure adapted from [50].

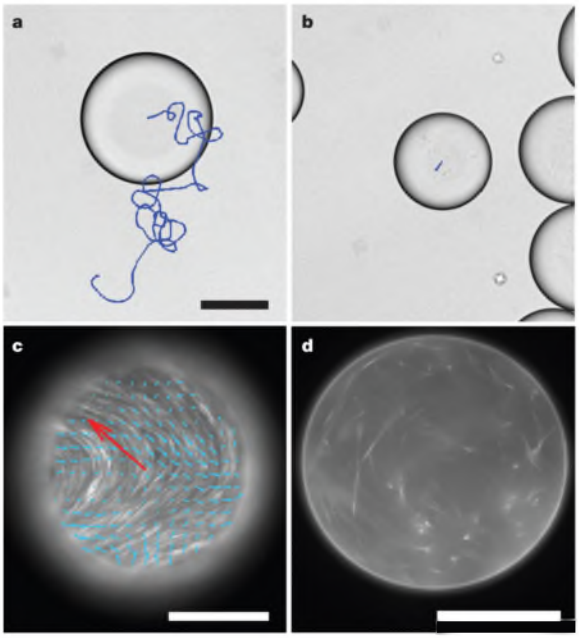

Figure 1.7: **(a)** Droplets containing microtubulues bundles exhibit spontaneous autonomous motility, when partially compressed between chamber surfaces. A droplet trajectory taken over a time interval of 33 minutes is overlaid onto a bright-field droplet image. **(b)** In the absence of ATP, passive droplets exert no internal forces, and the only contribution to their movement is minor drift. **(c)** Fluorescence image of active microtubules bundles which spontaneously adsorb onto the oil-water interface. The resulting active liquid crystalline phase exhibits streaming flows, indicated with blue arrows. Red arrow indicates instantaneous droplet velocity. **(d)** Image of the droplet taken at a mid-plane indicates that the droplet interior is largely devoid of microtubules bundles.

1.2. ACTIVE MATTER CONFINED IN DROPLETS

In most biological contexts, active fluids are often confined to the *cytoplasm*, the material within a cell enclosed by cell membrane. Such confinement leads to the emergence of coherent flows that enhances cellular transport. The effect of confinement has been studied by Sanchez et al. [160], enclosing the same microtubules bundles, described in the previous section, in aqueous droplets emulsified in fluorinated oil (Fig. 1.7). When squeezed between two surfaces, these water-in-oil active droplets exhibit a mesmerizing persistent autonomous motility (see for instance the blue trajectory in Fig. 1.7a). By contrast, in absence of any chemical fuel in the suspension droplets remain still (Fig. 1.7b). Microtubules bundles extend and push against the water-oil interface, eventually being absorbed onto the interface. When in frictional contact with a hard surface, these internal flows drive the motility of the entire droplet (Fig. 1.7c). Scanning through the bulk of these motile droplets reveals that their interior is largely devoid of microtubules bundles relative to their surface (Fig. 1.7d). Starting from the seminal work of Sanchez *et al.*, recent experiments have shown that the presence of an active fluid can favour droplet self-propulsion through several mechanisms, based on chemical reactions [218], spontaneous symmetry breaking and Marangoni effects [57, 80, 87, 160]. Such experiments motivated numerous theoretical studies, with the aim of developing minimal models capable of capturing features of particular relevance in biology (as active droplets can mimic the spontaneous motion of cells [10, 16, 66, 191]) or in the design of bio-inspired materials [87]. In Chapter 4 two new models for self propulsion

will be presented and discussed.

1.3. RHEOLOGY

Active fluids also display very interesting rheological properties. Different experiments have shown that super-fluidic regimes can be observed in bacteria suspensions under an external applied shear. In addition reduction or increase of the solvent apparent viscosity may occur, depending on the nature of the micro-organisms dispersed in the suspension. In the experiment of Lopez et al. [120] the apparent viscosity of a suspension of *E. Coli* bacteria was measured with a *Couette* rheometer. Activity is controlled fixing the level of O_2 in the system. Fig.1.8 shows the results for a fixed, low value of shear rate. A null apparent viscosity is measured even when the rheometer is rotating. Panel (b) shows the measured apparent viscosity as the concentration of the suspension varies. For sufficient values of dilution the linear theoretical behaviour is confirmed, while increasing the concentration of the suspension a plateau is reached. Surprisingly, negative apparent viscosity values are observed for a short transient after the rheometer is switched off.

Experiments by Gachelin et al. [62] confirmed these results. Again a suspension of *E. Coli* bacteria is considered and the relative viscosity measured looking at the displacement of the interface between the suspension and a reference fluid while they flow in a channel. Fig. 1.9a confirms the reduction in the apparent viscosity comparing between active and passive suspension. As evident from Fig. 1.9b, for low concentrations the suspension displays the same apparent viscosity of the control fluid, whereas for higher concentrations the apparent viscosity increases. In this experiment it has been possible to look directly to the statistics of bacteria in the flow direction. Experiments also confirm that the observed apparent viscosity behaviour is due only to activity, and not to different bacteria distribution.

In another experiment by Rafai et al. [151], the rheology of a suspension of *Chlamydomonas Reinhardtii* algae is analysed. Differently from the previous case, an increased apparent viscosity is observed in a suspension of living cells compared to the case of dead cells dispersed (Fig. 1.9). Comparing the different experiments it is evident how the different kinds of swimming mechanism are of crucial importance, as will be explained in the next Chapter.

1.4. OUTLINE OF THE THESIS

Understanding and control the peculiar properties of active fluids here discussed is of fundamental importance for the design of new active materials and devices with pioneering applications. To this aim in Chapter 2 I will provide an overview of continuum approaches suitable to model active matter in fluid environments, starting from a coarse-grained description of the active constituents and their active effect on the surrounding fluid. Then in Chapter 3 I will provide an overview of the basic features of Lattice Boltzmann, the numerical method implemented to integrate dynamical equations of active matter and present some details regarding the parallelization of the code used for simulations. Chapter 4 and 6 will be devoted to the study of the two phenomena here presented, namely spontaneous motion of active droplets and rheological characterization of active emulsions.

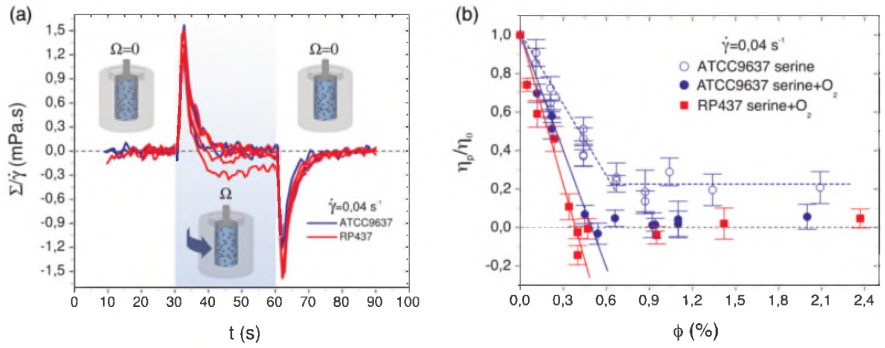

Figure 1.8: **Experiment by Lopez et al.** [120]. **(a)** Apparent viscosity for two different families of *E. Coli* bacteria. The *Couette* rheometer is put into rotation at time $t = 30\ \ s$ with an angular velocity Ω, so to have a shear rate of $\dot{\gamma} = 0.4\ \ s^{-1}$. At time $t = 60\ \ s$ the rotation is stopped. **(b)** Relative viscosity versus suspension concentration. Blue circles refers to higher values of activity with respect to white circles, while red squares refers to the second *E. Coli* family considered.

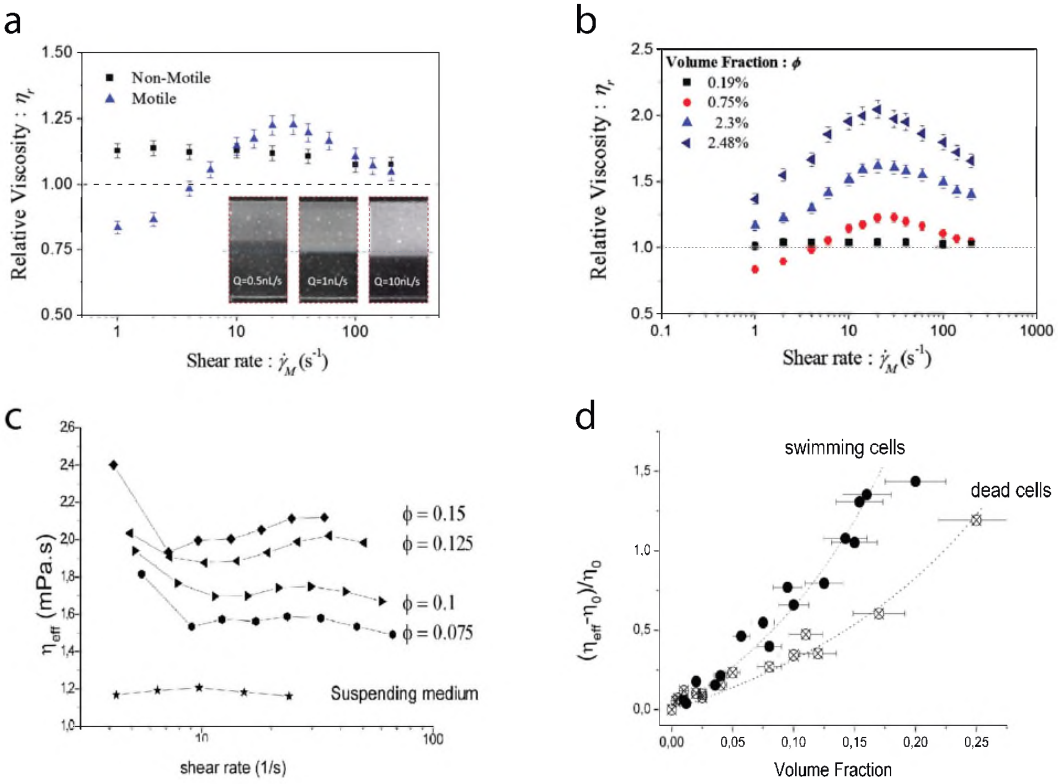

Figure 1.9: **Experiments by Gachelin et al. (a-b) and Rafai et al. (c-d)** [62, 151]. **(a)** Relative viscosity as a function of shear rate, for a volume fraction of $\phi = 0.8\%$, in the case of motile and immotile bacteria. **(b)** Relative viscosity for different values of volume fraction. Inset in **(a)** shows the displacement of the interface between the suspension and the control fluid for different flow values Q. From the interface displacement it is possible to measure the relative viscosity. **(c)** Apparent viscosity versus shear rate for different values of volume fraction. **(d)** Relative apparent viscosity of the suspension. Dotted lined refer to a fit with the semi-empirical Krieger e Dougherty law.

2

DYNAMICAL MODELS FOR MULTIPHASE AND ACTIVE FLUIDS

Capturing the dynamical properties of active systems is a challenging task and many models have been advanced so far to replicate their entangled behaviour ranging from a molecular dynamics approach to modified versions of the Navier-Stokes equation. However, a good model for active fluids must have some fundamental traits apt to correctly capture the mechanisms at the base of phenomena occurring in active matter. One of them – probably the most important – is the natural tendency of active units to assemble and align in long-ranged ordered structures, whose patterns closely resemble those observed in passive liquid crystals. Because of this, active fluids are often addressed as *living* or *active liquid crystals*. In active gel models, the emerging orientational order at mesoscopic scales is captured by proper order parameters, such as the polarization vector $\mathbf{P}(\mathbf{r}, t)$ or the tensor $\underline{\underline{\mathbf{Q}}}(\mathbf{r}, t)$, as in the Landau-De Gennes theory for their passive counterpart. It is natural to think of the direction of the vector field (or in turn the primary axes of the Q-tensor) as the mean direction of the forcing exerted by swimmers on their surrounding – a simple observation that is at the base of the intuition of Simha and Ramaswamy when they first introduced the *active* stress tensor in their seminal work [169]. Since then, the resulting *active nemato-hydrodynamic* theory was able to successfully replicate a certain number of phenomena occurring in active gels (from spontaneous motion, to active turbulence). In this regard, it is worth noting that active gel theory correctly reproduce the low Reynolds-number[1] found in experimental systems – a feature that not any theory for active matter is able to replicate.

In this Chapter I will first introduce the notions of order parameter and topological defect, then the field theory developed to capture the thermodynamics of *passive* liquid crystal. This approach consists in writing a Landau-like free energy functional, written in terms of powers of the order parameter and its gradients, so to respect the symmetries of the disordered phase. In Section 3 I show, following the work of Simha and Ramaswamy, how a coarse-grain procedure can be used to obtain an *active stress*

[1] At low Reynolds number advective mechanism are highly suppressed in a Newtonian fluid, leading to laminar, ordered flows, where viscous effects overcome advective mechanisms. On the contrary, when advection becomes important, hence at high Reynolds numbers, the flow becomes chaotic, a regime commonly addressed as *turbulence*.

tensor to plug into the Navier-Stokes equation to couple the hydrodynamics of the underlying fluid with the dynamics of the suspended particles. Finally in Section 4, I will present the set of partial differential equations that rule the evolution of active gels.

2.1. ORDER PARAMETERS

The continuum fields describing polar and nematic order are the vector field $P_\alpha(\mathbf{r}, t)$ or the tensor field $Q_{\alpha\beta}(\mathbf{r}, t)$ (Greek subscripts denote the Cartesian components). They emerge either from a coarse grained description of a microscopical model [39] or from a theory based on general symmetry arguments [8, 128]. Following, for instance, the former approach, for a system of arrow-like particles the polarization field can be defined as

$$\mathbf{P}(\mathbf{r}, t) = \langle \nu(\mathbf{r}, t) \rangle = \int \mathrm{d}\Omega f_P(\nu, \mathbf{r}, t)\nu, \tag{2.1}$$

where $f_P(\nu, \mathbf{r}, t)$ is the probability density, encoding all the information coming from the microscopical model, of finding a particle at position $\mathbf{r}$ and at time t oriented along the direction ν, and the integration is carried out over the solid angle Ω. The polarization can be also written as

$$\mathbf{P}(\mathbf{r}, t) = P(\mathbf{r}, t)\mathbf{n}(\mathbf{r}, t), \tag{2.2}$$

where $\mathbf{n}(\mathbf{r}, t)$ is a unit vector defining the local mean orientation of particles in the neighbourhood of $\mathbf{r}$, and $P(\mathbf{r}, t)$ is a measure of the local degree of alignment, ranging from 0 (in an isotropic state) to 1 (in a perfectly polarized state).

Differently, the nematic phase cannot be described by a vector field, as both orientations ν and $-\nu$ equally contribute to the same ordered state, due to the head-tail symmetry of the constituents. For a system of rod-like particles, the order is described by a nematic tensor which, in the uniaxial approximation (i.e. when a liquid crystal is rotationally symmetric around a single preferred axis), can be defined as

$$Q_{\alpha\beta}(\mathbf{r}, t) = \langle \nu_\alpha \nu_\beta - \frac{1}{d}\delta_{\alpha\beta} \rangle = \int \mathrm{d}\Omega f_Q(\nu, \mathbf{r}, t)(\nu_\alpha \nu_\beta - \frac{1}{d}\delta_{\alpha\beta}). \tag{2.3}$$

Again $f_Q(\nu, \mathbf{r}, t)$ is the probability density to find a nematic particle oriented along ν at position $\mathbf{r}$ and time t, while d is the dimensionality of the system. As for the polarization field, the nematic tensor can be also written in terms of the versor $\mathbf{n}$ (usually called *director* field) defining the local mean orientation of the particles

$$Q_{\alpha\beta}(\mathbf{r}, t) = S(\mathbf{r}, t)\left[n_\alpha(\mathbf{r}, t) n_\beta(\mathbf{r}, t) - \frac{1}{d}\delta_{\alpha\beta} \right]. \tag{2.4}$$

Note that, by defining the nematic tensor in this way, one can separate local anisotropic features out of isotropic ones. Indeed, the only scalar quantity that can be derived from a tensorial object, *i.e.* its trace, is identically null. In Eq. (2.4) $S(\mathbf{r}, t)$ plays the same role of $P(\mathbf{r}, t)$ in defining the degree of alignment of the molecules in the nematic phase. In fact, by multiplying Eq. (2.3) and (2.4) by $n_\alpha n_\beta$, summing over spatial components and comparing them, one gets (in three dimensions)

$$S(\mathbf{r}, t) = \frac{1}{2}\langle 3\cos^2\theta - 1 \rangle, \tag{2.5}$$

Table 2.1: The table summarizes bulk and elastic contributions to free energy for polar and nematic, both uniaxial and biaxial (see Section 2.2), systems. Splay, twist and bending contributions have been written explicitly in terms of different elastic constants κ_i $(i = 1,2,3)$ for both polar and uniaxial nematic gels, while in the most general case of a biaxial nematic we did not distinguish between different contributions. The last line in the Table shows how the elastic contribution looks like assuming that the medium is elastically isotropic, *i.e.*, $\kappa_1 = \kappa_2 = \kappa_3 = \kappa$.

Free energy contributions		Polar Gel	Nematic Gel	
			Uniaxial	Biaxial
Bulk		$a\mathbf{P}^2 + b\mathbf{P}^4$	$rS^2 - wS^3 + uS^4$	$\tilde{r}Q_{ij}Q_{ji} - \tilde{w}Q_{ij}Q_{jk}Q_{ki} + \tilde{u}(Q_{ij}Q_{ji})^2$
Elastic	Splay	$\frac{\kappa_1}{2}(\nabla\cdot\mathbf{P})^2$	$\frac{\kappa_1}{2}(\nabla\cdot\mathbf{n})^2$	$\frac{L_1}{2}(\partial_k Q_{ij})^2 + \frac{L_2}{2}(\partial_j Q_{ij})^2 + \frac{L_3}{2}Q_{ij}(\partial_i Q_{kl})(\partial_j Q_{kl})$
	Twist	$\frac{\kappa_2}{2}(\mathbf{P}\cdot\nabla\times\mathbf{P})^2$	$\frac{\kappa_2}{2}(\mathbf{n}\cdot\nabla\times\mathbf{n})^2$	
	Bend	$\frac{\kappa_3}{2}(\mathbf{P}\times\nabla\times\mathbf{P})^2$	$\frac{\kappa_3}{2}(\mathbf{n}\times\nabla\times\mathbf{n})^2$	
Single constant approximation		$\kappa(\nabla\mathbf{P})^2$	$\kappa(\nabla\mathbf{n})^2$	$L_1(\partial_k Q_{ij})^2$

where $\cos\theta = \mathbf{n}\cdot\nu$ is a measure of the local alignment of particles. The scalar order parameter S achieves its maximum in the perfectly aligned state, where $\langle\cos^2\theta\rangle = 1$, while it falls to zero in the isotropic phase where the probability density f_Q is uniform over the solid angle and $\langle\cos^2\theta\rangle = 1/3$. Assuming $\mathbf{n}$ to be parallel to a Cartesian axis, one can soon verify from Eq. (2.4) that $Q_{\alpha\beta}$ has two degenerate eigenvalues $\lambda_2 = \lambda_3 = -S/3$ (whose associated eigenvectors lie in the plane normal to the particle axes) and a third non-degenerate one $\lambda_1 = 2S/3$, greater in module than λ_2 and λ_3 and related to the director itself. Such formalism can be also extended to treat the case of biaxial nematics, *i.e.* liquid crystals with three distinct optical axis. Unlike an uniaxial liquid crystal which has an axis of rotational symmetry (hence the Q-tensor has two degenerate eigenvalues), a biaxial liquid crystal has no axis of complete rotational symmetry and no degenerate eigenvalue. In this case the Q-tensor cannot be expressed any more in terms of a single vector field. Indeed, in the most general case, liquid crystal molecules can have two alignment directions, a preferential one, defined by the director field $\mathbf{n}$ and a secondary one that I will denote here with $\mathbf{m}$. In this case the Q-tensor will be written as the sum of two contributions:

$$Q_{\alpha\beta}(\mathbf{r},t) = S(\mathbf{r},t)\left[n_\alpha(\mathbf{r},t)n_\beta(\mathbf{r},t) - \frac{1}{d}\delta_{\alpha\beta}\right] + V(\mathbf{r},t)\left[m_\alpha(\mathbf{r},t)m_\beta(\mathbf{r},t) - \frac{1}{d}\delta_{\alpha\beta}\right], \quad (2.6)$$

where the scalar field V defines the local degree of biaxiality of the liquid crystal. In the following, except if differently stated, the liquid crystal is not forced to be uniaxial, hence the fully tensor notation $Q_{\alpha\beta}$ will be adopted.

2.2. FREE ENERGY

In this Section we will shortly review the free-energy functional encoding the equilibrium properties of a polar or nematic suspension and often employed to study active fluids. The free-energy depends on the actual configuration of the order parameters.

The free energy functional describing the ground state of the theory can only contain terms which respect the symmetries of the disordered phase, in the spirit of Landau's symmetry principle. Since the disordered phase of both polar and nematic system

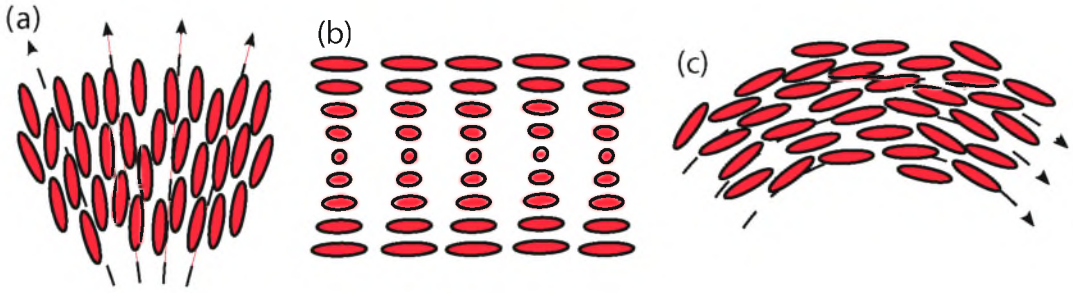

Figure 2.1: Cartoon of three modes of elastic deformation: **(a)** splay, **(b)** twist and **(c)** bend.

is invariant under roto-translations, the free-energy F will only contain scalar terms, proportional to the powers of the order parameters and their gradient. For a vectorial order parameter, the only scalar objects of the form $\mathbf{P}^{2m}$ can be considered, with m positive integer, usually arresting the expansion to the fourth order. For the nematic order parameter scalar quantities are of the form $\mathrm{Tr}(\underline{\underline{\mathbf{Q}}}^m)$; note that there is no impediment here to odd power terms, by virtue of the invariance of $\underline{\underline{\mathbf{Q}}}$ under inversions, but no linear term will appear in the expansion since $\mathrm{Tr}\underline{\underline{\mathbf{Q}}}$ is identically null by definition. The most relevant difference between a polar and a nematic theory is due to the presence of a third order term in the polynomial expansion of the bulk free-energy. Indeed, while a system described by means of a vector order parameter undergoes a second-order phase transition between the ordered and disordered phase, a nematic system undergo a first-order phase transition, characterized by the establishment of metastable phases [29].

In order to take into account the energetic cost due to continuous deformations of the order parameters, elastic terms are also included in the free energy functional. In both polar and nematic systems three different kinds of deformations can be identified (Fig. 2.1): splay, twist and bending, gauged to the theory through (in general) different elastic constants $\kappa_1, \kappa_2, \kappa_3$, giving the energetic cost associated to the three different kinds of deformations. While splay is related to the formation of radial patterns of the director and polarization field (see for instance panel (a) in Fig. 2.1), bending generates rounded circular patterns. Instabilities associated to such deformations underlie the establishment of topological defects in the liquid crystal arrangement, as it will be make more clear in the next Section. Twist is instead related to the coiling of the director field around an axis normal to the director itself (panel (b) in Fig. 2.1). Because of this, twist is only allowed in full 3D geometries, while there is no topological impediment to the development of splay and bending in bidimensional systems.

Table 2.1 summarizes the various contributions to free energy, both for polar and nematic systems. Here I made a distinction between uniaxial and biaxial nematics. As stated before, uniaxial nematics can be described by expanding the Q-tensor in terms of the only director field $\mathbf{n}$. In this fashion, the uniaxial free energy can be derived from the biaxial case by writing the $\underline{\underline{\mathbf{Q}}}$ tensor through Eq. (2.4).

Table 2.1 also provides a picture of the energetic cost due to different kinds of deformations in terms of $\mathbf{P}$ and $\mathbf{n}$, respectively for polar systems and uniaxial nematics, under the assumption of uniform ordering ($S = cost$). The most general case is pro-

vided by the elastic contributions in biaxial nematics and still applies to the uniaxial case with $S = S(\mathbf{r})$. In order to exploit which terms are related to which deformations, one should expand the $\underline{\underline{\mathbf{Q}}}$ tensor into the elastic biaxial free energy in terms of the director through Eq. (2.4); doing so and grouping splay, twist and bend contributions one finds, after some algebraic effort, that

$$L_1 = \frac{\kappa_3 + 2\kappa_2 - \kappa_1}{9S^2},$$

$$L_2 = \frac{4(\kappa_1 - \kappa_2)}{9S^2},$$

$$L_3 = \frac{2(\kappa_3 - \kappa_1)}{9S^3},$$

given that the Frank constants κ_i fulfil the condition $\kappa_3 \geqslant \kappa_1 \geqslant \kappa_2$ to guarantee the positivity of L_i [162]. In many practical situations it is convenient to adopt the single constant approximation, consisting in setting all elastic constants equal to the same value, leading to a much simpler form for the elastic free energy [29].

2.2.1. CHIRAL LIQUID CRYSTALS

Liquid crystal under certain conditions may also exhibit chiral features. Chiral nematic phase is similar to a nematic with the molecules on average pointing along a director and having no positional order of their centres of gravity. On a larger scale, however, the non-centrosymmetric molecules cause the director to be non-uniform and slowly rotate along a direction perpendicular to it (Fig. 2.2), giving rise to helicoidal patterns that breaks the mirror symmetry. The distance over which the director completes a full rotation is called the pitch, p. Chirality can be modelled [213] by introducing a suitable term in the free-energy that favours twist deformations:

$$f^{\text{cholesteric}} = (\nabla \times \underline{\underline{\mathbf{Q}}} + 2q_0 \underline{\underline{\mathbf{Q}}})^2 \tag{2.7}$$

in the free energy. The constant q_0 rules the cholesteric strength of the liquid crystal and is related to the helix pitch in accordance of the following relation $p_0 = 2\pi/q_0$.

Chirality plays a fundamental role in many biological systems which display a tendency to arrange in helicoidal structures [135, 220]. The most famous example of chiral biological material is the double helix of DNA filaments, that are known to arrange in cholesteric structures. A concentrated solution of DNA has long been known to exhibit a cholesteric or blue-phase in different salt conditions [116, 117]. This system can be also made motile when interacting with DNA- or RNA-polymerases or with motor proteins. Even actin filaments, exhibit chiral features: they are twisted in a right-handed direction [45] so that myosin motors tend to rotate the filaments while pulling them, generating a torque dipole that act as a source of angular momentum on the surrounding fluid.

2.2.2. ANCHORING

Boundary conditions of the director field, that is the alignment of liquid crystals molecules on the edge of the system volume, strongly control the liquid crystal structure. Because

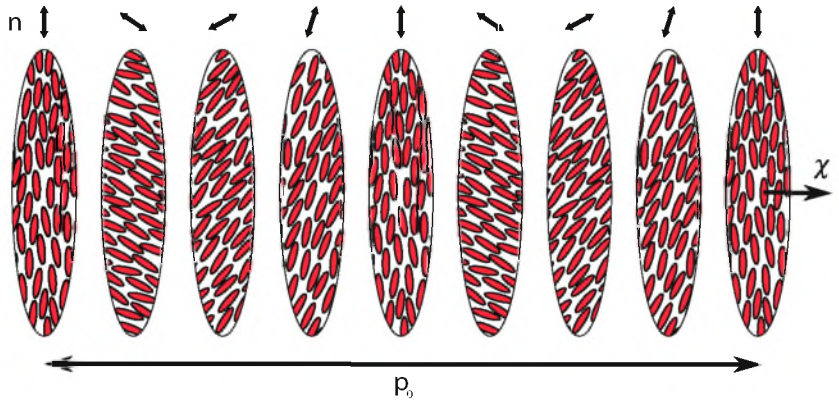

Figure 2.2: Structure of a chiral nematic. Locally the molecules have an average direction and therefore a director can be determined. On a longer scale, the chirality of the phase induces rotation of the director field around an axis χ perpendicular to the director. The distance along χ over which the director rotates by 2π is called the pitch, p_0.

of elastic interactions, the orientation of the liquid crystal molecules on the surface can propagate deep into the bulk and rules its structure and properties. Usually the orientation near a surface can be controlled with specific molecular interactions. More specifically, in most liquid crystals, molecules are hydrophobic and their tails do not combine with polar molecules such as water or glycerol. In this way it is possible to have a tangential (planar) orientation of oil-like liquid crystal molecules (Fig. 2.3a). Alternatively, on surfaces with long perpendicular apolar chains, the tails of molecules can penetrate such a layer and cause the director to be perpendicular (Fig. 2.3b).

Anchoring can be modelled with a surface energy term, which penalizes deviations of the order parameter $\mathbf{n}$ from a preferred direction $\mathbf{n}_0$. Following the Rapini-Popoul model [138] this term has the following form :

$$f^{\text{anchoring}} = -\frac{W}{2}(\mathbf{n}-\mathbf{n}_0)^2 , \tag{2.8}$$

where W determines the strength of the anchoring.

Yet another situation is the tendency of liquid crystal molecules to align in a preferential direction at the interface between two fluids. For instance microtubules bundles tend to anchor in a planar fashion at the interface between an oil-water interface, as

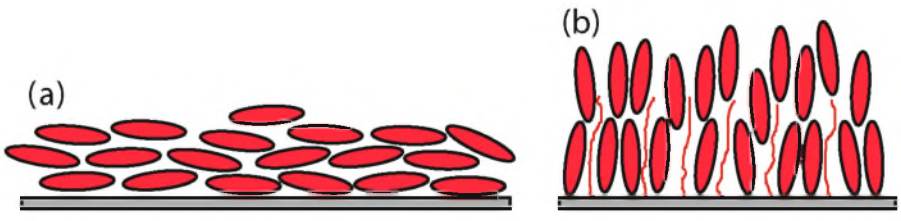

Figure 2.3: Cartoon of different orientations of liquid crystals molecules on interfaces: **(a)** tangential orientation is also called planar anchoring and **(b)** orientation normal to the interface is called homeotropic anchoring.

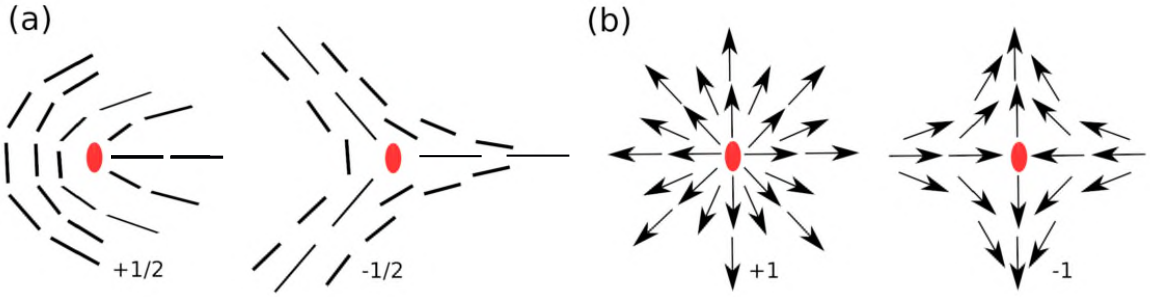

Figure 2.4: Sketch of (a) half-integer topological defects in 2D nematic liquid crystals, and (b) integer topological defects in polar liquid crystals. These can only host defects with integer winding number (see main text).

discussed in the Chapter 1. To include this feature in a thermodynamic description, a concentration field ϕ is needed to describe the phase separation between the two fluids. Anchoring of the liquid crystal molecules can be modelled at a thermodynamic level by adding a further term to the free-energy functional of the kind:

$$f_{\phi}^{anchoring} = -\tilde{W}\nabla\phi \cdot \underline{\underline{Q}} \cdot \nabla\phi. \tag{2.9}$$

In this case, anchoring will be tangential if $\tilde{W} > 0$ or hometropic otherwise.

Anchoring plays a fundamental role in active fluids. In fact, in the case of bacterial swimmers, it is commonly observed that, close to the boundaries, they orient along the wall direction [112]. In actomyosin solutions, the actin filaments can also be assumed to be anchored parallel to the walls due to focal adhesion [212]. Moreover, it has been shown that the orientation at the boundaries strongly influences the overall dynamical behaviour of the system, so that boundary conditions and anchoring properties must be chosen wisely to correctly model active suspensions. I will go back to the choice of the anchoring later in Section 2.3.1 where I will present a free energy functional that we made use of to model a polar active emulsion.

2.2.3. TOPOLOGICAL DEFECTS

Topological defects in a liquid crystal are commonly addressed as *disclinations, i.e.* regions where the order is lost and the order parameter cannot be properly defined [29, 39]. They play a relevant role in the dynamics of liquid crystals and are found to be closely related to the flow evolution in active fluids.

A topological defect can be characterized by looking at the configuration of the order parameter far from its core. This can be done by computing the *winding* number (or topological charge), which is a measure of the strength of the topological defect and is defined as the number of times that the order parameter turns of an angle of 2π while moving along a close contour surrounding the defect core. The allowed topological charges critically depend upon the nature of the order parameter: while polar systems only admit topological defects with integer winding numbers, nematic systems offer instead a wider scenario. In fact, by virtue of the head-tail symmetry, the headless nematic director can give rise to disclination patterns that also allows for half-integer winding numbers.

Fig. 2.4 shows the streamlines of the nematic (panel a) and polar (panel b) pattern in the neighbourhood of the defect core of defect of semi-integer and integer charge re-

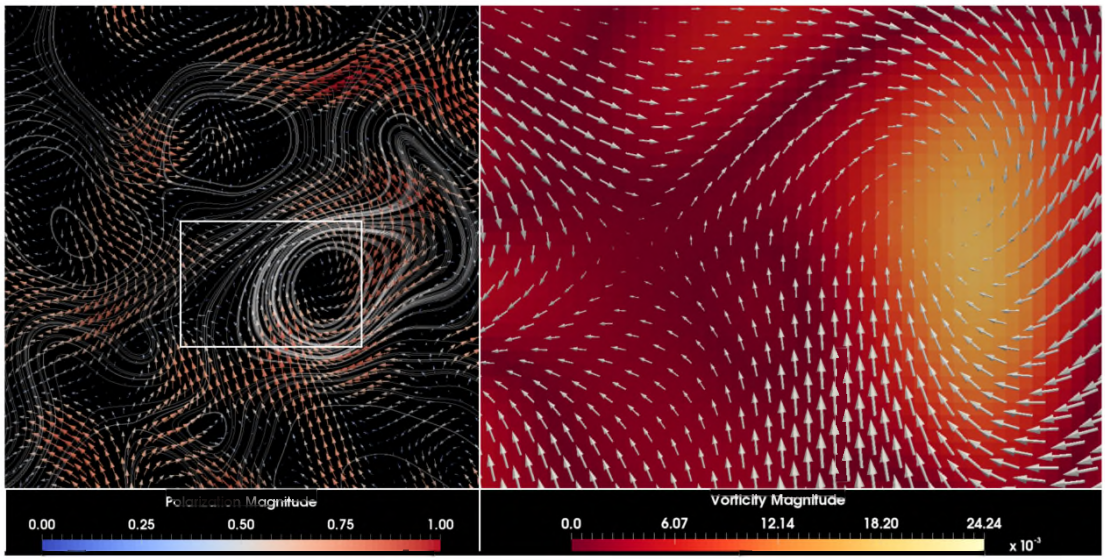

Figure 2.5: Defect dynamics in active polar systems. The left panel shows the polarization field, represented by arrows, with the superposition of velocity streamlines; red/long arrows correspond to ordered regions, while blue/short arrows are associated with the presence of topological defects, surrounded by regions with strong deformations of the polarization. Note that +1 defects act as a source of vorticity: indeed, most of the closed streamlines wrap the core of a defect. This is also shown in the right panel with the polarization field superimposed to the vorticity contour plot in the region highlighted by the white box in the left panel. Here two defects of charge ±1 are close. In proximity of the defect cores the polarization magnitude is approximately null and order is locally lost. These results have been produced integrating the dynamical equations presented in this Chapter with the hybrid lattice Boltzmann solver presented in the next Chapter. The parameter used are given in Chapter 5.

spectively, in a pure bidimensional system. It is worth to stress that there is no impediment for a nematic to set up into a integer defect configuration. Topological defects can develop in different geometries (a three-dimensional system, or a closed manifold – the surface of a sphere, for instance). In this latter case, it may happen that a topological defect is never stable and can always be reduced to an uniform configuration. Let us take, as an example, the +1 defect in panel (b) of Fig. 2.4 and let us allow the polarization field to have a component in the third dimension. The system would be then a *quasi*-2D system. In this situation, the topological defect can be easily removed by rotating the polarization so to have a uniform phase with all vectors normal to the plane where they were initially confined. This procedure shows that there are certain topologies that do not allow for *any* topological defect to be stable. Indeed a defect is said to be *topologically stable* if the configuration of the order parameter in the neighbourhood of the defect itself cannot be reduced to a uniform state by an homeomorphism – namely continuous transformation between two topological spaces. A general criterion to establish whether a defect is topologically stable or not, is to look at the dimension n of the order parameter. In a d-dimensional space, the condition that all the n components of the order parameter must vanish at the defect core defines a "surface" of dimension $d - n$. Hence defects exist if $n \leq d$. In Fig. 2.5, for example, we have a two-dimensional system ($d = 2$) with an order parameter (the polarization $\mathbf{P}$) having two components ($n = 2$), and the defects allowed are points (or vortices). However, point defects are unstable in quasi-2D systems, as in such case one would have $n > d$: indeed as we showed before in the previous example the vector field in proximity of a vortex can remove the defect

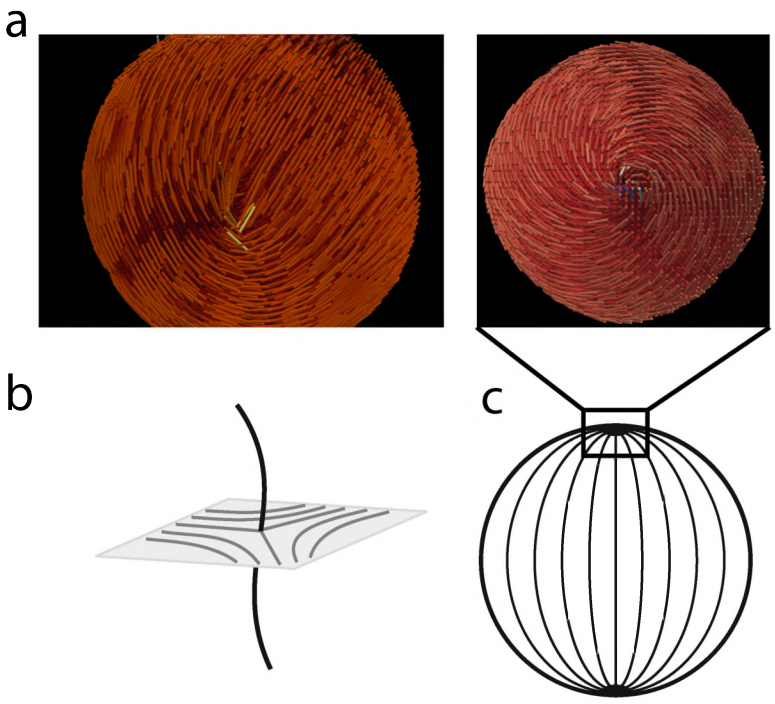

Figure 2.6: Half-integer winding number **(a)** are terminal points of disclination lines **(b)**. Integer winding numbers correspond to point defects called boojums **(c)**. These results have been produced integrating the dynamical equations presented in this Chapter with the hybrid lattice Boltzmann solver presented in the next Chapter. The parameter used are given in Chapter 4.

by *escaping* in the third dimension. In full three-dimensional systems ($d = 3$) one may have either point or line defects.

Point defects can also appear in bidimensional manifolds embedded in the full three-dimensional space. In this case, the sum of all topological charges in polar or nematic system confined to lay on the manifold obey a conservation law, which is connected to the Euler characteristic of the manifold [91]. For spherical confinement and planar alignment, the Poincaré-Hopf theorem requires a +2 total topological charge on the surface, which corresponds to the Euler characteristic of a sphere [84, 102]. For example, Fig. 2.6 shows on the top panel two possible configurations, achievable on the surface of a liquid crystal droplets under tangential anchoring conditions. On the right a +1 defect is visible, so that another defect of the same charge is formed at the antipodal point. On the left panel a 1/2 defect is shown and three other +1/2 defects are expected to form on the surface of the droplet to satisfy the Poincaré-Hopf theorem. In this latter case, the semi-integer defects are connected in pair by disclination lines that pierce the droplet so that the defect structure propagate even in the interior of the system.

The situation is yet different if homeotropic anchoring is imposed. In this case a defect is expected to form in the bulk, with a topological bulk charge that equals the half of the Euler characteristic of the respective geometry, according to the Gauss-Bonnet theorem, while the total topological surface charge is zero [84]. A nematic droplet would then relax into a configuration with a +1 point defect at the center with the outer pattern resembling a radial configuration (Fig. 2.7 left panel). But if the liquid crystal is chiral the situation becomes even more fascinating. For medium cholesteric power the point defect continuously deforms into an equatorial disclination line (Fig. 2.7 middle

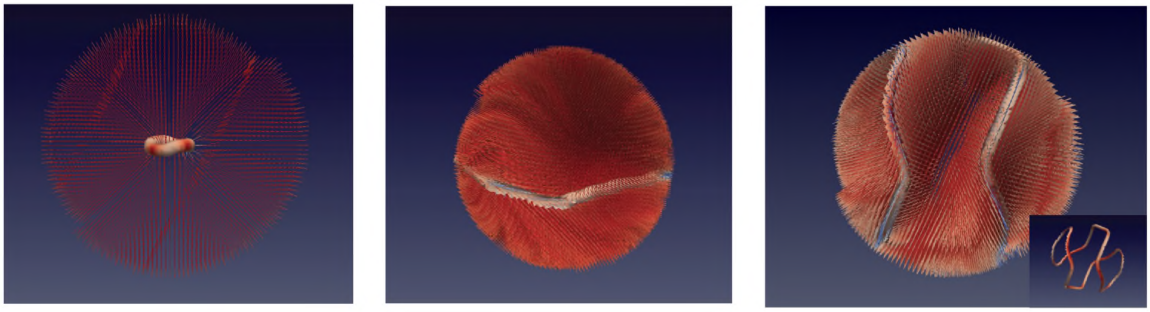

Figure 2.7: A nematic droplet with homeotropic anchoring relax to a configuration with a point defect at the center (left panel), while for medium cholesteric power a equatorial disclination line appear (middle panel). High cholesteric power causes the defects line to twist and the droplet relax to the *tennis ball* configuration (right panel).These results have been produced integrating the dynamical equations presented in this Chapter with the hybrid lattice Boltzmann solver presented in the next Chapter. The parameter used are given in Chapter 4.

panel) that may eventually end up, at stronger cholesteric power, into the *tennis ball* configuration, shown in the right panel of Fig. 2.7.

For what concerns active matter, topological defects were found to play a fundamental role in the set up of active turbulence and more in general in the flow properties of the system and, as I will report in Chapter 4, they also provide a route to motility in active cholesteric droplets. To better address how topological defects affect the hydrodynamics of an active fluid I plotted in Fig. 2.5 the polarization field in proximity of two defects of charge ± 1 in a full bidimensional active polar system. Here two competing mechanisms operate to determine the nematohydrodynamics: on one hand elastic relaxation of the nematic pattern tend to set up an ordered pattern, on the other hand activity enhances its deformations. More in the detail, because of elastic interactions the mutual attraction between the two oppositely charged defect generate a back-flow that couples their dynamics to the one of the underlying fluid [69, 196]. This is the mechanism driving the ordering dynamics of a passive liquid crystal where the nemato-hydrodynamic interaction set up by the attraction of oppositely charged defects move them closer, eventually leading to annihilation with each other. Activity plays instead the opposite role, since the regions interested by greater deformations are the ones where more energy is injected. Indeed, Fig. 2.5 also shows how defects act as a source of vorticity with the velocity field tilted with respect to polarization. If strong enough, activity may drive defects of opposite topological charge apart and suppress pair annihilation [69, 160] or under suitable conditions it may even furnish to the system enough energy to excite a pair of oppositely charged defects, starting from a totally ordered state. I will comment more on the interconnection between deformation of the liquid crystal and activity later on in this Chapter, when I will present how spontaneous flow emerges as the result of the bending/splay instability in active gels.

2.3. ACTIVE FORCES

So far I reviewed the well known theoretical description for liquid crystals and non-Newtonian fluids with anisotropic order parameters. I comment now on how the active behaviour of the constituents of the fluid can be expressed into a theoretical framework. The most direct way to develop the equations of motion for active systems at con-

tinuum level is by explicitly coarse-graining more detailed particle-based models [123, 154]. Before getting involved into the theoretical description, I will spend a few words in describing the swimming mechanism of some micro-organisms.

In general, the propulsive motion of active agents dispersed in a fluid creates a circulating flow pattern around each swimmer. The specific swimming mechanism of bacteria, for example, causes fluid to be expelled both forwards and backwards along the fore-aft axis, and drawn inwards radially towards this axis, creating an *extensile* flow pattern (Fig. 2.8). In some cytoskeleton extracts (such as the actomyosin protein complex), motor proteins can pull the filaments among themselves, causing them to contract lengthwise and giving rise to a *contractile* flow opposite to that of the previous example (Fig. 2.8).The typical flow pattern may be complicated in the near field, but in the far field is generically equivalent, at the lowest order, to the action of a force dipole [144] and can be represented as such. By summing the contributions from each force dipole and coarse-graining [169], it is possible to show that the stress exerted by the active particles on the fluid has the form

$$\sigma_{\alpha\beta}^{\text{active}} = -\zeta\phi Q_{\alpha\beta}, \tag{2.10}$$

where ζ is a phenomenological parameter that measures the activity strength, being negative for contractile systems and positive for extensile ones, while ϕ represents the concentration of the active material. Usually only terms linearly proportional to ζ are considered. In the case of polar active liquid crystals, the description can be carried out considering only the polarization field, re-expressing $\underline{\underline{\mathbf{Q}}}$ as a function of $\mathbf{P}$. The active stress in terms of the dynamical variable $\mathbf{P}(\mathbf{r}, t)$ takes the form

$$\sigma_{\alpha\beta}^{\text{active}} = -\zeta\phi\left(P_\alpha P_\beta - \frac{1}{d}|\mathbf{P}|^2\delta_{\alpha\beta}\right) . \tag{2.11}$$

The expressions Eq. (2.10)) and Eq. (2.11), have been largely applied in the study of active gels, but are not the only possible source of energy injection.

Previously, I commented on the importance of chirality on many biological mechanisms fundamental for the correct functioning of living entities, basically at cellular and intracellular level. It is then reasonable to investigate how chirality may influence local

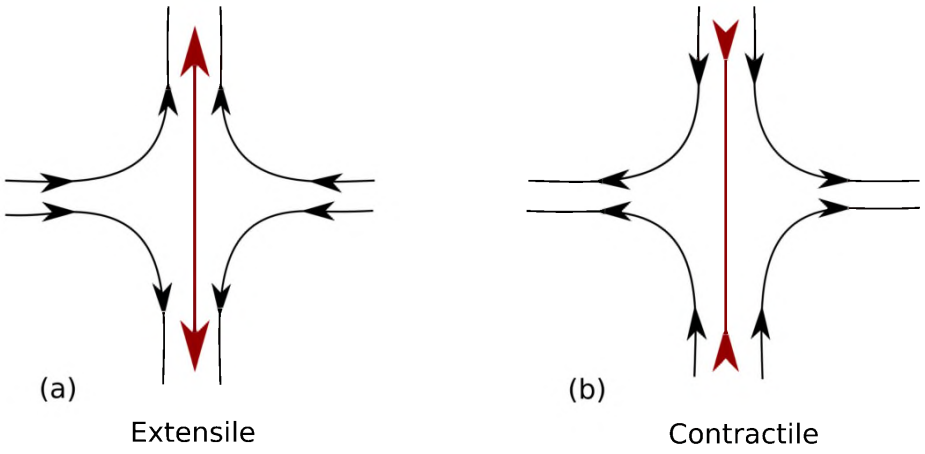

Figure 2.8: Cartoon of **(a)** extensile and **(b)** contractile flow (black lines), and force dipoles (red arrows).

energy supply. The effect of chirality, more than being taken into account by a suitable cholesteric term in the free energy, thus describing the cholesteric features of the fundamental constituents, can be incorporated in the description adding to the active stress extra terms, providing a source of angular momentum, that may arise due to the twisting motion of the active agents under suitable conditions. For instance, if the active particles act on the surrounding fluid with a net torque monopole, a coarse-graining procedure [61] shows that a suitable choice for the nematic chiral stress tensor is given by $\zeta_2 \epsilon_{\alpha\mu} Q_{\mu\beta}$ [122], where $\epsilon_{\alpha\mu}$ is the second order Levi-Civita tensor. Analogously, if the net torque is null but torque dipoles do not vanish, the corresponding stress tensor is given by $\zeta_2' \epsilon_{\alpha\beta\mu} \partial_\nu \phi (P_\mu P_\nu)$ [195], with $\epsilon_{\alpha\beta\mu}$ the third order Levi-Civita tensor. The sign of the second activity parameter ζ_2 or ζ_2' determines whether the stress generates a flux parallel ($\zeta_2, \zeta_2' > 0$) or antiparallel ($\zeta_2, \zeta_2' < 0$) with respect to the helicity of the twisting deformation. These terms drive the system out of equilibrium by injecting energy into it, and, once again, cannot be derived from a free energy functional. In this approach the active stress tensor enters the hydrodynamic equations governing the motion of the self-propelled particles suspension, as it will be discussed in Section 2.4. These are constructed from general principles, by assuming that an active gel may be described by (a) "conserved" variables, which take into account the fluctuations of the local concentration of suspended particles and the total (solute plus solvent) momentum density, and (b) "broken-symmetry" variables, which, in the nematic phase, is the deviation of the director field from the ground state.

A more general way to construct the equations of motion at a coarse-grained level, is to generalize the forces-and-fluxes approach [77] to active systems [99]. Considering for example an active gel characterized by polarization $\mathbf{P}$ and velocity $\mathbf{v}$, or equivalently by the strain rate tensor $u_{\alpha\beta} = (\partial_\alpha v_\beta + \partial_\beta v_\alpha)/2$, the generalized hydrodynamic equations can be derived using Onsager relations, thus expanding fluxes $\partial_t \mathbf{P}$ and the stress tensor in terms of their conjugate forces $-\delta F/\delta \mathbf{P}$ and $u_{\alpha\beta}$ respectively, with F polarization free energy. Active dynamics is obtained holding the system out of equilibrium by introducing a further pair of conjugate variables, namely the chemical potential difference between ATP and hydrolysis products and the rate of ATP consumption [99]. This approach can be further generalized [153] including thermal fluctuations, recasting the forces-and-fluxes approach in the language of coupled generalized Langevin equations [130].

2.3.1. FLUID MIXTURES WITH AN ACTIVE COMPONENT

The active stress expressions of Eqs. (2.10) and (2.11) depend on the concentration of the active material. This quantity in turn can be a dynamical field if one would like to take into account a inhomogeneous presence of the active material in the solution. At level of particle description, different kinds of models for mixtures of self propelled and passive units have been considered. For example, Brownian-like simulations [78, 131, 176] focused on the role of activity in separating the two components of the mixtures. In a continuum description, binary fluids with an active component have been studied in [10, 189, 191, 192] showing that the active part may cause instabilities on an active-passive interface. Here we only introduce, as an example among the different models that can be used to describe fluid mixtures with an active component, the free-energy

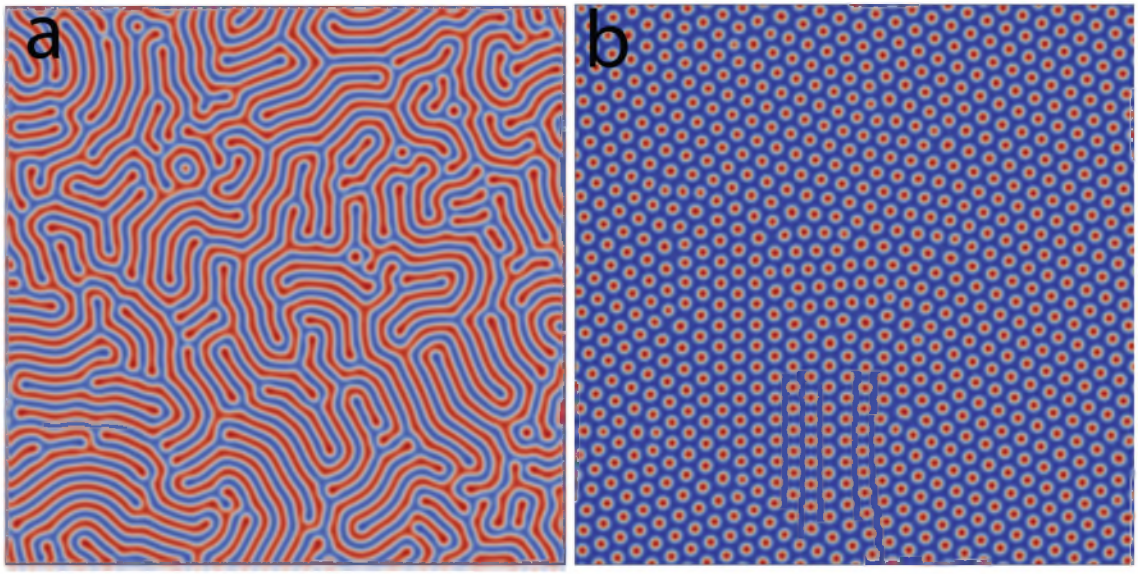

Figure 2.9: Snapshots of numerical simulations of the model having free energy given in Eq. (5.1), for symmetric **(a)** and asymmetric **(b)** compositions. Here, as in all the next images from numerical simulations, red corresponds to the polar phase, while blue corresponds to the isotropic one. These results have been produced integrating the dynamical equations presented in this Chapter with the hybrid lattice Boltzmann solver presented in the next Chapter. The parameter used are given in Chapter 5.

for a binary mixture where the active component is a polar gel [189]. It is given by

$$F\ [\phi,\mathbf{P}] = \int d\mathbf{r}\{\frac{a}{4\phi_{cr}^4}\phi^2(\phi-\phi_0)^2 + \frac{k}{2}\left|\nabla\phi\right|^2 \qquad (2.12)$$
$$-\ \frac{\alpha}{2}\frac{(\phi-\phi_{cr})}{\phi_{cr}}|\mathbf{P}|^2 + \frac{\alpha}{4}|\mathbf{P}|^4 + \frac{\kappa}{2}(\nabla\mathbf{P})^2 + \beta\mathbf{P}\cdot\nabla\phi\}\ .$$

The first term, multiplied by the phenomenological constant $a > 0$, describes the bulk properties of the fluid; it is chosen in order to create two free-energy minima, one ($\phi = 0$) corresponding to the passive material and the other one ($\phi = \phi_0$) corresponding to the active phase. The second one determines the interfacial tension between the passive and active phase, with k positive constant. The third and the fourth terms control the bulk properties of the polar liquid crystal. Here α is a positive constant and $\phi_{\rm cr} = \phi_0/2$ is the critical concentration for the transition from isotropic ($|\mathbf{P}| = 0$) to polar ($|\mathbf{P}| > 0$) states. The choice of $\phi_{\rm cr}$ is made to break the symmetry between the two phases and to confine the polarization field in the active phase $\phi > \phi_{\rm cr}$. The term proportional to $(\nabla\mathbf{P})^2$ describes the energetic cost due to elastic deformations in the liquid crystalline phase (see Table 2.1) in the single elastic constant approximation. Finally, the last term is a dynamic anchorage energy and takes into account the orientation of the polarization at the interface between the two phases. If $\beta \neq 0$, $\mathbf{P}$ preferentially points perpendicularly to the interface (normal anchoring): towards the passive (active) phase if $\beta > 0$ ($\beta < 0$). This choice for the anchoring is suggested by experimental observations. For instance, bacterial orientation at water-oil interfaces results from a relatively hydrophobic portion of each cell being rejected from the aqueous phase of the system [127].

Such model can be also extended to study active nematic gels, by using the nematic tensor in place of the polarization field [10, 48, 66, 69]. In this case the coefficients of the expansion of $Tr(\underline{\underline{\mathbf{Q}}}^n)$ in bulk free energy (see Table 1) would depend on the scalar field ϕ and the elasticity, again written in the single elastic constant approximation, would include a term of the form $L\partial_\alpha\phi Q_{\alpha\beta}\partial_\beta\phi$ (with L constant) to guarantee a perpendicular anchoring of the liquid crystal at the interface. This free energy, in absence of activity, gives rise to a lamellar phase (Fig. 2.9 a) for symmetric composition, and to a droplet phase for asymmetric one (Fig. 2.9 b).

We finally mention a recent generalization of such models where emulsification of the active component is favoured by the presence of surfactant added to the mixture [12]. This is done by allowing negative values of the binary fluid elastic constant k and by including a term of the form $\frac{c}{2}(\nabla^2\phi)^2$ (with c positive constant) to guarantee the stability of the free-energy.

A different continuum model, specifically introduced to study the motility induced phase separation (MIPS) without direct appeal to orientational order parameters $\mathbf{P}$ or $\underline{\underline{\mathbf{Q}}}$, but only to the scalar concentration field ϕ, is the so called Active-model H [187]. In the old classification by Hohenberg and Halperin [88], the passive model H considers a diffusing, conserved, phase separating order parameter ϕ coupled to an isothermal and incompressible fluid flow through the advection-diffusion equation that will be introduced in Section 2.4. The chemical potential that enters the dynamic equation of the passive model H is given by

$$\mu = \frac{\delta F}{\delta \phi} = a\phi + b\phi^3 - k\nabla^2\phi\,, \tag{2.13}$$

with a, b, k constants appearing in the Landau free energy for binary mixtures [15] (with a negative in order to have phase separation between the two fluid components and b and k positive for stability). The same terms appear in Eq. (5.1) without the polarization contributions. The active model is then constructed by adding a leading order time-reversal breaking active term of the form $\mu_a = \lambda_a\left(\nabla\phi\right)^2$ (with λ_a constant), not stemming from the free energy functional [187]. The deviatoric stress $\underline{\underline{\sigma}}$, that enters in the NS equations for the fluid flow, is, in d dimensions,

$$\sigma^{\text{active}}_{\alpha\beta} = -\hat{\zeta}\left(\partial_\alpha\phi\partial_\beta\phi - \frac{1}{d}\left(\nabla\phi\right)^2\delta_{\alpha\beta}\right), \tag{2.14}$$

and can be obtained from the free energy, according to the formula reported in the second row of Table 2.2, only if $\hat{\zeta} = k$. If $\hat{\zeta} \neq k$ this is not true any more and Eq. (2.14) is the sole leading-order contribution to the deviatoric stress for scalar active matter. Again here, $\zeta < 0$ describes contractile systems while $\zeta > 0$ the extensile ones. While μ_a has been found to create a jump in the thermodynamic pressure across interfaces and to alter the static phase diagram [210], the active stress $\underline{\underline{\sigma}}^{\text{active}}$ creates a negative interfacial tension in contractile systems that arrests the coarsening [187]. In Chapter 4 we will present a new scalar active matter to study the role of compressibility in self-motility.

Table 2.2: Explicit expressions of the elastic (first row) and the interface (second row) stress, and of the term **S** in the Beris-Edwards equation (2.21) (fourth row) for polar and nematic gels. The molecular field Ξ is a vector, with components h_α, for polar gels and a tensor $H_{\alpha\beta}$, for nematic gels, as shown in the third row. κ is the elastic constant of the liquid crystal; the flow-alignment parameters ξ and ξ' are respectively related to the polarization field **P** and to the nematic tensor $\underline{\underline{\mathbf{Q}}}$ and depend on the geometry of the microscopic constituents (for instance $\xi > 0$, $\xi < 0$ and $\xi = 0$ for rod-like, disk-like and spherical particles, respectively). In addition, these parameters establish whether the fluid is flow aligning ($|\xi| > 1$) or flow tumbling ($|\xi| < 1$) under shear. $\underline{\underline{D}} = (\underline{\underline{W}} + \underline{\underline{W}}^T)/2$ and $\underline{\underline{\Omega}} = (\underline{\underline{W}} - \underline{\underline{W}}^T)/2$ represent the symmetric and the antisymmetric parts of the velocity gradient tensor $W_{\alpha\beta} = \partial_\beta v_\alpha$.

	Polar Gel	Nematic Gel
$\sigma^{elastic}_{\alpha\beta}$	$\frac{1}{2}(P_\alpha h_\beta - P_\beta h_\alpha) - \frac{\xi}{2}(P_\alpha h_\beta + P_\beta h_\alpha) - \kappa \partial_\alpha P_\gamma \partial_\beta P_\gamma$	$2\xi'\left(Q_{\alpha\beta} - \frac{\delta_{\alpha\beta}}{3}\right) Q_{\gamma\nu} H_{\gamma\nu} - \xi' H_{\alpha\gamma}\left(Q_{\gamma\beta} + \frac{\delta_{\gamma\beta}}{3}\right)$ $-\xi'\left(Q_{\alpha\gamma} + \frac{\delta_{\alpha\gamma}}{3}\right) H_{\gamma\beta} - \partial_\alpha Q_{\gamma\nu} \frac{\delta \mathscr{F}}{\delta \partial_\beta Q_{\nu\gamma}} + Q_{\alpha\gamma} H_{\gamma\beta} - H_{\alpha\gamma} Q_{\gamma\beta}$
$\sigma^{interface}_{\alpha\beta}$	$\left(f - \phi \frac{\delta F}{\delta \phi}\right)\delta_{\alpha\beta} - \frac{\partial f}{\partial(\partial_\beta \phi)} \partial_\alpha \phi$	$\left(f - \phi \frac{\delta F}{\delta \phi}\right)\delta_{\alpha\beta} - \frac{\partial f}{\partial(\partial_\beta \phi)} \partial_\alpha \phi$
Ξ	$h_\alpha = \frac{\delta F}{\delta P_\alpha}$	$H_{\alpha\beta} = \frac{\delta F}{\delta Q_{\alpha\beta}} - \left(\frac{\delta F}{\delta Q_{\gamma\gamma}}\right)\delta_{\alpha\beta}$
S	$-\Omega_{\alpha\beta} P_\beta + \xi D_{\alpha\beta} P_\beta$	$[\xi' D_{\alpha\gamma} + \Omega_{\alpha\gamma}]\left(Q_{\gamma\beta} + \frac{\delta_{\gamma\beta}}{3}\right) + \left(Q_{\alpha\gamma} + \frac{\delta_{\alpha\gamma}}{3}\right)[\xi' D_{\gamma\beta} - \Omega_{\gamma\beta}]$ $-2\xi'\left(Q_{\alpha\beta} + \frac{\delta_{\alpha\beta}}{3}\right)(Q_{\gamma\delta}\, \partial_\gamma v_\delta)$

2.4. HYDRODYNAMIC EQUATIONS

In this Section I will introduce the hydrodynamic equations for active liquid crystals. Evolution equations for mass density $\rho(\mathbf{r}, t)$ and velocity $\mathbf{v}(\mathbf{r}, t)$ are given by

$$\partial_t \rho + \nabla \cdot (\rho \mathbf{v}) = 0, \tag{2.15}$$

$$\rho\,(\partial_t + \mathbf{v} \cdot \nabla)\,\mathbf{v} = -\nabla p + \nabla \cdot \underline{\underline{\sigma}}, \tag{2.16}$$

with the energy balance equation generally neglected in this context, since temperature fluctuations can be neglected. Eq. (2.15) is the continuity equation for mass density. In most of active matter systems Mach numbers Ma, defined as the ratio of the stream velocity and the speed of sound, is small; in such limit, this equation reduces to the solenoidal condition for the velocity field

$$\nabla \cdot \mathbf{v} = 0 + \mathscr{O}(Ma^2), \tag{2.17}$$

so that the fluid in this regime can be assumed at all practical effects as incompressible. Eq. (2.16) is the Navier-Stokes equation, where p is the fluid pressure enforcing the imcompressibility condition, and $\underline{\underline{\sigma}}$ is the stress tensor [8] that can be split into the equilibrium/passive and non-equilibrium/active contributions:

$$\underline{\underline{\sigma}} = \underline{\underline{\sigma}}^{passive} + \underline{\underline{\sigma}}^{active}. \tag{2.18}$$

The passive part is, in turn, the sum of three terms:

$$\underline{\underline{\sigma}}^{passive} = \underline{\underline{\sigma}}^{viscous} + \underline{\underline{\sigma}}^{elastic} + \underline{\underline{\sigma}}^{interface}. \tag{2.19}$$

The first term is the viscous stress, written as $\sigma^{viscous}_{\alpha\beta} = \eta(\partial_\alpha v_\beta + \partial_\beta v_\alpha)$, where η is the shear viscosity[2]. An explicit form for the elastic and interface stress is reported for the polar and nematic cases in Table 2.2.

The order parameter Ψ of the active liquid crystal (that is $\underline{\underline{\mathbf{Q}}}$ for nematics and $\mathbf{P}$ for polar systems) evolves according to

$$(\partial_t + \mathbf{v}\cdot\nabla)\,\Psi - \mathbf{S} = -\Gamma\Xi\,, \tag{2.21}$$

known as *Beris-Edwards equation*, within the theory of liquid crystal hydrodynamics described through the $\underline{\underline{\mathbf{Q}}}$-tensor. The term $\mathbf{S}$ accounts for the response of the orientational order to the extensional and rotational components of the velocity gradient and is reported for the polar [101, 175] and nematic [39] case in the fourth row of Table 2.2. The molecular field Ξ governs the relaxation of the orientational order to equilibrium, and is multiplied by a collective rotational-diffusion constant Γ. Its expressions are given in the third row of Table 2.2. The left-hand side of Eq. (2.21) is commonly addressed as material derivative of the order parameter Ψ, and can be formally derived making use of Liouville equations. In fact one can write $D_t\Psi = \partial_t\Psi + \{\Psi, \mathscr{H}\}$, where $\{...\}$ are the Poisson brackets and the Hamiltonian is $\mathscr{H} = F + \frac{1}{2}\int \rho\mathbf{v}^2$.

A more phenomenological procedure to derive the material derivative explicitly is based on the fact that order parameters can be advected by the fluid. Here we outline the procedure referring only to the polarisation field. We first note that the relative position $\tilde{\mathbf{r}}$ of two close points in the fluid evolves according to the following equation:

$$D_t\tilde{\mathbf{r}} = \partial_t\tilde{\mathbf{r}} + (\mathbf{v}\cdot\nabla)\tilde{\mathbf{r}} + \underline{\underline{D}}\cdot\tilde{\mathbf{r}} + \underline{\underline{\Omega}}\cdot\tilde{\mathbf{r}}, \tag{2.22}$$

where $\underline{\underline{D}}$ and $\underline{\underline{\Omega}}$ have been defined in Table 2.2. The first two contributions are the usual lagrangian derivative terms, while the third and fourth ones account respectively for rigid rotations and deformations of the fluid element. Thus the material derivative for the polarisation field will include the first three terms since a vector advected by the flow is capable to follow any rigid motion; for what concerns the last term in Eq. (2.22), this cannot enter directly into the material derivative of a vector field, but it must be weighted through an alignment parameter ξ, ruling the dynamical behavior of the vector field under enlargement and/or tightening of flow tubes. This allows us to obtain the material derivative for the polarization field simply substituting $\mathbf{P}$ in place of $\tilde{\mathbf{r}}$.

Finally the time evolution of the concentration field $\phi(\mathbf{r}, t)$ of the active material is governed by an advection-diffusion equation

$$\partial_t\phi + \nabla\cdot(\phi\mathbf{v}) = \nabla\cdot\left(M\nabla\frac{\delta F}{\delta\phi}\right), \tag{2.23}$$

where M is the mobility and $\delta F/\delta\phi$ is the chemical potential. A more generalized form of the material derivative has been used to model self advective phenomena, for example, actin polymerization in motile eukaryotic cells [191], by substituting $\nabla\cdot(\phi\mathbf{v}) \rightarrow \nabla\cdot(\phi\mathbf{v} + w\mathbf{P})$, where w is a constant related to the velocity of actin polymerization.

[2] In the compressible case, the viscous stress tensor also includes a term proportional to the divergence of the velocity, such that:

$$\sigma^{viscous}_{\alpha\beta} = \eta(\partial_\alpha v_\beta + \partial_\beta v_\alpha) + \left(\tilde{\zeta} - \frac{2\eta}{d}\right)\partial_\gamma v_\gamma \delta_{\alpha\beta}, \tag{2.20}$$

where we denoted the bulk viscosity with $\tilde{\zeta}$.

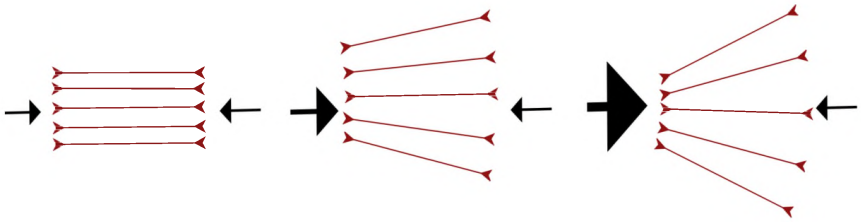

Figure 2.10: Sketch of instability and spontaneous symmetry breaking mechanism for contractile systems. When the system is completely ordered (left panel) force dipoles compensate each other, while if a splay deformation is present (middle panel) the density of contractile forces is greater on the left than on the right. This determines a flow that produces further splay (right panel), resulting in a macroscopic flowing state. Adapted from [125].

2.5. SPONTANEOUS FLOW

Many remarkable phenomena in the physics of active fluids are related to the flow behaviour induced by the presence of active forcing in the dynamical description of the system. The first effect that was studied, to which this section is devoted, is the occurrence of spontaneous flow in fluids with sufficiently strong activity.

This phenomenon occurs in active gels as the effect of the development of nematohydrodynamic instabilities to bending/splay deformations in the liquid crystal pattern, when extensile/contractile activity is considered. The mechanism underlying the onset of self-sustained flows lies in the structure of the active stress tensor that is proportional to the Q-tensor, so that the active forcing it is proportional to its gradients $\nabla \cdot \underline{\underline{Q}}$. Perturbations of an ordered state in the liquid crystal arrangement may generate a flow field that may eventually propagate so to drive the system out of the quiescent state, strengthening deformations and the corresponding flow, until the system sets either in a stationary state characterized by a net flux of momentum or in a chaotic state where flow coherence is lost.

Extensile and contractile suspensions exhibit different instabilities according to the particular kind of deformation. To gain an insight into the onset of spontaneous flows, let us consider the case of contractile dipoles initially perfectly ordered, as in the sketch on the left of Fig. 2.10. In this situation the force dipoles balance each other and the net flow, obtained by the sum of those due to single dipoles as represented in Fig. 2.8, is null. However, if a small splay deformation is present (middle panel in Fig. 2.10), the density of contractile forces on the left is larger than that on the right, and a flow sets up. Such flow causes further splay which destabilizes the system that starts to flow macroscopically. For extensile activity, under the same splay deformation, the initial flow (directed to the left in this case, see Fig. 2.8) would align the dipoles and no net macroscopic flow would appear. By a similar argument, it can be shown that extensile fluids get unstable to bend deformations.

To give a simple quantitative proof for the occurrence of instability we can consider a simple quasi one dimensional geometry. Let us consider an active slab confined between two planes, perpendicular to the x axis, at $x = 0$ and $x = L$. For simplicity we also assume that dipoles always lies in the xy plane with constant concentration $\phi = 1$. As initial state we take an active fluid in the disordered phase with all the components of the velocity v_α, $\alpha = x, y$, and the polarization p_α set to zero. In this simplified geome-

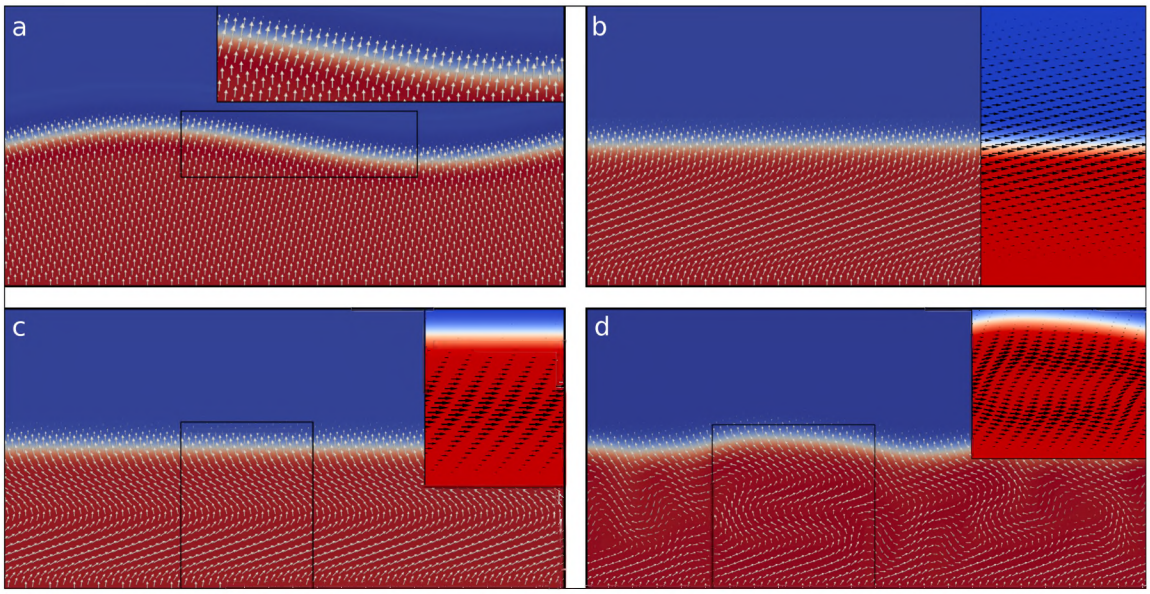

Figure 2.11: Instability and spontaneous flow in extensile mixtures. The polarization field is confined in one of the phases of a binary mixture and satisfies homeotropic anchoring both at the lower bound of the channel and at the interface between the two fluid components; moreover the interface is modulated in a sinusoidal fashion, determining a weak splay instability in the polarization field, as shown in panel (a). Inset shows detail of the polarization at interface. Starting from this configuration and turning on extensile activity, two regimes are found. For weak active doping ($\zeta = 5 \times 10^{-4}$), shown in panel (b), the interface relaxes towards a flat profile and the polarization pattern undergoes bending deformations, while the velocity field, shown in the right part of panel (b), is parallel to direction of the channel and confined in proximity of the interface. If activity is raised ($\zeta = 10^{-3}$), the bending deformations are tightened (as clearly visible in panel (c)) and a unidirectional flow field develops in centre of the polar fluid and mostly parallel to the walls (see the corresponding inset). When active doping exceeds a critical threshold ($\zeta = 3 \times 10^{-3}$ in panel (d)) the polarization field undergoes instabilities leading to the formation of chaotic non-stationary patterns. In such condition the interface loses its flat profile, although the velocity field remains roughly parallel to the channel direction. The velocity field plotted in insets of panels (b), (c) and (d) has been rescaled for readability (the averaged velocity magnitude grows from $|\mathbf{v}| \simeq 3.5 \times 10^{-3}$ to $\simeq \times 10^{-2}$ in lattice units when ζ goes from 5×10^{-4} to 3×10^{-3}). The free energy used in these simulations is given in Eq. (5.1) with $a = 4 \times 10^{-2}$, $k = 4 \times 10^{-1}$, $\alpha = 10^{-3}$, $\kappa = 10^{-2}$ and $\beta = 10^{-2}$, while mobility $M = 10^{-1}$ and aligning parameter $\xi = 1.1$. These results have been produced integrating the dynamical equations presented in this Chapter with the hybrid lattice Boltzmann solver presented in the next Chapter. The parameter used are given in Chapter 5.

try we can assume $\mathbf{v} = (0, v(x), 0)$, and the only non zero component of the active stress $\sigma^{\text{active}}_{xy} = q(x)$. The hydrodynamic equations then read:

$$\partial_t v = \eta \partial_x \partial_x v - \zeta \partial_x q, \tag{2.24}$$

$$\partial_t q = K \partial_x \partial_x q - a q + \xi \partial_x v, \, . \tag{2.25}$$

Here K is a diffusive term, with the physical meaning of elastic constant, penalizing changes in the orientational order. These oversimplified equations are enough to trigger a non equilibrium phase transition from a quiescent disordered phase to a spontaneously flowing state. Rewriting the above equations in Fourier space,

$$\partial_t \hat{v} = -k^2 \eta \hat{v} - ik\zeta \hat{q} \tag{2.26}$$

$$\partial_t \hat{q} = -K k^2 \hat{q} - a \hat{q} + \xi \partial_x v \ , \tag{2.27}$$

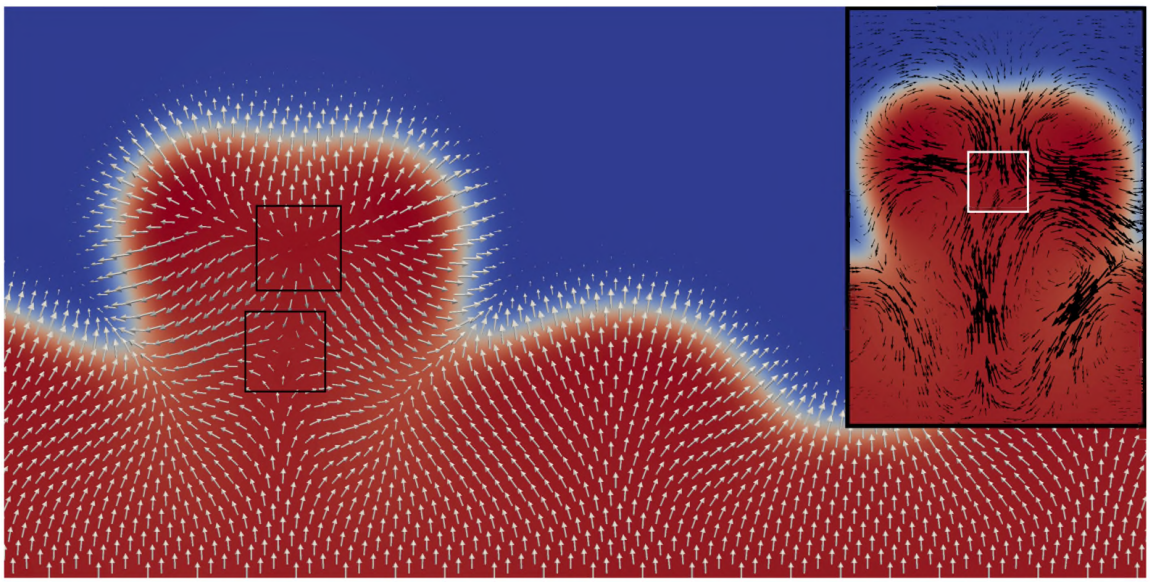

Figure 2.12: Splay deformation and defect formation in a contractile mixture ($\zeta = -3 \times 10^{-2}$). Other free-energy parameters and initial conditions are the same as in Fig. 2.11. The strong contractile activity leads to a catastrophic dynamics: the polarization splay deformation of the initial condition is tightened until the initial sinusoidal shape in the interface between the two fluids is completely lost and replaced with an undulated profile, as clearly visible in the centre of the system. Notice also the formation of two defects of opposite charge that have been framed with two black squares. Defect formation strongly influences the hydrodynamics of the system, as shown in the inset, where the velocity field develops a quadrupolar flow in their neighbourhood. These results have been produced integrating the dynamical equations presented in this Chapter with the hybrid lattice Boltzmann solver presented in the next Chapter. The parameter used are given in Chapter 5.

and recasting in matrix form, we have

$$\partial_t \begin{pmatrix} \hat{v} \\ \hat{q} \end{pmatrix} = \underbrace{\begin{pmatrix} -\eta k^2 & -ik\zeta \\ ik\xi & -a - k^2 K \end{pmatrix}}_{A} \begin{pmatrix} \hat{v} \\ \hat{q} \end{pmatrix} .$$

We want to evaluate the stability of the disordered state, and to to that we have to add small fluctuations around this state and follow the evolution of the velocity and polarization. This problem, in our linearised version, is equivalent to finding the eigenvalues of the operator A. If they are both negative, the disordered quiescent state is stable, with any fluctuations decaying exponentially with time. If at least one of the eigenvalues is positive, the state is unstable and the system would start to flow. Considering that eigenvalues of a 2×2 matrix can be expressed in terms of the trace (tr) and determinant (det)

$$\lambda_{1,2} = \frac{1}{2}\left(\mathrm{tr} \pm \sqrt{\mathrm{tr}^2 - 4det}\right) , \tag{2.28}$$

and given the fact that in our case

$$\begin{aligned} \det A &= \eta k^2 (a + k^2 K) - k^2 \xi \zeta \\ \mathrm{tr} A &= -a - k^2 (K + \eta) < 0 , \end{aligned} \tag{2.29}$$

we see that either both eigenvalues are negative, or $\lambda_1 < 0$ and $\lambda_2 < -\lambda_1$. The latter condition implies that the quiescent state is unstable to small perturbations for extensile systems ($\zeta > 0$).

The spontaneous flow instability for contractile systems was analysed in [202] for the simple geometry of a bidimensional thin film confined on a one-dimensional substrate, with planar anchoring on the confining boundaries. For small thickness or small activity, boundary effects are prevailing and the gel remains in an unperturbed, static, homogeneously polarized state. Above a critical thickness or a critical activity, a polarization tilt appears and the system flows with a finite shear gradient. The study has been later extended to films where undulations of the free surface are also considered [123, 161]. In particular Sankararaman et. al [161] constructed dynamical equations for the concentration and the polarization field, and for the height of the film thickness. Activity was found to have two main effects on the evolution of the height field: (i) a splay induced flow that tilts the free surface and (ii) an active contribution to the effective tension. The latter can be understood by noting that active stresses pull (contractile) or push (extensile) the fluid in the direction of the long axis of the particles, giving additional elastic contribution to the stretching along that axis. By stability analysis arguments they found that, for contractile stresses, splay destabilizes the surface, while the activity contribution to tension tends to stabilize it. For extensile activity the opposite happens.

The previous results are illustrated in Figs. 2.11 and 2.12. Here the onset of instability and spontaneous flow are shown for the polar active binary mixture described in Section 2.3.1, in which an active polar gel (red) coexists with a passive component. Homeotropic anchoring is set both at the lower bound of the channel and at the interface between the two fluid components. In order to study stability with respect to bending, the interface is initially modulated by a sinusoidal perturbation. This determines a weak splay pattern in the polarization field, as shown in Fig. 2.11(a) and in its inset, in which white arrows represent the polarization field. As expected, the extensile system is stable under the initial splay deformations, so that, by increasing activity, these are replaced by stationary bending patterns (see Fig. 2.11(b)). They are accompanied by macroscopic flows, as it can be seen by looking at the velocity field, denoted with black vectors in the zooms of panels 2.11(b) and 2.11(c), with the magnitude of velocity growing linearly with ζ. Then, further increasing activity, the polarization field becomes unstable (Fig. 2.11(d)) and the flow looses laminar character. Bends in the pattern give rise to non uniform fluxes, generating complex structures in the velocity field. A different behaviour results with contractile activity. When it is strong enough, it tightens splay deformations of the initial condition of the polar field until, as shown in Fig. 2.12, the initial sinusoidal shape of the interface between the two fluids is completely lost and replaced by an irregular profile driven by splay polarization deformations. Fig. 2.12 also shows the presence of two defects of opposite charge (+1 and −1), framed with two black squares. They strongly influence the velocity pattern of the system, as shown in the inset where a quadrupolar flow can be observed in their neighbourhood.

Spontaneous flow was systematically analysed numerically in [124, 125]. A slab of active nematic liquid crystal confined between two fixed parallel plates at a distance L was studied by a hybrid version of LBM, with different anchoring conditions. The active nematic model is the same of that described in previous sections. The dynamics of the order parameter $\underline{\underline{\mathbf{Q}}}$ is governed by Eq. (2.21), with Ξ replaced by $\underline{\underline{\mathbf{Q}}}$ and $\mathbf{S}$ given in the last row of Table 2.2, with an extra active term, besides the active stress term in the Navier-Stokes equations, of the form $\lambda\underline{\underline{\mathbf{Q}}}$ on the right-hand side of Eq. (2.21). This

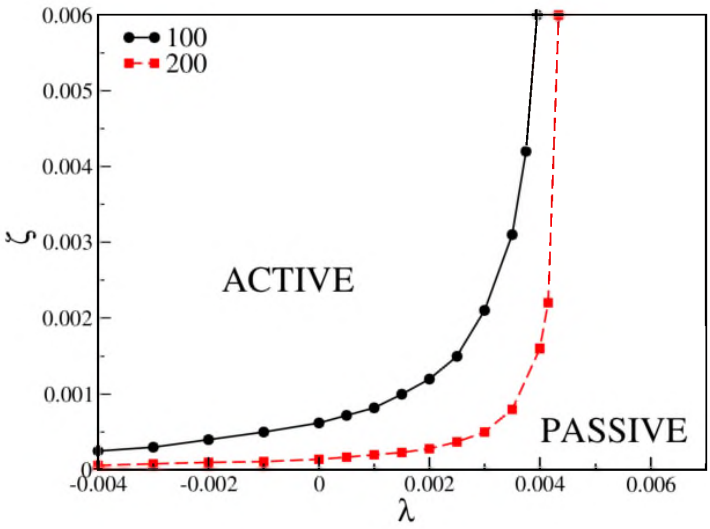

Figure 2.13: Phase diagram for spontaneous flow obtained by Marenduzzo *et al.* [125], in the two activity parameters plane (λ,ζ) for an active nematic liquid crystal. The lines separate regions of passive immotile state, and active, macroscopic motile state for two different system sizes. A slab of material is considered with homogeneous anchoring at the boundaries and flow aligning parameter $\xi = 0.7$.

term was suggested on the basis of symmetry considerations and also obtained by a microscopic derivation in [154]. Though a linear term in the nematic stress tensor also appears in the molecular field, the extra term here introduced can be regarded as *active*, also because no counterpart is included in the stress tensor. Positive (negative) values of λ enhance (attenuate) self-aligning features of the nematic network, so that $\lambda > 0$ can be chosen to model actomyosin suspensions at high concentration, and $\lambda < 0$ to model dilute emulsions.

The main results concerning the occurrence of spontaneous flow are summarized in Fig. 2.13 for two different system widths $L = 100,200$, which confirm the presence of a transition between a passive and an active phase as predicted analytically. Flow properties in the active phase are reported not to depend on the value of λ. For small ζ there is no flow and the polarization field is homogeneous. If ζ is strong enough, the system sets in the active phase, where a spontaneous flow is observed, while decreasing L leads to a reduction of the active region in the parameter space. Alongside the activity parameters ζ and λ, the other key parameter is the flow alignment parameter ξ (see Table 2.2). In fact, the transition is attained for sufficiently extensile suspensions, in the case of flow-aligning ($|\xi| > 1$) liquid crystals, and for sufficiently contractile ones for flow-tumbling materials ($|\xi| < 1$). In the flow-aligning case the velocity profile is characterized by the presence of bands, i.e. areas of constant shear rate, separated by narrow regions where the shear gradient reverses, similar to shear bands in non active materials [58] with the number of wavelengths in the channel increasing with ζ. Flow tumbling materials rearrange themselves so that only the two boundary layers flow in steady state. Simulations with periodic boundary conditions show additional instabilities, with the spontaneous flow appearing as patterns made up of convection rolls. Boundary conditions for the model in [124] are described in detail in [126], while the numerical method in [141]. The phase diagram was studied, for a quasi-1d system, in [51], extending previous works to the whole (ξ,ζ) plane, varying also the initial orientation of the director field.

A detailed numerical study of the dynamical spontaneous flow transition in polar active films is presented in [67]. In this work the effects of varying concentration were explicitly taken into account. The free-energy of the model is similar in spirit to that of Eq. (5.1) but only one phase for the concentration of the active fluid is considered (the free-energy is at most quadratic in the concentration field and no phase separation can occur). The transition to spontaneous flow is characterized by a phase diagram in a plane of two variables, related to activity ζ and to a parameter controlling self-advection[3]. For high values of activity and self-advection parameters a phase characterized by spontaneous periodic oscillatory banded flows is observed. The latter, accompanied by strong concentration inhomogeneities, can also arise in active nematics, although with a physically distinct origin.

The occurrence of spontaneous flow may also be accompanied by the formation of topological defects. In fact the dynamics of order parameter and velocity fields are interconnected through a feedback loop (see Fig. 2.12). The hydrodynamical instabilities give rise to lines of distortions in the order parameter field that are unstable to the formation of defect pairs [69]. In [184, 185] an extensile active nematic has been considered and the dynamics of defects characterized. Two main stages have been identified: first, ordered regions undergo hydrodynamic instability generating lines of strong bend deformation that relax by forming oppositely charged pairs of defects. Then, annihilation of defect pairs of different charge restores nematic ordered regions which may then undergo further instabilities. In passive liquid crystals the coupling between the order parameter and the flow has significant effects on the motion of defects, generating a more intense flow around positively charged defects than for negatively charged ones [196]. This phenomenon is still present in active liquid crystals, as suggested by the quadrupolar flow centred around the +1 defects in the inset of Fig. 2.12. The presence of activity gives rise to an even richer phenomenology. Full defects hydrodynamics in $2d$ polar active fluids was studied by lattice Boltzmann simulations with a hybrid scheme in [53]. In this paper it was found that extensile activity favours spirals and vortices, like the defect highlighted by a square in Fig. 2.11d, while contractile activity favours aster-like defects in the polarization field like the ones boxed in Fig. 2.12. Defect-defect interactions have also been studied. In a contractile fluid two asters repel each other reaching a steady state with a fixed distance, that increases at larger activity. In the extensile case two asters turn into two rotating spirals, leading to a final state where the rotation continues at approximately constant rotational velocity. For low activity the angular velocity increases with ζ, while above a critical value an oscillatory behaviour is observed, where half clockwise rotation is followed by half anticlockwise one, resembling the previous cited oscillatory and then chaotic behaviours appearing in spontaneous flow transition for high activity [124].

As we saw in this chapter, confinement of polar/nematic pattern triggers the formation of defects, thus their dynamics is found to be particularly rich in drops of active fluids.

[3] In [67], together with the active stress tensor $\sigma^{\text{active}}_{\alpha\beta}$ of Eq. (2.11), the term $\tilde{\beta}(\partial_\beta P_\alpha + \partial_\alpha P_\beta)$ is also considered. This, primary to polar systems, arises from "self-propulsion" of the active units, taking into account higher order contributions in gradients in the coarse-graining [169] procedure that leads to Eq. (2.11). This extra contribution complements the modified advected term in the evolution equations of the order parameters (discussed at the end of Section 2.4) that allows for the description of self advective phenomena.

3

LATTICE BOLTZMANN METHODS

A certain number of numerical approaches are available when dealing with the description of fluid systems; each of them can be classified according to the level of spatial approximation. The full spectrum of scales in fluid flows ranges from nanometres, like in nano fluids, to kilometres, like in clouds. The various flow regimes are classified according to the Knudsen number, $\epsilon = \lambda/L$, which is the ratio of the mean free path of molecules λ to a characteristic flow length L. As ϵ goes from zero to infinity, the flow exhibits four regimes: continuum ($\epsilon < 0.01$), slip flow ($0.01 < \epsilon < 0.1$), transitional flow ($0.1 < \epsilon < 10$) and free molecular flow ($\epsilon > 10$). The Navier-Stokes equation is only valid in the hydrodynamic regime, while the Boltzmann equation is valid in all the flow regimes.

Since the 1970s, general-purpose computational fluid dynamics (CFD), based on solving the Reynolds-averaged Navier–Stokes (RANS) equations, has been developed to compute fluid flow, heat transfer and combustion with considerable success. With the availability of more computational resources, more accurate but computationally demanding methods such as large eddy simulation (LES) and direct numerical simulation (DNS) have been in increasing use. These macroscopic methods, however, are all based on the assumption of continuum, which makes it difficult or even impossible to treat certain physical phenomena, especially at micro- and meso-scales.

More fundamental approaches are particle-based (i.e. molecular cluster-based) discrete methods, such as molecular dynamics (MD), direct simulation Monte Carlo (DSMC), dissipative particle dynamics (DPD) and multi-particle collision dynamics (MPCD). These methods are capable of simulating phenomena where the continuum assumption breaks down. On the other hand, these methods have a high computational cost for the majority of problems of practical concern. The lattice Boltzmann (LB) method, is placed in the middle of the hierarchy of modelling and simulation methods (Fig. 3.1). The corner stone of the LB method is the Boltzmann equation

$$\partial_t f + \xi_\alpha \partial_\alpha f + \frac{F_\alpha}{\rho} \partial_{\xi_\alpha} f = \Omega(f) \ , \tag{3.1}$$

where $\Omega(f)$ is the collision operator, and F_α the body force. The Boltzmann equation describes the evolution of the distribution function $f(\mathbf{r}, \xi, t)$, which represents the density of particles with velocity ξ at position $\mathbf{r}$ and time t. At steady state, in absence

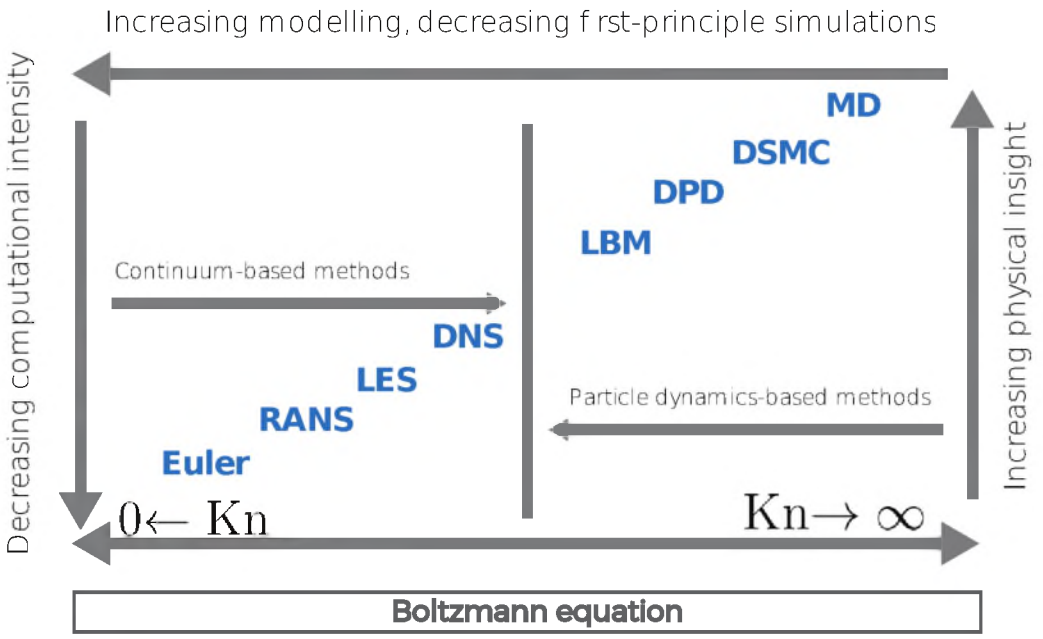

Figure 3.1: Hierarchy of simulation approaches.

of any external force, the solution of the Boltzmann equation becomes the Maxwell-Boltzmann distribution function f^{eq}

$$f^{eq}(\rho, \mathbf{v}, T, \xi) = \frac{\rho}{(2\pi RT)^{d/2}} \exp\left(-\frac{(\xi - \mathbf{v})^2}{2RT}\right) , \tag{3.2}$$

written in terms of the macroscopic density ρ, velocity $\mathbf{v}$ and temperature T. In the above expression d is the number of spatial dimensions and R the gas constant. A proper choice of the collision operator $\Omega(f)$ allows some relevant quantities to be conserved during time-evolution. These are the moments of the distribution functions that bridge the mesoscopic dynamics to the continuum hydrodynamic theory (here written for $d = 3$):

$$\int f(\mathbf{r}, \xi, t) d^3\xi = \rho(\mathbf{r}, t) , \tag{3.3}$$

$$\int f(\mathbf{r}, \xi, t) \xi d^3\xi = \rho(\mathbf{r}, t)\mathbf{v}(\mathbf{r}, t) , \tag{3.4}$$

$$\int f(\mathbf{r}, \xi, t) \frac{\xi^2}{2} d^3\xi = \rho(\mathbf{r}, t) E(\mathbf{r}, t) , \tag{3.5}$$

$$\int f(\mathbf{r}, \xi, t) \frac{|\xi - \mathbf{v}|^2}{2} d^3\xi = \rho(\mathbf{r}, t) e(\mathbf{r}, t) , \tag{3.6}$$

$$\tag{3.7}$$

where $E(\mathbf{r}, t)$ is the total energy, while $e(\mathbf{r}, t)$ the internal energy. By taking the continuum limit, *i.e.* by requiring the Knudsen number to be small enough, these relations let to recover the Navier-Stokes equation starting from the Boltzmann equation. The idea at the base of the lattice Boltzmann method is to exploit this property and to simulate the evolution of the distribution functions of fluid system by means of a discretized

version of Eq. (3.1). As I will make clear in the following, this approach has a number of peculiarities that make it successful in the treatment of fluid flows because of its stability and accuracy features. This Chapter is devoted to lattice Boltzmann method and I will first go through a general introduction of the method in Section 3.1, while in Section 3.2 I will show how the continuum equations can be recovered starting from the algorithm by means of a Chapman-Enskog expansion. The case of a simple fluid is treated in Section 3.3 while a procedure to adapt the numerical scheme to the case of multiphase flows and liquid crystal is provided in Sections 3.4 and 3.5, respectively. The boundary condition problem is taken into account in Section 3.6 while the last Sections are devoted to some numerical tests concerning error analysis (Section 3.7) and code-scalability features of lattice Boltzmann in parallel computing.

3.1. GENERAL FEATURES OF LATTICE BOLTZMANN METHOD

The lattice Boltzmann approach to hydrodynamics is based on a phase-space discretized form of the Boltzmann equation [7, 32, 159, 177, 211] for the distribution function $f(\mathbf{r}, \xi, t)$, describing the fraction of fluid mass at position $\mathbf{r}$ moving with velocity ξ at time t. Since space and velocities are discretized, the algorithm is expressed in terms of a set of discretized distribution functions $\{f_i(\mathbf{r}_\alpha, t)\}$, defined on each lattice site $\mathbf{r}_\alpha$ and related to a discrete set of N lattice speeds $\{\xi_i\}$, labelled with an index i that varies from 1 to N (see Fig. 3.2). In the case of the *collide and stream* version of the algorithm, the evolution equation for the distribution functions has the form

$$f_i(\mathbf{r} + \xi_i \Delta t, t + \Delta t) - f_i(\mathbf{r}, t) = \mathscr{C}(\{f_i\}, t), \tag{3.8}$$

where $\mathscr{C}(\{f_i\}, t)$ is the collisional operator that drives the system towards equilibrium, and depends on the distribution functions; its explicit form will depend upon the particular implementation of the method. Eq. (3.8) describes how fluid particles collide in the lattice nodes and move afterwards along the lattice links in the time step Δt towards neighbouring sites at distance $\Delta x = \xi_i \Delta t$. This latter relationship is no more considered in finite difference lattice Boltzmann models (FDLBM) [22, 36, 109, 132, 170, 172]. In this kind of models the discrete velocity set can be chosen with more freedom, making possible to use non uniform grids, selecting lattice velocities independently from the lattice structure. This approach is found to be extremely useful when it is necessary to release the constraint of having a constant temperature in the system [72, 207]. Moreover it might be also helpful in the case of LB models for multicomponent systems where the components have different masses and this would result in having different lattice speeds, one for each fluid species. Beside the wider range of applicability of the FDLBM with respect to the LBM, the latter furnishes a simple and efficient way to solve hydrodynamic equations.

When dealing with FDLBM it is useful to introduce more than only one set of distribution functions $\{f_{ki}\}$, where the extra index k labels different sets of discrete velocities $\{\xi_{ki}\}$, with index i still denoting the streaming direction. The evolution equation for distribution functions for the FDLBM reads:

$$\partial_t f_{ki} + (\xi_{ki} \cdot \nabla) f_{ki} = \mathscr{C}(\{f_{ki}\}, t). \tag{3.9}$$

Here differential operators must be discretized: Runge-Kutta or midpoint schemes can

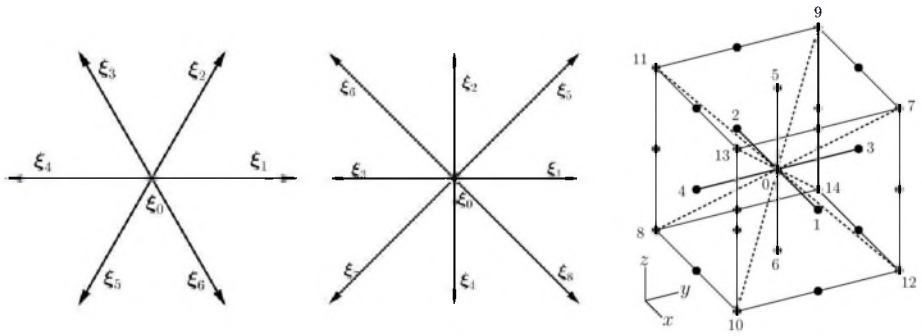

Figure 3.2: Graphical representation of lattice velocities for the triangular $d2Q7$, face centered squared $d2Q9$ and $d3Q15$ lattices, respectively, shown in the left, center and right panels. Cartesian components of lattice vectors ξ_i are found in Table 3.1.

be used to compute the time derivative while there are several possibilities to compute the advective term on the left-hand side of the previous equation.

In the case of a simple fluid, in absence of any external force, assuming the BGK approximation with a single relaxation time [9], one writes

$$\mathscr{C}(\{f_i\},t) = -\frac{1}{\tau}(f_i - f_i^{eq}), \tag{3.10}$$

where f_i^{eq} are the equilibrium distribution functions and τ is the relaxation time, connected to the viscosity of the fluid, as it will be seen. The mass and momentum density are defined as

$$\rho(\mathbf{r},t) = \sum_i f_i(\mathbf{r},t), \tag{3.11}$$

$$\rho(\mathbf{r},t)\mathbf{v}(\mathbf{r},t) = \sum_i f_i(\mathbf{r},t)\xi_i, \tag{3.12}$$

where summations are performed over all discretized directions at each lattice point. By assuming both mass and momentum density to be conserved in each collision, it is found that conditions in Eq. (3.11), (3.12) must hold also for the equilibrium distribution functions:

$$\rho(\mathbf{r},t) = \sum_i f_i^{eq}(\mathbf{r},t), \tag{3.13}$$

$$\rho(\mathbf{r},t)\mathbf{v}(\mathbf{r},t) = \sum_i f_i^{eq}(\mathbf{r},t)\xi_i. \tag{3.14}$$

Moreover, it is necessary to introduce further constraints on the second moment of the equilibrium distribution functions to recover continuum equations, as it will become more evident in the following. Further constraints on higher order moments may become necessary to simulate more complex systems: for instance full compressible flows or supersonic adaptation of the algorithm may require the specification of moments up to the third, while for a complete hydrodynamic description in which heat transfer is also taken into account, even the fourth moment needs to be specified [207].

Requiring suitable isotropy conditions and Galilean invariance [31], it is possible to show analytically [150] that the equilibrium distribution functions can be written in a

more general way as

$$f_i^{eq} = \rho\omega_i \left| 1 + 3\frac{v_\alpha \xi_{i\alpha}}{c^2} - \frac{3}{2}\frac{v^2}{c^2} + \frac{9}{2}\frac{(v_\alpha \xi_{i\alpha})^2}{c^4} \right|, \tag{3.15}$$

where the weights ω_i are given in Table 3.1. Here the quantity $c = \Delta x/\Delta t$ has been introduced as the ratio between the lattice spacing Δx and the time step Δt. In the next paragraph 3.2 it will be shown that the algorithm here presented correctly reproduces Eqs. (2.15) and (2.16).

Due to the fact that sufficient lattice symmetry is required to recover the correct Navier-Stokes equation in the continuum limit [60], not all the possible lattice structures can be adopted. By denoting the space dimension by d and the number of lattice speeds by Q, Table 3.1 shows the velocities $\{\xi_i\}$ and the corresponding weights in the equilibrium distribution functions (see next Section) for the most frequent choices. Figure 3.2 explicitly illustrates some lattice structures in the two-dimensional and three-dimensional cases.

To choose a suitable discretization in velocity space, one usually relies on considerations based on the quadrature of a Hermite polynomial expansion of the Maxwell-Boltzmann distribution [166]. The idea is to obtain a discretized lattice Boltzmann equation that allows the exact recovery of a finite number of leading order moments of the equilibrium distribution functions. Additionally, when dealing with hydrodynamics, one is not interested in the evolution of the distribution functions, but of their moments that can be exactly evaluated as a discrete sum over the polynomial integrands at specific points ξ_i (abscissae). Thus, f^{eq} becomes discrete rather than continuous in velocity space. The nodes ξ_i can be derived following the Gauss theory of quadrature and can be interpreted as the allowed directions for the fluid mass elements in the lattice. As it will be more clear in the next Section, the choice of the lattice also influences the constant c. Some details concerning the properties of some lattices (including the ones shown in Fig. 3.2) are shown in Table 3.1. All the results presented in this thesis, besides the ones regarding the comparison with finite difference LB presented in this chapter, are obtained using the so called collision-streaming LB. Overall, the core LB collision-streaming algorithm consists of a cyclic sequence of sub-steps, with each cycle corresponding to one time step. These steps are visualized in Fig. 3.3:

- Compute macroscopic moments $\rho(\mathbf{r},\mathbf{t})$ and $\mathbf{v}(\mathbf{r},\mathbf{t})$ from $f_i(\mathbf{r},\mathbf{t})$
- Obtain equilibrium distribution functions $f_i^{eq}(\mathbf{r},\mathbf{t})$
- If necessary write the macroscopic moments (output)
- Perform collision (relaxation)

$$f_i^*(\mathbf{r},t) = f_i(\mathbf{r},t) - \frac{\Delta t}{\tau}(f_i(\mathbf{r},t) - f_i^{\mathrm{eq}}(\mathbf{r},t)) \ , \tag{3.16}$$

  where $f_i^*(\mathbf{r},t)$ represents the distribution function after collision.
- Perform streaming (propagation) $f_i(\mathbf{r}+\xi_\mathbf{i}\Delta t, t+\Delta t) = f_i^*(\mathbf{r},t)$
- Increase the time step, setting t to $t+\Delta t$, and go back to the first step until the last time step has been reached.

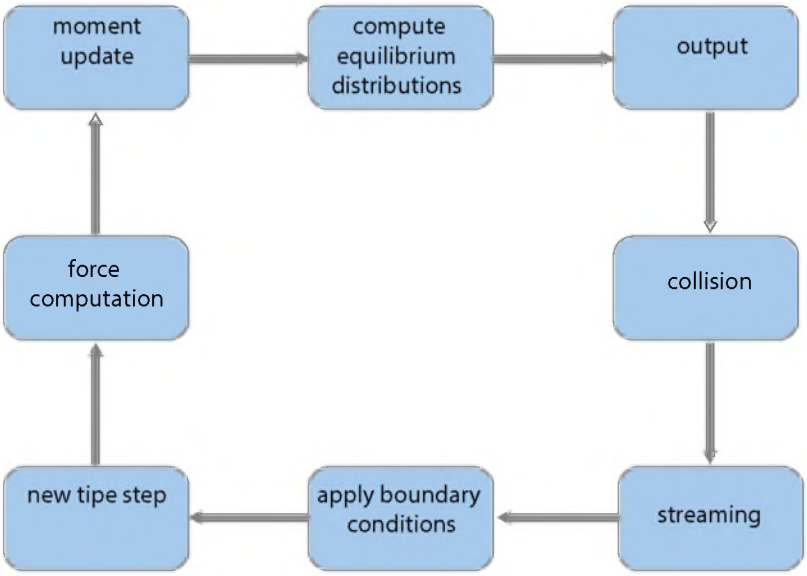

Figure 3.3: Sketch of collision-streaming LB algorithm.

3.1.1. THE KEYSTONE OF LB METHOD: GAUSS-HERMITE QUADRATURE

In this section we will derive the LBE from continuum kinetic theory. To do this we will use the Hermite-Gauss approach. In other words we want to put in connection the discretized Boltzmann equation in the BGK approximation and the continuum BGK equation with no external force

$$\partial_t f + \xi_\alpha \partial_\alpha f = -\frac{1}{\tau}(f - f^{\mathrm{eq}}) \ . \tag{3.17}$$

To develop this formal connection we first expand the distribution function in Hermite polynomials [1]. The Hermite polynomial of degree k is defined by the k-*th* derivative of the Gaussian weight function

$$\omega(\xi) = \frac{1}{(2\pi)^{1/2}} \exp\left(-\frac{\xi^2}{2}\right), \tag{3.18}$$

so to write the Hermite polynomial of degree k as

$$H_k(\xi) = \frac{(-1)^k}{\omega(\xi)} \partial_\xi^k \omega(\xi) \ . \tag{3.19}$$

Concluding this very brief summary on Hermite polynomials it is important to mention that they form a set of orthonormal bases of the Hilbert space equipped with the inner product $< f, g >= \int \omega f g d\xi$, and the following ortonormality property holds

$$\int_{-\infty}^{+\infty} H_k(\xi)\omega(\xi)H_l(\xi)d\xi = \delta_{kl} \ . \tag{3.20}$$

The distribution function projected on Hermite bases reads

$$f(x,\xi,t) = \omega(\xi) \sum_{k=0}^{\infty} M_k(x,t) H_k(\xi) \ , \tag{3.21}$$

[1] For the seek of simplicity we consider only one space and velocity dimension.

where $\omega(\xi)$ is the standard Gaussian-weight function (Eq. (3.18)) and the moments are given by scalar product in Hilbert space:

$$M_k(x,t) = \int_{-\infty}^{+\infty} f(x,\xi,t) H_k(\xi) d\xi \,. \tag{3.22}$$

Multiplying Eq. (3.17) by $H_l(\xi)$ and integrating upon velocity space we get

$$\partial_t M_l + \partial_\alpha \int_{-\infty}^{+\infty} \xi f(x,\xi,t) H_l(\xi) d\xi = -\frac{1}{\tau}(\rho_l^{eq} - \rho_l) \,, \tag{3.23}$$

where have used the orthogonality condition (3.20).

Hermite series expansions is a suitable expansion method since the equilibrium distribution functions have the same form as the Hermite weight function. It can be shown that that the coefficients in the Hermite series expansion of the equilibrium distribution function are related to the conserved moments; in particular, the first three coefficients are connected to density, momentum and energy. But there is also another compelling reason to use the Hermite polynomials. Gauss quadrature theory allows for the computation of integrals of functions by summing the values that the function assumes in correspondence of a small number of discrete points, called *abscissae*. Following this idea, evaluation of the integrals with respect to velocity by Gauss-Hermite numerical quadrature reads as follows:

$$M_l(x,t) = \sum_{i=0}^{b} \omega_i p(x,\xi_i,t) H_l(\xi_i) \,, \tag{3.24}$$

and

$$\mathscr{I}_l(x,t) = \int_{-\infty}^{+\infty} \xi f(x,\xi,t) H_l(\xi) d\xi = \sum_{i=0}^{b} \omega_i \xi_i p(x,\xi_i,t) H_l(\xi_i) \,, \tag{3.25}$$

where the polynomial distribution have been introduced

$$p(x,\xi,t) = \frac{f(x,\xi,t)}{\omega(\xi)} \,. \tag{3.26}$$

Inserting Eq. (3.24) and (3.25) in Eq. (3.23) we obtain the evolution equation for the polynomial distribution functions

$$\partial_t f_i + \partial_x(\xi_i f_i) = -\frac{1}{\tau}(f_i - f^{eq}) \,, \tag{3.27}$$

where

$$f_i = \omega_i p_i = \frac{\omega_i}{\omega(\xi_i)} f(x,\xi_i,t) \,. \tag{3.28}$$

It is important to note that the weights of the Gauss-Hermite quadrature ω_i do not identify with $\omega(\xi_i)$, that is the Gaussian weight evaluated at node $\xi = \xi_i$. Using an explicit Euler-forward scheme along the characteristics $\Delta x_i = \xi_i t$, and integrating explicitly in time the collision term, we obtain the LBGK equation

$$f_i(x + \xi_i \Delta t, t + \Delta t) - f_i(x,t) = \frac{1}{\tau} \Delta t (f_i^{eq} - f_i) \,. \tag{3.29}$$

It is known that Gauss-Hermite quadrature with (b+1) nodes, integrates exactly polynomials $p(\xi)$ up to order $2(b+1)-1$. It follows that a D1Q3 lattice geometry reproduces the continuum equations up to fifth order. In other words, the Gauss–Hermite quadrature provides a route for the optimal sampling of the velocity space, thus allowing for recovering the evolution equations of the lowest-order kinetic moments (frequent events) that are the ones of interest in fluid-dynamics. Capturing higher-order moments (rare events), is beyond the scope hydrodynamics, even if this is still possible by truncating the Hermite expansion at superior orders, thus increasing the number of nodes and weights needed for the computation of the integrals that define the moments of interest.

The simplified derivation here presented shows that Hermite expansion of the continuum BGK, as combined with Gauss–Hermite quadrature, gives rise to the LBGK scheme [166]. The same reasoning can be applied to higher dimensions by expanding on tensor Hermite polynomials. This procedure encapsulates the LBGK formalism within the general box of computational kinetic theory. This is an elegant result, which shows that the discrete speeds – so far chosen based on pure symmetry considerations – can be identified with the nodes of the Gauss-Hermite quadrature, namely the zeros of the Hermite polynomials.

3.1.2. LATTICE BOLTZMANN FOR A SIMPLE FLUID

In this Section I will present a basic lattice Boltzmann algorithm to solve the hydrodynamic equations (2.15) and (2.16) for a simple fluid. In this case the on the right hand side of the Navier-Stokes equation (2.16) reduces to the pressure gradient plus the mere viscous contribution $\partial_\beta \sigma^{viscous}_{\alpha\beta}$, if no external force is acting on the fluid.

Conditions (3.13) and (3.14) can be satisfied by expanding the equilibrium distribution functions up to the second order in the fluid velocity $\mathbf{v}$ [30]:

$$f_i^{eq} = A_s + B_s v_\alpha \xi_{i\alpha} + C_s v^2 + D_s v_\alpha v_\beta \xi_{i\alpha}\xi_{i\beta}, \tag{3.30}$$

where index $s = |\xi_i|^2/c^2$ relates the i-th distribution function to the square module of the corresponding lattice velocity, and the Greek index denotes the Cartesian component. This expansion is valid as far as the Mach number $Ma = v/c_s$ is kept small, c_s being the speed of sound, whose explicit expression in turn depends upon the lattice discretization [166]. The present assumption has the important consequence that LB models based on the previous expansion of the equilibrium distribution functions have great difficulty in simulating compressible Euler flows, that usually take place at high Mach numbers. This issue arises in standard LB approaches because of the appearance of third order non-linear deviations from the Navier-Stokes equation [79]. Qian and Orzsag demonstrated in [149] that such nonlinear deviations grow together with Ma^2, so that they can be neglected in the low Mach number regime but become important in the compressible limit[2]. For such reasons it is necessary to ensure that velocities never exceed a critical threshold that can be reasonably chosen such that $Ma \lesssim 0.3$ [149].

[2] In order to overcome the limit posed by the low Mach number regime, many variations of the standard LBM have been developed. Alexander *et al.* proposed a model where the high Mach number regime could be achieved by decreasing the speed of sound [3]; discrete-velocity models [134, 181] were later introduced allowing for simulation of the compressible Euler equation in a wider range of Mach numbers. Other implementations are based on a Taylor expansion of the equilibrium distributions up to higher orders together with suitable constraints on the third and fourth moments [94, 95, 166].

Table 3.1: Lattice speeds with their weights ω_i for spatial dimensions $d = 2$ and $d = 3$ and number of neighbouring nodes Q.

Lattice	ξ_i	ω_i
$d2Q7$	$(0,0)$	$1/2$
	$c(\cos(i\pi/3), \sin(i\pi/3))$	$1/12$
$d2Q9$	$(0,0)$	$4/9$
	$(\pm c, 0)$ $(0, \pm c)$	$1/9$
	$(\pm c, \pm c)$	$1/36$
$d3Q15$	$(0,0,0)$	$2/9$
	$(\pm c, 0, 0)$ $(0, \pm c, 0)$ $(0, 0, \pm c)$	$1/9$
	$(\pm c, \pm c, \pm c)$	$1/72$
$d3Q19$	$(0,0,0)$	$1/3$
	$(\pm c, 0, 0)$ $(0, \pm c, 0)$ $(0, 0, \pm c)$	$1/18$
	$(\pm c, \pm c, 0)$ $(\pm c, 0, \pm c)$ $(0, \pm c, \pm c)$	$1/36$
$d3Q27$	$(0,0,0)$	$8/27$
	$(\pm c, 0, 0)$ $(0, \pm c, 0)$ $(0, 0, \pm c)$	$2/27$
	$(\pm c, \pm c, 0)$ $(\pm c, 0, \pm c)$ $(0, \pm c, \pm c)$	$1/54$
	$(\pm c, \pm c, \pm c)$	$1/216$

Besides constraints expressed by Eq. (3.13) and (3.14), an additional condition on the second moment of the equilibrium distribution functions is imposed so that

$$\sum_i f_i^{eq} \xi_{i\alpha} \xi_{i\beta} = \frac{c^2}{3} \rho \delta_{\alpha\beta} + \rho v_\alpha v_\beta. \tag{3.31}$$

This is a necessary condition to recover the Navier-Stokes equation in the continuum limit. By substituting the expansion in Eq. (3.30) in constraints introduced in Eq. (3.13), (3.14) and (3.31), a suitable choice for the expansion coefficients is found to be

$$A_0 = \rho - 20A_2 \qquad A_1 = 4A_2 \qquad A_2 = \frac{\rho}{36} \tag{3.32}$$

$$B_0 = 0 \qquad B_1 = 4B_2 \qquad B_2 = \frac{\rho}{12c^2} \tag{3.33}$$

$$C_0 = -\frac{2\rho}{3c^2} \qquad C_1 = 4C_2 \qquad C_2 = -\frac{\rho}{24c^2} \tag{3.34}$$

$$D_0 = 0 \qquad D_1 = 4D_2 \qquad D_2 = \frac{\rho}{8c^4}, \tag{3.35}$$

where for the sake of clarity we have explicitly chosen a $d2Q9$ lattice geometry.

Finally, we mention that it would be possible to introduce small thermal fluctuations into the algorithm, in a controlled way, by means of a stochastic collision operator. The fluctuation-dissipation theorem can then be satisfied by requiring consistency with fluctuating hydrodynamics [1]. Since to the best of our knowledge there are no LB models for active systems including thermal noise, we do not give further details, since the role of thermal fluctuations will not be addressed in the study presented in this thesis.

3.2. CHAPMAN-ENSKOG EXPANSION

In Section 3.1.2 we presented a LB algorithm to solve the hydrodynamics of a simple fluid. We show here that Eqs.(2.23) and (2.16) can be recovered in the continuum limit, starting from the evolution equation (3.8) for the distribution functions f_i. Two approaches can be followed. The first one starts from a Taylor expansion of the left-hand side of Eq. (3.8) [140], whereas the second one, discussed below, uses a Chapman-Enskog method, that is an expansion of the distribution functions about equilibrium, which assumes that successive derivatives are of increasingly higher order in the Knudsen number $\epsilon = \lambda/L$. For small values of ϵ ($\epsilon \ll 1$) the mean free path is much smaller than L and a continuum theory is a good approximation. To take into account both ballistic and diffusive scales, spatial density fluctuations of order $\mathcal{O}(\epsilon^{-1})$ are assumed to relax over time scales of order $\mathcal{O}(\epsilon^{-2})$. A suitable expansion for temporal and spatial derivatives as well as for distribution functions is

$$f_i = f_i^{(0)} + \epsilon f_i^{(1)} + \epsilon^2 f_i^{(2)}, \tag{3.36}$$

$$\partial_t = \epsilon \partial_{t_1} + \epsilon^2 \partial_{t_2}, \tag{3.37}$$

$$\partial_\alpha = \epsilon \partial_{\alpha_1}, \tag{3.38}$$

built assuming that there is a diffusion time scale t_2 slower than the convection one t_1. We start by expanding the left-hand side of equation (3.8) to the second order in Δt:

$$\Delta t(\partial_t + \xi_{i\alpha}\partial_\alpha) f_i + \frac{(\Delta t)^2}{2}\left(\partial_t^2 + 2\xi_{i\alpha}\partial_\alpha\partial_t + \xi_{i\alpha}\xi_{i\beta}\partial_\alpha\partial_\beta\right) f_i = -\frac{1}{\tau}(f_i - f_i^{eq}), \tag{3.39}$$

where Eq. (3.10) has been used to express the collision operator. By substituting Eq. (3.36), (3.37) and (3.38) into Eq. (3.39) one obtains

$$\begin{aligned}
&\Delta t\left[(\epsilon\partial_{t_1} + \epsilon^2\partial_{t_2}) + \epsilon\xi_{i\alpha}\partial_{\alpha_1}\right](f_i^{(0)} + \epsilon f_i^{(1)} + \epsilon^2 f_i^{(2)}) \\
&+(\Delta t)^2\left[\frac{1}{2}(\epsilon\partial_{t_1} + \epsilon^2\partial_{t_2})^2 + \epsilon\xi_{i\alpha}\partial_\alpha(\epsilon\partial_{t_1} + \epsilon^2\partial_{t_2})\right. \\
&\left.+\frac{1}{2}\epsilon^2\xi_{i\alpha}\xi_{i\beta}\partial_{\alpha_1}\partial_{\beta_1}\right](f_i^{(0)} + \epsilon f_i^{(1)} + \epsilon^2 f_i^{(2)}) \\
&= -\frac{1}{\tau}(f_i^{(0)} + \epsilon f_i^{(1)} + \epsilon^2 f_i^{(2)} - f_i^{eq}).
\end{aligned} \tag{3.40}$$

By retaining at most terms of second order in ϵ, the previous equation reads

$$\begin{aligned}
&\epsilon\Delta t\left(\partial_{t_1} f_i^{(0)} + \xi_{i\alpha}\partial_{\alpha_1} f_i^{(0)}\right) \\
+\ &\epsilon^2\left[\Delta t\left(\partial_{t_1} f_i^{(1)} + \xi_{i\alpha}\partial_{\alpha_1} f_i^{(1)} + \partial_{t_2} f_i^{(0)}\right)\right. \\
+\ &\left.\Delta t^2\left(\frac{1}{2}\partial_{t_1}^2 + \frac{1}{2}\xi_{i\alpha}\xi_{i\beta}\partial_{\alpha_1}\partial_{\beta_1} + \xi_{i\alpha}\partial_{\alpha_1}\partial_{t_1}\right) f_i^{(0)}\right] \\
=\ &-\frac{f_i^{(0)} - f_i^{eq}}{\tau} - \frac{\epsilon f_i^{(1)} + \epsilon^2 f_i^{(2)}}{\tau}.
\end{aligned} \tag{3.41}$$

Finally, grouping terms of same order in ϵ, we get

$$f_i^{(0)} = f_i^{eq} + \mathcal{O}(\epsilon), \tag{3.42}$$

$$\partial_{t_1} f_i^{(0)} + \xi_{i\alpha}\partial_{\alpha_1} f_i^{(0)} = -\frac{1}{\tau\Delta t} f_i^{(1)} + \mathcal{O}(\epsilon), \tag{3.43}$$

$$\begin{aligned}&\partial_{t_1} f_i^{(1)} + \xi_{i\alpha}\partial_{\alpha_1} f_i^{(1)} + \partial_{t_2} f_i^{(0)} \\ &+ \frac{\Delta t}{2}\left(\partial_{t_1}^2 + 2\xi_{i\alpha}\partial_{\alpha_1}\partial_{t_1} + \xi_{i\alpha}\xi_{i\beta}\partial_{\alpha_1}\partial_{\beta_1}\right) f_i^{(0)} \\ &= -\frac{1}{\tau\Delta t} f_i^{(2)} + \mathcal{O}(\epsilon).\end{aligned} \tag{3.44}$$

In the following paragraphs we will use these relations to recover continuum equations up to second order in the Knudsen number.

3.2.1. RECOVER CONTINUITY EQUATION

To recover the continuity equation one can start by summing Eq. (3.42) over lattice velocities with the constraints given in Eqs. (3.13) and (3.14). One then gets

$$\sum_i f_i^{(0)} = \rho, \qquad \sum_i f_i^{(1)} = \sum_i f_i^{(2)} = 0, \tag{3.45}$$

and, by using again Eq. (3.14),

$$\sum_i f_i^{(0)}\xi_{i\alpha} = \rho u_\alpha, \qquad \sum_i f_i^{(1)}\xi_{i\alpha} = \sum_i f_i^{(2)}\xi_{i\alpha} = 0. \tag{3.46}$$

By performing a summation over lattice velocities in Eq. (3.43), one gets

$$\partial_{t_1}\rho + \partial_{\alpha_1}(\rho u_\alpha) = 0 + \mathcal{O}(\epsilon), \tag{3.47}$$

which is the continuity equation at first order in the Knudsen number. To recover the complete time derivative according to Eq. (3.37), we need to explicitly compute the term $\partial_{t_2}\rho$. By applying the differential operators $\epsilon\partial_{t_1}$ and $\epsilon\xi_{i\beta}\partial_{\beta_1}$ to Eq. (3.43) we obtain

$$\partial_{t_1}^2 f_i^{(0)} + \xi_{i\alpha}\partial_{\alpha_1}\partial_{t_1} f_i^{(0)} = -\frac{1}{\tau\Delta t}\partial_{t_1} f_i^{(1)} + \mathcal{O}(\epsilon^2), \tag{3.48}$$

$$\xi_{i\beta}\partial_{\beta_1}\partial_{t_1} f_i^{(0)} + \xi_{i\alpha}\xi_{i\beta}\partial_{\alpha_1}\partial_{\beta_1} f_i^{(0)} = -\frac{1}{\tau\Delta t}\xi_{i\beta}\partial_{\beta_1} f_i^{(1)} + \mathcal{O}(\epsilon^2), \tag{3.49}$$

and, summing both equations:

$$(\partial_{t_1}^2 + 2\xi_{i\alpha}\partial_{\alpha_1}\partial_{t_1} + \xi_{i\alpha}\xi_{i\beta}\partial_{\alpha_1}\partial_{\beta_1}) f_i^{(0)} = -\frac{1}{\tau\Delta t}(\partial_{t_1} + \xi_{i\beta}\partial_{\beta_1}) f_i^{(1)} + \mathcal{O}(\epsilon^2). \tag{3.50}$$

Note that the left-hand side of this equation is exactly the term in round brackets of Eq. (3.44), that now becomes

$$\partial_{t_2} f_i^{(0)} + \left(1 - \frac{1}{2\tau}\right)(\partial_{t_1} + \xi_{i\alpha}\partial_{\alpha_1}) f_i^{(1)} = -\frac{1}{\tau\Delta t} f_i^{(2)} + \mathcal{O}(\epsilon). \tag{3.51}$$

By summing over lattice directions and using Eqs. (3.45) and (3.46), we get

$$\partial_{t_2}\rho = 0 + \mathcal{O}(\epsilon^2), \tag{3.52}$$

that, summed with Eq. (3.47), gives

$$(\epsilon\partial_{t_1} + \epsilon^2\partial_{t_2})\rho + \epsilon\partial_{\alpha_1}(\rho v_\alpha) = 0 + \mathcal{O}(\epsilon^2). \tag{3.53}$$

Finally, after restoring the canonical differential operators (through Eqs. (3.37) and (3.38)), we get the continuity equation

$$\partial_t \rho + \partial_\alpha(\rho v_\alpha) = 0 + \mathcal{O}(\epsilon^2), \tag{3.54}$$

at second order in the Knudsen number.

3.2.2. RECOVER NAVIER-STOKES EQUATIONS

The procedure to recover the Navier-Stokes equation is analogous, albeit less straightforward, than that used for the continuity equation. We will proceed by calculating the first-order moment of Eq. (3.43) and Eq. (3.44). First, one multiplies by $\xi_{i\beta}$ both members of Eq. (3.43) and sums over index i, to get

$$\partial_{t_1}(\rho v_\alpha) + \partial_{\beta_1}\left(\frac{c^2}{3}\rho\delta_{\alpha\beta} + \rho v_\alpha v_\beta\right) = 0 + \mathcal{O}(\epsilon). \tag{3.55}$$

To get the Navier-Stokes equation to second order in the Knudsen number we need to calculate the first-order moment of equation (3.44). We can then multiply Eq. (3.51) by $\xi_{i\gamma}$ to obtain

$$\partial_{t_2}\xi_{i\gamma}f_i^{(0)} + \left(1 - \frac{1}{2\tau}\right)(\partial_{t_1} - \xi_{i\alpha}\partial_{\alpha_1})\xi_{i\gamma}f_i^{(1)} = -\frac{1}{\tau\Delta t}\xi_{i\gamma}f_i^{(2)} + \mathcal{O}(\epsilon^2), \tag{3.56}$$

and, by summing over lattice velocities, we are left with

$$\partial_{t_2}(\rho v_\alpha) - \left(1 - \frac{1}{2\tau}\right)\partial_{\beta_1}\left[\sum_i f_i^{(1)}\xi_{i\alpha}\xi_{i\beta}\right] = 0. \tag{3.57}$$

Now we must determine an expression for the summation in square brackets. From Eqs. (3.42) and (3.43) we note that

$$\begin{aligned}\sum_i f_i^{(1)}\xi_{i\alpha}\xi_{i\beta} &= -\tau\Delta t(\partial_{t_1} + \xi_{i\gamma}\partial_{\gamma_1})\left(\sum_i f_i^{eq}\xi_{i\alpha}\xi_{i\beta}\right) \\ &= -\tau\Delta t\left[\partial_{t_1}\left(\frac{c^2}{3}\rho\delta_{\alpha\beta} + \rho v_\alpha v_\beta\right) + \partial_{\gamma_1}\left(\sum_i f_i^{eq}\xi_{i\alpha}\xi_{i\beta}\xi_{i\gamma}\right)\right],\end{aligned} \tag{3.58}$$

where we have used Eq. (3.31) in the second equality. The second term of the second line of Eq. (3.58) can be written in terms of the equilibrium distribution functions given in Eq. (3.15) and of the related coefficients in Eq. (3.33)

$$\partial_{\gamma_1}\left(\sum_i f_i^{eq}\xi_{i\alpha}\xi_{i\beta}\xi_{i\gamma}\right) = \frac{c^2}{3}\partial_{\gamma_1}\left[\rho(\delta_{\alpha\beta}v_\gamma + \delta_{\alpha\gamma}v_\beta + \delta_{\beta\gamma}v_\alpha)\right], \tag{3.59}$$

while the first round bracket in the second line of Eq. (3.58) can be written by means of Eq. (3.47) and Eq. (3.55) as

$$\begin{aligned}\partial_{t_1}\left(\frac{c^2}{3}\rho\delta_{\alpha\beta} + \rho v_\alpha v_\beta\right) &= -\frac{c^2}{3}\partial_{\gamma_1}(\rho v_\gamma)\delta_{\alpha\beta} + v_\beta\partial_{t_1}(\rho v_\alpha) + v_\alpha\partial_{t_1}(\rho v_\beta) - v_\alpha v_\beta\partial_{t_1}\rho \\ &\simeq -\frac{c^2}{3}\left[\partial_{\gamma_1}(\rho v_\gamma)\delta_{\alpha\beta} + (v_\alpha\partial_{\beta_1}\rho + v_\beta\partial_{\alpha_1}\rho)\right].\end{aligned} \tag{3.60}$$

In the last line terms of order v^3 were neglected, an approximation valid as far as the Mach number is kept small. Now substituting Eqs. (3.60) and (3.59) into Eq. (3.58) we find, after some algebra, that

$$\sum_i f_i^{(1)} \xi_{i\alpha} \xi_{i\beta} = -\tau \Delta t \frac{c^2}{3} \rho \left[\partial_{\beta_1} v_\alpha + \partial_{\alpha_1} v_\beta \right]. \tag{3.61}$$

This term, in turn, enters Eq. (3.57), which now reads

$$\partial_{t_2} (\rho v_\alpha) - \left(\tau - \frac{1}{2} \right) \Delta t \frac{c^2}{3} \partial_{\beta_1} \left[\rho \left(\partial_{\beta_1} v_\alpha + \partial_{\alpha_1} v_\beta \right) \right] = 0. \tag{3.62}$$

Finally, summing this equation with Eq. (3.55) and using the canonical differential operators (i.e. Eqs. (3.37) and (3.38)), we obtain the Navier-Stokes equation

$$\partial_t (\rho v_\alpha) + \partial_\beta \left(\rho v_\alpha v_\beta \right) = -\partial_\alpha p + \Delta t \left(\tau - \frac{1}{2} \right) \frac{c^2}{3} \partial_\beta \left[\rho \left(\partial_\beta v_\alpha + \partial_\alpha v_\beta \right) \right], \tag{3.63}$$

where $p = (c^2/3)\rho$ is the isotropic pressure and the shear viscosity is given by

$$\eta = \frac{\rho c_s^2 \Delta t}{3} \left(\tau - \frac{1}{2} \right), \tag{3.64}$$

where $c_s = \frac{c}{\sqrt{3}}$ is the speed of sound.

3.3. LBM BEYOND SIMPLE FLUIDS

So far we have implemented a lattice Boltzmann method for a simple fluid in absence of any forcing term, with only viscous contribution to the stress tensor. On the other hand when dealing with more complex systems, such as multicomponent or multiphase fluids, the stress tensor may include further contributions (such as elastic and interfacial ones, see Table 2.2) which have a non-trivial dependence on order parameters and their derivatives. In this Section we will show two different strategies adopted to numerically implement such terms. Briefly, while in the first one they are included in an extra term, appearing in the second moment of the equilibrium distribution functions, in the second one they enter through an external forcing added to the collision operator in the lattice Boltzmann equation.

3.3.1. STRESS TENSOR IN THE SECOND MOMENT

To implement a general symmetric stress tensor contribution in the lattice Boltzmann scheme previously introduced, we again impose the constraints of Eq. (3.13) and Eq. (3.14) on the zeroth and on the first moment of the equilibrium distribution functions, while constraint on the second moment previously given in Eq. (3.31) is modified according to the following relation

$$\sum_i f_i^{eq} \xi_{i\alpha} \xi_{i\beta} = -\sigma_{\alpha\beta} + \rho v_\alpha v_\beta. \tag{3.65}$$

Here $\sigma_{\alpha\beta}$ stands for the total stress tensor including pressure contributions, but deprived of viscous ones. Note that, due to the symmetry of the left hand side of Eq. (3.65),

this algorithm can be applied to models that involve only symmetric contributions to the stress tensor. For instance, this method is suitable to study binary mixtures, as the stress tensor associated to the concentration contribution is indeed symmetric, but not liquid crystals, as the antisymmetric part of the relative stress tensor does not vanish (see Table 2.2). This latter case will be discussed in the following Sections. To satisfy Eq. (3.65) [44, 142], the equilibrium distribution functions can be expanded as follows

$$f_i^{eq} = A_s + B_s v_\alpha \xi_{i\alpha} + C_s v^2 + D_s v_\alpha v_\beta \xi_{i\alpha}\xi_{i\beta} + G_s^{\alpha\beta}\xi_{i\alpha}\xi_{i\beta}\,, \tag{3.66}$$

where an extra term, quadratic in lattice velocities, has been added with respect to the case of a simple fluid (see Eq. (3.30)), to include a general stress tensor in the model. As for a simple fluid, the coefficients of the expansion can be calculated by imposing constraints of Eq. (3.13), Eq. (3.14) and Eq. (3.65). For a $d2Q9$ geometry a suitable choice is given by

$$\begin{aligned}
A_0 = \rho - 20A_2 \quad A_1 = 4A_2 \quad A_2 &= \frac{\mathrm{Tr}\,\sigma}{24c^2} \\
B_0 = 0 \quad B_1 = 4B_2 \quad B_2 &= \frac{\rho}{12c^2} \\
C_0 = -\frac{2\rho}{3c^2} \quad C_1 = 4C_2 \quad C_2 &= -\frac{\rho}{24c^2} \\
D_0 = 0 \quad D_1 = 4D_2 \quad D_2 &= \frac{\rho}{8c^4} \\
G_s^{\alpha\beta} = 0 \quad G_s^{\alpha\beta} = 4G_2^{\alpha\beta} \quad G_2^{\alpha\beta} &= \frac{\sigma^0_{\alpha\beta}}{8c^2},
\end{aligned} \tag{3.67}$$

where we denoted by $\sigma^0_{\alpha\beta}$ the traceless part of $\sigma_{\alpha\beta}$.

One can now proceed to recover the Navier-Stokes equation by using a Chapman-Enskog expansion[3]. Assuming that the fluid is flowing at small Mach numbers, so to ignore third-order terms in the fluid velocity, and taking the first moment of Eq. (3.43), one gets

$$\partial_{t_1}(\rho v_\alpha) + \partial_{\beta_1}\left(\rho v_\alpha v_\beta\right) = \partial_{\beta_1}\sigma_{\alpha\beta} + \mathcal{O}(\epsilon), \tag{3.68}$$

which is the Navier-Stokes equation at first order in Knudsen number. To recover the Navier-Stokes equation at second order, we start from Eq. (3.57), where we need to evaluate the second moment of $f_i^{(1)}$

$$\begin{aligned}
\sum_i f_i^{(1)}\xi_{i\alpha}\xi_{i\beta} &= -\tau\Delta t(\partial_{t_1} + \xi_{i\gamma}\partial_{\gamma_1})\left(\sum_i f_i^{eq}\xi_{i\alpha}\xi_{i\beta}\right) \\
&= -\tau\Delta t\left[\partial_{t_1}\left(-\sigma_{\alpha\beta} + \rho v_\alpha v_\beta\right) + \partial_{\gamma_1}\left(\sum_i f_i^{eq}\xi_{i\alpha}\xi_{i\beta}\xi_{i\gamma}\right)\right].
\end{aligned} \tag{3.69}$$

The first time derivative in square brackets is negligible at the leading order, while

$$\partial_{t_1}(\rho v_\alpha v_\beta) = v_\alpha\partial_{t_1}(\rho v_\beta) + v_\beta\partial_{t_1}(\rho v_\alpha) \tag{3.70}$$

[3]The second moment constraint on the equilibrium distribution functions is not necessary for the derivation of the continuity equation. Hence the procedure to recover this equation is not affected by the modifications introduced in the new version of the algorithm, with respect to the case of a simple fluid.

that shows, together with Eq. (3.68), that this term gives a null contribution. Finally, using Eq. (3.59) we get the same result of Eq. (3.61) which allows one to restore the Navier-Stokes equation.

3.3.2. FORCING SCHEME

An alternative route to the solution of the LB equation (3.8) relies on the use of a pure forcing method [113, 186]. In this case the total stress tensor enters the model via a forcing term $\mathscr{F}_i$, without any additional constraint on the second moment of the equilibrium distribution functions, with condition given in Eq. (3.31). The collision term $\mathscr{C}_{f_i}$ assumes the simple form of the BGK approximation supplemented by a forcing term

$$\mathscr{C}(\{f_i\},t) = -\frac{1}{\tau}[f_i(\mathbf{r},t) - f_i^{eq}(\mathbf{r},t)] + \Delta t \mathscr{F}_i, \tag{3.71}$$

where the equilibrium distribution functions f_i^{eq} are again expressed as a second-order expansion in the velocity $\mathbf{v}$ of the Maxwell-Boltzmann distribution [150]. The fluid momentum is now given by the average between the pre- and post-collisional values of the velocity $\mathbf{v}$, as usually done when using a forcing term [19, 165]

$$\rho v_\alpha = \sum_i f_i \xi_{i\alpha} + \frac{1}{2} F_\alpha \Delta t, \tag{3.72}$$

where F_α is the cartesian component of the force density acting on the fluid. The choice of the equilibrium distribution functions and their constraints is kept as in Section 3.1.2, with coefficients given by Eqs. (3.32)-(3.35) for a $d2Q9$ lattice. The term $\mathscr{F}_i$ can be written as an expansion at the second order in the lattice velocity vectors [104]:

$$\mathscr{F}_i = \omega_i \left[A + \frac{B_\alpha \xi_{i\alpha}}{c_s^2} + \frac{C_{\alpha\beta}(\xi_{i\alpha}\xi_{i\beta} - c_s^2 \delta_{\alpha\beta})}{2c_s^4} \right], \tag{3.73}$$

where coefficients A, B_α and $C_{\alpha\beta}$ are functions of F_α. In order to correctly reproduce hydrodynamic equations, the moments of the force term must fulfil the following relations

$$\begin{aligned} \sum_i \mathscr{F}_i = A \qquad & \sum_i \mathscr{F}_i \xi_{i\alpha} = B_\alpha \\ \sum_i \mathscr{F}_i \xi_{i\alpha}\xi_{i\beta} = c_s^2 A \delta_{\alpha\beta} + \frac{1}{2}\left[C_{\alpha\beta} + C_{\beta\alpha}\right], & \end{aligned} \tag{3.74}$$

which lead to [83]

$$\mathscr{F}_i = \left(1 - \frac{1}{2\tau}\right) \omega_i \left[\frac{\xi_{i\alpha} - v_\alpha}{c_s^2} + \frac{\xi_{i\beta} v_\beta}{c_s^4} \xi_{i\alpha} \right] F_\alpha. \tag{3.75}$$

To recover the continuity (2.15) and the Navier-Stokes (2.16) equations it suffices to require that

$$F_\alpha = \partial_\beta (\sigma_{\alpha\beta}^{total} - \sigma_{\alpha\beta}^{viscous}). \tag{3.76}$$

From the Chapman-Enskog expansion it results that the fluid viscosity in Eq. (2.20) is $\eta = \frac{\rho \Delta t c_s^2}{3}(\tau - 1/2)$. No extra contributions appear in the continuum equations (2.15) and (2.16), apart from a term of order v^3 which can be neglected if the Mach number is kept small.

Other approaches to the numerical solution of the LB equation introduce spurious terms which cannot always be kept under control [83]. The one presented here has proved to be effective for simple fluids [83], multicomponent [73] and multiphase fluid systems [34, 174].

3.4. COUPLING WITH ADVECTION-DIFFUSION EQUATION

The aim of lattice Boltzmann methods goes far beyond the treatment of Navier-Stokes equation; indeed, it has proven to be a fundamental tool to solve general conservation equations [4]. Moreover, beside many implementations devoted to hydrodynamics studies, such as the ones cited at the end of the previous Section, recently a LBM approach has also been used to solve Einstein equations for gravitational waves [89].

We devote this Section to report on characteristic ways to solve the dynamics of order parameters coupled to hydrodynamic flow. Because of its relevance in the study of complex fluids we will focus on the treatment of the advection-diffusion equation (2.23) for a concentration field. The first possibility is to develop a full LBM approach in which the advection-diffusion equation is solved by introducing a new set of distribution functions $\{g_i(\mathbf{r}, t)\}$ connected to the concentration field, beside the distribution functions $\{f_i(\mathbf{r}, t)\}$ needed to solve the Navier-Stokes equation. Another route is to follow a hybrid approach where the advection-diffusion equation is solved via a standard finite difference algorithm while hydrodynamics is still solved through a LB algorithm. This is the route followed to solve the dynamic equations in this thesis.

3.4.1. FULL LBM APPROACH

To solve the hydrodynamic equations for a binary system through a full LB approach the introduction of a new set of distribution functions $\{g_i(\mathbf{r}, t)\}$ is needed [214, 215]. The index i again assigns each distribution function to a particular lattice direction indicated by the velocity vector ξ_i. The concentration field $\phi(\mathbf{r}, t)$ is thus defined as

$$\phi(\mathbf{r}, t) = \sum_i g_i(\mathbf{r}, t). \tag{3.77}$$

As in Eq. (3.8), distribution functions g_i evolve according to the following equation

$$g_i(\mathbf{r} + \xi_i \Delta t, t + \Delta t) - g_i(\mathbf{r}, t) = -\frac{1}{\tau_\phi}(g_i - g_i^{eq}), \tag{3.78}$$

where the BGK approximation for the collisional operator has been used. A new relaxation time τ_ϕ has been introduced since the relaxation dynamics of the concentration field may consistently differ from that of the underlying fluid. In Eq. (3.78) we have also introduced the set of equilibrium distribution functions $\{g_i^{eq}(\mathbf{r}, t)\}$ that fulfil the following relation

$$\sum_i g_i^{eq}(\mathbf{r}, t) = \phi(\mathbf{r}, t). \tag{3.79}$$

This ensures that the concentration field is conserved during the evolution.

To recover the advection-diffusion equation in the continuum limit, it is necessary to impose the following constraints on the first and second moments of the equilibrium

distribution functions

$$\sum_i g_i^{eq} \xi_{i\alpha} = \phi v_\alpha, \tag{3.80}$$

$$\sum_i g_i^{eq} \xi_{i\alpha} \xi_{i\beta} = \phi v_\alpha v_\beta + c^2 \chi \mu \delta_{\alpha\beta}. \tag{3.81}$$

Here the mobility parameter χ tunes the diffusion constant M that appears on the right-hand side of the advection-diffusion equation, while μ is the chemical potential. A suitable choice of the distribution function which fulfils Eq. (3.79), Eq. (3.80) and Eq. (3.81) can be written as a power expansion up to the second order in the velocity

$$g_i^{eq} = H_s + J_s v_\alpha \xi_{i\alpha} + K_s v^2 + M_s v_\alpha v_\beta \xi_\alpha \xi_\beta, \tag{3.82}$$

where the coefficients of the expansion can be computed from Eqs. (3.67) through the formal substitution

$$\rho \to \phi \qquad \sigma_{\alpha\beta} \to -c^2 \chi \mu \delta_{\alpha\beta}. \tag{3.83}$$

The continuum limit of the advection-diffusion equation can be obtained through a Taylor expansion of the left-hand side of Eq. (3.78) and by using Eqs. (3.79)-(3.81) [217]. This leads to the following expression of the diffusion constant

$$M = \chi c^2 \Delta t \left(\tau_\phi - \frac{1}{2} \right). \tag{3.84}$$

This algorithm can be generalized to describe the evolution of more complex order parameters, such as the nematic tensor $Q_{\alpha\beta}$, whose dynamics is governed by the Beris-Edwards equation of motion (Eq. (2.21)). Since $Q_{\alpha\beta}$ is a traceless symmetric tensor, in d dimensions, at least $d(d+1)/2 - 1$ extra distribution functions $\{G_{i,\alpha\beta}(\mathbf{r}, t)\}$ are needed, which are related to $Q_{\alpha\beta}$ through

$$Q_{\alpha\beta} = \sum_i G_{i,\alpha\beta}. \tag{3.85}$$

The rest of the algorithm can be thus developed as the one presented for the concentration field. In Section 3.5 we will go back to LBM for liquid crystal dynamics and we will present another algorithm that employs a predictor-corrector numerical scheme for the collision term.

3.4.2. HYBRID LBM APPROACH

An alternative approach to solve the Navier-Stokes equation and an advection-diffusion equation for an order parameter is based on a hybrid method, where a standard LBM solves the former while a finite-difference scheme integrates the latter equation.

Let us consider, for instance, the evolution Eq. (2.23) of the concentration field $\phi(\mathbf{r}, t)$. Space $\mathbf{r}$ and time t can be discretized by defining a lattice step Δx_{FD} and a time step Δt_{FD} for which $\Delta x_{FD} = \Delta x_{LB}$ (namely the scalar field is defined on the nodes of the same lattice used for the LB scheme) and $\Delta t_{LB} = m \Delta t_{FD}$, with m positive integer. At each time step the field ϕ evolves according to Eq. (2.23) and is updated in two partial steps.

1. Update of the convective term by means of an explicit Euler algorithm

$$\phi^*(\mathbf{r}_\alpha) = \phi - \Delta t_{FD}(\phi\partial_\alpha v_\alpha + v_\alpha\partial_\alpha\phi), \tag{3.86}$$

where all variables appearing at the right-hand side are computed at position $\mathbf{r}_\alpha$ and time t. Note that the velocity field $\mathbf{v}$ is obtained from the lattice Boltzmann equation.

2. Update of the diffusive part

$$\phi(\mathbf{r}_\alpha, t+\Delta t_{FD}) = \phi^* + \Delta t_{FD}\left(\nabla^2 M\frac{\delta\mathscr{F}}{\delta\phi}\right)_{\phi=\phi^*}. \tag{3.87}$$

Note that one could use more elaborate methods to solve convection-diffusion equations. For instance, one can combine predictor-corrector schemes for the treatment of the advective term with a wealth of finite-difference schemes for the numerical solution of parabolic equations [56]. Nevertheless one has to always keep in mind consistency between the order of accuracy of combined different numerical schemes used. However, the method here described, besides being relatively simple to implement, combines a good numerical stability with a reduced memory requirement with respect to the full LBM approach [186], as it will be discussed in Section 3.8.

3.5. LBM FOR ACTIVE FLUIDS

As outlined in Chapter 2, many properties of active matter are captured by liquid crystal hydrodynamics. Here we describe a LB method that solves both the Navier-Stokes equation and the Beris-Edwards equation through a full LB approach, a method often employed to numerically investigate active matter [28, 44].

As the liquid crystal stress tensor entering the Navier-Stokes equation is generally not symmetric, one could either (i) build an algorithm in which it is fully included through an external forcing term (as described in Section 3.3.2) or (ii) separate the symmetric part from the antysimmetric one, by including the former in the second moment of the equilibrium distribution functions and treating the latter as an external forcing term. Although the two procedures are equivalent, only the second approach, first introduced by Denniston *et al.* [44], has been developed so far.

In this method two sets of distribution functions, $\{f_i\}$ and $\{G_{i,\alpha\beta}\}$, are defined and are connected to the hydrodynamic variables (i.e. density, momentum) and to the order parameter through Eqs. (3.11), (3.12) and (3.85). Their lattice evolution equations are solved by using a predictor-corrector-like scheme

$$f_i(\mathbf{r}+\xi_i\Delta t, t+\Delta t) - f_i(\mathbf{r},t) = \frac{\Delta t}{2}\left[\mathscr{C}(\{f_i\},\mathbf{r},t) + \mathscr{C}(\{f_i^*\},\mathbf{r}+\xi_i\Delta t, t+\Delta t)\right], \tag{3.88}$$

$$G_{i,\alpha\beta}(\mathbf{r}+\xi_i\Delta t, t+\Delta t) - G_{i,\alpha\beta}(\mathbf{r},t) = \frac{\Delta t}{2}\left[\mathscr{C}(\{G_{i,\alpha\beta}\},\mathbf{r},t) + \mathscr{C}(\{G^*_{i,\alpha\beta}\}\mathbf{r}+\xi_i\Delta t, t)\right], \tag{3.89}$$

where f_i^* and $G^*_{i,\alpha\beta}$ are, respectively, first order approximation to $f_i^*(\mathbf{r}+\xi_i\Delta t, t+\Delta t)$ and $G^*_{i,\alpha\beta}(\mathbf{r}+\xi_i\Delta t, t+\Delta t)$ obtained by setting $f_i^* \equiv f_i$ and $G^*_{i,\alpha\beta} \equiv G_{i,\alpha\beta}$ in Eq. (3.88)

and (3.89). The collisional terms are given by a combination of the usual collision operator in the BGK approximation plus a forcing term

$$\mathscr{C}(\{f_i\},\mathbf{r},t) = -\frac{1}{\tau_f}(f_i - f_i^{eq}) + p_i, \tag{3.90}$$

$$\mathscr{C}(\{G_{i,\alpha\beta}\},\mathbf{r},t) = -\frac{1}{\tau_G}(G_{i,\alpha\beta} - G_{i,\alpha\beta}^{eq}) + M_{i,\alpha\beta}, \tag{3.91}$$

where τ_f and τ_G are two distinct relaxation times, and p_i and $M_{i,\alpha\beta}$ are the two additional forcing terms.

In order to recover continuum equations one must impose constraints on the zeroth, first and second moments of the equilibrium distribution functions and on the forcing terms. The local conservation of mass and momentum is ensured by (3.13) and (3.14), while the second moment is given by Eq. (3.65), in which the stress tensor on the right hand side includes the sole symmetric part. The antisymmetric contribution $\sigma_{\alpha\beta}^{anti}$ is introduced through the forcing term p_i, which fulfills the following relations

$$\sum_i p_i = 0, \qquad \sum_i p_i \xi_{i\alpha} = \partial_\beta \sigma_{\alpha\beta}^{anti}, \qquad \sum_i p_i \xi_{i\alpha}\xi_{i\beta} = 0. \tag{3.92}$$

The remaining distribution functions $G_{i,\alpha\beta}$ obey the following equations

$$\sum_i G_{i,\alpha\beta}^{eq} = Q_{\alpha\beta},$$
$$\sum_i G_{i,\alpha\beta}^{eq} \xi_{i\gamma} = Q_{\alpha\beta} v_\gamma,$$
$$\sum_i G_{i,\alpha\beta}^{eq} \xi_{i\gamma}\xi_{i\delta} = Q_{\alpha\beta} v_\gamma v_\delta,$$

while the forcing term $M_{i,\alpha\beta}$ satisfies

$$\sum_i M_{i,\alpha\beta}^{eq} = \Gamma H_{\alpha\beta} + S_{\alpha\beta},$$
$$\sum_i M_{i,\alpha\beta}^{eq} \xi_{i\gamma} = \left(\sum_i M_{i,\alpha\beta}^{eq}\right) v_\gamma.$$

We finally note that the predictor-corrector scheme has been found to improve numerical stability of the algorithm and to eliminate lattice viscosity effects (usually emerging from the Taylor expansion and appearing in the viscous term, in the algorithms discussed so far) to the second order in Δt. To show this, one can Taylor expand Eq. (3.88) to get

$$(\partial_t + \xi_{i\alpha}\partial_\alpha) f_i(\mathbf{r},t) - \mathscr{C}(\{f_i\}) = -\frac{\Delta t}{2}(\partial_t + \xi_{i\alpha}\partial_\alpha)\left[(\partial_t + \xi_{i\alpha}\partial_\alpha) f_i - \mathscr{C}(\{f_i\})\right] + \mathscr{O}(\Delta t^2). \tag{3.93}$$

The left-hand side is $\mathscr{O}(\Delta t)$ and coincides with the term in square brackets. One could then write at second order in Δt

$$(\partial_t + \xi_{i\alpha}\partial_\alpha) f_i(\mathbf{r},t) = \mathscr{C}(\{f_i\}) + \mathscr{O}(\Delta t^2). \tag{3.94}$$

An analogous calculation for $G_{i,\alpha\beta}$ shows that

$$(\partial_t + \xi_{i\gamma}\partial_\gamma)G_{i,\alpha\beta}(\mathbf{r},t) = \mathscr{C}(\{G_{i,\alpha\beta}\}) + \mathscr{O}(\Delta t^2), \tag{3.95}$$

thus recovering the proper lattice Boltzmann equations.

A hybrid version of the algorithm, widely employed in the study of active matter, solves the Navier-Stokes equation through a predictor-corrector Lattice-Boltzmann approach and the Beris-Edward equation by means of a standard finite-difference method [28, 84].

Further models involving more than just one order parameter have been developed in recent years, such as the theory discussed in Section 2.3.1, in which the liquid crystal order parameter (the polarization field) is coupled to the concentration field of a binary fluid mixture. Again a hybrid approach, in which both equations of the concentration and of the polarization have been solved through finite difference methods, has been used [12, 136].

3.6. BOUNDARY CONDITIONS

In many practical situations, such as in a system under shear flow, one may be interested in studying the physics of the system within a confined geometry. Here we describe the implementation of boundary conditions of a sheared bidimensional fluid defined on a lattice of size $L_x \times L_y$ and confined between two parallel flat walls located at $y = 0$ and $y = L_y$. Two key requirements are necessary for a correct description of the physics:

- no flux accross the walls,
- fixed velocity v_x^* along the walls,

which correspond to the following relations on the wall sites:

$$\sum_i f_i \xi_{ix} = \rho v_x^*, \qquad \sum_i f_i \xi_{iy} = 0. \tag{3.96}$$

Assuming a $d2Q9$ lattice geometry (see Fig. 3.2) with the walls located along the lattice links (i.e. along the lattice vectors ξ_1,ξ_3), one can explicitly write the previous relations at $y = 0$ (the bottom wall):

$$f_2 + f_5 + f_6 - f_4 - f_7 - f_8 = 0, \tag{3.97}$$

$$f_1 + f_5 + f_8 - f_3 - f_6 - f_7 = \rho v_x^*. \tag{3.98}$$

Note that after the propagation step, functions f_0, f_1, f_4, f_7 and f_8 are known, so that one can use relations (3.97) and (3.98) to determine the three unknown distribution functions f_2, f_5, f_6. This system of equations can be closed by adding the bounce-back rule:

$$f_2 = f_4. \tag{3.99}$$

The two remaining distribution functions f_5 and f_6 are then given by [223]

$$f_5 = \frac{1}{2}(2f_7 + f_3 - f_1 + \rho v_x^*) \tag{3.100}$$

$$f_6 = \frac{1}{2}(2f_8 + f_1 - f_3 - \rho v_x^*). \tag{3.101}$$

With this choice for inward-pointing distributions, the desired momentum at the boundary is achieved. Unfortunately this scheme does not allow for the local conservation of mass since, after the collision step, inward-pointing distributions are not streamed. In [106] an improvement of this scheme was proposed to overcome such a problem. In the following we will use notation f_{pi} to identify the outgoing distribution function in a wall lattice site at time $t-\Delta t$, while f_i denotes those streamed from neighbouring sites at time t. Besides conditions in (3.96) it is required that the fraction of mass moving towards the wall or eventually still on a wall site at time $t-\Delta t$ is the same that moves from the wall or stay still on the walls at time t. This is expressed for a bottom-wall site by the following relation:

$$f_{p0}+f_{p7}+f_{p4}+f_{p8}=f_0+f_5+f_2+f_6, \tag{3.102}$$

where f_0 must be determined by solving the system of Eqs. (3.96) and (3.102) together with the bounce-back condition (3.99). This leaves unchanged the solutions for the unknown f_5 and f_6 in Eqs. (3.100) and (3.101), but provides a new expression for f_0 that is thus given by:

$$f_0=\rho-(f_1+f_3)-2(f_4+f_7+f_8). \tag{3.103}$$

Such scheme can be easily adjusted to the case of the pure forcing method presented in Section 3.3.2. The only difference lies in the momentum conservation relations [93] that in such case read as follows,

$$\sum_i f_i\xi_{ix}+\frac{\Delta t}{2}F_x=\rho v_x^*, \qquad \sum_i f_i\xi_{iy}+\frac{\Delta t}{2}F_y=0. \tag{3.104}$$

The system of Eqs. (3.104) together with Eq. (3.102) admits the following solutions:

$$f_5=\frac{1}{2}\left(2f_7+f_3-f_1+\rho v_x^*-\frac{\Delta t}{2}(F_x+F_y)\right), \tag{3.105}$$

$$f_6=\frac{1}{2}\left(2f_8+f_1-f_3-\rho v_x^*+\frac{\Delta t}{2}(F_x-F_y)\right), \tag{3.106}$$

$$f_0=\rho-(f_1+f_3)-2(f_4+f_7+f_8)+\frac{\Delta t}{2}F_y, \tag{3.107}$$

where the outward-pointing distribution f_2 was fixed by the bounce back condition (3.96).

3.7. ERROR ANALYSIS AND COMPARISON WITH FINITE DIFFERENCE LATTICE BOLTZMANN: WHEN COLLISION-STREAMING IS ENOUGH

In this section we will do a comparison between the standard collision-streaming LB and finite difference LB. This will help us in discussing error analysis and validate the algorithm used to produce results presented in this thesis.

When using the finite-difference LB model in this section, the evolution equation is solved by using the third order total variation diminishing (TVD) Runge-Kutta (RK-3) time stepping procedure,[75, 86, 168, 197] together with the fifth-order weighted essentially non-oscillatory (WENO-5) scheme for the advection [20, 63, 91]. Since FDLB will

be used only in this section for a comparison with CSLB, we will not discuss the details of its implementation. More details are given in [137].

Using the Chapman-Enskog method, it can be shown that, when the fluid satisfies the Navier-Stokes equation, the non-dimensionalized value of the kinematic viscosity is given by

$$\nu_{\mathrm{FD}} = \frac{\tau_{\mathrm{FD}} T}{m} \tag{3.108}$$

where τ_{FD} is the relaxation time non-dimensionalized with respect to the finite difference conventions, T is the non-dimensionalized value of the local fluid temperature and m is the non-dimensionalized value of the fluid particle mass.

In order to relate the non-dimensional values for a quantity $\tilde{A}$ (the tilde indicates a dimensional quantity), obtained using two non-dimensionalization conventions (A_1 and A_2), the following formula can be used[216]:

$$A_1 = A_2 \frac{\tilde{A}_{\mathrm{ref};2}}{\tilde{A}_{\mathrm{ref};1}}, \tag{3.109}$$

since $\tilde{A} = A_1\ \tilde{A}_{\mathrm{ref};1} = A_2\ \tilde{A}_{\mathrm{ref};2}$.

We wish to simulate the same fluid system using both the FD and the CS lattice Boltzmann models. Since the reference values used in these models may be different, but the computer simulations are usually performed using non-dimensionalized quantities, we need the conversion relations between the non-dimensionalized values of the physical quantities used to describe the fluid properties and the flow geometry within each model. In the sequel, we will use the subscripts FD and LU to denote the physical quantities in the FD and the CS models, respectively. We choose to use LU (which stands for "lattice units") since this notation is frequently encountered in the LB literature dealing with CS models.

Let us consider a fluid system whose characteristic length is $\tilde{L}$, in which an ideal fluid with viscosity $\tilde{\nu}$ is maintained at the constant temperature $\tilde{T}_0 = T_0 \tilde{T}_{\mathrm{ref}}$. Here, we assume that the reference temperature $\tilde{T}_{\mathrm{ref}}$, the reference pressure $\tilde{P}_{\mathrm{ref}}$, the reference mass $\tilde{m}_{\mathrm{ref}}$, as well as the reference density $\tilde{\rho}_{\mathrm{ref}}$ are identical in both the CS and the FD models.

The reference speed in the two models is:

$$\tilde{c}_{\mathrm{ref;LU}} = \tilde{c}_{\mathrm{ref;FD}} = \sqrt{\frac{\tilde{K}_B \tilde{T}_{\mathrm{ref}}}{\tilde{m}_{\mathrm{ref}}}}, \tag{3.110}$$

where $\tilde{K}_B$ is the Boltzmann constant, and $\tilde{T}_{\mathrm{ref}}$ is the reference temperature in both models.

Let the reference length in the FD approach be the system size $\tilde{L}_{\mathrm{ref;FD}} = \tilde{L}$, while in the CS approach, it is the lattice spacing. Considering that the CS simulation is performed on a lattice containing N_{LU} nodes along the characteristic length $\tilde{L}$, the reference length in the CS model is

$$\tilde{L}_{\mathrm{ref;LU}} = \frac{\tilde{L}}{N_{\mathrm{LU}}} = \frac{\tilde{L}_{\mathrm{ref;FD}}}{N_{\mathrm{LU}}}. \tag{3.111}$$

The reference time in the FD approach is

$$\widetilde{t}_{\text{ref;FD}} = \frac{\widetilde{L}}{\widetilde{c}_{\text{ref;FD}}}. \tag{3.112}$$

The reference time in the LU approach is:

$$\widetilde{t}_{\text{ref;LU}} = \frac{\widetilde{L}}{N_{\text{LU}}\widetilde{c}_{\text{ref;LU}}} = \frac{\widetilde{t}_{\text{ref;FD}}}{N_{\text{LU}}}. \tag{3.113}$$

In order to ensure that the same system is being simulated, the viscosity must be fixed. The reference viscosity in the FD approach is:

$$\widetilde{\nu}_{\text{ref;FD}} = \frac{\widetilde{t}_{\text{ref;FD}}\widetilde{P}_{\text{ref}}}{\widetilde{\rho}_{\text{ref}}} = \frac{\widetilde{L}\widetilde{P}_{\text{ref}}}{\widetilde{c}_{\text{ref;FD}}\widetilde{\rho}_{\text{ref}}}, \tag{3.114}$$

being independent of the simulation details, such as number of nodes or time step, where $\widetilde{P}_{\text{ref}}$ is the reference pressure. The LU reference viscosity reads:

$$\widetilde{\nu}_{\text{ref;LU}} = \frac{\widetilde{\nu}_{\text{ref;FD}}}{N_{\text{LU}}}. \tag{3.115}$$

Thus, the LU reference viscosity depends on the number of lattice nodes N_{LU}.

This result, as well as the expression of the non-dimensionalized viscosity value in the CS model

$$\nu_{\text{LU}} = \left(\tau_{\text{LU}} - \frac{\delta t}{2}\right), \tag{3.116}$$

allows us to get the relation between the non-dimensionalized FD relaxation time τ_{FD} and the corresponding value of τ_{LU}:

$$\tau_{\text{LU}} = \nu_{\text{LU}} + \frac{\delta t_{\text{LU}}}{2} = N_{\text{LU}}\tau_{\text{FD}} + \frac{\sqrt{3}}{6}, \tag{3.117}$$

where the last term represents the numerical correction typical for collision-streaming simulations.

Cartesian shock problem

As a first test problem we consider the Cartesian shock problem. The test consists of a one-dimensional Riemann problem: In an isothermal ideal gas at temperature T, the density is initialized as follows:

$$\begin{cases} \rho(x) & = \rho_{\text{L}} \quad \text{if} \quad x \le x_0 \\ \rho(x) & = \rho_{\text{R}} \quad \text{otherwise}\,, \end{cases} \tag{3.118}$$

where ρ_{L} and ρ_{R} are the values of the density to the left and to the right of the initial discontinuity, which is located at $x = x_0$. Since in our simulation set-up, the density is related to the pressure P through $\rho = mP/T$, where T is considered to be constant, we expect no contact discontinuity to appear in our simulation results. This can be seen by considering the Euler equations, reproduced below for the one-dimensional flow of an isothermal fluid:

$$\partial_t \rho + \partial_x(\rho u) = 0, \qquad \partial_t(\rho u) + \partial_x(\rho u^2 + P) = 0. \tag{3.119}$$

Introducing the similarity variable

$$\xi = \frac{x - x_0}{t}, \tag{3.120}$$

it can be seen that Eq. (3.119) reduces to:

$$\frac{\partial u}{\partial \xi} = \frac{\xi - u}{\rho}\frac{\partial \rho}{\partial \xi}, \qquad \frac{\partial P}{\partial \xi} = (\xi - u)^2 \frac{\partial \rho}{\partial \xi}. \tag{3.121}$$

Noting that $P = \rho c_s^2$, where $c_s = \sqrt{T/m}$ is the non-dimensionalised speed of sound in an isothermal fluid, the above equations are satisfied either when ρ and u are constant, or when

$$u = \xi \pm c_s. \tag{3.122}$$

The above solution corresponds to a rarefaction wave travelling to the left (+) or to the right (−). We note that the solution $u = \xi$ (corresponding to the contact discontinuity) does not appear in the case of isothermal flows.

Assuming that $\rho_L > \rho_R$, the rarefaction wave propagates to the left, in which case the velocity can be seen to increase linearly according to:

$$u_*(\xi_*) = \xi_* + c_s, \tag{3.123}$$

where the star $(*)$ is employed to indicate that the analysis is restricted to the rarefaction wave. From Eq. (3.123) it can be seen that the head of the rarefaction wave travels with constant velocity

$$\xi_r = -c_s. \tag{3.124}$$

The tail of the rarefaction wave corresponds to the value ξ_c of the similarity variable, for which the velocity takes the constant value on the plateau, $u = u_c$:

$$\xi_c = c_s(\zeta - 1), \qquad \zeta = \frac{u_c}{c_s}, \tag{3.125}$$

where the dimensionless quantity ζ was introduced for future convenience. The value of u_c will be determined further below.

Inserting Eq. (3.123) into Eq. (3.121) gives the solution

$$\rho_*(\xi_*) = \rho_L \exp\left(-\frac{\xi_* - \xi_r}{\xi_r}\right) = \rho_L \exp\left[-\zeta \frac{u_*(\xi_*)}{u_c}\right]. \tag{3.126}$$

It can be seen that the density on the central plateau, ρ_c, can be determined once ζ is known using the equation

$$\rho_c = \rho_L e^{-\zeta}. \tag{3.127}$$

Let us now consider the Rankine-Hugoniot junction conditions for a discontinuity having the similarity variable ξ_s:

$$\rho_+(u_+ - \xi_s) = \rho_-(u_- - \xi_s), \qquad \rho_+ u_+(u_+ - \xi_s) + P_+ = \rho_- u_-(u_- - \xi_s) + P_-, \tag{3.128}$$

where + and − denote the fluid properties to the right and to the left of the discontinuity, respectively. Specializing the above equations to the case of the shock front, where $\rho_+ = \rho_R$ and $u_+ = 0$, the following relations are obtained:

$$\xi_s = \frac{\rho_c \zeta c_s}{\rho_c - \rho_R}, \qquad \rho_c - \zeta^2 \frac{\rho_c \rho_R}{\rho_c - \rho_R} - \rho_R = 0. \tag{3.129}$$

Inserting ρ_c from (3.127) in the above relations, the value of ζ can be found by solving the following nonlinear equation:

$$2+\zeta^2-\frac{\rho_{\mathrm{L}}}{\rho_{\mathrm{R}}}e^{-\zeta}-\frac{\rho_{\mathrm{R}}}{\rho_{\mathrm{L}}}e^{\zeta}=0. \tag{3.130}$$

In order to obtain the full solution, the value of ζ must be inserted in Eqs. (3.125) and (3.127) to obtain the velocity ξ_c of the tail of the rarefaction wave and the density ρ_c of the central plateau. The velocity ξ_s of the shock front can be obtained from Eq. (3.129):

$$\xi_s=\frac{\zeta c_s}{1-\frac{\rho_{\mathrm{R}}}{\rho_{\mathrm{L}}}e^{\zeta}}. \tag{3.131}$$

We now discuss our numerical results. We consider that the fluid temperature is the reference temperature, such that $T=T_{\mathrm{LU}}=T_{\mathrm{FD}}=1$, where subscripts LU and FD refer to lattice units and finite difference units receptively. Hence the non-dimensionalized sound speed in both LB models is $c_s=1$. In order to reduce the errors due to compressibility effects, we take $\rho_{\mathrm{L}}=1.1$ and $\rho_{\mathrm{R}}=0.9$, where the reference density is taken to be the average of ρ_{L} and ρ_{R}. In this case, $\zeta\simeq 0.10035$ and the relevant finite difference quantities are given below:

$$\xi_r=-1,\quad \xi_c\simeq -0.900,\quad u_c=\zeta\simeq 0.10035,\quad \rho_c\simeq 0.995,\quad \xi_s\simeq 1.051. \tag{3.132}$$

The discontinuity in density makes the simulation of shock waves propagation a good test for the numerical methods used. The initial density jump creates a density wave traveling from high density regions to lower density ones. We fixed the number of nodes at $N_x=N_{LU}=2048$ and considered two values of the relaxation time, namely $\tau_{\mathrm{FD}}=\{10^{-4},10^{-3}\}$, corresponding to $\tau_{\mathrm{LU}}=\{0.493,2.33\}$. In Fig. 3.4, the density and velocity profiles obtained with the two methods are represented at time $t_{\mathrm{FD}}\simeq 0.1128$ (attained after 400 iteration using CSLB), alongside the analytic solution for the inviscid case. The curves show good agreement between the two models for the considered values of viscosity.

In the CSLB implementation, $(\delta t)_{\mathrm{LU}}=1/\sqrt{3}$ corresponds to the time step $(\delta t)_{\mathrm{FD}}=1/N\sqrt{3}\simeq 2.82\times 10^{-4}$. The Courant-Friedrichs-Lewy number, $\mathrm{CFL}=c_l\delta t/\delta s$, is equal to one for this choice of parameters. In the FDLB implementation, the time step is bounded by the CFL condition $\mathrm{CFL}\leq 1$, such that the maximum time step permitted is that employed in the CSLB implementation. The time step in the FDLB implementation is further restricted to obey $(\delta t)_{\mathrm{FD}}<\tau_{\mathrm{FD}}$, in order to prevent the collision term from becoming stiff. Thus, at $\tau_{\mathrm{FD}}=10^{-3}$, we performed the FDLB simulations using $(\delta t)_{\mathrm{FD}}=1/N\sqrt{3}$, while at $\tau_{\mathrm{FD}}=10^{-4}$, the time step was decreased by a factor of 3, $(\delta t)_{\mathrm{FD}}=1/3N\sqrt{3}\simeq 9.40\times 10^{-5}$, such that 1200 iterations were required to reach the state shown in Fig. 3.4.

Shear waves

In order to compare numerical viscosity effects in the two models, we analyse in this subsection the evolution of shear waves. We consider waves of wavelength $\lambda=1$ in an ideal gas with density $\rho=1$ at temperature $T=1$.

In the simulations performed, the wave vector $\boldsymbol{k}$, $|\boldsymbol{k}|=2\pi/\lambda=2\pi$, was aligned along the horizontal axis and its Cartesian components were $(2\pi,0)$.

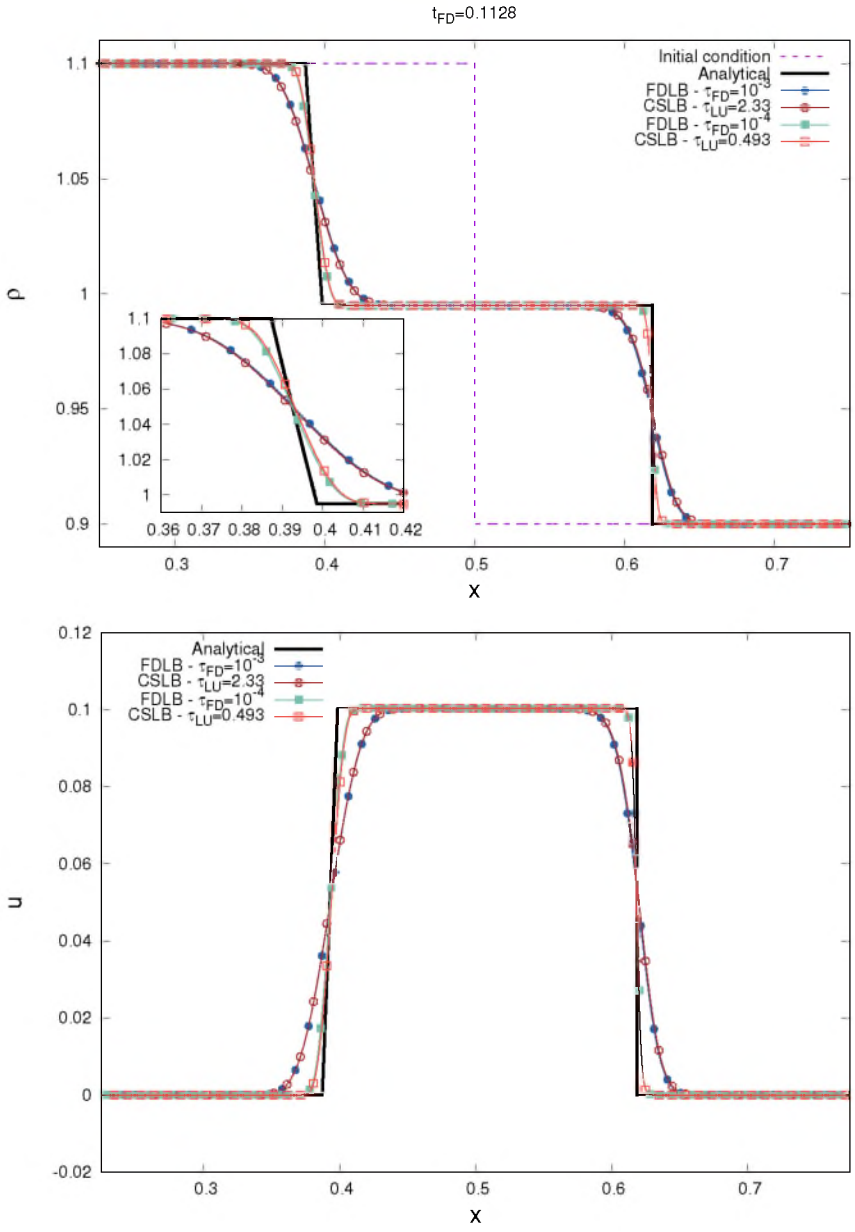

Figure 3.4: Comparison of FDLB and CSLB results in the context of the Cartesian shock problem at the level of the density **(upper panel)** and velocity **(lower panel)** profiles, obtained at $t_{\mathrm{FD}} \simeq 0.1128$ for various values of the relaxation time. The **inset** shows the shock front.

		CSLB		FDLB	
τ_{LU}	N_x	ν_{app}	Rel. err.	ν_{app}	Rel. err.
0.2986	20	0.0005073	0.0154	0.0005271	0.0542
0.3036	30	0.0005032	0.0065	0.0005039	0.0078
0.3086	40	0.0005017	0.0034	0.0005009	0.0018
0.3136	50	0.0005015	0.0021	0.0005003	0.0006
0.3186	60	0.0005006	0.0013	0.0005001	0.0002

Table 3.2: Apparent kinematic viscosity ν_{app}, expressed using the FD adimensionalization, measured as a numerical fit of Eq. (3.135) in the context of the damping of shear waves.

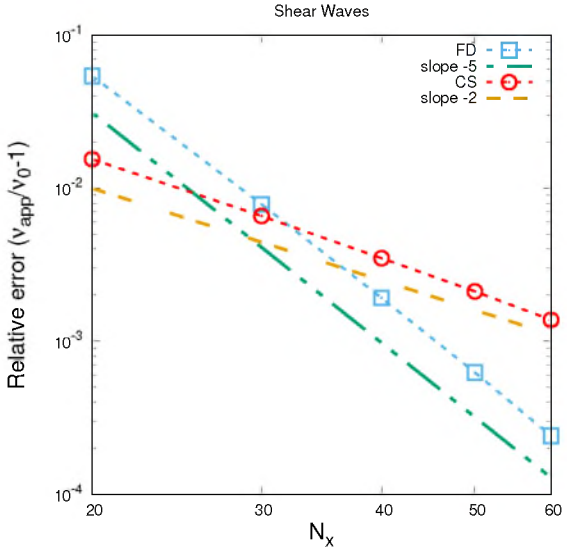

Figure 3.5: Relative error of the measured kinematic viscosity ν_{app} expressed with respect to the expected analytic value ν_0, extracted from the numerical simulations of the decaying shear waves problem, expressed with respect to the number of nodes N_x. A second second order convergence is recovered for the CSLB method, while for the FDLB method, the convergence is of fifth order.

Let $\boldsymbol{u}(\boldsymbol{x}, t)$ be the fluid velocity vector. In both series of simulations, the velocity field was initialized according to:

$$u_x(\boldsymbol{x}, 0) = 0, \tag{3.133a}$$
$$u_y(\boldsymbol{x}, 0) = U \sin(\boldsymbol{k} \cdot \boldsymbol{x}), \tag{3.133b}$$

with $U = 0.01$. When the fluid is not too far from the equilibrium (i.e., when the relaxation time is small enough), the fluid evolves according to the Navier-Stokes equations. In the set-up of the shear waves problem, we have $u_x(\boldsymbol{x}, t) = 0$ and there is no spatial variation of the velocity vector along the y direction. Under these circumstances and assuming that the fluid is isothermal and incompressible, the Navier-Stokes equations reduce to:

$$\partial_t u_y(\boldsymbol{x}, t) - \nu_0 \partial_x^2 u_y(\boldsymbol{x}, t) = 0. \tag{3.134}$$

Assuming that for $t > 0$, $u_y(\boldsymbol{x}, t) = \widetilde{u}(t) \sin(\boldsymbol{k} \cdot \boldsymbol{x})$, the solution is:

$$\widetilde{u}(t) = U e^{-k^2 \nu_0 t}, \tag{3.135}$$

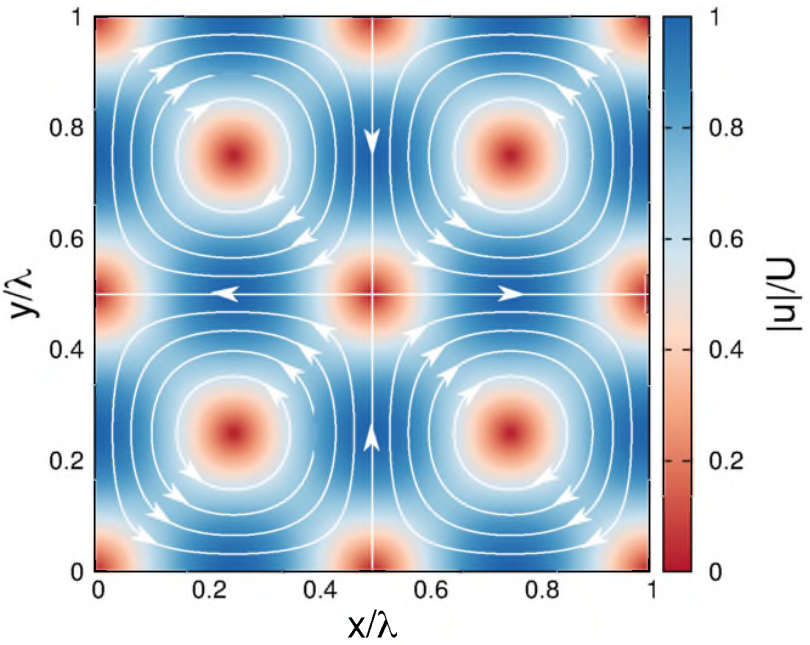

Figure 3.6: Initial structure of a Taylor-Green vortex flow. Contour plot of the velocity field module is shown, with superimposed velocity stream lines.

where ν_0 is the analytic kinematic viscosity.

We fixed the value of the kinematic viscosity in FD units at $\nu_{0;\mathrm{FD}} = \tau_{\mathrm{FD}} = 5 \times 10^{-4}$, and the simulations were performed for various values of $N_x = N_{LU}$. For a given value of ν_{FD} and number of lattice nodes N_x, we used Eq. (3.117) to obtain the corresponding value of τ_{LU}, in order to simulate the exact same system with the CS and FD models. For the FD model we used a time step of $(\delta t)_{\mathrm{FD}} = 5 \times 10^{-4}$ and lattice spacing $(\delta s)_{\mathrm{FD}} = 1/N_x$. In the CS model, the time step $(\delta t)_{\mathrm{LU}} = 1/\sqrt{3}$ corresponds to $(\delta t)_{\mathrm{FD}} = 1/N_x\sqrt{3} \simeq 5 \times 10^{-4} \times (1155/N_x)$, which for $20 \leq N_x \leq 60$ is around 20 to 60 times larger than the time step employed in the FDLB implementation.

In order to perform a quantitative analysis, a numerical fit of Eq. (3.135) was performed, which allows the parameter ν_{app} to be extracted. The measured values of ν_{app} are reported in Table 3.2 with the corresponding relative error. The latter is plotted in Fig. 3.5, showing a second order convergence for CS and a fifth order one for FD and confirming the expected numerical accuracy of the used models. It is worth noting that at $N_x = 20$, the relative error when the CSLB method is employed is roughly 3.5 times smaller than the one corresponding to the FDLB method. The relative error of the FDLB results becomes smaller than that corresponding to the CSLB method when $N_x \gtrsim 30$.

Damping of 2D Taylor-Green vortices

We now consider the damping of 2D Taylor-Green vortices.

The system is initialized as follows:

$$\begin{aligned} u_x &= U \sin(kx)\cos(ky), \\ u_y &= -U \cos(kx)\sin(ky), \end{aligned} \tag{3.136}$$

where the amplitude is $U = 0.01$ and the wave vector is $\boldsymbol{k} = (k, k)$, with $k = 2\pi/\lambda = 2\pi$.

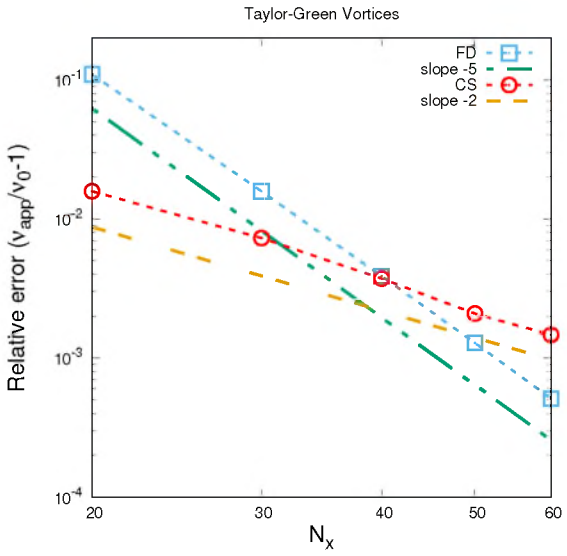

Figure 3.7: Relative error of the measured kinematic viscosity ν_{app} expressed with respect to the expected analytic value ν_0, extracted from the numerical simulations of the decaying Taylor-Green vortices, expressed with respect to the number of nodes N_x. A second order convergence is recovered for the CSLB method, while for the FDLB method, the convergence is of fifth order.

Similarly to the shear wave case, if we assume that for $t > 0$, Eq. (3.136) holds with the amplitude U replaced by $\widetilde{u}(t)$, then

$$\widetilde{u}(t) = Ue^{-2k^2\nu_0 t}. \tag{3.137}$$

Fig. 3.6 shows the initial structure of a Taylor-Green vortex flow. The flow maintains the same structure while decaying exponentially.

We fixed again the value of the kinematic viscosity in FD units at $\nu_{0;FD} = 5 \times 10^{-4}$, and the simulations were performed on square lattices having various number of nodes $N_x = N_y = N_{LU} = N$. The measured values of ν_{app}, obtained by numerically fitting the simulation results with Eq. (3.137), are reported in Table 3.3 alongside the corresponding relative error.

The latter is plotted in Fig. 3.7, showing again a second order convergence for CS and a fifth order one for FD with respect to the number of nodes. At $N = 20$, the relative error obtained using the CSLB model is about 7 times smaller than the one corresponding to the FDLB results. The relative error of the FDLB results becomes smaller than the corresponding CSLB error when $N_x \gtrsim 40$.

Liquid-vapor interface

Finally we want to compare FDLB ans CSLB in the case of a multiphase fluid system, in particular a liquid-gas system. In order to simulate this fluid system we use a lattice Boltzmann model with a van der Waals equation of state. Thermodynamics enters the model via a free-energy dependent term, added as a body force to the LBE [205], and a redefined equilibrium distribution functions as in [33] so that the fluid locally satisfies the van der Waals equation of state:

$$p^w = \frac{3\rho T}{3-\rho} - \frac{9}{8}\rho^2 \tag{3.138}$$

		CSLB		FDLB	
τ_{LU}	N_x	ν_{app}	Rel. err.	ν_{app}	Rel. err.
0.2986	20	0.0005078	0.0157	0.0005548	0.1096
0.3036	30	0.0005036	0.0072	0.0005079	0.0158
0.3086	40	0.0005018	0.0037	0.0005019	0.0039
0.3136	50	0.0005010	0.0020	0.0005006	0.0013
0.3186	60	0.0005007	0.0014	0.0005002	0.0005

Table 3.3: Apparent kinematic viscosity ν_{app}, expressed using the FD adimensionalization, measured as a numerical fit of Eq. (3.137) in the context of the damping of the Taylor-Green vortices.

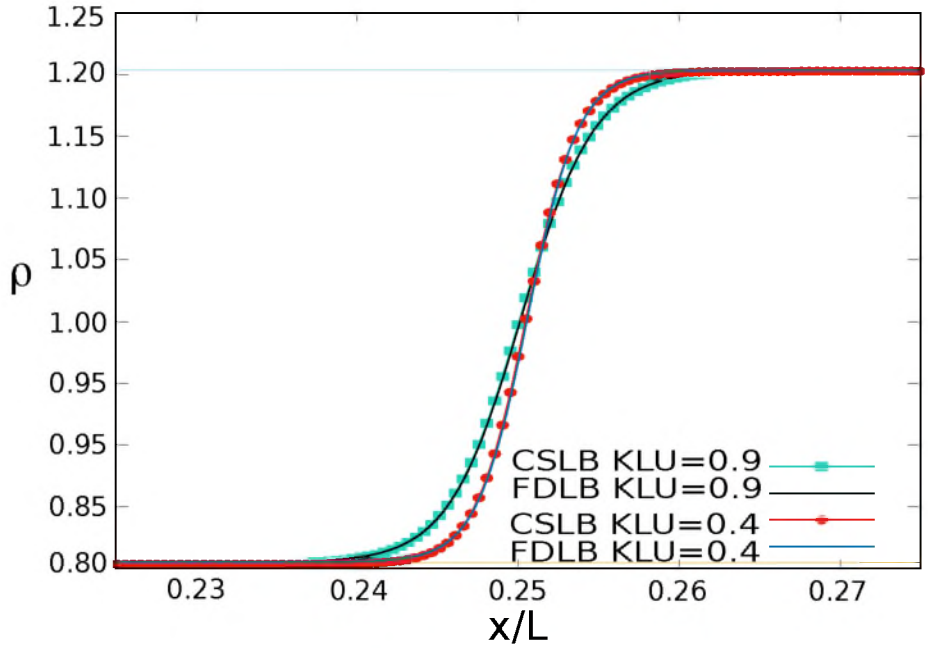

Figure 3.8: Comparison between CSLB and FDLB of a liquid-vapor interface.

where ρ is the fluid density and T the temperature. More details on the LB implementation and a study on the kinetics of the phase separation are presented in Appendix A.

The key to a successful simulation of liquid-gas systems is the faithful representation of the interface [204] between the two phases. This is well described by the approximate solution [205]

$$\rho(x) = \rho_v + \frac{\rho_l - \rho_v}{2}\left[1 + \tanh\left(\frac{x}{\sqrt{2k/(1/T-1)}}\right)\right], \tag{3.139}$$

where k is the parameter that controls the interface width and ρ_l and ρ_v are the equilibrium density values of the liquid and vapor phase obtained via the usual Maxwell construction.

We performed simulations in 2d using both CSLB [34] and FDLB [173]. Density is

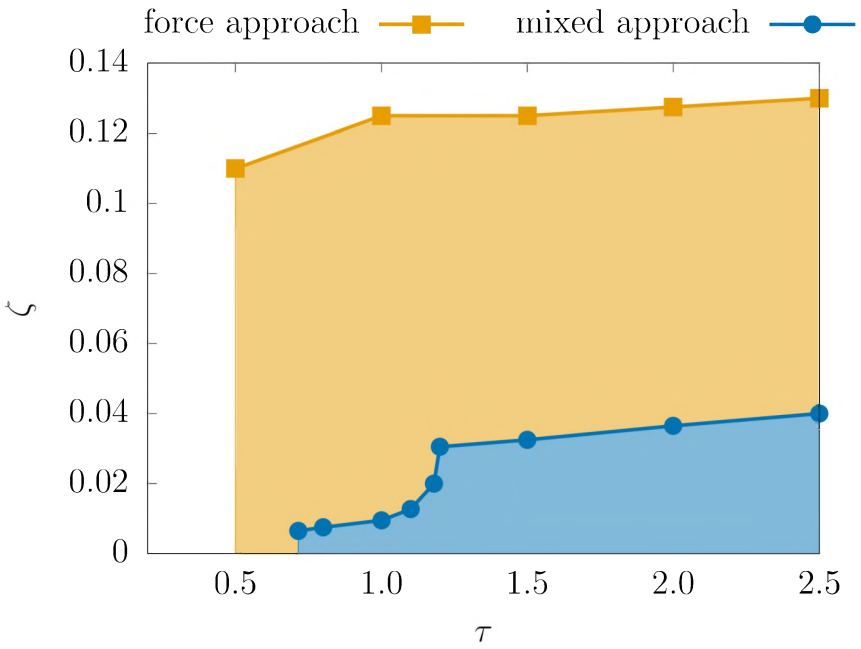

Figure 3.9: Stability of two hybrid LB codes, for a polar binary mixture, treating the stress tensor by a full-force approach (squared/yellow dots) and a mixed approach (circle/blue dots). The codes are stable for parameters under their corresponding curves. Simulations were performed on a computational grid of size 64×64, checking stability for 10^5 LB iterations.

initialized as follows:

$$\begin{cases} \rho(x) & = \rho_l \quad \text{if} \quad x \leq x_0 \\ \rho(x) & = \rho_v \quad \text{otherwise}\,, \end{cases} \tag{3.140}$$

where ρ_l and ρ_v are the values of the density to the left and to the right of the initial discontinuity, on a system of size $L = 2048$, which is located at $x = x_0 = L/2$. Temperature is fixed to $T = 0.95$, that is below the critical value for phase separation $T = 1$. The initial density profile relax towards the tanh form displayed before. Fig. 3.8 shows results of the comparison for two different values of the interface parameter k.

From this comparison we can argue that both LB models, FDLB and CSLB, are able to simulate the same physical system, in the range of validity of the Navier-Stokes equation. Furthermore, since the collision-streaming algorithm is less computationally expensive one can argue that is indeed the optimal choice in this regime. When the continuum hypothesis breaks (e.g rarefied gases) the CSLB is no longer a suitable choice and FDLB is the way to go.

3.8. STABILITY, EFFICIENCY AND PARALLELIZATION

In the previous Sections we presented different LB algorithms for the treatment of the hydrodynamics of complex and active fluids. We will comment here on the stability of two different $d2Q9$ hybrid LB codes solving the equations of an active polar binary mixture (the hydrodynamics is solved by means of LB while the order parameter dynamics is integrated by a finite difference algorithm implementing first order upwind scheme and fourth order derivative accuracy), described by the free energy in Eq. (5.1), treating the symmetric part of the stress tensor with two different approaches. The first is

a *mixed approach*, where the symmetric part of the stress tensor enters in the definition of the second moment of the distribution functions (see Eq. (3.65)) while the antisymmetric part is treated by means of the forcing term p_i (see Eqs. (3.90) and (3.92)). In the second approach the total stress tensor is treated by means of the only forcing term. To compare the stability of the two algorithms we fixed the mesh spacing and the time resolution ($\Delta x = 1$, $\Delta t = 1$), and we let vary the relaxation time τ and the intensity of active doping ζ appearing in the active stress tensor (2.11). The results of the stability test in Fig. 3.9 show that the full-force approach is definitely more stable than the mixed one. In this latter case the code is found to be stable for $\tau > 0.715$ in the passive limit ($\zeta = 0$) while to simulate active systems ($\zeta > 0$), the relaxation time must be accurately chosen to ensure code stability. In the full-force approach the code is found to be stable for $\tau > 0.5$, almost independently of ζ.

The rest of this Section is devoted to a brief discussion of some performance aspects, such as efficiency and parallelization of the LB codes used for the results presented in Chapter 4-5. LBM is computationally efficient if compared to other numerical schemes. The reason lies in the twofold discretization of the Boltzmann equation in the physical and velocity space. For instance, computational methods such as finite-difference (FD) and pseudo-spctral (PS) methods require high order of precision to ensure stability [56] and to correctly compute non-linearities in the NS equation (2.16). This introduces non-local operations in the computational implementation that reduce the throughput of the algorithm. LBM, on the contrary, is intrinsically local, since the interaction between the nodes is usually more confined, according to the particular choice of the lattice, while non linearities of the NS equation is inherently reproduced at the level of the collision operator. For instance, while the number of floating point operations needed to integrate the hydrodynamics equations on a d-dimensional cubic grid is $\sim L^d$ for LBM, it is instead of order $\sim (\ln L) L^d$ for pseudo-spectral models [178]. Nevertheless LB algorithms are definitely much more memory consuming, since for *each* field to evolve, one needs a number of distribution functions equal to the number of lattice velocities. From this perspectives, the hybrid version of the code is somewhere in the middle between the two approaches, since it allows one to exploit both computational efficiency and simplicity typical of LB approaches and, at the same time, to keep the amount of memory to be allocated at runtime lower than that necessary for a full LB treatment.

LB algorithms are particularly suitable for parallelization. The reason still lies in the local character of LB, since at the base of the efficiency of any parallelization scheme is the compactness of the data that must be moved among the different devices that take part in the program execution. Parallelization approaches involving both CPUs, *i.e.* MPI or OpenMP, and GPUs, such as CUDA and OpenCL, or even both (CUDA aware MPI) can be used when dealing with LB [98]. Most of them, such as OpenMP or GPU-based approaches, aim at rising the amount of floating operations per unit time, while a different technique consists in splitting the global computational domain in sub-domains and assign each of them to a different computational unit (usually threads of one or more processors). This is usually done with MPI.

Fig. 3.10 shows the results of a strong scaling test performed on a hybrid code integrating the hydrodynamics of a polar binary mixture [12, 136], implementing the full-force algorithm used for the stability analysis. This test consists in changing the amount of processors used to perform a certain task, while keeping fixed the size of the compu-

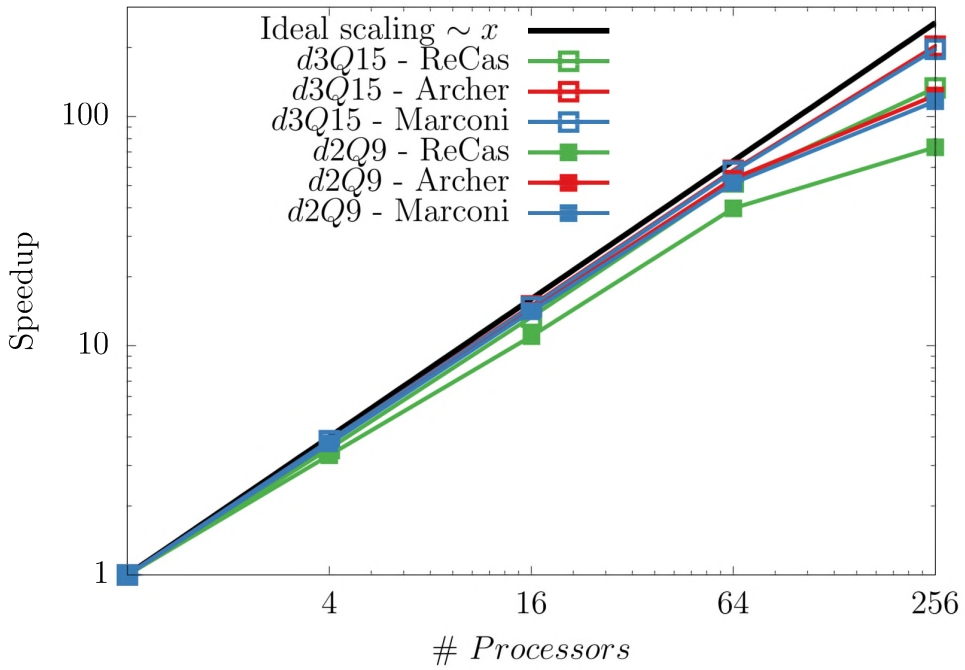

Figure 3.10: Speed-up, as defined in the text, versus number of processors for an MPI parallelized hybrid LBM code, coupled to the dynamics of a concentration scalar field and a polar vector field. Simulations were performed in $2d$ on a square computational grid (512^2) and in $3d$ in 128^3 cubic domain, on different HPC farms: Archer UK National Supercomputing Service (*http://www.archer.ac.uk/*), CINECA Marconi - Skylake partition (*http://www.hpc.cineca.it/*) and ReCas-Bari (*https://www.recas-bari.it/*).

tational grid and measuring the speed-up, namely the ratio of time spent to perform the operation with only one processor over the time taken when more processors are used. Simulations were performed both with $d2Q9$ (hollow dots) and $d3Q15$ (full dots) lattice structures on different computational infrastructures (Archer (red), Marconi (blue) and ReCas (green)). While for a few number of processors the scaling is approximately linear, thus close to the ideal linear behaviour (black line), as the number of processors increases, it progressively deviates from the ideal scaling law. This is due to a number of issues that may depend both on the infrastructure characteristics (bandwidth, cache size, latency, *etc.*) and on the program implementation (bottlenecks, asynchrony among processor, *etc.*). Moreover, code scalability is found to be significantly better in three-dimensional grids than in their bidimensional version. This is because the fraction of time spent by the $3d$ code to perform parallel operations (sending and receiving data, reduction operations, synchronization, *etc.*) is consistently reduced compared with its $2d$ counterpart.

4

SELF PROPELLED DROPLETS

Geometrical constraints and spontaneous flow are known to significantly alter the hydrodynamics of active fluids. In the past LB simulations have shown, for example, that if a sample of active gel is sandwiched between two parallel plates, the onset of a spontaneous flow crucially depends on the anchoring of the director field at the walls [124]. If the active fluid is confined in a spherical geometry, for instance in a droplet, the physics is even richer, as Joanny and Ramaswamy [92] have theoretically demonstrated. Active stress can in fact generate flows driving the spreading process of a droplet, whose shape is significantly affected by the nature of topological defects. Recent experiments have shown that the presence of an active fluid can favour droplet self-propulsion through several mechanisms, based on chemical reactions [2, 218], spontaneous symmetry breaking and Marangoni effects [57, 80, 87, 160]. Such experiments motivated numerous theoretical studies, with the aim of developing minimal models capable of capturing features of particular relevance in biology (as active droplets can mimic the spontaneous motion of cells [10, 16, 66, 191]) or in the design of bio-inspired materials [87, 160].

Most of the studies conducted so far regarded two-dimensional systems, and despite they managed to unveil some important attributes of active droplets, the axial-symmetric approximation still precludes to investigate many other properties that only full $3D$ system can exhibit [147]. For instance, the effect of chirality – a generic feature of most biological matter [152, 221] – can be properly addressed only in fully three-dimensional environment. A right-left asymmetry may arise at either the microscopic or macroscopic level, and be due to thermodynamic (passive) or non-equilibrium (active) effects. For instance, a microtubule-motor mixture breaks chiral symmetry in two ways. First, microtubules are intrinsically helical [219]. Second, kinesin or dynein motors exploit ATP hydrolisis to twist their long chains and apply a nonequilibrium active torque on the fibres they walk along [206]. Similarly, bacteria such as *Escherichia coli*, but also sperm cells, are equipped with long helical flagella. Motor proteins anchored to the cellular membrane generate torques to impart rotational motion on the flagella, whose helix generates a flow in the viscous environment leading to cell propulsion [148, 157]. Understanding the outcome of the interplay between chirality and activity is an important and timely question and most of this Chapter will be devoted to the analysis of results obtained for a chiral nematic active droplet in a newtonian background.

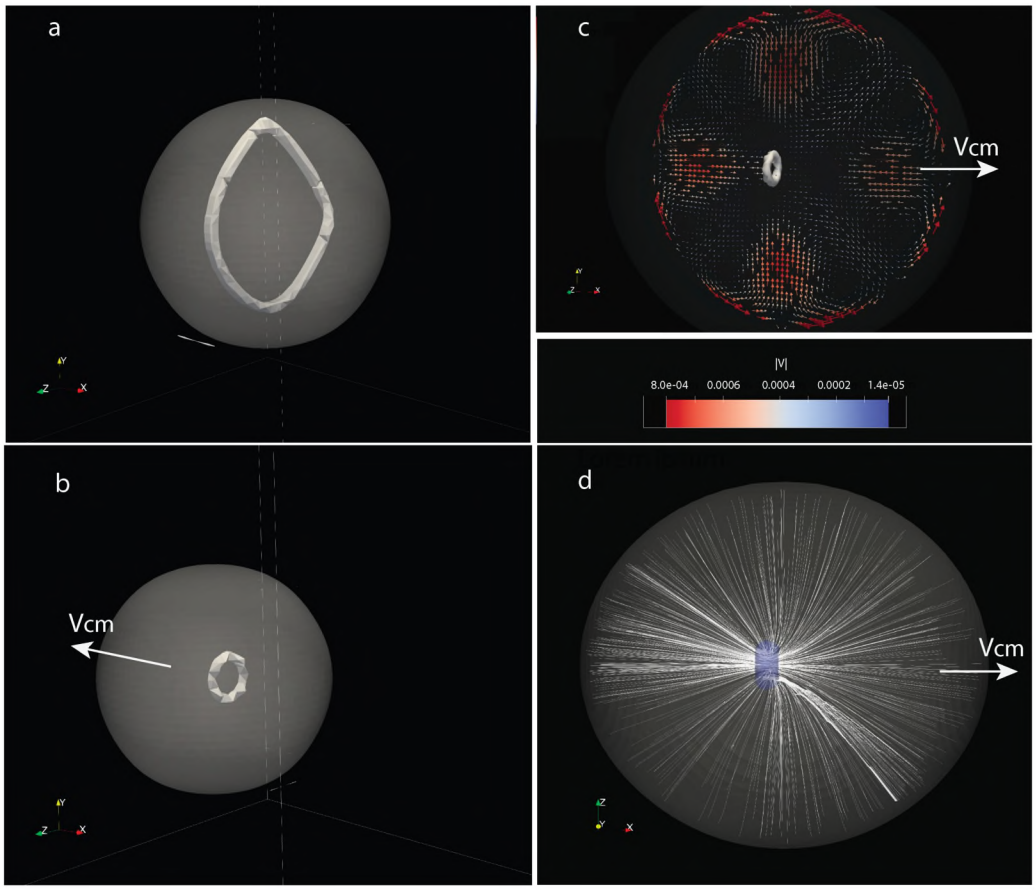

Figure 4.1: *Active nematic droplet.* Small Contractile activity (here $\zeta = -0.0001$) is able to put into motion a nematic droplet with homeotropic anchoring. During the initial relaxation of the droplet, a disclination ring is formed inside the droplet (contour plot of the biaxiality parameter in panel **(a)**), and relax in a configuration characterized by the presence of a *hedgehog* at the center of the droplet, as discussed in Chapter 2. Due to active pumping the disclinations line slightly moves (panel (b)), breaking the spherical symmetry, and the droplet starts to move. Self propulsions is sustained by splay instability (as can be appreciated looking at the order parameter stream lines in panel **(d)**), that creates a net flow from the back of the droplet towards the front (panel **(c)**).

To understand the physics at the base of droplet motility, the first two sections provides a overall picture of dynamical regimes in an active liquid crystals droplet, to address the mechanism of spontaneous symmetry breaking. In Section 4.3 the role of chirality is taken into account and I will show there how the interplay between active forces and chiral features is key to turn rotation into propulsion. Finally, in Section 4.4 a scalar model for active droplets is studied to spot out the role of compressibility in self propulsion.

4.1. SPONTANEOUS SYMMETRY BREAKING AND SELF-PROPULSION

The physics of an active gel under spherical confinement has been often described in terms of the continuum Eqs. (2.16)-(2.21)-(2.23), presented in Chapter 2. Such model can reproduce spontaneous division and motility (Giomi et al. [66] have demonstrated that) of an active nematic droplet surrounded by an isotropic Newtonian fluid – a situation closely resembling the functioning of living cells. In particular for 2d contractile

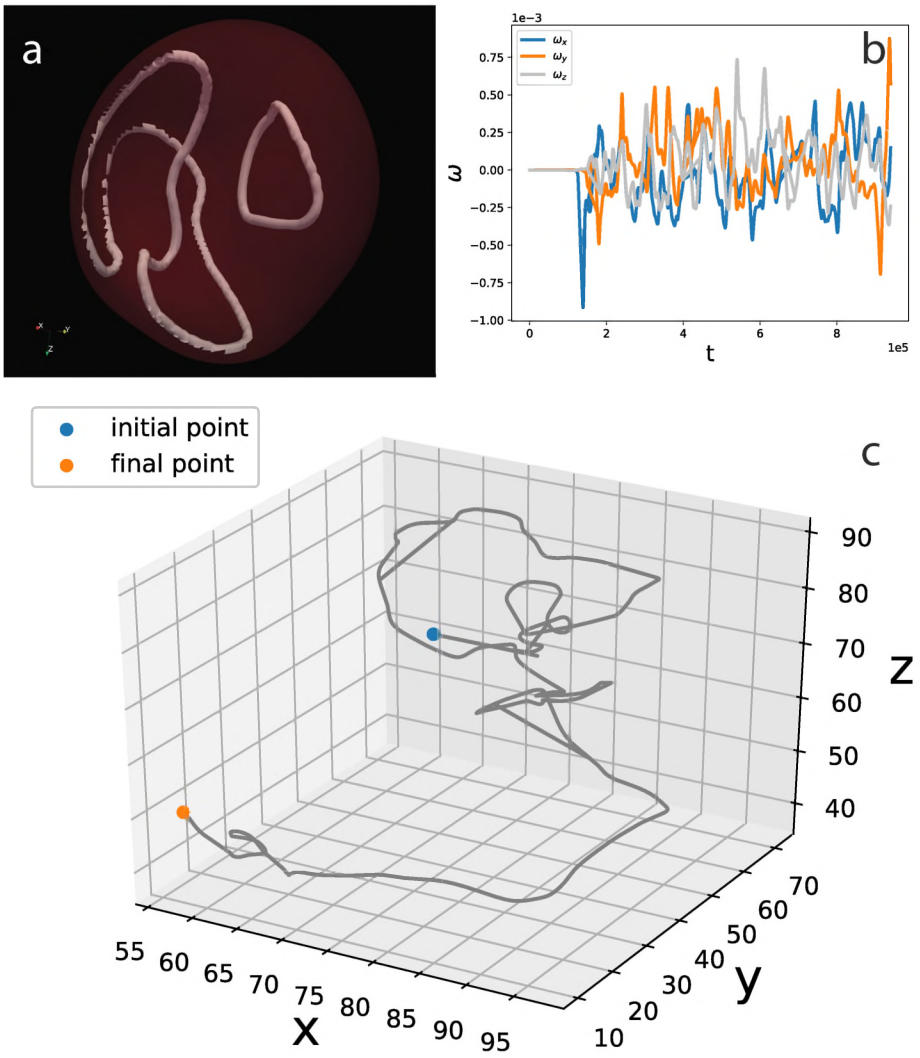

Figure 4.2: *Active nematic droplet in turbulent regime.* For $\zeta = -0.01$ the nematic droplet enters in a regime characterized by the formation of disclinations loops (panel **(a)**), as those shown for passive cholesteric droplets in Chapter 2. The droplet sets in a chaotic motion characterized by irregular rotation (as can be seen looking at the components of the angular velocity in panel **(b)**), and trajectory (panel **(c)**).

active nematic droplet, in presence of homeotropic anchoring, motility results from the combination of the initial elongation of the droplet (whose stability is guaranteed by a balance between viscous and pressure forces and the surface tension) and the instability of the active fluid to deformations of the LC pattern. When, for instance, the contractile active stress is strong enough, splay instability dominates over relaxation first leading to axial symmetry breaking, then triggering the formation of spontaneous flows promoting self-propulsion. Eventually active stress may even overcome the surface tension: in this case the droplet over-stretches and splits in two daughter droplets that may undergo a similar dynamics leading to a chain process that ends when the size of the daughter droplets becomes too small to sustain activity-induced deformations of the liquid crystal pattern. The generic mechanism of motility of active droplets has been investigated both analytically in [209] and numerically in [191] by using the polar theory described in Chapter 2. Here it is shown that the self-propulsion of a contractile

droplet stems from the spontaneous symmetry breaking of polarity inversion symmetry, which, in turn, triggers the formation of intense splay distortions that act as a source of kinetic energy, leading to motion. Symmetry breaking can be viewed as a continuous nonequilibrium phase-transition from a non-motile to a motile state observed for a sufficiently high activity. This model offers a simplified example of a cell, as a droplet containing an actomyosin solution, and suggests that motility can arise solely because of myosin contractility, rather than from its combination with actin polymerization, as often occurs [16]. The same hydrodynamic theory has been used to model the physics of an active polar droplet confined on a solid substrate, a situation resembling that of a crawling cell [192]. Here the droplet is made of an active polar fluid with contractility throughout, but actin polymerization confined in a layer close to the substrate. Such minimal description has been proven capable of capturing shapes (such as the lamellipodium [16, 194]) exhibiting self-motile regimes (such as oscillatory modulations of shape [16, 194]) by only considering a few key ingredients, i.e. actin polymerization, myosin contractility and interface anchoring. More specifically, planar anchoring induces rotational motion in contractile droplets, while normal anchoring has the same effect in extensile ones. In both cases rotation stems from an active torque, due to a pair of bulk elastic distortions whose formation is controlled by a careful balance between activity and interface anchoring conditions. The same nemato-hydrodynamic theory has been used to model the physics of an active polar droplet confined on a solid substrate, a situation resembling that of a crawling cell [192].

To better illustrate the mechanism behind the spontaneous symmetry breaking we start by showing some results regarding a 3d contractile nematic droplet with homeotropic anchoring. This same situation was studied, as already said, in 2d by Giomi et al., and in 3d for polar systems by Tjhung et al. [191].

We use the continuum model for nematic liquid crystals introduced in Chapter 2, considering homeotropic anchoring. The dynamical equations governing the evolution of the system have been discussed in Chapter 2, namely Eqs. (2.16), (2.21) and (2.23). These are solved in 3D with the hybrid LB method described in section 3.4. In addition we made use of a parallel approach implementing Message Passage Interface (MPI) to parallelize the code. We divided the computational domains in slices, and assigned each of them to a particular task in the MPI communicator. Activity is introduced through a coarse grained description of force dipoles [65]. These result in a non-equilibrium stress tensor that can be expressed as $\sigma^{af}_{\alpha\beta} = -\zeta\phi Q_{\alpha\beta}$.

In this system, the main control parameter is the dimensionless activity $\theta = \zeta R^2/K$, (with R the radius of the droplet and K the elastic constant of the LC) which measures the relative contribution of activity and elasticity.

Small Contractile activity is able to put into motion a nematic droplet with homeotropic anchoring. Fig. 4.1 refers to the case $\zeta = -10^{-4}$. During the initial relaxation of the droplet, a disclination loop is formed inside the droplet (contour plot of the biaxiality parameter[1] in panel **(a)** of Fig. 4.1), and relax in a configuration characterized by the presence of a *hedgehog* at the centre of the droplet, as discussed in Chapter 2. Due to active pumping the disclinations line slightly moves (panel (b) of Fig. 4.1), breaking the

[1] The degree of biaxiality of the LC has been computed by following the approach of Ref. [21] as the second parameter of the Westin metrics $c_p = 2(\tilde{\lambda}_2 - \tilde{\lambda}_3)$, where $\tilde{\lambda}_1$, $\tilde{\lambda}_2$ and $\tilde{\lambda}_3$ (with $\tilde{\lambda}_1 \geq \tilde{\lambda}_2 \geq \tilde{\lambda}_3$) are three eigenvalues of the positive definite diagonalised matrix $G_{\alpha\beta} = Q_{\alpha\beta} + \delta_{\alpha\beta}/3$.

spherical symmetry, and the droplet starts to move. Self propulsions is sustained by splay instability (as can be appreciated looking at the order parameter stream lines in panel **(d)**), that creates a net flow from the back of the droplet towards the front (panel **(c)** of Fig. 4.1).

Enlarging contractile activity the nematic droplet enters in a regime characterized by the formation of disclinations loops (panel **(a)** of Fig. 4.2), as those shown for passive cholesteric droplets in Chapter 2. The droplet sets in a chaotic motion characterized by irregular rotation (as can be seen looking at the components of the angular velocity[2] in panel **(b)** of Fig. 4.2), and trajectory (panel **(c)** Fig. 4.2).

In the next section we will consider the case of extensile activity and tangential anchoring, and show how in this case the spontaneous symmetry breaking mechanism only leads to a spontaneous rotation, or a chaotic regime for high activity.

4.2. NEMATIC DROPLET WITH ACTIVE FORCE DIPOLE AND TANGENTIAL ANCHORING: SPONTANEOUS ROTATION

We now describe the dynamics of a nematic droplet, with active force dipole, with tangential anchoring. This is a useful limit to which the chiral results will be compared. As the dimensionless activity θ is increased, three possible regimes arise. For low values of θ the droplet is static, and the director field attains a boojum-like pattern, with two antipodal surface defects of topological charge +1. This is one of the patterns which can be found in *confined passive nematics* with tangential anchoring, and satisfies the hairy-ball theorem [52] which states that the sum of the topological charges of a vector field tangential to a closed surface is equal to its Euler characteristic (which is +2 for a sphere). As activity is increased, this *quiescent phase* gives way to another regime, where the droplet spontaneously rotates in steady state (Fig. 4.3, Movie 1[3]). The quiescent droplet has spherical symmetry , whereas it deforms in the rotating phase, attaining the shape of a prolate ellipsoid of revolution (Fig. 4.3a,b). The director field on the droplet surface exhibits bending deformations, typical of extensile suspensions, that strengthen at the equator – thus acting as a momentum source (see yellow arrow in Fig. 4.3a) – and power stable rotational motion . The flow has the pattern of a single vortex inside the droplet, which is stronger close to the surface. The rotational flow exhibits quadrupolar symmetry in the equatorial plane, and is compensated by a counteracting velocity field outside the droplet – ensuring overall angular momentum conservation. The rotational velocity, ω, is linearly proportional to the activity ζ. This scaling can be rationalised by dimensional analysis, or by equating the torque per unit volume introduced by activity, which should scale as ζ, to the one which is dissipated, given by $\gamma_1\omega$, where γ_1 is the rotational viscosity.

For still larger θ, the droplet rotates and moves in a chaotic manner (Fig. 4.3e). This regime is the droplet analogue of what is known as *active turbulence* [183, 198] – the chaotic dynamics observed in an active nematic fluid. In the chaotic regime, motion is random and the cylindrical symmetry of the droplet shape is lost (Fig. 4.3b). De-

[2]The angular velocity of the droplet has been computed as: $\omega = \int d\mathbf{r}\phi \frac{\Delta\mathbf{r}\times\Delta\mathbf{v}}{|\Delta\mathbf{r}|^2}$, where $\Delta\mathbf{r} = \mathbf{r} - \mathbf{R}$ and $\Delta\mathbf{v} = \mathbf{v} - \mathbf{V}$, being $\mathbf{R}$ and $\mathbf{V}$ respectively the position and the velocity of the center of mass of the droplet.

[3]Movies are described in Appendix D, and can be found at the following link: https://www.dropbox.com/sh/qs7fbvk8p2ttcst/AAC988O90RnPSYLhsX8sf13ua?dl=0

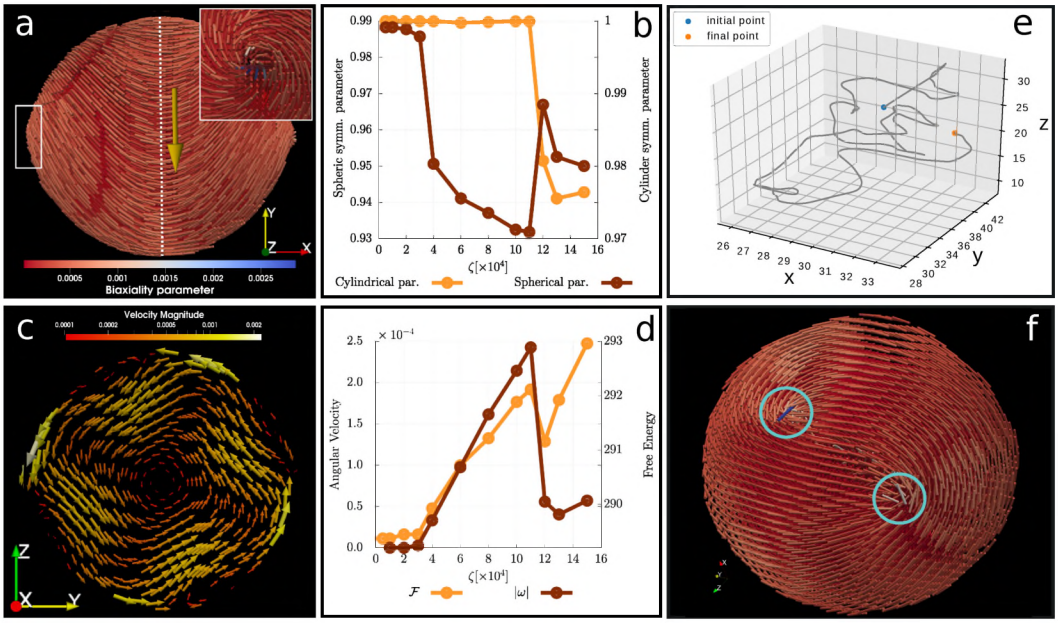

Figure 4.3: *Active nematic droplet.* Panel (a) shows the configuration of the director field **n** on the droplet surface for the case in the rotational regime at $\zeta = 10^{-3}$. Two stationary +1 boojums are formed at antipodal points in the x direction. The inset in panel (a) shows the director field in proximity of the boojum framed with a white box. Bending deformations occur transversally to the long axes of the droplet and generate an active force in the direction of the yellow arrow, thus powering rotational motion in the yz plane. Panel (c) shows the velocity field on the equatorial cross section of the droplet, depicted with a dashed white line in panel (a). The flow, induced and sustained by energy injection due to the bendings in the nematic pattern, exhibits quadrupolar symmetry. In panel (b) the spherical and cylindrical deformation parameters are used to characterize the transition from the quiescient state to the rotational regime then to the chaotic regime. These have been computed as computed as d_{min}/d_{max} and d_{min}/d_{med} respectively, with $d_{max} \geqslant d_{med} \geqslant d_{min}$ the time-averaged eigenvalues of the positive-definite Poinsot matrix associated to the droplet. Analogously panel (d) shows the angular velocity and the free energy as the activity parameter ζ is varied. Panel (e) shows the trajecotry of the centre of mass of an active nematic droplet for $\zeta = 2 \times 10^{-3}$. For the same value of the active parameter panel (f) shows the the director field on the surface of the droplets. In this regime half integer defects continuously form ad annihilate.

fect dynamics on the surface is also erratic, and we observe the nucleation of additional defects (Fig. 4.3f), not present in the quiescent or rotating regimes. These defects are topologically the ends of disclination lines which often depin from the surface and pierce the interior of the droplet (Suppl. Movie 2). The onset of the chaotic regime is due to the fact that the energy coming from activity can no longer be dissipated by a regular rotation, but is used up to generate additional defects on the surface. As the chaotic regime sets in – characterized by the loss of cylindrical symmetry – concurrently the free energy of the system decreases (Figs. 4.3d), signalling that the shape change is thermodynamically favoured. The subsequent increase in $\mathscr{F}$ at larger θ is due to defect nucleation.

So far we have shown how splay instability is able to sustain self-propulsion in a nematic contractile droplet with homeotropic anchoring. We discussed previous results on this set-up and showed some results obtained with our implementation of the LB solver discussed in Chapter 3. Using the same approach we have shown how bending instability is responsible of putting a nematic extensile droplet with tangential anchor-

ing into rotation. In this latter case we now ask if it is also possible to have self propulsion. The answer will be yes as long as chiral symmetry is broken. This will be discussed in the next section.

4.3. ROTATION AND PROPULSION IN 3D ACTIVE CHIRAL DROPLETS

We want now to uncover what happens if chiral symmetry is broken. Here we use a generalized version of the nematic model introduced in Chapter 2 to account for chirality:

$$\mathscr{F}[\phi, Q_{\alpha\beta}] = \int dV \left| \frac{a}{4}\phi^2(\phi-\phi_0)^2 + \frac{k_\phi}{2}(\nabla\phi)^2 + A_0 \left| \frac{1}{2}\left(1-\frac{\chi(\phi)}{3}\right)\mathbf{Q}^2 - \frac{\chi(\phi)}{3}\mathbf{Q}^3 + \frac{\chi(\phi)}{4}\mathbf{Q}^4 \right| + \frac{K_Q}{2}\left[(\nabla\cdot\mathbf{Q})^2 + (\nabla\times\mathbf{Q} + 2q_0\mathbf{Q})^2\right] + W(\nabla\phi)\cdot\mathbf{Q}\cdot(\nabla\phi) \right|, \quad (4.1)$$

where the constants a, k_ϕ define the surface tension and the interface width among the two phases, whose minima are found in 0 and ϕ_0. The liquid crystal phase is confined in those regions where $\chi(\phi) = \chi_0 + \chi_s\phi > 2.7$, with $\chi_0 = 10\chi_s = 2.5$. The gradient terms in K_Q account for the energy cost of elastic deformations in the one-constant approximation. The number of twists of the cholesteric helix is controlled by the parameter $q_0 = 2\pi/p_0$ ($q_0 > 0$ for right-handed chirality) through the pitch length p_0. In order to compare the cholesteric pitch with the size of the droplet $p_0 = 4R/N$. Where N is the number of π twists the cholesteric liquid Crystal would display over a distance of $2R$ if not confined. Tangential anchoring is obtained for $W > 0$. Again the dynamical equations governing the evolution of the system are the same discussed in Chapter 2, namely Eqs. (2.16), (2.21) and (2.23). We performed 3d LB simulations with the same hybrid LB method described in section 3.4, with MPI implementation for parallelization. The values of free energy parameters used [4] are $a = 0.07$, $k_\phi = 0.14$, $A_0 = 1$, $K_Q = 0.01$, and $W = 0.02$. The rotational diffusion constant Γ is set to 2.5, while the diffusion constant to $M = 0.1$.

As stated in the introduction of this Chapter, chiral symmetry can be broken at two levels. The first one regards the intrinsic chirality of the system, which can be modelled by the free energy (4.1). The second level is the *active* one. To do so we have to take into account both force and torque dipoles [65], in our coarse grained description. These result in a non-equilibrium stress tensor that can be respectively expressed as $\sigma^{af}_{\alpha\beta} = -\zeta\phi Q_{\alpha\beta}$ (force dipoles) and $\sigma^{at}_{\alpha\beta} = -\bar{\zeta}\epsilon_{\alpha\beta\mu}\partial_\nu(\phi Q_{\mu\nu})$ (torque dipoles), where ϕ is the concentration of active material, $\epsilon_{\alpha\beta\mu}$ the Levi-Civita tensor, while ζ and $\bar{\zeta}$ are proportional to the strength of active force and torque dipoles respectively. Positive values of ζ correspond to extensile force dipoles, whereas if $\zeta < 0$ the force dipole activity is contractile. For active torque dipoles, a negative value of $\bar{\zeta}$ corresponds to an inward pair of torques, similar to that used to open a bottle cap. Conversely, $\bar{\zeta} > 0$ correspond to an outward torque pair, similar to that used to close a bottle cap. Unless otherwise stated, here we restrict for concreteness to the case where $\zeta > 0$ and $\bar{\zeta} < 0$.

[4] The same values have been used to produce the results presented at the beginning of this Chapter. When homeotropic anchoring has been considered in the previous sections $W = -0.01$ has been chosen.

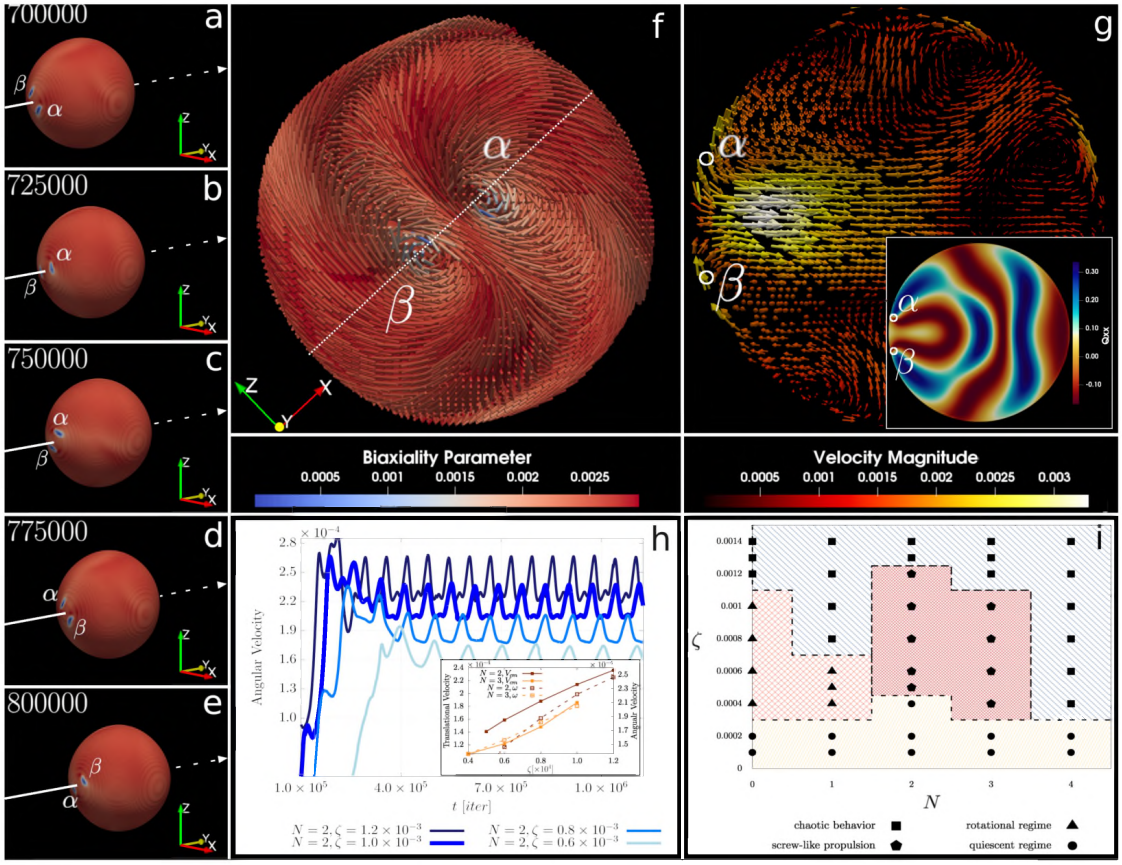

Figure 4.4: *Screw-like propulsion in a chiral droplet with active force dipoles.* Panels (a-e) show snapshots at different times of a chiral active droplet for the case at $N = 2$ and $\zeta = 10^{-3}$. The contour-plot of the biaxility parameter on the droplet surface serves to identify the position of the two +1 defects, labelled with Greek characters α and β, whose configuration can be appreciated by looking at panel (f). The screw-like rotational motion generates a strong velocity field in the interior of the droplet in proximity of the two defects. The velocity field has been plotted in panel (g) on a plane transversal to the plane of rotation of the two defects (dashed line in panel (f)). The inset shows the contour plot, on the same plane, of the Q_{xx} component of the Q-tensor, exhibiting an arrangement similar to the *radial spherical structure*. Panel (h) shows the time evolution of the angular velocity of the droplet for some values of ζ. The inset shows the mean angular velocity and the translational velocity of the droplet as a function of ζ both for $N = 2$ and $N = 3$. Panel (i) summarizes the droplet behaviour as a function of ζ and N.

4.3.1. CHOLESTERIC DROPLET WITH ACTIVE FORCE DIPOLES: SCREWLIKE PROPULSION

We now consider the case of a cholesteric droplet, still with active force dipoles only. The two key control parameters are now θ and N. For a fixed value of N, increasing ζ again leads to three possible regimes, as in the nematic limit. For sufficiently large cholesteric power (e.g., $N = 2$, Fig. 4.4, Movie 3), the first active regime encountered is, however, fundamentally different from the rotating phase of active nematics. Now the surface defect pattern is a pair of nearby +1 defects, reminiscent of a *Frank-Price structure*[5] which is seen in passive cholesterics, but only with much larger N ($N \geq 5$ [110]). The configuration of director field which we observe is known as *radial spherical struc-*

[5] *Frank-Price structure* has been observed in passive cholesteric droplets for high twisting power $qR > 1$. It consists of a hedgehog with an attached $s = +2$ defect line of length R.

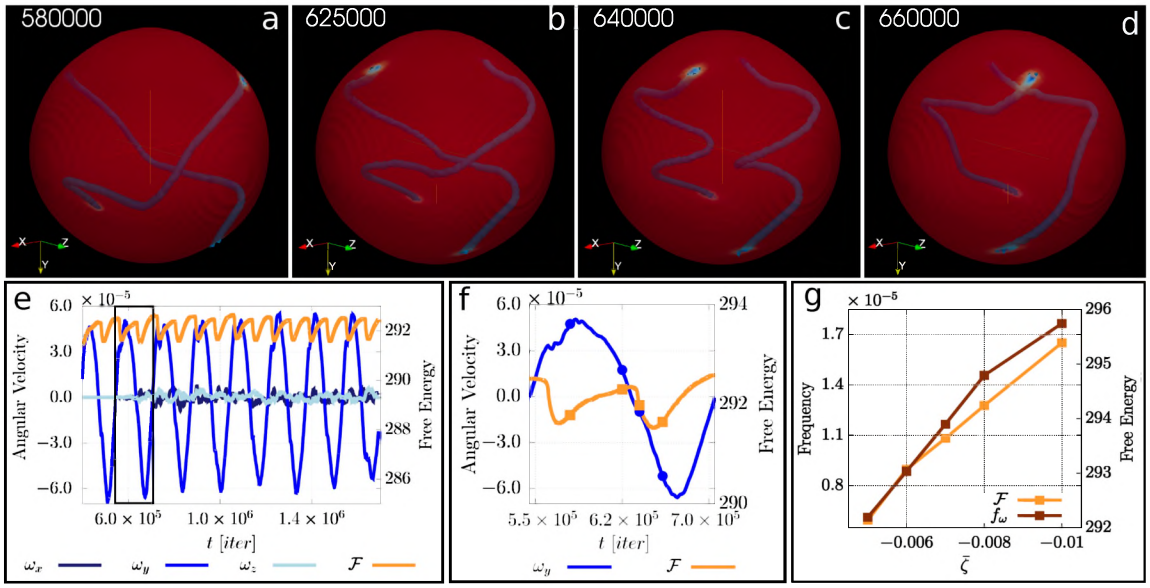

Figure 4.5: *Disclination dance in a chiral droplet with active torque dipoles.* Panels (a-d) show snapshots of the droplet and the disclination lines for the case at $N = 1$ and $\bar{\zeta} = -5 \times 10^{-3}$. The four +1/2 defects rotate in pairs in opposite directions (top defects rotate anti-clockwise, while bottom defects rotate oppositely). As the defects rotate the two disclination lines first create a link (b), then they recombine (c) and finally relax into a configuration close to the initial one (a) but rotated. The angular velocity, null on average, oscillates from positive to negative values as shown in panel (e). Here the time evolution of the free energy shows that $\mathcal{F}$ oscillates with a double frequency. Inset shows the behaviour of ω_y and $\mathcal{F}$ in the region framed with the black box. Marked dots here denote the points corresponding to the snapshots. Panel (g) shows that oscillation frequency and mean free energy linearly depend on the intensity of active torque $\bar{\zeta}$.

ture [164, 222], with some additional distortions in the cholesteric layers due to activity (as suggested by the inset in Fig. 4.4g that gives an insight into the cholesteric arrangement in the interior of the droplet). There is a suggestive analogy between this structure and a magnetic monopole – representing the radial orientation of the helical structure at the droplet centre – with its attached *Dirac string* [102, 222], joining the centre of the droplet with the defect pair. In our simulations the latter represents the region of maximal layer distortion and energy injection, as suggested by the intensity of the velocity field, plotted in Fig. 4.4g.

The two surface defects rotate around each other: as they do so, the pair periodically separates and reconvenes (Movie 3). At the same time, the droplet undergoes a global rotation with oscillating angular velocity (Fig. 4.4h). Remarkably, this time the rotation is accompanied by a translation along the direction of the rotation axis – thereby resulting in a screw-like motion, with the axis of the rototranslation parallel to the *Dirac string*. This motility mode is compatible with the chiral symmetry of the system, which introduces a generic non-zero coupling between rotations and translations. Strong deformations induced by the two close rotating +1 defects are responsible of the intense flows that develops internally at the droplet and is maximum at the rear (see Fig. 4.4g) thus powering propulsion. Symmetry of the flow corresponds to that of a macroscopic pusher. Mechanistically, therefore, activity is required to power droplet rotation, and chirality is needed to couple rotation to motion. As the motion is screw-like, the linear and the angular velocity are proportional to each other – a similar argument to that

used for active nematics also shows that they should both scale approximately linearly with θ, and we found this to hold for our simulations (Fig. 4.4h, inset).

A phase diagram in a portion of the (N,ζ) plane is shown in Fig. 4.4i. The results, not depending on the (random) initial conditions, show that for small activity the droplet sets into a quiescent regime independently of the cholesteric power: this is characterized by weak bending deformation of the LC network on the droplet surface, which are not enough to power any self-sustained motion. As activity is increased different behaviours arise: for null or weak cholesteric power ($N \leqslant 1$) stationary rotational motion sets up while screw-like propulsion needs the defects to relocate to one hemisphere creating a dipolar pattern. This is found to be only possible for a limited range of ζ and only for $N = 2,3$. Indeed, at higher cholesteric power ($N \geqslant 4$), the droplet sets into the chaotic phase even at intermediate activity, a regime characterized by defect nucleation and disordered droplet motility that can be found at any N for sufficiently large values of ζ.

4.3.2. CHOLESTERIC DROPLETS WITH ACTIVE TORQUE DIPOLES: ROTATION AND DISCLINATION DANCE

We next consider the case of a cholesteric droplet with active torque dipoles. These are able to introduce a nonequilibrium twist in a nematic droplet [188], whose handedness may reinforce or oppose the handedness of the thermodynamic twist, which is determined by q_0. The strength of the nonequilibrium twist can be measured by the dimensionless number $\bar{\theta} = |\bar{\zeta}|R/K$, whilst that of the equilibrium one can be assessed by N.

We find that the most interesting dynamics, in the case of a right-handed twist ($q_0 > 0$), occurs for $\bar{\zeta} < 0$ (torque dipole corresponding to bottle cap opening, leading to a conflict between the nonequilibrium and equilibrium twist). In this situation, for $N = 1$, we find that the droplet is pierced by two disclination lines which end in $+1/2$ surface defects at $\bar{\zeta} = -5 \times 10^{-5}$. The droplet regularly alternates opposite sense rotations, along $\pm\hat{y}$, which are tightly regulated by the disclination dynamics (Fig. 4.5, Movie 4[6]). The helical axis is here approximately parallel to $\hat{z}$, with the director almost parallel to $\hat{x}$ in the centre of the droplet.

At the beginning of the rotation cycle shown in Fig. 4.5, the disclinations wind once around each other in a right-handed fashion. Equivalently, if we were to orient both the disclinations along the positive $\hat{y}$ axis, we can associate the single crossing visible in the projection of Fig. 4.5a with a positive writhe [6] (as the top disclination can be superimposed on the bottom one via an anticlockwise rotation). As the system evolves, due to the internal torque dipoles, the pair of surface defects in the top hemisphere rotates counterclockwise, while that in the bottom hemisphere rotates clockwise (Fig. 4.5b). This motion increases the winding of the disclinations, until they rewire to form two separate right-handed helices (Fig. 4.5c – if we were to extend the two disclinations along $\hat{z}$, they would be unlinked). The regular switches in the sense of droplet rotation beat the time of the disclination dance visualised in Fig. 4.5a-d and Suppl. Movie 4. Rotation inversion occurs just at the time when the defect rewiring happens as the effect of the top/bottom asymmetry in the disclination configuration: these are regions of

[6]Movies are described in Appendix D, and can be found at the following link: https://www.dropbox.com/sh/qs7fbvk8p2ttcst/AAC988O90RnPSYLhsX8sf13ua?dl=0

strong deformation leading to greater energy injection, thus strengthening the vortical flow in the corresponding hemisphere and leading to the consequent oscillation of the angular velocity. We find that the evolution of the angular velocity mirrors that of the overall free energy of the system, with a small time delay: we argue that this is because the stress stored in the elastic deformations plays a large role in powering the motion. Moreover, the frequency of the free-energy oscillation is twice that of the angular velocity f_w (see panels (e-f)), a behaviour in line with the fact that configurations in panel (a) and (d) are specular with respect to the rotation plane and energetically equivalent.

Unlike in the active nematic case, where rotation is powered by force dipoles, here the dynamics is driven by torque dipoles.

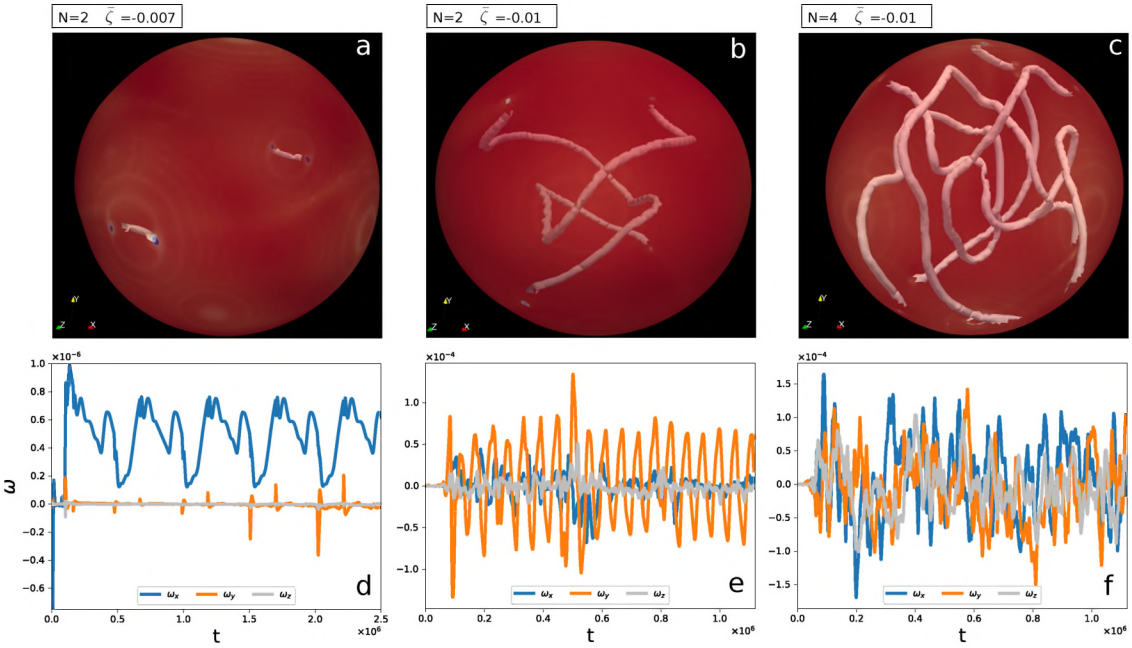

Figure 4.6: *Active torque dipoles.* Panel a shows a snapshot of the droplet and the disclination lines for the case at $N = 2$ and $\bar{\zeta} = -7 \times 10^{-3}$. In this case the droplet sets into rotational motion (notice the difference of the order of magnitude of the angular velocity in panel d with respect to the analogue cases presented in the main text for a droplet fuelled by force dipoles only). Panel b and e show the case at $N = 2$ and $\bar{\zeta} = -10^{-2}$, characterized by the dancing of the disclination lines. Panel c shows a snapshot of the droplet and its disclination lines for the case at $N = 4$ and $\bar{\zeta} = -10^{-2}$, in the chaotic regime – see panel f – characterized by nucleation of surface defects (panel c).

The scenario concerning the properties of a cholesteric droplet fuelled by torque dipoles, is highly sensitive to both the active doping and the twisting number N. Indeed, the dynamics described so far at $N = 1$ is stable only for a limited range of activity ($5 \times 10^{-3} \leqslant |\bar{\zeta}| \leqslant 12 \times 10^{-3}$). Small values of $|\bar{\zeta}|$ ($< 5 \times 10^{-3}$), are not enough to excite the splitting of the two boojums and generate instead bending deformations of the LC pattern at $N = 1$, similar to those shown in Fig. 4.3a. In this case the droplet sets into a stationary rotational motion characterized by small angular velocity ($|\omega| \sim \mathcal{O}(10^{-6})$) (Fig. 4.6). If activity exceeds a critical threshold, $|\bar{\zeta}| > 12 \times 10^{-3}$, nucleation of further defects on the droplet surface leads to droplet deformation with consequent chaotic dynamics (Fig. 4.6). The competition between active and equilibrium chirality has important effects when N is changed. Indeed, a further key dimensionless number to determine

the behaviour of a cholesteric droplet with active torque dipoles is $\bar{\zeta}/(q_0 K)$, or equivalently, the ratio between the pitch and the "active torque length" $K/\bar{\zeta}$. The latter can be thought of as the nonequilibrium pitch, or the modulation in twist due to the action of the active flow. We would then expect that for larger q_0 (i.e., larger N at fixed R), a rotating regime as in Fig. 4.5 can be obtained by increasing $\bar{\zeta}$ (Supp. Fig. 1). Our simulations confirm, indeed, that the range of stability of stationary rotation widens as N is increased, while the set up of the mirror rotation regime moves towards more intense $|\bar{\zeta}|$. Nevertheless, if $N \geqslant 4$, the droplet directly moves from the rotational to the chaotic regime, analogously to what happens in a cholesteric droplet fuelled by force dipoles only.

It is notable that the disclination dance which we observe at intermediate $|\bar{\zeta}|$ is also reminiscent of that seen experimentally in active nematic shells [81, 96, 219] made up of microtubule-molecular motor mixtures. Despite the confined geometry is different, our results suggest that the underlying mechanism powering rotation observed in the aforementioned studies, may be related to torque rather than force dipoles.

4.3.3. OVERVIEW AND THE ROLE OF HANDNESS

Our simulations show that the interplay between activity and thermodynamic chirality in a $3D$ fluid droplet leads to a strikingly rich phenomenology. This includes screw-like droplet motion – for dipolar active forces – and global rotation with periodic sense inversion – for dipolar active torques.

Screw-like motion arises due to the coupling between thermodynamic chirality and a rotational flow, which is powered by extensile dipolar force activity due to spontaneous bend deformation at the droplet surface and its interior, compatible with tangential anchoring. This motility mode is therefore a rototranslation that is similar to that performed by a helical propeller. For a fluid with active torque dipoles, instead, global rotations with intermittent sense arise when the active torque favours a different twist with respect to that introduced by the thermodynamic chirality. Here the rotation is coupled to the rotation of helical disclination lines which pierce the droplet interior.

For both screw-like and intermittent rotation, the surface defects arising due to tangential anchoring play a fundamental role. For the former phenomenon, defect rotation – induced by activity – is converted into translatory motion due to the underlying chirality. For the latter, disclination rewiring determine the change in rotation sense. The mechanisms underlying motility regimes are therefore defect-dependent, and qualitatively different from those analysed in [188], which occur in defect-free droplets, but are associated with large deformation of the droplet shape.

We now ask what happens if we change the handedness of the LC. A simple change of the sign of q_0, keeping fixed N and the strength of activity ζ shows that left-handed chiral droplets ($N = 2, 3$), fuelled by force dipoles only, exhibit the propulsive mode at intermediate activity with an opposite direction of rotation with respect to the cases previously discussed (Fig. 4.7). If the droplet is instead fuelled by active torque dipoles, we found the handedness of the LC to determine the handedness of the helicoidal structures formed by the disclination lines as in Fig. 4.5c: contrary to what happens for the case here presented, in a left-handed cholesteric droplet the two helices are found to arrange in a left-handed fashion, while the remaining properties (rotation inversion, coiling and recoiling dynamics, *etc.*) stay unchanged.

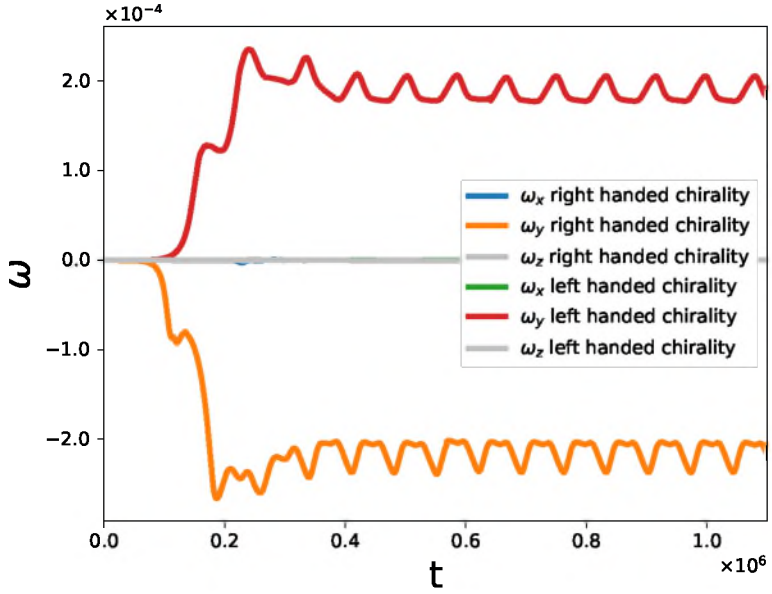

Figure 4.7: *Effect of the change of the handedness of the LC.* Different components of the angular velocity ω of a chiral ($N = 2$) droplet with only active force dipoles ($\zeta = 10^{-3}$), with right-handed ($q_0 > 0$) and left-handed ($q_0 < 0$) chirality. Left-handed chiral droplets, exhibit the propulsive mode with an opposite direction of rotation with respect to the case of right-handed chirality.

It is of interest to think of the generic models presented in this section with respect to the dynamics of self-motile and rotating living active gels, which are found in bacterial and eukaryotic cells. In both cases, the cytoplasm includes chiral cytoskeletal filaments, composed of either MreB or actin, which are dynamical helical fibre and which, in the absence of any activity, would self-assemble into cholesteric phases. Additionally, molecular motors walking on such helical fibres will generically create active forces and torque dipoles, either in the bulk or in a cortex close to the surface. In some cases, such as that of *Spiroplasma* [103] bacteria, or of single-cell parasites [111, 158], screw-like motility is observed. This has often been associated to the twisting or rotation of cytoskeletal filaments, which generates translatory motion, so that the underlying mechanism is that of a helical propeller, as in our droplets in Fig. 4.4. Our results, together with those previously reported in [188], show that there are multiple motility modes which chiral active micro-organism may employ, and it would be of interest to look more closely for analogues of these in nature.

Our novel *active cholesteric droplets* may also be realised in practice by self-assembling active liquid crystalline droplets synthetically (a possible mapping between numerical and physical units has been provided in Table B.1 in Appendix B, based on similar (nematic) experimental systems [81, 160]). This could be done, for instance, by using active nematics with a chiral dopant [160]. Although these systems usually form shells on the interface of an oil-water emulsion, we expect that the resulting motility modes would be qualitatively similar to those we found in our systems where the active component is fully three-dimensional. In these active liquid crystal shells, anchoring of the director field (the microtubule orientation in [160]) is tangential as in our droplets, so defect topology should play a key role for both systems. Another potential candidate system

is a cholesteric DNA or chromatin globule interacting with molecular motors [13, 17].

4.4. HYDRODYNAMICS OF CONTRACTION-BASED MOTILITY IN A COMPRESSIBLE ACTIVE FLUID

Having analysed the role of chirality in self-propelled droplets, which led us to discovery of a new motility mode, that can be in principle inegnerized, we want to look at the problem of motility in a more fundamental and simple way.

Models of contraction-induced motility have been proposed in Refs. [41, 71, 155, 190]. All these considered the case of an active droplet moving inside a simple (Newtonian) and passive outer fluid. In some cases, the material inside the droplet was an active liquid crystal, in which case the onset of motility required rectifications of orientational splay fluctuations of an order parameter linked to actin polarisation [41, 190]. Here instead we study by lattice Boltzmann simulations a simpler, single-phase, compressible actomyosin system, where a high density droplet (actomyosin blob) simply emerges due to active contraction. For sufficiently strong activity, we find the self-assembled droplet swims inside a low density actomyosin background. The setup we consider could be studied experimentally with quasi-2d or 3d compressible actomyosin suspensions. Additionally, once the droplet emerges, the system is approximately equivalent to an active compressible actomyosin droplet swimming inside a generic compressible and passive fluid (as the density of motors in the background is very small). Therefore, our results can be qualitatively compared to experiments studying the motion of cells or cell extracts within polymeric or viscoelastic fluids. Indeed, we show that the hydrodynamic flows in the region outside the droplet are reminiscent of the flow of matrigel [7] surrounding swimming cells.

4.4.1. HYDRODYNAMIC MODEL

We model an actin suspension as a compressible fluid with local density ρ, and myosin via its concentration field ϕ. Rather than considering the case in which actin is enclosed in a droplet [71], we study a single-fluid set-up with a compressible actin gel initially uniform in the simulation domain. The dynamical equation of motion for the actin density ρ is the continuity equation,

$$\partial_t \rho + \partial_\alpha \rho v_\alpha = 0 \ , \tag{4.2}$$

with v_α the velocity of the actin fluid. The latter obeys the following Navier-Stokes momentum balance equation,

$$\partial_t \rho v_\alpha + \partial_\beta (\rho v_\alpha v_\beta) = F_\alpha^{\text{int}} + F_\alpha^{\text{active}} + F_\alpha^{\text{interface}} + F_\alpha^{\text{viscous}} \ , \tag{4.3}$$

where $F_\alpha^{\text{viscous}} = \partial_\beta [\eta(\partial_\beta v_\alpha + \partial_\alpha v_\beta)]$ is the usual viscous term, with η shear viscosity of the fluid. The term

$$F_\alpha^{\text{int}} = -\partial_\alpha P^i + \partial_\alpha G \rho \ , \tag{4.4}$$

accounts for pressure-driven flows. The quantity $P^i = \rho T$ is the usual ideal pressure. The presence of the additional term proportional to G gives a compressibility proportional to $T - G$. Hence G measures the deviation from the ideal behaviour of the fluid,

[7] At least at large times, matrigel can be viewed as a viscous fluid rather than a solid.

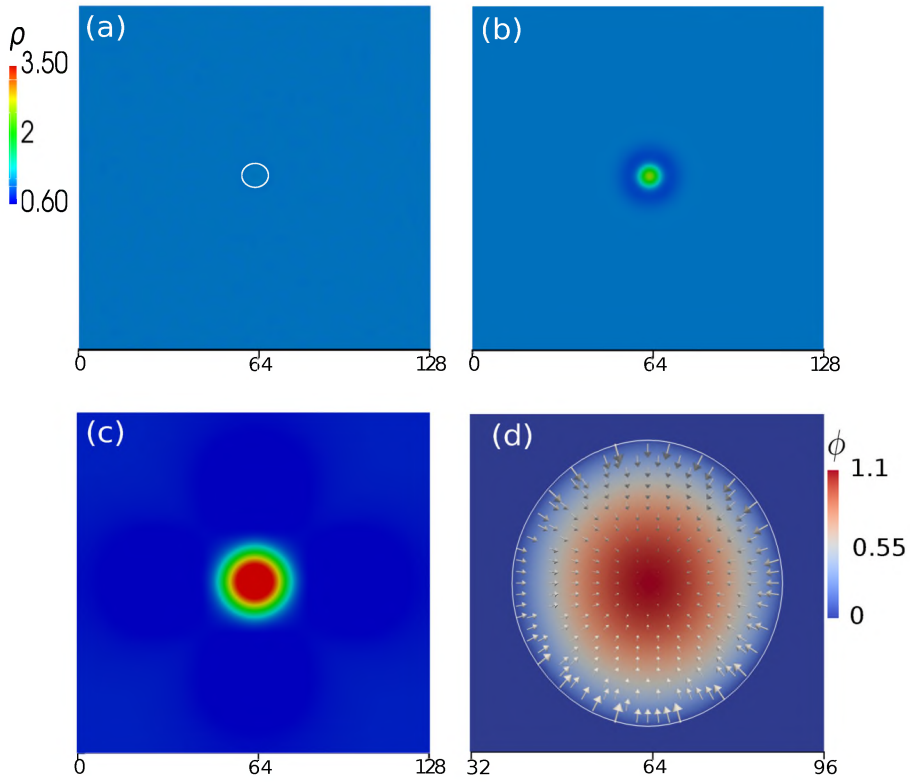

Figure 4.8: **(a-c)** Snapshots of the evolution of ρ, for a simulation in which ρ has been initialized randomly around 1(panel (a)), while ϕ as a droplet of radius $R = 3$ (isoline for $\phi = 1$ in panel (a)), for $\zeta = 0.1$ and $G = 0.95$. **(d)** Contour plot of ϕ with superimposed active force, for the same configuration shown in (c). The isoline for $\rho = 2$ is plotted in white.

being temperature fixed in our simulations. The third term

$$F_\alpha^{\text{interface}} = k\rho\partial_\alpha(\nabla^2\rho) \tag{4.5}$$

represents interfacial forces, with the constant k controlling the surface tension of actin (which controls the width of interfaces between high and low actin densities). The presence of the active component (myosin motors with local density ϕ), and its effects on the fluid, are encoded in the final term,

$$F_\alpha^{\text{active}} = \zeta\partial_\alpha\phi\,, \tag{4.6}$$

which accounts for an active isotropic pressure – if $\zeta > 0$ this active pressure is contractile. The parameter ζ measures the strength of myosin-induced contraction. Contractility depends also on the concentration of myosin motors ϕ, which evolves according to the following advection-diffusion equation:

$$\partial_t\phi + \nabla.(\phi\mathbf{v}) = D\nabla^2\phi - B\nabla^2\rho - K(\nabla^2)^2\phi\,. \tag{4.7}$$

Here the local advection velocity of myosin equals that of actin, meaning that all motors are permanently attached to the actomyosin gel. The parameter D is the myosin diffusion coefficient, while K controls the myosin surface tension, quantifying the ability of the myosin droplet to oppose deformation. The term proportional to B is an effective non-equilibrium term, whose effect is to ensure that myosin remains enclosed in

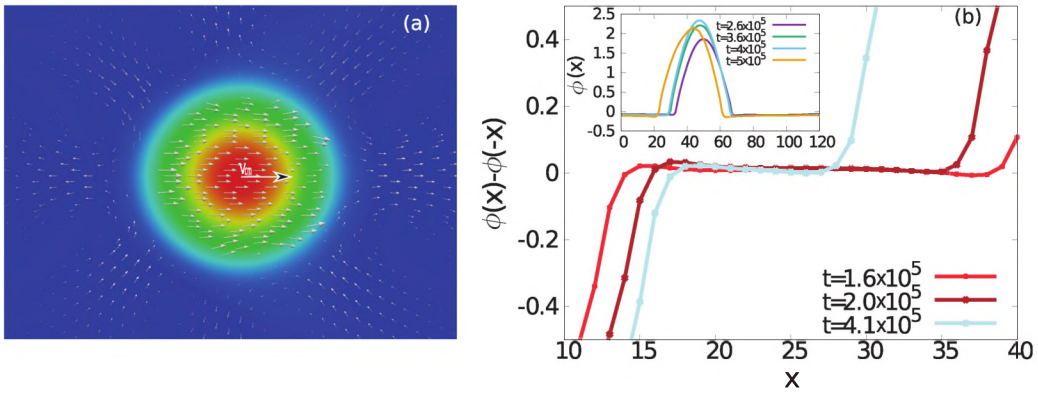

Figure 4.9: **(a)** Contour plot of the density ρ with superimposed velocity field, for $G = 0.88$ and $\zeta = 0.3$. The colour code here is the same of that displayed in Figure 4.8. **(b-main figure)** Plot of the quantity $\phi(x) - \phi(-x)$, at different times, and **(b-inset)** ϕ profiles along the x-direction at different times, for the same case of figure **(a)**. The cyan curve corresponds to the time when the droplet starts moving along the x-direction.

actin domains. Higher order gradients terms can in principle be added, but they would not alter the following results. The study is conducted by varying G ("compressibility modulus") and the activity parameter ζ.

The equations of motion are solved by means of a hybrid lattice Boltzmann (LB) scheme, as the one described in Chapter 3.

Simulations have been performed on a periodic square lattice of size $L = 128$, for the 2d case, and a periodic cubic lattice of size $L = 128$ for 3d simulations. Unless otherwise stated, initial conditions are $\phi = 1$ inside a droplet of radius $R_1 = 3$, and 0 outside , while ρ set equal to $\rho = 1$ inside a droplet of radius $R_2 = 15$, and $\rho = 0.4$ elsewhere. Parameter values are, $T = 0.97$, $k = 0.1$, $D = 10^{-3}$, $B = D$, $K = 10^{-3}$. All quantities in the text are reported in lattice (simulation) units.

4.4.2. CONTRACTION INDUCED CLUSTERING AND MOTILITY

We start by presenting the results of our 2d simulations.

The first finding is that contractility alone is able to create a droplet of active fluid (actin, represented by ρ) even in the absence of a free energy favouring phase separation in the passive limit ($\zeta = 0$). Initialising the system with $\rho = \rho_0 + \delta\rho$, where $\rho_0 = 1$ and $\delta\rho$ some small random fluctuations, whereas ϕ (motor concentration) initially set to 1 inside a droplet of radius $R_1 = 3$ and zero elsewhere, nucleation of a droplet at the centre of the system is observed. Droplet formation occurs for any value of the activity ζ. This clustering phenomenon is due to the interplay between myosin contraction and the cross diffusion term proportional to B in Eq. (4.7), which recruits myosin to regions of high actin concentration. Similar results are obtained with ϕ fluctuating around a uniform value. In all cases, we observe the formation of a single droplet in steady state. Some snapshots of the evolution of the actin density field ρ are reported in Figure 4.8, together with the steady state contour plots of both ρ and ϕ.

In addition, for every value of the parameter G there is a critical value of activity ζ for which motion occurs. To become motile, the droplet first needs to polarise, breaking the circular symmetry in the myosin distribution. The asymmetry in ϕ can be quantified by analysing the quantity $(\phi(x) - \phi(-x))$, with x a position along a line oriented with

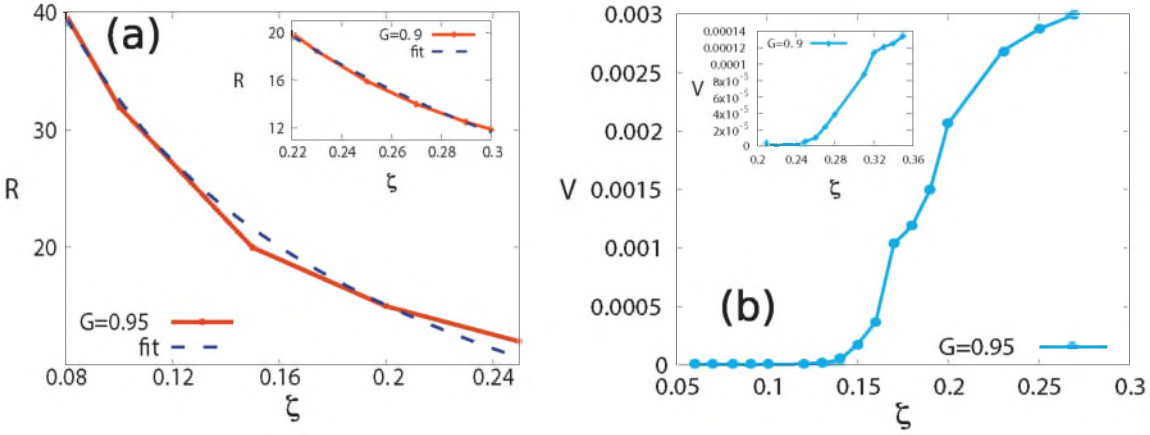

Figure 4.10: **(a)** Critical value of the radius of the droplet R_c as activity varies (continuous curves), for $G = 0.95$ **(main figure)**, and $G = 0.9$ **(inset)**, and the result of the fit (dashed lines) with the proportionality law reported in the text(Eq. 4.9).**(b)** Steady state center of mass velocity V as activity varies, for $G = 0.95$ **(main figure)**, and $G = 0.9$ **(inset)**.

the direction of motion, and passing through the centre of mass of the actin droplet. For an isotropic droplet, we expect $(\phi(x) - \phi(-x))$ to be identically zero. Figure 4.9(b) shows how the myosin field asymmetry develops over time for $G = 0.88$ and $\zeta = 0.3$ (a case for which we have motion). At early times ϕ is nearly symmetric (red curve in the main plot), whereas later myosin redistributes until an asymmetric steady state is reached (cyan curves in the main and inset of Fig. 4.9(b)), and the droplets starts to move (brown curve in the inset of Figure 4.9(b)).

Figure 4.9(a) also shows the velocity field of our compressible active system. Inside the droplet, the active contractily-driven flows rearrange to give a simple directed flow. There is an opposing flow outside the droplet, which is required for overall momentum conservation (as there are no boundaries or other momentum sinks). The counteracting flow involves a number of vortices which upon azimuthal averaging give a net flow in the direction opposing that of the droplet motion. Whilst vortex patterns are associated with spurious microcurrents in a passive phase-separated systems in lattice Boltzmann simulations [203], the magnitude of the flow is over an order of magnitude larger in our active case, and the pattern is different as the vortices in front and behind of the droplet are much larger.

To better investigate this point we compared the azimuthal flow of the active droplet with that of a passive liquid droplet. Tho do that we performed LB simulations of a van der Waals fluid (as explained in Chapter 3). We measured the averaged azimuthal flow v(θ) in the droplet reference system. We fitted the profiles with a truncated Legendre polynomial

$$f(x) = a\sin(x) + b\sin(2x) + c\sin(3x) + d\sin(4x)\,, \tag{4.8}$$

that has been used to model the predefined axis-symmetric tangential velocity distribution on the surface of self propelled spherical particles [114].

Fig. 4.11 shows the results for a self propelled active droplet (left) and for a stationary liquid droplet. We note that the spurious active flow is well fitted while in the passive case it is not. In addition, the averaged velocity measured on a semicircle near

the droplet surface is of order $\mathcal{O}(10^{-4})$, suggesting that there is, in the active case, a net flow towards the droplet back, in the opposite direction of motion.

All these considerations suggest that the flow observed in the active case is not pathologically affected by spurious velocities, and on the contrary it has a reliable physical meaning.

In experiments with cell swimming in a viscous fluid, for instance in a matrigel, the environment is fully 3-dimensional. It is therefore of interest to ask whether contraction-driven flows can rearrange to yield motility in a periodic 3D geometry. To answer this question, we performed simulations in a cubic domain of size $L = 128$. Remarkably, we find that also in 3d droplets – again assembled through myosin-mediated contraction of the compressible actin fluid – become self-motile for sufficiently strong activity. Intriguingly, the solvent flow counteracting droplet motion has now a different form (Figure 4.12). Two vortex–like structures originate from the poles perpendicular to the migration axis and converge toward the droplet rear, while the outer fluid is pushed away in front of the droplet. This pattern is similar both to that observed experimentally in cells "swimming" in 3d matrigel [147], and to that reported in previous numerical simulations of a self-motile active-liquid crystal droplet [193]. The emergence of this flow patterns is interesting, as our model is significantly simpler than the ones previously considered. We interpret the similarity in the flow patterns far from the droplet as due to the fact that the dilute actomyosin background within which the droplet moves may be viewed as an essentially passive viscous polymeric fluid (such as matrigel).

We argue that the mechanism giving rise to the symmetry-breaking instability of a non–motile configuration and ensuring directional motility of a self-propelling cell, is a positive feedback loop, closely related to the one leading to actin accumulation (Figure 4.8). Here, after *e.g.* a fluctuation in actin density creates an asymmetry in gradients, the flow generated by contraction is also asymmetrical, and recruits motors faster along the regions where gradients are steeper. This leads to further asymmetric contraction, and to a motile pattern due to the flow imbalance, hence creating an auto-catalytic effect [129]. The coupling leads to build motor concentration, which is limited by surface tension and diffusion, resisting the runaway and providing a compensating term which is necessary to achieve a steady state. The droplet breaks symmetry and becomes motile when the activity parameter exceeds a threshold. The threshold behaviour originates from the fact that the total myosin stress needs to overcome the effects of actin viscosity and myosin diffusion. Increasing activity for a given value of G, or decreasing G for a given value of ζ, the droplet assumes an accentuated elliptical form.

To understand more quantitatively the effect of the model parameters on the droplet motion, we measured the radius of the self-assembled actin droplet and its velocity in steady state, as a function of the activity parameter ζ, and for different values of the parameter G. The droplet radius at the onset of motion is plotted in Figure 4.10(a) for two values of G ($G = 0.95$ in the main figure and $G = 0.9$ in the inset). It follows to a good approximation an inverse square root law:

$$R_c \sim \sqrt{\frac{1}{\zeta}}\,. \tag{4.9}$$

Such a dependency was suggested by linear stability analysis of a related problem [71].

Figure 4.10(b) shows a plot of the center of mass velocity versus ζ for two values of

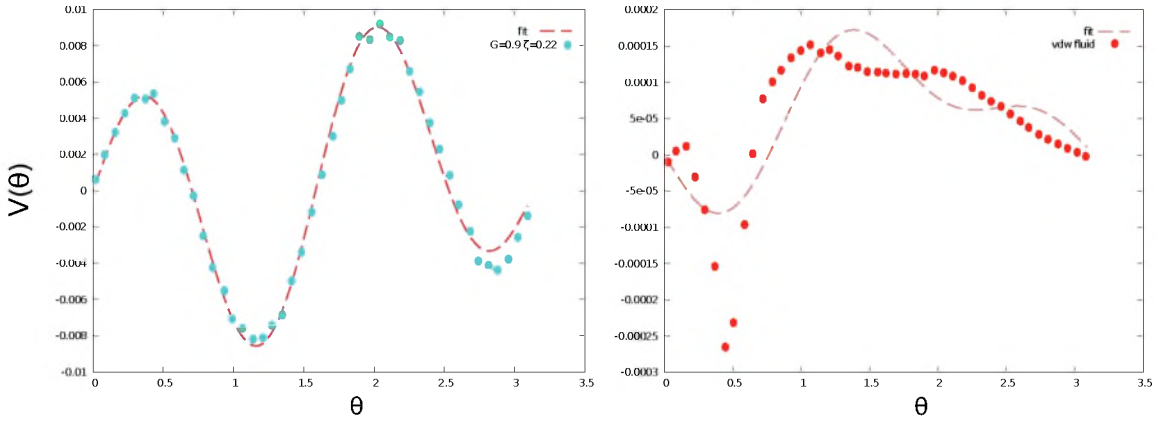

Figure 4.11: Azymuthal flows for a self propelled active droplet (left) and a stationary liquid droplet (right), with the results of the fit with the function given in the text (Eq. (4.8)).

G ($G = 0.95$ in the main figure and $G = 0.9$ in the inset). A phase diagram in the $(G-\zeta)$ plane is instead shown in Figure 4.12 b. The steady droplet velocity increases with activity and is bigger for higher values of G. At the same time, decreasing the elastic modulus of the gel – i.e., approaching the incompressible limit $G = 0$ – leads to an increase in the activity threshold above which motion is observed. This is consistent with the intuitive expectation that active isotropic contraction cannot lead to motion in this limit (as it is simply equivalent to a redefinition of the pressure). Here for the values of activity ζ we are constrained by the stability of our LB implementation, and for the values of G by the chosen values of T. We checked that fixing T to other values does not change the physical picture discussed, as it solely change the location of the transition line to a motile droplet.

Finally it is useful to put in relation our parameters choice with the order of magnitude of relevant quantities measured in real systems. Using $\Delta t = \eta/\zeta_c$ and $\Delta x = \sqrt{D\eta/\zeta_c}$ as time and space units, where ζ_c is a reference value for contractility, it is possible to get the order of magnitude of our model parameters. We set relevant length, time, and viscosity scales for cell extracts and actomyosin droplets as $\Delta t \sim 1s$, $\Delta x \sim 1\mu m$, and $\eta \sim 10$Pa s [139]. Hence $D \sim 1\mu m^2 s^{-1}$, and $\zeta_c \sim 10$Pa. The former value is close to the *in vivo* myosin diffusion coefficient, while for the latter we note that a myosin concentration of $\phi_0 \sim 1\mu$M [139], creates a contractility of $\zeta \sim 2\zeta_c$.

To summarize, in this Section we have shown that myosin–driven contraction can lead to directed motion within a compressible active fluid. In particular, we have found that within a single compressible actomyosin fluid, the interplay between myosin contraction and cross diffusion is responsible for the self-organization of an actin droplet. Motion requires symmetry breaking, which can arise due to a fluctuation. Once symmetry is broken, a positive feedback mechanism is responsible for the motion. Motors lead to asymmetric contraction, this recruits additional myosin by advection, which reinforces the contraction asymmetry. A steady state is reached because of the competition between this simple positive feedback on one hand, and diffusive and viscous effects on the other hand. Unlike previous work on contraction-driven motility, here we have focused on the effect of compressibility. We have found that compressibility has the effect to facilitate motility, as it decreases the value of the isotropic contractile stress beyond which the droplet starts to move.

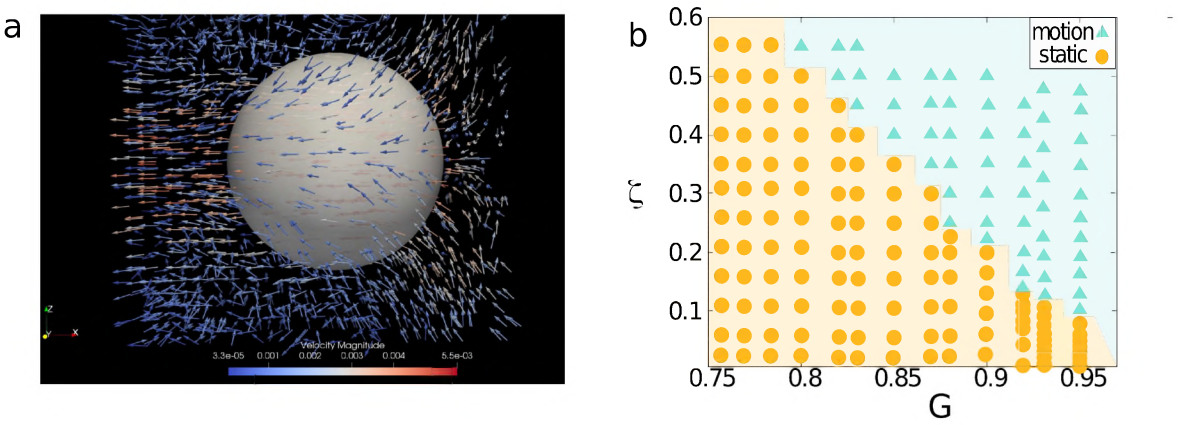

Figure 4.12: **(a)** Isosurface at $\rho = 2$, with superimposed flow field for $\zeta = 0.34$ and $G = 0.87$, in $3D$. **(b)** Phase diagram in the ζ (activity)-G(compressibility) plane, for the transition to motile droplet.

We have also shown that the actin flow inside the droplet is a simple and directed one, whereas the counteracting flow in the compressible solvent has different shapes in 2d and 3d. In 3d, the pattern is reminiscent of that observed experimentally for cell swimming in matrigel. This may be because in steady state the self-assembled droplet swims within a low density actomyosin background which can be approximately viewed as a passive compressible polymeric fluid.

Our results could in principle be directly tested experimentally by studying pattern formation in compressible actomyosin suspensions. They should also be relevant to the physics of cell swimming inside gels with different compressibility.

5

MORPHOLOGICAL AND RHEOLOGICAL PROPERTIES OF ACTIVE EMULSIONS

So far we have analysed the behaviour of a single active droplet and the mechanisms leading to its self-motility properties, that are fundamental for the understanding of the functioning of many biological systems, as we discussed in detail in the previous Chapter. Another challenging topic in Active matter is understanding how active droplets mutually interact when they are suspended in a fluidic background. This is situation is actually the most common in nature, since active entities – ranging from bacteria in culture to cells in a tissue – exhibit the tendency to gather together forming large clusters. Active emulsions constitute a challenging class of systems with many potential novel applications. For instance, active emulsions may be used as building-blocks for designing novel active soft materials. An example may be an emulsion in which active matter is encapsulated in one of the two phases, an expedient that may be used in devices for drug delivery. Biomimetic material may also be designed with suitable active matter systems so to create a soft tissue made up of highly-packed active droplets capable to resist to intense deformations. Thus, active emulsions may play a fundamental role in overcoming current major challenges affecting the design of active devices, such as controlling fuel arrival and waste removal [87, 160]; this is indeed an essential feature to create sustainable active materials, capable of preserving their active properties over long periods of time.

Active emulsions are currently a matter of experimental study. Sanchez *et al.* [160] have recently produced an active emulsion with microtubule bundles activated through kinesin motor proteins. Here, the resulting nematic liquid crystal network is squeezed at the interface of an aqueous droplet emulsified in an oil background. As outlined in Chapter 1, the resulting active emulsions exhibit unexpected properties, such as autonomous motility, which are not observed in their passive analogues. This seminal work paved the way towards microscopic confinement of active matter.

Another challenging questions to be addressed regards the response of these active emulsions to external forcing. As discussed in Chapter 1, some bacteria suspensions display peculiar rheological properties, like super-fluidic regimes and even negative viscosities states.

From a numerical point of view, one may think to make use of a suitable model to replicate the behaviour of such experimental systems, by using for instance a multi-

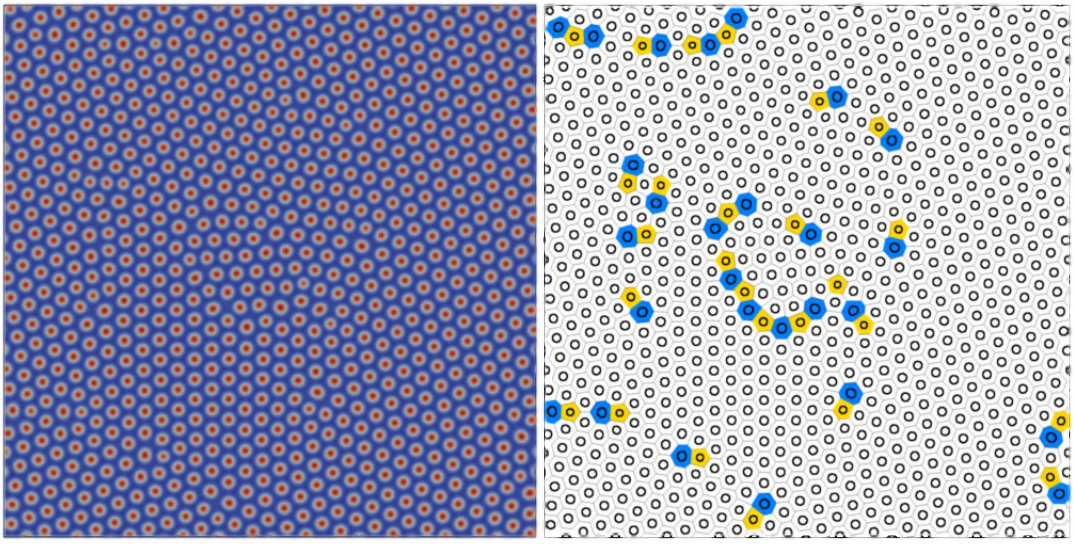

Figure 5.1: **(Left panel)** Snapshot of ϕ contour plot for a configuration in the stationary regime at $\zeta = 0$, for a system of size $L = 256$. The colour code displayed here is the same of all the contour plots in the rest of the work, where blue corresponds to passive phase ($\phi = 0$) and red to the active phase ($\phi = 2$). **(Right panel)** Voronoi tessellation for the same configuration in the **(Left panel)**.

phase approach, where each droplet is described by a different field. A different possibility is to consider the model presented in Chaper 2 (Sec 2.3.1). In order to model the presence of a surfactant that favours the emulsification of the binary mixture, it is necessary to allow for negative values of the elastic constant k, as discussed in Section 2.3.1.

Following this approach, I have studied how activity change the equilibirum morphological and flow patterns in active polar emulsions. This will be discussed in Section 5.1.

I will also present results regarding the rheological repsonse of an active polar emulsion in Section 5.2. The declared root of this kind of approach is that morphology can play a key role in the control of active fluids, as will be discussed in the following. The plethora of mesmerizing behaviours observed, and the transition between the various rheological regimes found can indeed be explained and controlled within our model.

5.1. MORPHOLOGICAL CHARACTERIZATION OF AN ACTIVE POLAR EMULSION: ACTIVITY ENHANCED HEXATIC ORDER

The equilibrium properties of an active polar emulsion are encoded in the free energy functional described in Section 2.3.1:

$$F[\phi,\mathbf{P}] = \int d\mathbf{r}\{\frac{a}{4\phi_{cr}^4}\phi^2(\phi-\phi_0)^2 + \frac{k}{2}\left|\nabla\phi\right|^2 + \frac{c}{2}(\nabla^2\phi)^2 - \frac{\alpha}{2}\frac{(\phi-\phi_{cr})}{\phi_{cr}}|\mathbf{P}|^2 + \frac{\alpha}{4}|\mathbf{P}|^4 + \frac{\kappa}{2}(\nabla\mathbf{P})^2 + \beta\mathbf{P}\cdot\nabla\phi\} \ .$$

The first term, multiplied by the phenomenological constant $a > 0$, describes the bulk properties of the fluid; it is chosen in order to create two free-energy minima, one

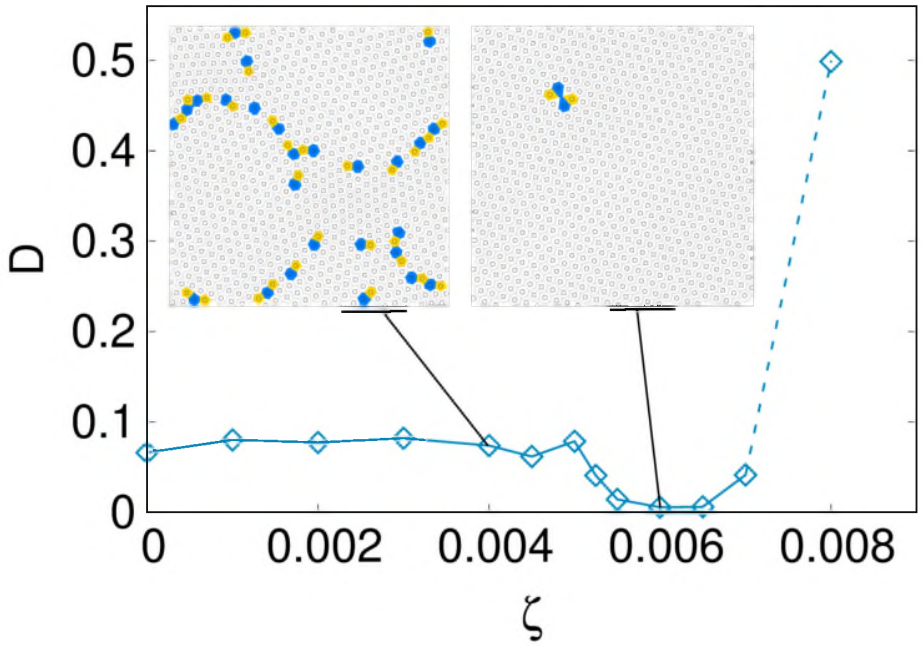

Figure 5.2: **(Main figure)** Defects ratio (droplets without 6 neighbours over the total number of droplets in the configuration) vs activity, in the stationary time regime, for systems of size $L = 256$. The figurative dashed line stands for the fact that increasing activity it is no more possible a coherent defects analysis, due to the formation of asters first and completely non definite structures for strong activity. **(Inset)** Voronoi tassellation for two different values of activity($\zeta = 0.004$ on the left and $\zeta = 0.006$ on the right).

($\phi = 0$) corresponding to the passive material and the other one ($\phi = \phi_0$) corresponding to the active phase. The second one determines the interfacial tension between the passive and active phase. The addition of the Brazowski term proportional to c allows us to consider negative values of k, favouring the formation of interfaces throughout the system, and hence the emulsification of the two phases. The third and the fourth terms control the bulk properties of the polar liquid crystal. Here α is a positive constant and $\phi_{cr} = \phi_0/2$ is the critical concentration for the transition from isotropic ($|\mathbf{P}| = 0$) to polar ($|\mathbf{P}| > 0$) states. The choice of ϕ_{cr} is made to break the symmetry between the two phases and to confine the polarization field in the active phase $\phi > \phi_{cr}$. The term proportional to $(\nabla\mathbf{P})^2$ describes the energetic cost due to elastic deformations in the liquid crystalline phase (see Table 2.1) in the single elastic constant approximation. Finally, the last term is a dynamic anchorage energy and takes into account the orientation of the polarization at the interface between the two phases. If $\beta \neq 0$, $\mathbf{P}$ preferentially points perpendicularly to the interface (normal anchoring): towards the passive (active) phase if $\beta > 0$ ($\beta < 0$).

The continuous fields follow the evolution equations presented in Chapter 2, namely Eqs. (2.16), (2.21) and (2.23). These are solved in 2D with the hybrid LB method described in section 3.4. In addition we made use of a parallel approach implementing Message Passage Interface (MPI) to parallelize the code.

Simulations have been performed on square lattice of size $L = 256$. The concentration ϕ ranges from $\phi \simeq 0$ (passive phase) to $\phi \simeq 2$ (active phase). Unless otherwise stated, parameter values are $a = 4 \times 10^{-3}$, $k_\phi = -6 \times 10^{-3}$, $c = 10^{-2}$, $\alpha = 10^{-3}$, $k_P = 10^{-2}$, $\beta = 0.01$, $\Gamma = 1$, $\xi = 1.1$, $\phi_0 = 2.0$, and $\eta_0 = 1.67$. All quantities in the text

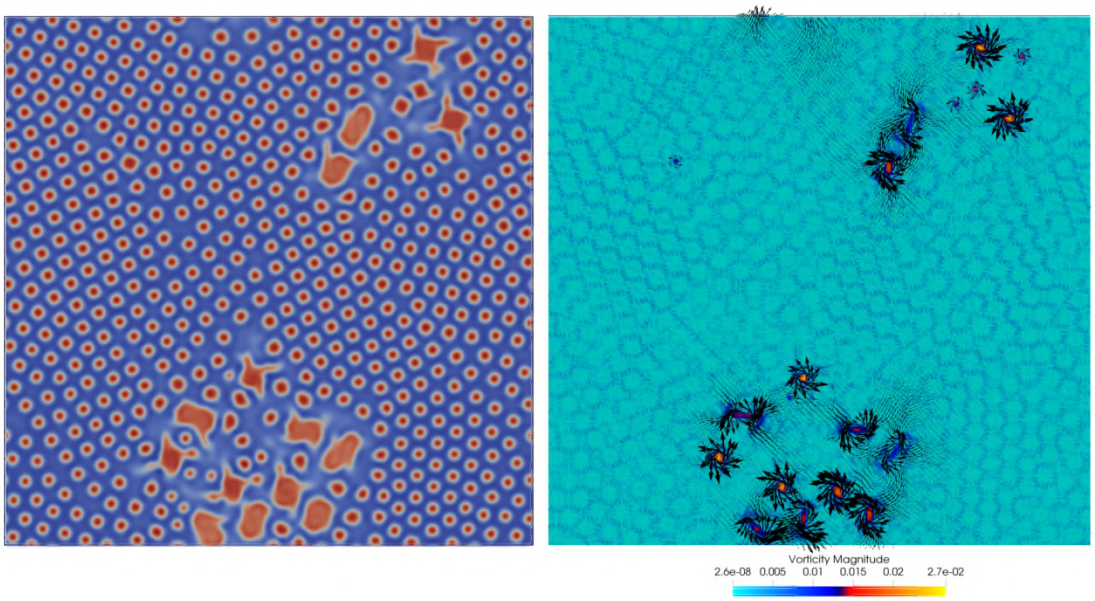

Figure 5.3: **(Left panel)** Contour plot of the concentration field ϕ for a system of size $L = 256$, for $\zeta = 0.0076$. **(Right panel)** Contour plot of vorticity magnitude with superimposed velocity field for the same configuration in the **(Left panel)**.

are reported in lattice units. We initialized the system starting from a uniform phase, with $\phi(\mathbf{r}) = \langle\phi\rangle + \delta\phi(\mathbf{r})$, where $\langle\phi\rangle = \phi_{cr}$ is the conserved (area) averaged value of the concentration field and $\delta\phi$ is a small perturbation field favouring phase separation and ranging in $\left[-\frac{\phi_{cr}}{10}, \frac{\phi_{cr}}{10}\right]$. The initial condition for the polarization field is completely random, being its orientation randomly distributed in the plane, while its intensity is randomly chosen in $[0, 1]$.

In the symmetric case, as stated in Chapter 2, a passive emulsion would arrange in a lamellar phase. How the equilibrium properties, in this case, are affected by the presence of activity has been studied by Bonelli et al. [11]. A moderate contractile activity (e.g., corresponding to emulsions containing actomyosin as the active ingredient) sets up interfacial shear flows which enhance and speed up lamellar ordering. Increasing the strength of contractile activity disrupts the passive lamellar ordering to create emulsions of passive droplets within an active self-stirring background. Extensile activity (for instance corresponding to mixtures where the active component is a bacterial fluid) leads to the self-assembly of a poly-disperse suspension of active rotating droplets in a passive background.

In the next section we will present our results regarding an asymmetric (10 : 90 ratio between active-passive phases) active polar emulsion.

5.1.1. ASYMMETRIC EMULSION

We now consider the case of asymmetric emulsions, in which the active phase represents only the 10% of the overall composition.

When activity is off, at equilibrium, the system is characterized by an ordered array of droplets as can be seen looking at the contour plot of the concentration ϕ in Fig 5.1. The droplets (and their centers of mass) can be easily pinpointed by putting a proper cutoff on the concentration field to distinguish active regions from passive ones. Each

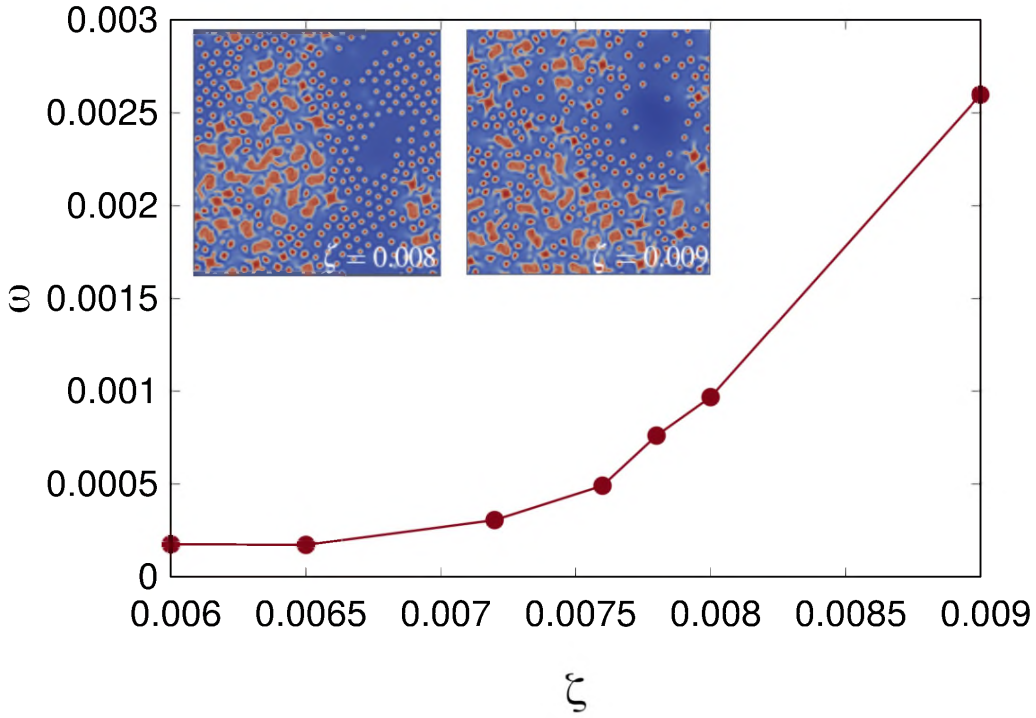

Figure 5.4: **(Main figurer)** Droplets mean angular velocity vs activity ζ. In the **(Inset)** contour plots of the concentration field ϕ for two values of activity $\zeta = 0.008$ on the left and $\zeta = 0.009$ on the right. As activity increases more asters are created and their angular velocity increases.

closed region of lattice sites that falls beyond the cutoff, is identified as a droplet. A good choice for the cutoff, given our choice of parameters is seen to be $\phi \sim 1.5$. Droplets are hexatically ordered – *i.e.* they occupy vertices of a triangular lattice – besides the presence of some defects in the droplet lattice, namely *dislocations*. *Voronoi tessellation* is used in order to unambiguously identify the nearest-neighbours network for the centers of mass of each droplet. This allows for establishing a partitioning of the space with one closed region for each center of mass, according to the following rule: the region associated to the i-th droplet contains all the points of the space that are closer to its center of mass than to any other droplets. In Fig. 5.1 it is shown the use of such analysis. Droplets with 5 nearest neighbours are highlighted in yellow, while those with 7 neighbours in blue.

Extensile activity

For non-zero, but still small (positive) values of ζ, the *hexatic-droplet* phase survives. At sufficiently high values of ζ, but still in the small activity regime, activity is able to reduce the number of defects, driving the system in an almost completely ordered phase.

In fact, for $\zeta = 0.006$ and slightly larger values of ζ, activity is such to let the droplets rearrange in an almost defect-free final configuration. In Fig. 5.2 the defects ratio D (with respect to the number of droplets) is reported as the activity varies, with corresponding Voronoi tassellation for two iconic values of ζ. We see that for very small values of activity, the hexatic order survives but there is no appreciable change in the number of defects with respect to the passive limit (first figure on left in the inset of Fig.5.2). However, for values of ζ around 0.006, or slightly larger, the hexatic order is enhanced as activity is such to remove the defects (figure on the right in the inset of

Fig.5.2), corresponding to a minimum in the defects ratio (main plot in Figure 5.2). At larger values of ζ a change in the overall morphological behavior of the mixture will be observed and the defects analysis looses significance.

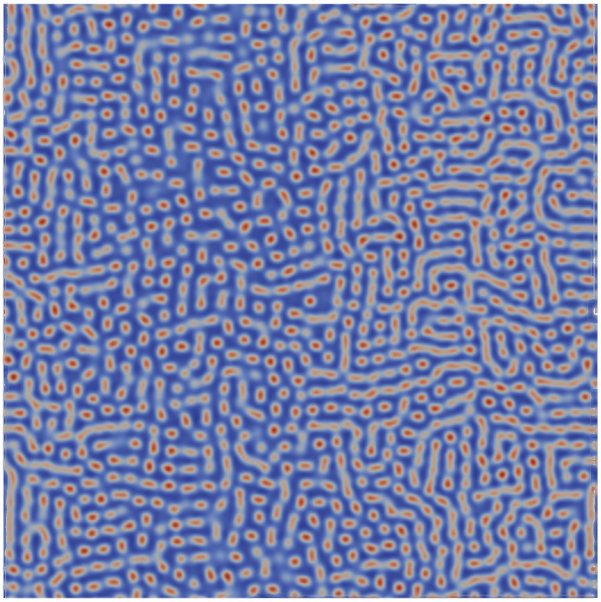

Figure 5.5: Contour plot of the concentration field ϕ for a system of size $L = 256$, for contractile activity $\zeta = -0.02$.

Enlarging activity, during the evolution, aster-like[1] rotating structures in the concentration field appear (Fig. 5.3). The characterization of their hydrodynamic state can be carried out by considering the vorticity magnitude and the velocity field, shown in the right panel of Figure 5.3. From the vorticity magnitude it is evident that small droplets are steady while asters rotate, eventually incorporating small droplets in their neighbourhood. At smaller activity, this mechanism allows for the rearrangement of the droplets configuration – eventually leading to almost defect-free configurations – while for stronger activity, phases of droplets and big rotating droplets coexists (insets of Fig. 5.4), and their angular velocity[2] increases with activity (main plot of Fig. 5.4).

For very intense values of activity, the morphology is totally dominated by asters, as can be seen by looking at configurations in the inset of Fig. 5.4, where a lowering in the number of small droplets, accompanied by the increase in the number of asters, is evident going from $\zeta = 0.008$ to $\zeta = 0.009$.

Contractile activity

Contractile activity ($\zeta < 0$) yet gives rise to a different behaviour, by setting up a local shear flow that pulls the droplets in the shear direction and, for sufficiently intense activity, leads to their merging (see the contour plot in Fig. 5.5 for the case at $\zeta = -0.02$).

[1] We refer as aster-like droplets, big rotating droplets or simply asters to non-circular droplets which have the shape of an aster associated to the formation of vortices in the velocity field. Usually in the literature the name asters has been associated to polarization patterns [99].

[2] The angular velocity of the droplets has been computed as: $\omega = \int d\mathbf{r}\phi \frac{\Delta\mathbf{r} \times \Delta\mathbf{v}}{|\Delta\mathbf{r}|^2}$, where $\Delta\mathbf{r} = \mathbf{r} - \mathbf{R}$ and $\Delta\mathbf{v} = \mathbf{v} - \mathbf{V}$, being $\mathbf{R}$ and $\mathbf{V}$ respectively the position and the velocity of the center of mass of each droplet. The measured angular velocity has been averaged over time and over the droplets in the system.

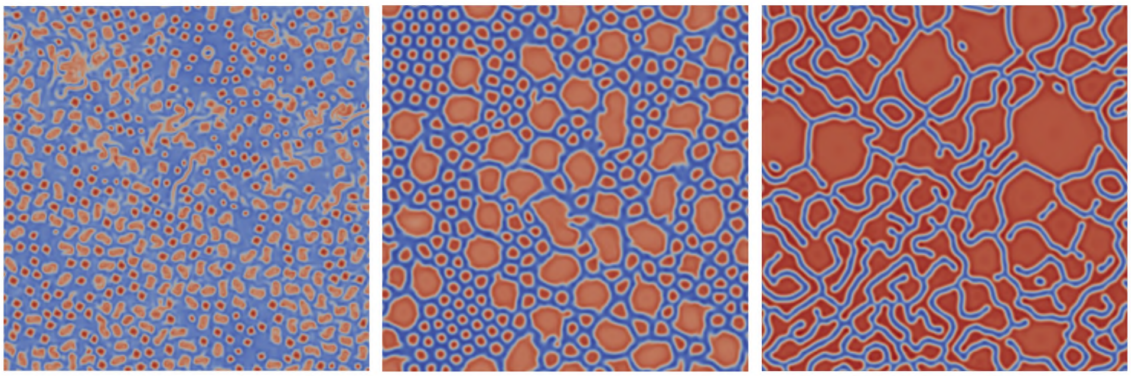

Figure 5.6: Contour plots of ϕ at non-equilibrium steady states of extensile 10:90 (left) and 50:50 (center) and 75:25 (right) mixtures rispectively at activity $\zeta = 0.008$, $\zeta = 0.004$ and $\zeta = 0.001$.

For more intense active doping, this mechanism affects the equilibrium configuration so strongly that is not any more possible to distinguish any kind of definite pattern [136].

5.1.2. OVERVIEW AND 3D MORPHOLOGIES

An active polar gel embedded in an isotropic passive fluid can manifest a wealth of structures by varying the relative amounts of the phases as well as the activity. So far, we have analysed an asymmetric composition $10:90$. It is also interesting to look at what happen if the active phase is the majority one. If extensile activity is considered we observe a net change in the overall behaviour of the system. At low concentration of active material, the hexatic array of active droplets remains stable until a certain critical value is reached, depending on the total amount of the active component. Beyond this threshold droplets start to merge giving rise to big rotating droplets, driven by bending instability of polarization under extensile flows. As the fraction of active material is increased, keeping fixed the intensity of active doping ζ, the system eventually undergoes demixing of the two phases. Remarkably, in highly asymmetric mixtures, where the majority is active, we found a background passive matrix, despite it is the minority component of the mixture (see Fig. 5.6).

Even in 3D the effect of activity on the morphology is highly surprising. We consider here a highly asymmetric preparation $(10:90)$ of the mixture. In the passive limit (see central panel of Fig. 5.7), analogously to what happens in the bidimensional case, an emulsion of droplets of the minority phase arranges in a cubic lattice with some dislocations in the arrangement. Droplets do not merge due to the presence of a suitable amount of surfactant, but if the minority phase is made active this ordered lattice structure is easily lost, whoever activity is contractile or extensile. In the former case, droplets for small values of $|\zeta|$ are first stretched by the flow, then as active doping is increased, droplets start to merge giving rise to tubular structures that span the system, creating a bicontinuous phase (Fig. 5.7). The underlying mechanism is the same as described in the bidimensional case. In the extensile case the morphological behaviour is relatively different from its bidimensional counterpart. If in 2d, bending instability in the polarization pattern acted as a source of vorticity, making droplets rotate, in 3d this is no more the case, since polarization is no more confined in a bidimensional plane and is free to rotate in space. Big amorphous ferromagnetic structures form in the sys-

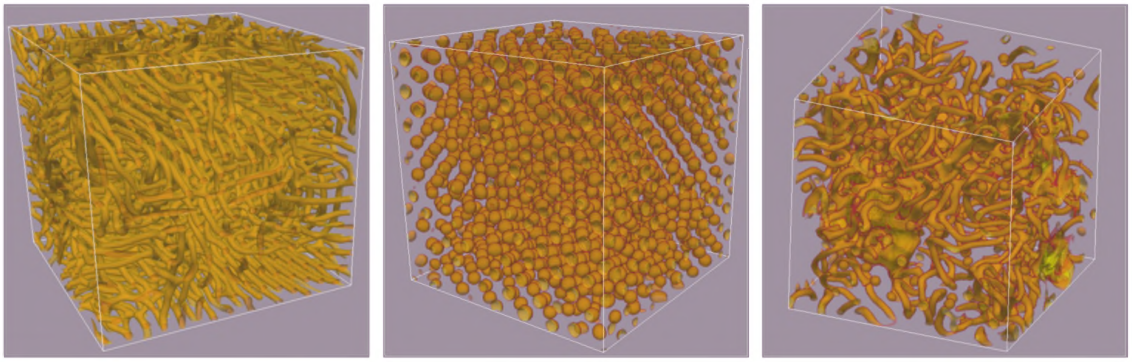

Figure 5.7: Isosurfaces at $\phi = 1.5$ of concentration field ϕ in $3d$ systems. The central panel shows the relaxed configuration consisting in a cubic array of droplets. If contractile activity is switched on ($\zeta = -0.005$) a tubular network of active domains form a bicontinous phase that spans the whole system. In extensile systems ($\zeta = 0.008$) ordered structures are lost in favour of amorphous and tubular shapes.

tem due to the increased effective surface tension. The thickening of active materials in such domains leads to formation of lighter structures in the rest of the system (see right panel in Fig. 5.7).

5.2. RHEOLOGY OF ACTIVE POLAR EMULSIONS

We now ask if the model so far considered can help to shed light on the peculiar rheological behaviours of active systems reviewed in Chapter 1.

The reach scenario hitherto pictured is further enriched if an external shear is applied in profound physical way. The interplay between local energy injection due to activity and the externally imposed shear flow is responsible for the appearance of unidirectional flow, intermittent viscosity states and even regimes characterized by negative viscosity states, as we will show in the following.

We considered flow in a channel with no-slip boundary conditions at the top and the bottom walls ($y = 0$ and $y = L$), implemented by bounce-back boundary conditions for the distribution functions [177], and periodic boundary conditions in the y direction. The flow is driven by moving walls, respectively with velocity v_w for the top wall and $-v_w$ for the bottom wall, so that the shear rate is given by $\dot{\gamma} = \frac{2v_w}{L}$.

Our choice of parameters is such that the Schmidt number ($Sc = \frac{\eta_0}{\rho D}$ where $D = 2Ma/\phi_{cr}^4$ is the diffusion constant, where M is the mobility and a the bulk free energy parameter (See Sec. 5.1)) is fixed at values typical for liquids, (~ 2000) where, in absence of activity, lamellae show low resistance to the flow and can easily order. It was shown in [90] that at smaller Sc lamellar domains hardly align to the flow and may eventually undergo pearling instability, persistent even in the long dynamics.

Moreover neutral wetting boundary conditions were enforced by requiring on the wall sites that the following relations hold:

$$\nabla_\perp \mu = 0\,, \quad \nabla_\perp (\nabla^2 \phi) = 0\,, \tag{5.1}$$

where $\nabla_\perp$ denotes the partial derivative computed normally to the walls and directed towards the bulk of the system. Here the first condition ensures density conservation, the second determines the wetting to be neutral. As mentioned in the introductory chapters, in the case of bacterial swimmers, it is commonly observed that, close to the

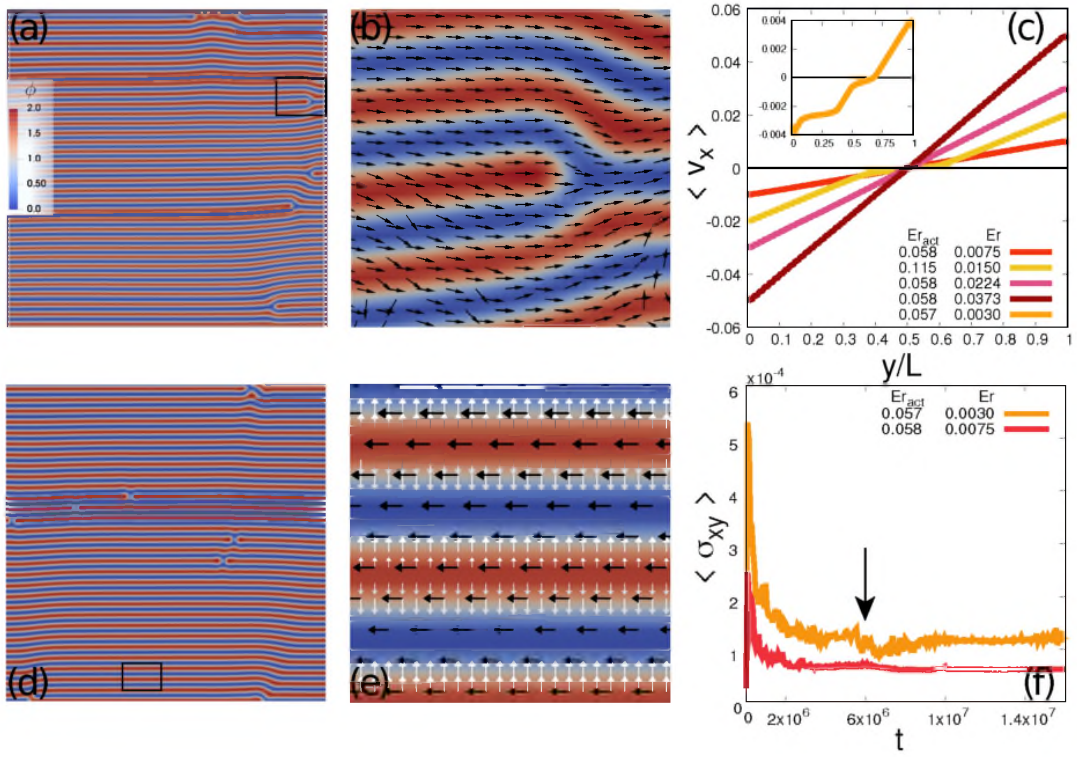

Figure 5.8: *Linear velocity profiles and lamellar phase.* Concentration contour plots at $Er_{act} = 0.057$, $Er = 0.0030$ and $Er_{act} = 0.058$, $Er = 0.0075$ are respectively shown in panels (a) and (d). Here (and in the rest of this Chapter) red regions correspond to the active phase ($\phi \approx 2.0$), while blue regions to the passive fluid ($\phi \approx 0.0$). Panels (b) and (e) show a zoom of the regions highlighted by the black squares in panels (a) and (d). Black and white vectors respectively denote velocity and polarization fields in panel (e), while only the velocity field has been plotted in panel (b). Panels (c) and (f) show the averaged velocity profile and the time evolution of the shear stress (red and orange curves correspond to the cases considered in panel (a) and (d)). Black arrow in panel (f) points to a jump in the relaxation of σ_{xy}, due to the annihilation of two dislocations. Note that in the present Figure, as well as in the followings, the colours of the velocity and the stress profiles have been chosen in relation to the colours of the corresponding region of the phase diagram of Fig. 5.17. In panels (c-f) the profiles have been plotted in such a way to make reference to the red/orange region of linear profiles.

boundaries, they orient along the wall direction [112]. In actomyosin solutions, the actin filaments can also be assumed to be anchored parallel to the walls due to focal adhesion [212]. Therefore, suitable boundary conditions for the polarization **P** is a strong anchoring condition with **P** aligned parallel to the walls

$$P_\perp|_{\text{walls}} = 0, \qquad \nabla_\perp P_\parallel|_{\text{walls}} = 0, \tag{5.2}$$

where $P_\perp$ and $P_\parallel$ denote, respectively, normal and tangential components of the polarization field with respect to the walls. In order to compare external and active forcing in our system, we make use of the Ericksen number, Er, and the *active* Ericksen number Er_{act} as relevant adimensional quantities. The former is often used in the study of liquid crystals to describe the deformation of the orientational order parameter field under flow and it is defined as the ratio of the viscous stress to the elastic stress. In particular in lamellar systems a suitable choice is given by:

$$\text{Er} = \frac{\eta_0 \dot{\gamma}}{B}, \tag{5.3}$$

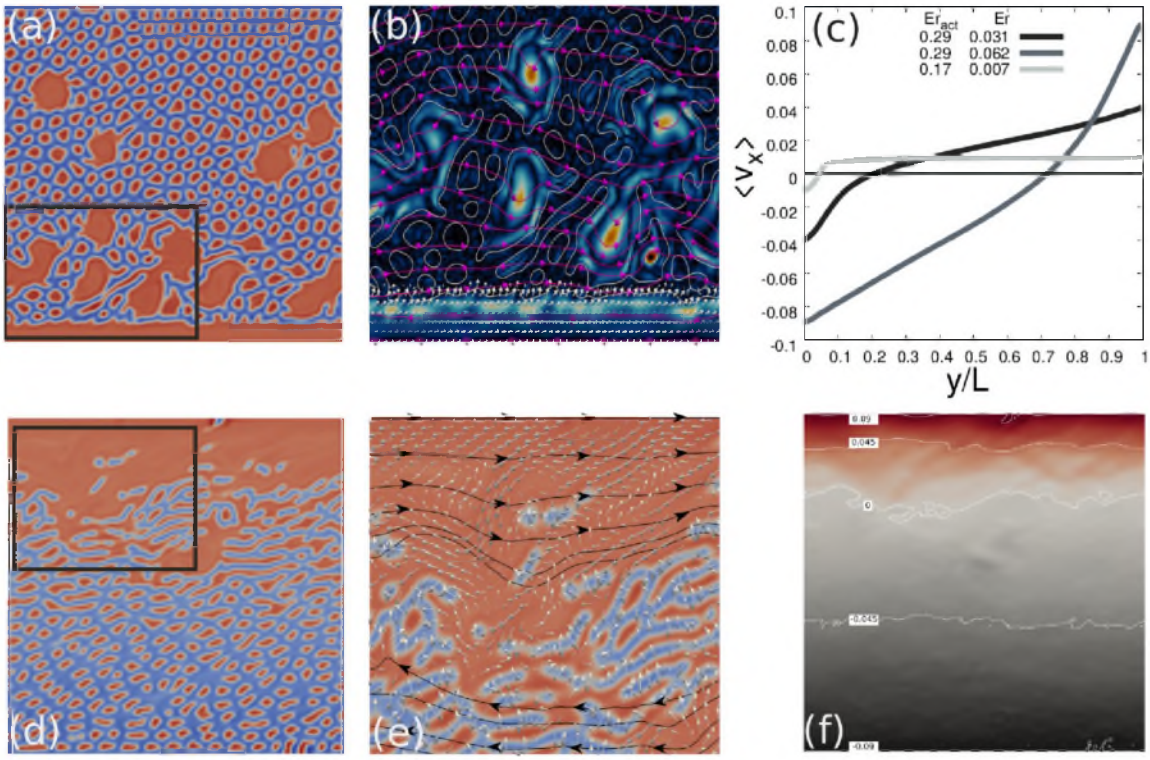

Figure 5.9: *Unidirectional motion.* (a) Concentration contour plot at $Er_{act} = 0.29$, $Er = 0.031$. (b) Contour plot of the vorticity $\omega = (\partial_y v_x - \partial_x v_y)/2$ (black corresponds to $\omega = 0$ and red to $\omega = 10^{-2}$) in the region framed with black box in panel (a); purple lines represent velocity streamlines while the polarization field is plotted in white (for graphical clarity, only in the bottom active layer). (d) Contour plot of the concentration field at $Er_{act} = 0.29$ and $Er = 0.062$ and (e) zoom of the region framed with black box in panel (d), with black lines representing **v** streamlines and **P** plotted in white. (f) Contour plot of the velocity field in the flow direction for the same case shown in panel (d), with few isolines plotted in white. Panel (c) shows $\langle v_x \rangle$ for the two cases considered and also for the case at $Er_{act} = 0.172$, $Er = 0.0075$.

where B is the lamellar compression modulus – namely the energy cost for the variation of the lamellar width $\lambda = 2\pi/\kappa$ per unit length, whose expression in terms of the parameter of the model is explicitly derived in the Appendix C. The active Ericksen number, suggested by Giomi for the first time in [70], is, in turn, defined as the ratio between the module of the activity parameter ζ and the compression modulus:

$$\mathrm{Er}_{act} = \frac{|\zeta|}{B}. \tag{5.4}$$

5.2.1. LINEAR FLOW AND SYMMETRY BREAKING TRANSITION

Before presenting specific results case we summarize the morphological phenomenology arising in an active extensile polar lamellar system at varying the activity parameter ($\zeta > 0$) in absence of any external forcing. Bonelli *et al.* [12] showed that the shear-free system is characterized by a transition at $Er_{act} \approx 0.11$ from the lamellar phase to an emulsion with moving active droplets. The bending instability, typical of extensile gels [169], favours this rearrangement. For $Er_{act} \gtrsim 1$ the system enters in a totally mixed phase, characterized by chaotic velocity patterns [136]. The following Sections will be devoted to present the different behaviours of the sheared system at varying both the intensity of active and external forcing.

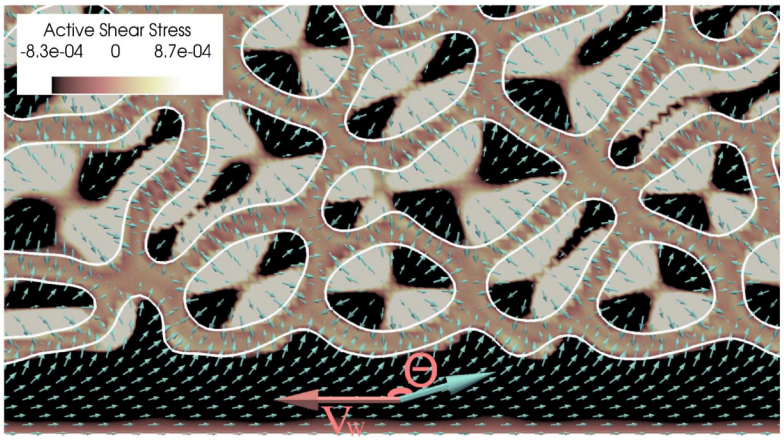

Figure 5.10: Active shear stress close to a wall at $Er = 0.0074$, $Er_{act} = 0.172$. The polarization field **P** (cyan arrows) exhibits a splayed profile under the mutual effect of strong anchoring to the wall (tangential) and to the interface (homeotropic), while the red arrow shows the direction of the imposed velocity v_w. The angle θ denotes the local orientation of the polarization, sketched by the magnified reference cyan arrow, with respect to the flow. White lines trace the interface ($\phi = \phi_{cr}$) between active and passive phases. Passive (beige) regions are almost stress free, while negative stress in the boundary layer (black) corresponds to a net force opposite to the flow direction. Droplets have quadrupolar structures.

5.2.2. LINEAR VELOCITY PROFILES AND LAMELLAR PHASE.

The scenario just described is strongly influenced by an external shear flow. Due to the tendency of lamellae to align with the flow, an applied shear, even small, is found to counter activity-induced bending, thus extending the range of stability of lamellar order towards larger Er_{act} ($Er_{act} \lesssim 0.18$) with respect to its unsheared counterpart. Under this threshold and for a vast range of shear rates, the system sets into a lamellar phase, as shown in panels (a) and (d) of Fig. 5.8. The region with these properties is red in Fig. 5.17, where flow regimes found by scanning the $Er - Er_{act}$ plane are summarized. At small shear, relaxation dynamics leads to the formation of long-lived dislocations in the lamellar pattern, as the one highlighted by the black box in panel (a) of Fig. 5.8. Panel (b) of the same Figure shows the detail of the velocity field in the neighborhood of the dislocation. If $\dot{\gamma}$ is weak enough, defects are capable to consistently alterate the velocity pattern, since dislocations develop flows trasversal to the direction of lamellar-alignment, thus leading to permanent shear bandings in the velocity profile (as shown by the red line in the inset of Fig. 5.8c). At greater values of shear rate, the superimposed flow is strong enough to eliminate dislocations (see for example panel (d) in Fig. 5.8 and Movie 1[3]), eventually leading to the formation of disruptions that are much less effective on the flow than dislocations, as confirmed by the linear behaviour of the corresponding velocity profile. In this regime lamellae are globally aligned to the flow, while the polarization field, homeotropically anchored to the interfaces (panel (e) of Fig. 5.8), is pointing towards the passive phase (blue regions in zoom of panel (e)). Panel (f) compares the time evolution of shear stress for the two cases considered. Dynamics at high shear leads to a smoother and faster relaxation towards lower values of σ_{xy}. When the imposed shear is weaker, oscillations or jumps, as the one marked by an arrow at $t = 6 \times 10^6$ in panel (f) of Fig. 5.8, are due to the annihilation of two dislocations.

[3]Movies are described in Appendix D, and can be found at the following link: https://www.dropbox.com/sh/qs7fbvk8p2ttcst/AAC988O90RnPSYLhsX8sf13ua?dl=0

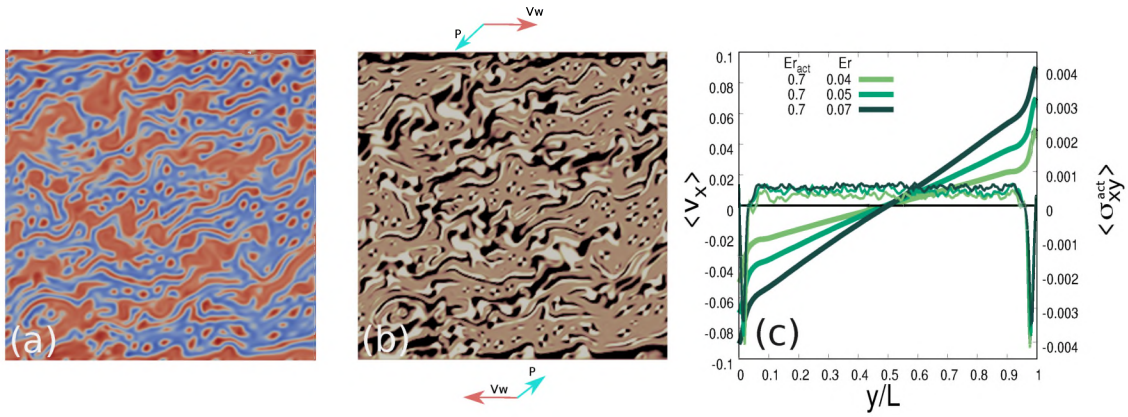

Figure 5.11: *Symmetric shear thinning profiles.* Concentration (a) and active shear stress (b) contour plot for the case at $Er_{act} = 0.70, Er = 0.04$. The colour code is the same of Fig.5.10. Red arrows denote the direction of the moving walls, and cyan ones the direction of the polarization, averaged within the active layers close to the walls. (c) Velocity $\langle v_x \rangle$ (thick lines) and active shear stress profiles $\langle \sigma^{act}_{xy} \rangle$ (thin) averaged along the flow direction, for the case corresponding to panels (a) and (b) and analogous ones.

5.2.3. UNIDIRECTIONAL MOTION.

The behaviour becomes more complex when activity is increased. The combination of activity and shear has dramatic consequences. The system undergoes a morphological transition from the lamellar phase towards an emulsion of active material in a passive background, a behaviour also found by Bonelli *et al.* [12] at lower active dopings. Fig. 5.9 shows two cases at $Er = 0.031$, $Er_{act} = 0.29$ (top row) and $Er = 0.062$, $Er_{act} = 0.29$ (bottom row) characterized by the formation of a thick layer of material close to *one* boundary (see dynamics in Movie 2), and small features on Brazovskii lengthscale $\lambda = 2\pi/\kappa$ coexisting with larger aggregates of active material elsewhere. Such symmetry breaking is mediated and sustained by the formation of these large active domains where bending polarization instabilities, typical of extensile systems, act as a source of vorticity (see panel (b)). Big active domains are mostly advected by the intense flow close to the walls, as shown by purple velocity streamlines, differently from what happens in shear-free systems where polarization bending results into the rotational motion of the bigger active droplets. Fig. 5.9c shows the related x-averaged velocity profile $\langle \mathrm{v_x} \rangle$ (grey curve): Instead of the linear behaviour of Fig. 5.8c, one observes banded flows with the higher gradient in correspondence of the wall with the active layer. Similar cases occur at different Er, Er_{act} with deposition of active material randomly on the top or bottom wall. Streamlines of $\mathbf{v}$ (in panels (b) and (e) of Fig. 5.9) show that the inversion of the fluid velocity takes place in correspondence of the interface of the active layer. The top-bottom symmetry breaking leads to a net flux of matter in the flow direction and has been named *unidirectional motion.* Cases exhibiting such property have been plotted in grey in Fig. 5.17. Moreover, as shear is increased, the position of flow inversion migrate towards the bulk of the system (see the dark grey profile at the larger Er in panel (c) and the corresponding $\mathrm{v_x}$ contour plot in panel (f)). Unidirectional flow (grey region in Fig. 5.17) may occur with almost everywhere vanishing gradient of $\langle \mathrm{v_x} \rangle$, and in this case it will be called *superfluidic* [27] (see light grey profile in Fig. 5.9c). It is worth to mention that inviscid motion occurs in the model of [82] only with symmetric profiles, with shear gradient all localized in the bulk.

Which are the mechanisms for the observed velocity profiles? And how to explain

the flow symmetry breaking transition? Due to complexity of the system we can only partially answer to these questions. The velocity behaviour is strictly related to that of polarization close to the walls. Thick layers as the one in Fig. 5.9a,d and in Fig. 5.10 are characterized by the bending of polarization due to competition between strong parallel anchoring to the walls and perpendicular orientation to domain interfaces, leading to a negative active shear stress contribution. This is shown in Fig. 5.10, where white/black regions correspond to positive/negative values and correspond to active domains, while beige ones are associated to the isotropic background and correspond to almost null values. Moreover, topological defects in the active layer are strongly inhibited by elastic energy, as suggested by the uniform polarization pattern in the black bottom layer.

Within the active layer $\sigma_{xy}^{act} \sim \frac{\zeta}{2}\phi_0(P_{eq})^2 \sin 2\theta$, where θ denotes the local orientation of polarization with respect to the imposed velocity ($0 \leq \theta \leq \pi$), thus generating an active force density in the flow direction ($f_{\parallel}^{act} = \partial_{\perp}\sigma_{xy}^{act}$, where $\partial_{\perp}$ denotes derivative in the direction normal to the walls). This can either reinforce the imposed flow if the polarization field is oriented as v_w (since $\partial_{\perp} \sin 2\theta > 0$), or lead to a reduction of the fluid velocity if opposite (since $\partial_{\perp} \sin 2\theta < 0$). However, between the two possible orientations, the one reinforcing the flow does not appear in the cases discussed so far. In order to clarify this point we define the average polarization P_w on each wall – it can be calculated as $P_w \sim \langle P_{\parallel}|_{\text{walls}} \rangle$, where here $\langle \cdot \rangle$ stands for the average over few layers close to the wall sites. For the unidirectional motion case, P_w is null at the wall where the thick active layer is absent, so that we denote such polarization state as **0**. If the polarization is opposite to v_w, as in the bottom/top of panel (b)/(e) of Fig. 5.9, we will indicate it with -. Following the notation just introduced, we will refer to the global states shown in Fig. 5.9 with **0**-, independently of the top-bottom asymmetry.

5.2.4. SYMMETRIC SHEAR THINNING PROFILES.

By further increasing both activity and shear rate, phase demixing is more pronounced (Fig. 5.11a) with the formation of an emulsions of amorphous active domains in a passive matrix. Active layers form on *both* walls so that symmetry is restored also at level of the velocity profiles $\langle v_x \rangle$, with gradients in the bulk of the system lower than the imposed one, as shown in panel c of Fig. 5.11 (thick lines). Symmetric cases exhibiting such phenomenology have been plotted in green in Fig. 5.17. Under these conditions, it may happen that the velocity gradient in the bulk of the system is either everywhere vanishing or, eventually, opposite to the one externally imposed (*negative viscosity*), despite such states are found to be unstable in the long term (see Sec. 5.2.6). To explain the flow properties presented, we analyse the active shear stress profiles $\langle \sigma_{xy}^{act} \rangle$ averaged in the flow direction (see thin lines in panel (c)). This confirms that the active stress is considerably different from zero only in the layer close to both walls, where it assumes negative values –thus leading to the sharp decrease of the intensity of the flow in the same region – while it is approximately null in the bulk. A contour plot of the active stress is also shown in panel b of Fig. 5.11, showing that the P_w polarization state at boundaries is in a – configuration.

Such behaviour is also accompanied by shear thinning, typical of extensile fluids as Er_{act} is increased. This is analysed in Fig. 5.12 where the ratio between the apparent viscosity $\eta = \langle \sigma_{xy}^{tot} \rangle / \dot{\gamma}$ (where $\langle \sigma_{xy}^{tot} \rangle$ denotes the time average of the total stress tensor),

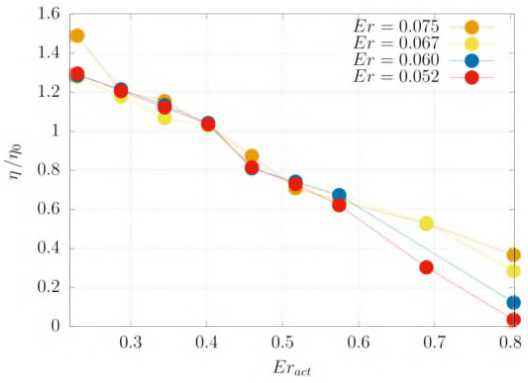

Figure 5.12: *Shear thinning in extensile mixtures.* Ratio between apparent viscosity η (measured as $\langle\sigma^{tot}_{xy}\rangle/\dot{\gamma}$) and shear viscosity η_0, while varying activity for some values of the Ericksen number.

and the shear viscosity η_0 has been plotted versus Er_{act}. We varied Er in the range $Er \gtrsim 0.05$, where viscosity states are found to be stable for any value of Er_{act}. Viscosity mainly depends on the intensity of the active doping, while no substantial dependence is found on the shear rate if $Er_{act} \lesssim 0.6$. This suggests that activity, inducing shear thinning, is a parameter capable of controlling the rheological property of extensile suspensions.

5.2.5. ACTIVITY QUENCH.

We further analysed the nature of the transition between the symmetric configurations at higher activity (green region in Fig. 5.17) and states with unidirectional flow at weaker activity, starting from a stationary states at $Er_{act} = 0.57$ and quenching the activity to $Er_{act} = 0.28$ at fixed $Er = 0.06$. Panels (a)-(c) in Fig. 5.13 show the quenching dynamics: starting from the symmetric configuration of panel (a) at $Er_{act} = 0.57$, amorphous active domains progressively stretch in the flow direction and cluster on the bottom boundary (see panel (b)). This accompanies the *melting* of the active layer close to the upper wall, finally generating the asymmetric configuration of panel (c) characterized by unidirectional flow. The evolution of velocity profiles is shown in panel (d). Panels (e)-(g) show the results of a similar experiment: this time we quenched the active parameter so to move from the grey region ($Er_{act} = 0.22$) with unidirectional motion, to the red one ($Er_{act} = 0.057$) with linear profiles, in Fig. 5.17, while keeping shear rate fixed at $Er = 0.01$. After the quench droplets are no more stable, since the active doping is not strong enough to maintain the bending instability. A lamellar phase progressively grows from the bottom of the system, where most of the active material was initially found, towards the upper wall. The final configuration is characterized by a symmetric, defect-free lamellar configuration, with linear velocity profile, whose evolution can be appreciated by looking at panel (h).

5.2.6. INTERMITTENT FLOW

Surprisingly, yet another behaviour appear in a vast region of the parameter plane at small shear, $Er \lesssim 0.04$, and sufficiently large activity, $Er_{act} \gtrsim 0.4$, (blue in Fig. 5.17). Under this condition, the system is symmetric and exhibits an intermittent flow regime. This is to be related, once again, to the polarization state at the boundaries. Indeed, this

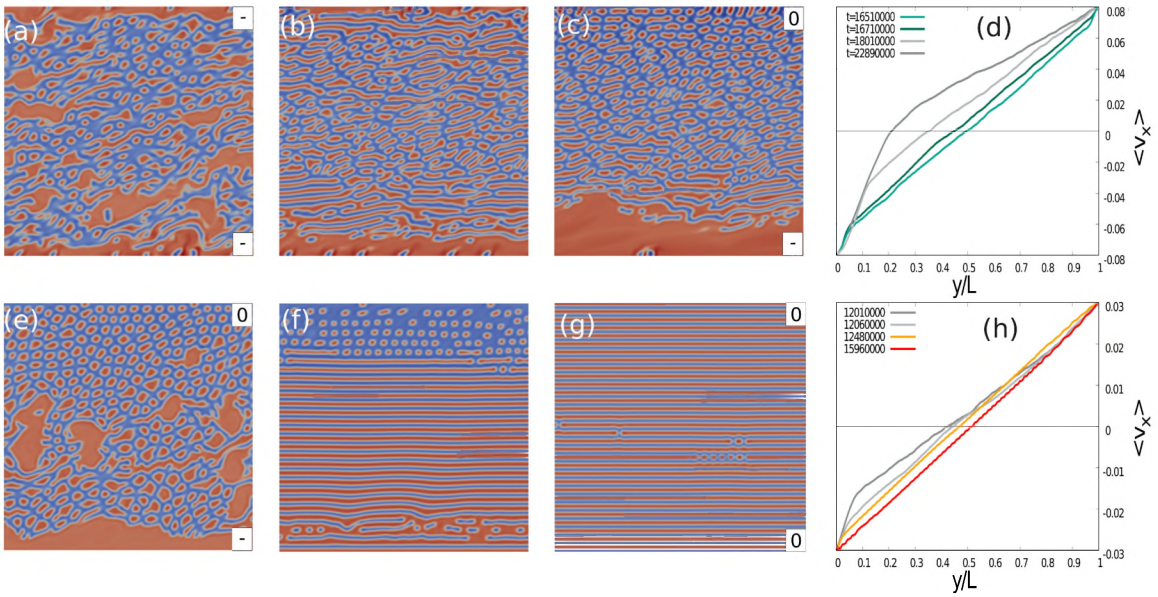

Figure 5.13: *Activity quench.* Panels (a)-(c) show the evolution of the system after that Er_{act} has been quenched from 0.57 to 0.28, thus moving from the green region of Fig. 5.17 to the grey one, at $Er = 0.06$. The colours of the profiles have been chosen in accordance to the colour of the corresponding region in the phase diagram of Fig. 5.17. Labels (**0** or -) at the top and at the bottom of initial and final panel denote the state of the polarization at the boundary. The evolution of velocity profiles is also shown in panel (d). Panels (e)-(g) show the same for the quench from the grey region ($Er_{act} = 0.22$) towards the red region ($Er_{act} = 0.057$) of Fig. 5.17 at $Er = 0.01$, with the evolution of velocity profiles in panel (h). Contour plots correspond to the first, third and last velocity profiles in panels (d) and (h)

.

time we find (unstable) configurations where P_w is oriented in the same direction of the imposed velocity, so that we will denote such state as **+**. The dynamics of the system is characteried by jumps between **++**, **-+** and **--** states.

Such intermittent behaviour is reflected in the evolution of the area averaged stress, as shown in Fig. 5.15a. Elastic contributions are on average constant, while active stress fluctuates around positive, negative or vanishing values. These are found to be largely determined by the portion of the system closer to boundaries (see Fig. 5.15c). For each wall the sign of active stress coincides with the one of P_w, so that positive and negative total stress correspond respectively to **++** and **--** P_w states, while total zero active stress comes from opposite P_w contributions (**-+** states). Viscosity jumps (Fig. 5.15 a) correspond to the inversion of the polarization on one of the two walls during evolution. The inversion of polarization on the boundaries, generally prevented by elastic effects and strong anchoring, can occur as a result of *catastrophic* events, such as collision of big domains with the active layer (see Movie 3,4[4]). This phenomenon is driven by the collision of active domains against the boundary layers. In Fig. 5.16 we show, for the case at $Er_{act} = 0.57, Er = 0.003$, a series of snapshots of a change of polarization on the bottom wall from the antiparallel alignment of **P** with respect to the imposed velocity ($-$ state) to a parallel configuration ($+$ state). The overall dynamics of the event can be better appreciated by looking at the attached Movie 3,4. Panel (a) of Fig. 5.16 shows the

[4]Movies are described in Appendix D, and can be found at the following link: https://www.dropbox.com/sh/qs7fbvk8p2ttcst/AAC988O90RnPSYLhsX8sf13ua?dl=0

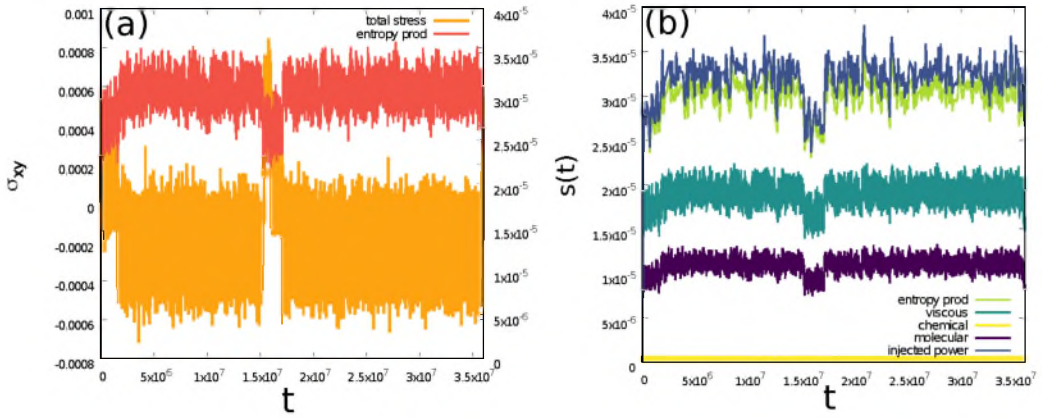

Figure 5.14: *Entropy production in multistable states.* (a) Time evolution of the total shear stress and entropy production at $Er_{act} = 2.30, Er = 0.00074$. Negative viscosity states, corresponding to $--$ configurations of polarization at the boundaries, live longer than others. Entropy production $s(t)$ assumes greater values in correspondence of these regions. Panel (b) shows time evolution of each contribution to entropy production and of the injected power. Each contribution to $s(t)$ has been measured by integrating on the computational domain the terms on the right-hand side of Eq. (5.13), while the injected power has been computed as the integral over the whole system of the quantity $(\boldsymbol{v}\cdot\nabla)\cdot\underline{\underline{\sigma}}^{inj}$, where $\underline{\underline{\sigma}}^{inj}$ is the sum of the stress on the fluid arising by the action of the active agents and the moving walls.

configuration at time $t = 52380$, before the event. Panel (b) shows a zoom at the same time of a colliding active domain, characterized by a typical vortical pattern in the polarization field, with a +1 defect, highlighted by a red square in panel (b). As the droplet merges with the layer, strong elastic interactions produce bendings of the liquid crystal network (see panel (c) at time $t = 53580$). In panel (d) at a close subsequent time $t = 56580$, the system is still found in a homogeneous $-P_w$ state on the wall, despite the polarization on the top part of the layer is now directed in the same direction of the imposed flow. The +1 defect has disappeared due to the interaction with the wall, thus generating a complex rearrangement dynamics. As a result of the advection and the elastic deformations, the polarization flap, directed along the flow direction and highlighted by the black box in panel (d), is pushed on the walls and adheres on it, resulting in a local change of the polarization state (see panel (e) at time $t = 58286$). After a similar event, not shown in Fig. 5.16, the overall hydrodynamic state changes, thus leading to a final homogeneous + state, shown in panel (f). We observe that flip dynamics generally takes place on time-scale of order $\sim\mathcal{O}(10^5)$ time-steps, much shorter than the lifetime of viscosity states that are found to be $\sim\mathcal{O}(10^7)$.

-- states typically live longer than others, as can be appreciated looking at the pdf of the total shear stress reported in Fig. 5.15b. The statistics of viscosity states has been constructed considering 40 different runs for the same couple of parameters $Er_{act} = 1.14$, $Er = 0.0075$. The typical length of each run is of about 10^7 lattice Boltzmann iterations. The data for the shear stress have been sampled under stationary conditions and then fitted with the sum of three normal distributions, centred at values marked with dotted lines in panel (b). These mean values are consistent with the average of the stress in the different states of Fig. 5.15a, and their probability of occurrence will correspond to the amount of time that the system spends in each of them.

To go deeper in the characterization of this behaviour we measured entropy production during the system time evolution. Generally, in non-equilibrium systems, the

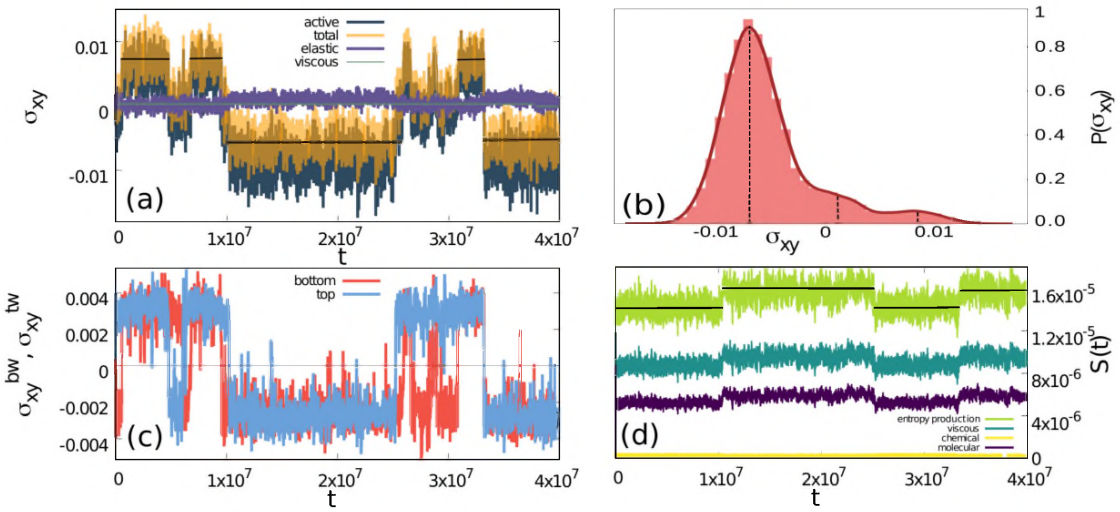

Figure 5.15: *Entropy production in multistable states.* (a) Time evolution of stress contributions at $Er_{act} = 1.14, Er = 0.00075$. The total stress is plotted in transparent yellow, while the active one is the dark blue curve underneath. Panel (b) shows the *pdf* of the total stress (data from 40 independent runs, fitted by 3 normal distributions peaked at $\sigma_{xy} = -0.0068, 0.0009, 0.0086$). (c) Total stress close to bottom and top walls, respectively computed as $\sigma_{xy}^{tw} = \int dx \int_{Ly-l}^{Ly} dy\, \sigma_{xy}$ and $\sigma_{xy}^{bw} = \int dx \int_{0}^{l} dy\, \sigma_{xy}$, where l is the width of the layer. Here $l = 15$. Nevertheless, as long as $l < Ly/2$, results remain unaltered. (d) Entropy production. Negative viscosity states, corresponding to -- configurations of polarization at the boundaries, live longer than others. Entropy production $s(t)$ assumes greater values in correspondence of these regions. Each contribution to $s(t)$ has been measured by integrating on the computational domain the terms on the right-hand side of Eq. (5.13).

entropy density $\Sigma(\mathbf{r}, t)$ obeys the continuity equation

$$\partial_t \Sigma + \nabla \cdot (\Sigma \mathbf{v}) = s, \tag{5.5}$$

where s is the rate of entropy production per unit volume, subject to the condition $s \geqslant 0$. This can be written in terms of generalized fluxes J_i and forces X_i, as [40]

$$Ts = J_i X_i, \tag{5.6}$$

with T the temperature – fixed at in our simulations ($T = 0.5$) since we are neglecting heat transfer. Thermodynamic forces are chosen as follows:

$$\tilde{X}_v = (\nabla \mathbf{v})^S \equiv \tilde{D}, \tag{5.7}$$

$$\mathbf{X}_P = -\frac{\delta F}{\delta \mathbf{P}} \equiv \mathbf{h}, \tag{5.8}$$

$$\mathbf{X}_\phi = \nabla \frac{\delta F}{\delta \phi} \equiv \nabla \mu, \tag{5.9}$$

where F is given by Eq. (5.1), $\tilde{D}$ is the strain rate tensor. Moreover, in our model the following linear phenomenological relations between forces and fluxes hold [99]:

$$\tilde{J}_v = \tilde{\sigma}^{tot}, \tag{5.10}$$

$$\mathbf{J}_P = \partial_t \mathbf{P} + (\mathbf{v} \cdot \nabla)\mathbf{P} + \tilde{\Omega} \cdot \mathbf{P} = \frac{1}{\Gamma}\mathbf{h} + \xi \tilde{D} \cdot \mathbf{P}, \tag{5.11}$$

$$\mathbf{J}_\phi = -M \nabla \mu, \tag{5.12}$$

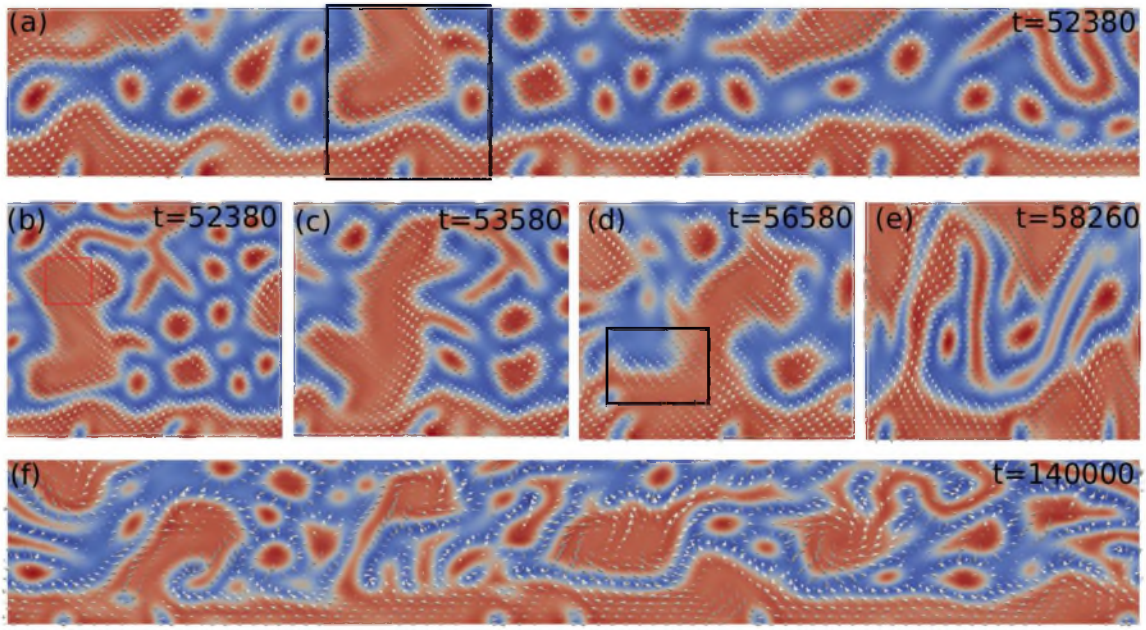

Figure 5.16: *Polarization flip.* Contour plots of concentration field ϕ for $\zeta = 0.005$ ($Er_{act} = 0.57$) and $\dot{\gamma} = 3.12 \times 10^{-5}$ ($Er = 0.003$). Panels (a) and (f) show the initial and final state, respectively, of the polarization at the bottom wall. Panels (b-e) show snapshots of the collision of a droplet with the bottom wall, which causes a local rearrangement of the polarization state. The red contour in panel (b) encloses a +1 defect in the polarization field pattern.

where we denoted with $\tilde{\Omega}$ the vorticity tensor, that is the antisymmetric part of the gradient velocity tensor. By substituting these relations into Eq. (5.6) we find that

$$Ts = 2\eta\tilde{D} : \tilde{D} + \frac{1}{\Gamma}\mathbf{h}\cdot\mathbf{h} + M(\nabla\phi)^2, \tag{5.13}$$

where we retained only those terms even under time reversal symmetry. We here identify three contributions: the first one is the entropy production due to viscous effects, $2\eta\tilde{D} : \tilde{D}$, while the second ($\frac{1}{\Gamma}\mathbf{h}\cdot\mathbf{h}$) and the third ($M(\nabla\phi)^2$) ones are respectively the molecular and the chemical terms, accounting for the entropy produced during the relaxation dynamics of $\mathbf{P}$ and ϕ. This expression is quadratic in the thermodynamic forces and satisfies all required conditions, among which invariance under Galilean transformations as well as the second principle of thermodynamics. In the stationary regime, entropy production must be equal to the energy injected into the system, due to the work of the walls and active pumping. We emphasize that activity ζ is a reactive parameter and therefore does not appear in the entropy production formula [100]. However activity influences the dynamics, acting as a velocity source through the active stress, thus contributing indirectly to dissipation. Fig. 5.14 refers to the case at $Er_{act} = 2.30$ and $Er = 0.00074$. In panel (a) the total stress and entropy production are compared. In the evolution of the stress one recognizes two regions of stability of negative viscosity, whose lifetime is $\mathcal{O}(10^7)$ LB iterations. These occur as an effect of $--$ polarization configurations at the boundaries. Entropy production $s(t)$ assumes here greater values than in other viscosity state. Panel (b) compares the different entropy production contributions to the injected active power (blue line) that match the total entropy production (green line) with an error of $\sim 3\%$.

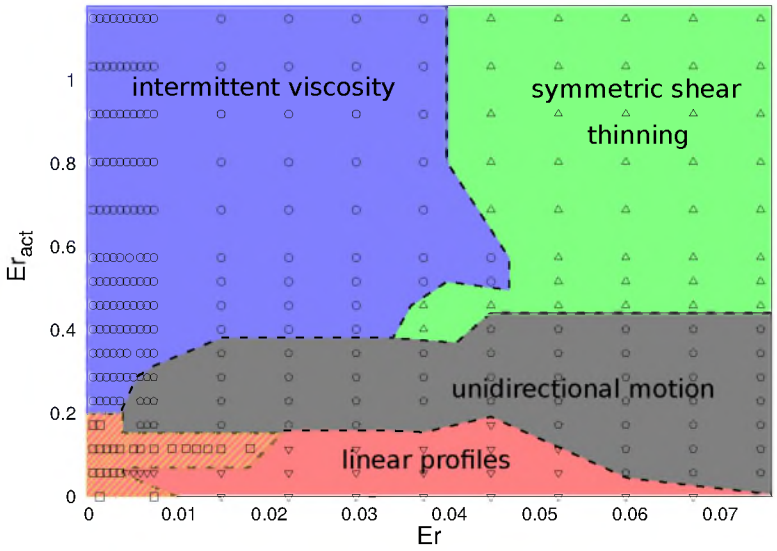

Figure 5.17: Flow regimes in the Er-Er_{act} plane, as described in the text. Hollow marks denote simulation points.

Panels (a) and (d) of Fig. 5.15 compare the behaviour of the stress and entropy production for $Er_{act} = 1.14$ and $Er = 0.00074$. The evolution of the stress is characterized by two regions of stability of negative viscosity – whose lifetime is $\mathcal{O}(10^7)$ LB iterations – that respectively occur from $t \approx 10^7$ to 2.5×10^7, and from $t \approx 3.2 \times 10^7$ to 4×10^7. These states have also the highest probability, as can be appreciated looking at the pdf of the total stress in panel (b) of Fig. 5.15. In Panel (d) the different entropy production contributions are shown. We first notice that the contribution due to diffusion/chemical (yellow line) is almost null. In addition, the viscous dissipation (blue line) is always greater than the contribution due to the molecular field (violet line). This suggests that the hydrodynamics of the system – driven by active injection and external forcing – is mainly countered by viscous dissipation phenomena. Moreover, the total entropy production oscillates around two different values and jumps during time evolution, with the highest value corresponding to the negative viscosity states. This behaviour, with prevalence of -- polarization states is typical of all the intermittent cases (blue region in Fig. 5.17), and is compatible with a maximum entropy production principle (*MaxEPP*). Various variational principles, related to entropy production rates, have been put forward to quantitatively select the most probable state in multi-stable systems. While much efforts have been spent in the search of a general principle and recent progress has been made [46] on a theoretical derivation of such a principle, questions about how this should be interpreted and applied have not been answered, especially for systems evolving far from thermodynamic equilibrium. In particular, a *MaxEPP* has been implemented as a selection criteria to study systems characterized by multiple non-equilibrium stationary states [46] and very recently the Schlögl model [163] – that is a simple, analytically solvable, one-dimensional bistable chemical model – has been used to demonstrate that the steady state with the highest entropy production is favoured [54]. In the system here considered, we found that entropy production $s(t)$ is higher for the most likely −− states, suggesting that *MaxEPP* may act as a thermodynamic principle in selecting non-equilibrium states.

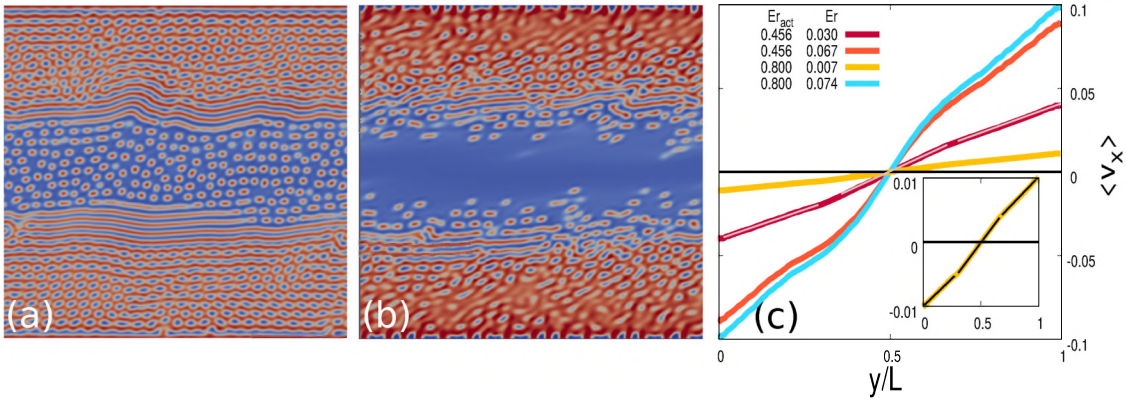

Figure 5.18: *Morphology and shear bandings in contractile mixtures.* (a-b) Contour plots of concentration field ϕ for $\zeta = -0.007$ ($Er_{act} = 0.8$) and $\dot{\gamma} = 7.8 \times 10^{-5}, 7.8 \times 10^{-4}$ ($Er = 0.007, 0.074$). (c) Corresponding averaged velocity profiles (blue and yellow curves). Orange and red curves correspond to the cases presented in Fig. 5. Linear trends have been marked with a continuous line (black or white) to ease visualization of shear bandings.

5.2.7. OVERVIEW AND PHASE DIAGRAM

The various behaviours found in the active polar emulsion under shear have been summarized in Fig. 5.17, at varying Er and Er_{act}. At small Er_{act}, the system arranges in a lamellar configuration. In this range, at small shear rates, few persistent defects (dislocations) give rise to slight deformations in velocity profiles (dashed-red region in Fig. 5.17). Increasing Er, dislocations are washed out by the flow and the system enters the region of linear velocity profiles (red region in Fig. 5.17). As activity is increased, morphology is characterized by a transition towards asymmetric configurations, with the formation of a thick layer of material close to *one* boundary, thus generating a non-vanishing flux of matter – a behaviour addressed as *unidirectional flow*. Such regime is stable for a broad range of Er at intermediate active dopings (grey region in Fig. 5.17). By further increasing activity, at high shear rate, phase demixing is more pronounced and this has important consequences on the flow. Active layers form on *both* walls and symmetry is restored. Under these conditions, it may happen that the velocity gradient in the bulk of the system is either everywhere vanishing or, eventually, opposite to the one externally imposed (*negative viscosity*), despite such states are found to be unstable in the long term. The region with stable symmetric profiles is green in Fig. 5.17. Cases in the blue region are instead characterized by the jumping dynamics described in the previous section.

We also remark that the results presented in this Chapter strictly hold for bidimensional geometries – as often happens in experimental realizations of active systems, where bacteria and cytoskeletal suspensions are usually confined at a water-oil interface [48, 208]. In full $3d$ environments – where both vortex stretching of the flow field and twisting of the polarization field are allowed – the proliferation of degrees of freedom may strongly affect the behaviour of the system that is indeed different even in absence of any internal and/or external forcing [24, 85].

We have showed how the competition between externally imposed shear and local energy injection results in a wealth of different rheological behaviours, that can be explained in terms of specific dynamical mechanisms. As an example, jumps between velocity profiles with positive and negative gradients are due to collisions between large

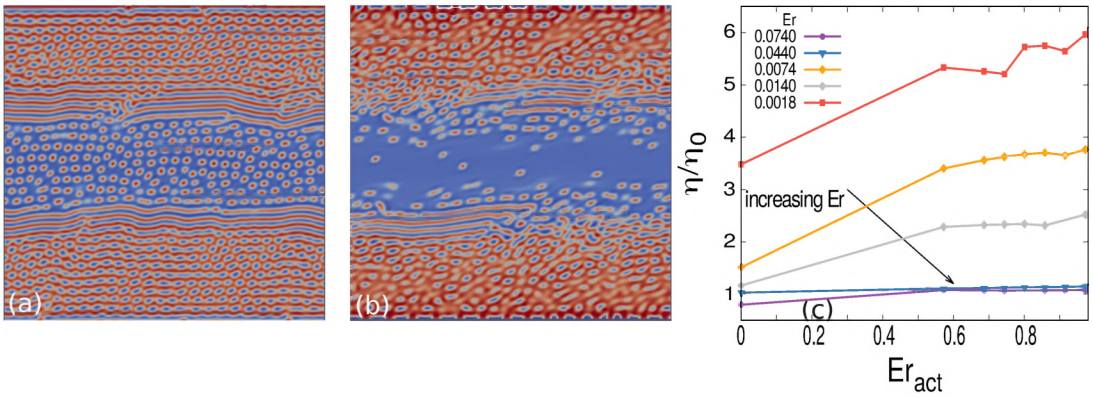

Figure 5.19: Concentration ϕ for contractiles at $Er = 0.030$ (a), 0.067 (b) and $Er_{act} = 0.456$. (c) Apparent viscosity behaviour.

active droplets or domains and active layers coagulated on the moving walls. The generalized active gel model proposed in this work has allowed us to perform a fully $2d$ analysis, by keeping under control the time evolution of the important variables, such as the local concentration and the orientation of the active constituents. Thus we confirmed, by varying both external and internal forcing, the existence of superfluidic and negative viscosity states found experimentally in bacterial suspensions [82, 119] whose first numerical confirmation by means of quasi-$1d$ simulations was furnished in [118]. Moreover, we also found that a maximum entropy production principle holds in selecting the most probable state in the intermittent viscosity regime.

Since most of the observed behaviours mainly arise due to the elastic properties of the order parameter, they are expected to stay valid also in nematic systems. This because the dynamics of polar systems differs from their nematic counterpart mainly for the allowed topological defects. THe hope is that this study can stimulate the design of new active materials and devices with pioneering applications.

5.2.8. RHEOLOGY OF CONTRACTILE EMULSIONS

So far we have analysed the behaviour of a symmetric extensile ($\zeta > 0$) polar emulsion. One may ask what happens if we change the sign of activity. In this section we analyse the behaviour of a contractile ($\zeta < 0$) polar emulsion.

As reported at the beginning of this chapter, the shear-free symmetric system shows a transition from lamellar phase to an emulsion of passive droplets in an active matrix at $\zeta \approx -0.007$ ($Er_{act} = 0.80$) [11]. This behaviour becomes more complex under shear.

As contractile activity is raised ($|\zeta| \gtrsim 0.0035$, $Er_{act} \gtrsim 0.4$) and the imposed shear rate is weak ($Er \lesssim 0.030$), the system sets into new morphological patterns. In the two regions close to the walls, an emulsion of passive droplets in an active background is formed (see panel (a) of Fig. 5.18 and of Fig. 5.19). A similar pattern was also found in shear-free contractile emulsions for $|\zeta| \gtrsim 0.005$. A new feature due to the imposed shear is that a channel of isotropic fluid, populated by small droplets of active material, develops in the middle of the system. This effect leads to slight shear-bandings, visible in the yellow velocity profile shown in Fig. 5.18(c) – also including results of the cases shown in Fig. 5.19. As shear strength is increased, active droplets are progressively washed away from the isotropic channel and almost disappear for $Er \gtrsim 0.055$ (panel (b) of Fig. 5.18

and of Fig. 5.19). Strong shear bandings is found in correspondence of the interfaces between the passive channel and the two regions characterized by presence of passive droplets dispersed in the active matrix, as shown by the blue line in panel (c) of Fig 5.18 (a similar $\langle v_x \rangle$ profile is also found for the case at $Er_{act} = 0.456$, $Er = 0.067$ (orange line), whose configuration is shown in Fig. 5.19(b)). For what concerns the rheological characterization, we confirm shear thickening for increasing activity (Fig. 5.19c), as found in other contractile fluids [59, 68, 124].

We now ask if activity alone is responsible for the formation of the channel. To this task, we performed a series of simulations starting from a configuration characterized, at stationarity, by the presence of a channel (left configuration in the first row from above in Fig. 5.20). If we switch off the externally applied shear, the system sets in a disordered lamellar array, as should be for the chosen value of activity. We then switch off activity and turn on again the imposed shear. What happens is that the system first creates a channel of polar droplet (right panel in central row of FIg. 5.20), that is found to be unstable in the long term, giving way to asymmetric configurations (left panel in the central row of Fig.5.20), resembling those discussed earlier in this Chapter for the case of extensile activity. To test if this system develops hysteresis feature, we now switch on activity again in both symmetric and asymmetric configurations. The lower row of Fig. 5.20 shows that activity is not capable of altering the initial configuration.

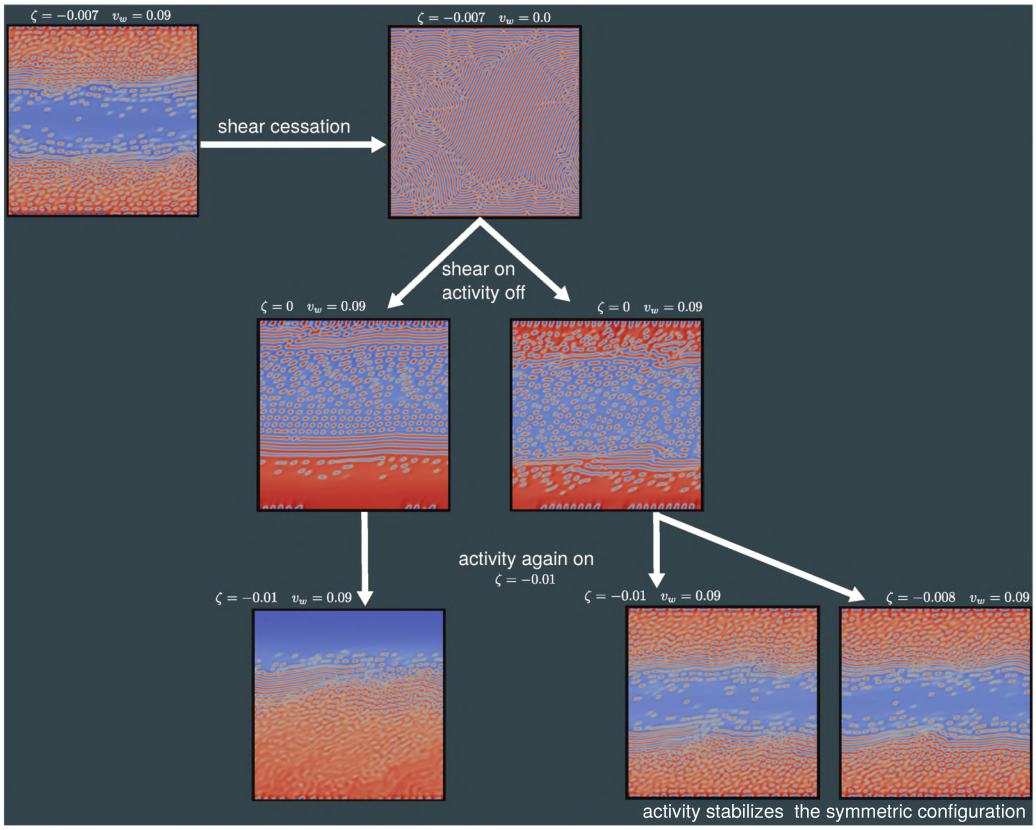

Figure 5.20: *Is activity responsible for the channel formation?* we performed a series of simulations starting from a configuration characterized, at stationarity, by the presence of a channel (left configuration in the first row from above in Fig. 5.20). If we switch off the externally applied shear the system set in a disordered lamellar array, as should be for the chosen value of activity. We then switch off activity and turn on again the imposed shear. What happens is that during the evolution the system first create a channel of active droplets (right panel in central row of Fig. 5.20), but eventually the spontaneous symmetry breaking described earlier in the chapter, bring the system in a asymmetric configuration (left panel in the central row of Fig.5.20). We now switch on activity starting both from the symmetric and the asymmetric configurations. The lower row of Fig. 5.20 shows the results of this final step. The Symmetric configuration is stabilized by activity, even if at stationarity the asymmetric one should be the final configuration for values of activity and shear rate considered.

6

CONCLUSIONS

In this thesis we have studied numerically different aspects of active fluids. First in Chapter 1 we have reviewed some experimental results concerning the two main features of active fluids we have been mostly interested in: emergence of spontaneous flow and peculiar rheological properties, that do not have a counterpart in ordinary matter.

In Chapter 2 we have analysed the continuos theory on which we rely for the modelisation of such systems. In particular we reviewed De Gennes' theory for Liquid Crystals, and we provided an overview on topological defects. We also introduced the dynamical equations of the theory. As an example of the success of such theories to model the behavior of an active fluids, we considered the phenomenon of spontaneous flow.

The numerical results presented in this thesis have been obtained integrating the evolution equations by means of a lattice Boltzmann approach, to whom is dedicated Capthr 3. After presenting the main features of LB, we also presented some results concerning the comparison between two different LB schemes – namely collision streaming LB and finite difference LB. In this Chapter we have also reported some tests concerning the numerical stability of the code and its scaling properties in parallel environments.

The rest of this dissertation is dedicated to some hot topics in the hydrodynamics of active matter. This is found to experience a certain number of interesting behaviour, ranging from spontaneous flows to negative viscosity. Understanding the Physics beyond the non-equilibrium phenomena driving active systems is key for their implementation in novel technological applications and for the understanding of more fundamental topics in Soft Matter – for instance the hydro-nematic interaction of topological defects. To this aim, in Chapter 4, I investigated the role of chirality in biological fluids. In particular we have analysed the hydrodynamic instabilities of an active chiral nematic droplet with tangential anchoring. We introduced activity as either a collection of dipolar forces or torques. Our simulations show that the interplay between activity and thermodynamic chirality in a $3d$ fluid droplet leads to a strikingly rich phenomenology. In the case of force-dipoles only we found a novel motility mode, whose screw-like propulsion arises as the effect of the non-trivial coupling between thermodynamic chirality and the active flow powdered by deformation of the liquid crystal pattern. For a fluid with active torque dipoles, instead, global rotations with intermittent sense arise when the active torque favours a different twist with respect to that introduced by the

thermodynamic chirality. The resulting defect dynamics strongly resembles the one observed recently in experiments on active nematic shells thus suggesting that chirality may play a fundamental role in the assembling and dynamical behaviour of actual experimental systems.

To characterize motility features of a droplet in a more fundamental way, I presented results coming from a compressible actomyosin system, where a high density droplet (actomyosin blob) emerges due to active contraction only. For sufficiently strong activity, we found the self-assembled droplet swims inside a low density actomyosin background. We thus conclude that motion requires symmetry breaking, which can arise due to fluctuations and hydrodynamic instabilities, in accordance to the kind of system considered. Once symmetry is broken, a positive feedback mechanism is responsible for the motion.

Finally, in Chapter 5 we presented results regarding the morphological and rheological characterization of a active polar emulsion in bidimensional geometries. We considered an emulsion made of an active polar component and a passive isotropic fluid for different preparations of the mixture. Even in this situation we found that weak activity is not capable to alter significantly the dynamics of the system, thus setting into a configuration made of an array of droplets if the mixture is asymmetric, or locally aligned lamellae if symmetric. In both cases we found that ordering arrests at early simulation times with some defects in the arrangements. For moderate values of activity, ordering does not arrest, since activity provides a perpetual source of energy that keep stirring the fluid thus favouring the elimination of defects. For strong activities, the flow develop chaotic features resembling the ones typical of hydrodynamic turbulence.

Having studied the different morphological and flow regimes we then characterized the rheological behaviour. To do so we confined the system between two moving walls. In order to compare external and active forcing in our system, we make use of the Ericksen number Er, proportional to shear, and the active Ericksen number Er_{act} as relevant adimensional quantities.

At small Er_{act}, the system arranges in a lamellar configuration. In this range, at small shear rates, few persistent defects (dislocations) give rise to slight deformations in velocity profiles (dashed-red region in Fig. 5.17). Increasing Er, dislocations are washed out by the flow and the system enters the region of linear velocity profiles (red region in Fig. 5.17). As activity is increased, morphology is characterized by a transition towards asymmetric configurations, with the formation of a thick layer of material close to *one* boundary, thus generating a non-vanishing flux of matter – a behaviour addressed as *unidirectional flow*. By further increasing activity, at high shear rate, phase demixing is more pronounced and this has important consequences on the flow. Active layers form on *both* walls and symmetry is restored. Under these conditions, it may happen that the velocity gradient in the bulk of the system is either everywhere vanishing or, eventually, opposite to the one externally imposed (*negative viscosity*), despite such states are found to be unstable in the long term, leading to a situation where the system is characterized by jumps from superfluidic to negative viscosity states. Moreover, we also found that a maximum entropy production principle holds in selecting the most probable state in this intermittent viscosity regime.

Since most of the observed behaviours mainly arise due to the elastic properties of the order parameter, they are expected to stay valid also in nematic systems. This

because the dynamics of polar systems differs from their nematic counterpart mainly for the allowed topological defects. We hope that this study can stimulate the design of new active materials and devices with pioneering applications.

PUBLICATIONS LIST

The material presented in Chapters 3-5 is based on the following publications:

- [1]G. Negro, A. Lamura, G. Gonnella and D. Marenduzzo, *Hydrodynamics of contraction-based motility in a compressible active fluid*, EPL (2019) 127(5) : 58001, https://iopscience.iop.org/article/10.1209/0295-5075/127/58001/meta
- [2]G. Negro, L. N. Carenza, A. Lamura, A. Tiribocchi and G. Gonnella, *Rheology of active polar emulsions: from linear to unidirectional and inviscid flow, and intermittent viscosity*, Soft Matter (2019) ,15, 8251-8265, https://pubs.rsc.org/en/content/articlelanding/2019/sm/c9sm01288e/unauth#!divAbstract
- [3]G. Negro, L.N. Carenza, P. Digregorio, G. Gonnella, A. Lamura, *Morphology and flow patterns in highly asymmetric active emulsions*, Physica A: Statistical Mechanics and its Applications (2018), 503, 464-475, https://www.sciencedirect.com/science/article/pii/S0378437118303194
- [4]G. Negro, S. Busuioc, V. E. Ambrus, G. Gonnella, A. Lamura and V. Sofonea, *Comparison between isothermal collision-streaming and finite-difference lattice Boltzmann models*, International journal of Modern Physics C (2019), 30(10), 1941005, https://www.worldscientific.com/doi/abs/10.1142/S0129183119410055
- [5]L.N. Carenza, G. Gonnella, D. Marenduzzo, and G. Negro, *Rotation and propulsion in 3D active chiral droplets*, PNAS (2019), 116(44), 22065-2207, https://www.pnas.org/content/116/44/22065/tab-article-info
- [6]L.N. Carenza, G. Gonnella, A. Lamura, G. Negro, and A.Tiribocchi, *Lattice Boltzmann methods and Active Fluids*, Eur. Phys. J. E (2019) 42 : 81, https://link.springer.com/article/10.1140/epje/i2019-11843-6
- [7]L.N. Carenza, G. Gonnella, A. Lamura and G. Negro, *Dynamically asymmetric and bicontinuous morphologies in active emulsions*, International journal of Modern Physics C (2019), 30(10), 1941002, https://www.worldscientific.com/doi/10.1142/S012918311941002X

Proceedings

- [8] G Negro, LN Carenza, P Digregorio, G Gonnella, A Lamura, *n silico characterization of asymmetric active polar emulsions*, AIP Conference Proceedings 2019, 2071, 020012, https://aip.scitation.org/doi/abs/10.1063/1.5090059

Physica A 503 (2018) 464–475

Contents lists available at ScienceDirect

Physica A

journal homepage: www.elsevier.com/locate/physa

Morphology and flow patterns in highly asymmetric active emulsions

G. Negro [a,*], L.N. Carenza [a], P. Digregorio [a], G. Gonnella [a], A. Lamura [b]

[a] Dipartimento di Fisica, Università degli studi di Bari and INFN, Sezione di Bari, Via Amendola 173, 70126 Bari, Italy
[b] Istituto Applicazioni Calcolo, CNR, Via Amendola 122/D, 70126 Bari, Italy

HIGHLIGHTS

- The morphology and the dynamics of an emulsion made of a polar active gel and an isotropic passive fluid is studied.
- We focus on the case of a highly off-symmetric ratio between the active and passive components.
- In absence of activity the stationary state is characterized by an hexaticaly ordered array of droplets.
- Small amount of activity favors the elimination of defects in the array of droplets.
- Rising activity new and interesting morphologies arises depending on whether the system is contractile or extensile.

ARTICLE INFO

Article history:
Received 4 November 2017
Received in revised form 16 February 2018
Available online 9 March 2018

ABSTRACT

We investigate numerically, by a hybrid lattice Boltzmann method, the morphology and the dynamics of an emulsion made of a polar active gel, contractile or extensile, and an isotropic passive fluid. We focus on the case of a highly off-symmetric ratio between the active and passive components. In absence of any activity we observe an hexatic-ordered droplets phase, with some defects in the layout. We study how the morphology of the system is affected by activity both in the contractile and extensile case. In the extensile case a small amount of activity favors the elimination of defects in the array of droplets, while at higher activities, first aster-like rotating droplets appear, and then a disordered pattern occurs. In the contractile case, at sufficiently high values of activity, elongated structures are formed. Energy and enstrophy behavior mark the transitions between the different regimes.

1. Introduction

The capability of different systems of using energy taken from their environment to go out of thermal equilibrium, gives rise to a wealth of behaviors [1]. They range from swarming, self-assembly, spontaneous flows to other collective properties [2–5]. This boosted a deep interest in addressing their study in order to look for possible new physics, explore common features between different systems, and develop new strategies in designing synthetic devices and materials with smart properties.

Self-propelled objects represent a remarkable example of active matter. Starting from the seminal model of Vicsek [6] for swarms, it was later realized that common features can be traced in several systems at different scales promoting the introduction of statistical models able to describe such behaviors [7–10]. Another example of active matter, sharing

* Corresponding author.
E-mail addresses: giuseppe.negro@ba.infn.it (G. Negro), l.carenza@studenti.uniba.it (L.N. Carenza), pasquale.digregorio@ba.infn.it (P. Digregorio), g.gonnella@ba.infn.it (G. Gonnella), a.lamura@ba.iac.cnr.it (A. Lamura).

https://doi.org/10.1016/j.physa.2018.03.011
0378-4371/

Rotation and propulsion in 3D active chiral droplets

Livio Nicola Carenza[a,1], Giuseppe Gonnella[a], Davide Marenduzzo[b], and Giuseppe Negro[a]

[a]Dipartimento di Fisica, Università degli Studi di Bari and Istituto Nazioneale di Fisica Nucleare, Sezione di Bari, Bari I-70126, Italy; and [b]Scottish Universities Physics Alliance, School of Physics and Astronomy, University of Edinburgh, Edinburgh EH9 3JZ, United Kingdom

Edited by Gareth P. Alexander, University of Warwick, Coventry, United Kingdom, and accepted by Editorial Board Member John D. Weeks September 20, 2019 (received for review June 25, 2019)

Chirality is a recurrent theme in the study of biological systems, in which active processes are driven by the internal conversion of chemical energy into work. Bacterial flagella, actomyosin filaments, and microtubule bundles are active systems that are also intrinsically chiral. Despite some exploratory attempt to capture the relations between chirality and motility, many features of intrinsically chiral systems still need to be explored and explained. To address this gap in knowledge, here we study the effects of internal active forces and torques on a 3-dimensional (3D) droplet of cholesteric liquid crystal (CLC) embedded in an isotropic liquid. We consider tangential anchoring of the liquid crystal director at the droplet surface. Contrary to what happens in nematics, where moderate extensile activity leads to droplet rotation, cholesteric active droplets exhibit more complex and variegated behaviors. We find that extensile force dipole activity stabilizes complex defect configurations, in which orbiting dynamics couples to thermodynamic chirality to propel screw-like droplet motion. Instead, dipolar torque activity may either tighten or unwind the cholesteric helix and if tuned, can power rotations with an oscillatory angular velocity of 0 mean.

active fluids | liquid crystals | chirality | cell motility

Chirality is a generic feature of most biological matter (1–3). A right–left asymmetry may arise at either the microscopic or macroscopic level and be due to thermodynamic (passive) or nonequilibrium (active) effects. For instance, a microtubule–motor mixture breaks chiral symmetry in 2 ways. First, microtubules are intrinsically helical (4). Second, kinesin or dynein motors exploit adenosine triphosphate hydrolysis to twist their long chains and apply a nonequilibrium active torque on the fibers they walk along (5). Similarly, bacteria, such as *Escherichia coli*, but also, sperm cells are equipped with long helical flagella. Motor proteins anchored to the cellular membrane generate torques to impart rotational motion on the flagella, the helix of which generates a flow in the viscous environment, leading to cell propulsion (6, 7).

Biological fluids are active, as they are internally driven by the constant injection of energy, which prevents them from relaxing toward any thermodynamic steady state (8). A simple and successful theory to model an active fluid is to approximate each of its microscopic constituents (e.g., a microtubule or a single bacterium) as an entity that exerts a dipolar force on the environment (9). The dipole direction introduces orientational order resembling that of liquid crystals (LCs). The resulting active nematic has been found, both experimentally and numerically, to develop unexpected and striking behaviors, such as spontaneous flow, active turbulence, and superfluidic states (10, 11). Much effort has been spent in the last decades to capture the essential dynamics of active fluids, ranging from multiparticle models to continuum theories (12–14). The theory has been able to capture experimentally observed features, like turbulent-like patterns in 2-dimensional bacterial films (15) or spatiotemporal pattern formation and topological defect dynamics in active emulsions containing microtubule–kinesin mixtures (16).

Understanding the outcome of the interplay between chirality and activity is an important and timely question. In stark contrast with the case of achiral active nematics, which has commanded a lot of attention in recent years, much less is known about the dynamics of chiral active systems (17–19). Previous work has mainly focused on cases where chirality only enters the system because of activity in the form of a nonequilibrium torque dipole (17, 18). Instead, we consider here a system that is inherently chiral and apolar and therefore, can be modeled—in the passive phase—as a cholesteric liquid crystal (CLC) (20, 21). Specifically, here we study a 3-dimensional ($3D$) active CLC droplet with tangential orientation of the director at its surface. In this setup, an active nematic droplet can only sustain uniform rotational motion driven by bend deformations localized around the equatorial circle of the droplet (Fig. 1). Instead, an intrinsically chiral droplet displays a much richer dynamical behavior. First, we find that a force dipole activity enables a motility mode where the rotational motion of the surface defects is converted into propulsion. This mechanism requires chirality to reconfigure the pattern of surface defects. It is not possible in a nematic, where the symmetry in defect position prevents any translational motion. Second, a torque dipole activity sets up a sustained mirror rotation of 2 pairs of disclinations, which periodically adsorb onto and depin from the droplet surface. Again, no such state can be found in an originally nematic system. We also characterize how the active flow and orientation patterns evolve as the ratio between the droplet size and pitch increases.

The ordering properties within the CLC droplet are described, in the uniaxial limit, by the nematic tensor $\mathbf{Q} = S(\mathbf{nn} - \mathbf{I}/3)$, where the director field $\mathbf{n}$ is a unit headless vector describing the local average orientation of the components and S is a scalar field expressing the degree of order. The equilibrium

Significance

Chirality plays an important role in many biological systems. Biomolecules, such as DNA, actin, or microtubules, form helical structures, which at sufficiently high density and in the absence of active forces, tend to self-assemble into twisted cholesteric phases. We study the effect of activity on a droplet of chiral matter, finding a surprisingly rich range of dynamical behaviors ranging from spontaneous rotations to screw-like motion. The phenomena that we uncover require both thermodynamic chirality and activity and are linked to the nontrivial topology of the defects that form by necessity at the droplet surface. It would be of interest to look for analogues of the motility modes found here in chiral microorganisms occurring in nature or in synthetic active matter.

Author contributions: L.N.C., G.G., D.M., and G.N. designed research, performed research, analyzed data, and wrote the paper.

The authors declare no competing interest.

This article is a PNAS Direct Submission. G.P.A. is a guest editor invited by the Editorial Board.

[1]To whom correspondence may be addressed. Email: livio.carenza@ba.infn.it.

This article contains supporting information online at www.pnas.org/lookup/suppl/doi:10.1073/pnas.1910909116/-/DCSupplemental.

First published October 14, 2019.

Eur. Phys. J. E (2019) **42**: 81
DOI 10.1140/epje/i2019-11843-6

THE EUROPEAN PHYSICAL JOURNAL E

Topical Review

Lattice Boltzmann methods and active fluids

Livio Nicola Carenza[1], Giuseppe Gonnella[1,a], Antonio Lamura[2], Giuseppe Negro[1], and Adriano Tiribocchi[3]

[1] Dipartimento di Fisica, Università degli Studi di Bari, and INFN Sezione di Bari, Via Amendola 173, Bari 70126, Italy
[2] Istituto Applicazioni Calcolo, CNR, Via Amendola 122/D, 70126 Bari, Italy
[3] Center for Life Nano Science@La Sapienza, Istituto Italiano di Tecnologia, 00161 Roma, Italy

Received 28 January 2019 and Received in final form 23 May 2019
Published online: 28 June 2019

Abstract. We review the state of the art of active fluids with particular attention to hydrodynamic continuous models and to the use of Lattice Boltzmann Methods (LBM) in this field. We present the thermodynamics of active fluids, in terms of liquid crystals modelling adapted to describe large-scale organization of active systems, as well as other effective phenomenological models. We discuss how LBM can be implemented to solve the hydrodynamics of active matter, starting from the case of a simple fluid, for which we explicitly recover the continuous equations by means of Chapman-Enskog expansion. Going beyond this simple case, we summarize how LBM can be used to treat complex and active fluids. We then review recent developments concerning some relevant topics in active matter that have been studied by means of LBM: spontaneous flow, self-propelled droplets, active emulsions, rheology, active turbulence, and active colloids.

1 Introduction

The goal of this paper is to describe the use of the lattice Boltzmann methods in the study of large-scale properties of active fluids [1–7], also showing the recent progress in few relevant topics. Active fluids are living matter or biologically inspired systems with the common characteristic of being composed by self-propelled (or active) units that burn stored or ambient energy and turn it into work giving rise, eventually, to systematic movement. An example in nature is given by the cell cytoskeleton or, in laboratory, by synthetic suspensions of cell extracts with molecular motors (*e.g.*, myosin or kinesin) [8, 9]. Molecular motors exert forces on cytoskeletal filaments (actin filaments and microtubules) [10] and trigger their motion in the surrounding fluid. These forces, exchanged through transient and motile contact points between filaments and motor proteins, result from the conversion of chemical energy, typically coming from ATP hydrolysis, into mechanical work.

Active systems show many interesting physical properties, of general character, related to their collective behavior, remarkable especially when compared with their analogue in passive or equilibrium systems. Pattern formation is an example. A disordered array of microtubules may arrange into spiral or aster configurations when the concentration of motor proteins like kinesin is sufficiently high [8]. Suspensions of bacteria, despite their low Reynolds numbers, can exhibit turbulent flow patterns [11, 12], characterized by traveling *jets* of high collective velocities and surrounding *vortices*. Active fluids can be classified according to their swimming mechanism as extensile or contractile, if they respectively push or pull the surrounding fluid. This difference marks all the phenomenology of active fluids and, in particular, has important effects on the rheological properties. Activity is either capable to develop shear-thickening properties in contractile systems [13–17], or to induce a *superfluidic* regime under suitable conditions in extensile suspensions [18–20]. Simulations of extensile active emulsions under constant shear have shown the occurrence of velocity profiles (for the component of velocity in the direction of the applied flow) with inverted gradient (*negative viscosity*) and also jumps in the sign of apparent viscosity [18–20].

Other striking properties have emerged in the study of fluctuation statistics [21–26] and of order-disorder phase transitions [6, 27, 28]. Fluctuations and phase transitions have been mainly analyzed in the context of agent-based models. The flocking transition [29], for instance, was the first one to be studied in a model of point-like particles moving at fixed speed and with aligning interaction [30]. Activity alone actually favors aggregation and can induce a phase transition, often called Motility-Induced Phase Separation (MIPS) [31]. This has been numerically studied by using simple models of active colloids with excluded volume interactions and various shapes [32–39]. The particle description has been also largely used in other contexts, to simulate, for example, the self-organization of cytoskeleton filaments described as semiflexible filaments [40].

[a] e-mail: Giuseppe.Gonnella@ba.infn.it

International Journal of Modern Physics C
Vol. 30, No. 8 (2019) 1941005 (14 pages)

DOI: 10.1142/S0129183119410055

Comparison between isothermal collision-streaming and finite-difference lattice Boltzmann models

G. Negro

Dipartimento di Fisica,
Università degli Studi di Bari and INFN
Sezione di Bari, via Amendola 173, Bari I-70126, Italy
giuseppe.settimio.negro@gmail.com

S. Busuioc* and V. E. Ambruş†

Department of Physics, West University of Timişoara
Bd. Vasile Pârvan 4, 300223 Timişoara, Romania
**sergiu.busuioc@e-uvt.ro*
†*victor.ambrus@e-uvt.ro*

G. Gonnella

Dipartimento di Fisica, Università degli Studi di Bari and INFN
Sezione di Bari, via Amendola 173, Bari I-70126, Italy
gonnella@ba.infn.it

A. Lamura

Istituto Applicazioni Calcolo, CNR
Via Amendola 122/D, I-70126 Bari, Italy
a.lamura@ba.iac.cnr.it

V. Sofonea

Center for Fundamental and Advanced Technical Research,
Romanian Academy Bd. Mihai Viteazul 24
300223 Timişoara, Romania
sofonea@gmail.com

Received 30 November 2018
Accepted 12 February 2019
Published 11 July 2019

We present here a comparison between collision-streaming and finite-difference lattice Boltzmann (LB) models. This study provides a derivation of useful formulae which help one to properly compare the simulation results obtained with both LB models. We consider three physical problems: the shock wave propagation, the damping of shear waves, and the decay of Taylor–Green vortices, often used as benchmark tests. Despite the different mathematical and computational complexity of the two methods, we show how the physical results can be related to obtain relevant quantities.

Keywords: Lattice Boltzmann models; finite-difference; collision-streaming; viscosity.

PACS Nos.: 47.11.–j, 05.70.Ln, 51.10.+y.

A Letters Journal Exploring the Frontiers of Physics

September 2019

EPL, **127** (2019) 58001
doi: 10.1209/0295-5075/127/58001

www.epljournal.org

Hydrodynamics of contraction-based motility in a compressible active fluid

G. Negro[1], A. Lamura[2], G. Gonnella[1] and D. Marenduzzo[3]

[1] *Dipartimento di Fisica, Universitá degli studi di Bari and INFN, Sezione di Bari - Via Amendola 173, 70126 Bari, Italy*
[2] *Istituto Applicazioni Calcolo, CNR - Via Amendola 122/D, 70126 Bari, Italy*
[3] *SUPA, School of Physics and Astronomy, University of Edinburgh - Peter Guthrie Tait Road, Edinburgh EH9 3FD, UK*

received 6 May 2019; accepted in final form 28 August 2019
published online 9 October 2019

PACS 87.17.Aa – Modeling, computer simulation of cell processes
PACS 87.10.-e – Biological and medical physics: General theory and mathematical aspects
PACS 87.64.Aa – Computer simulation

Abstract – Cell motility is crucial to biological functions ranging from wound healing to immune response. The physics of cell crawling on a substrate is by now well understood, whilst cell motion in bulk (cell swimming) is far from being completely characterized. We present here a minimal model for pattern formation within a compressible actomyosin gel, in both 2D and 3D, which shows that contractility leads to the emergence of an actomyosin droplet within a low density background. This droplet then becomes self-motile for sufficiently large motor contractility. These results may be relevant to understand the essential physics at play in 3D cell swimming within compressible fluids. We report results of both 2D and 3D numerical simulations, and show that the compressibility of actomyosin plays an important role in the transition to motility.

Introduction. – Understanding how cells move around their surroundings is a fascinating question that has gained much attention in the recent past. Answering this question would constitute a substantial step-forward in dissecting the fundamental mechanisms underlying biomedical problems like wound-healing and tissue self-assembly during embryogenesis [1]. Spontaneous movement and deformation are physically driven by the cell cytoskeleton. The cytoskeleton consists of protein filaments and motors which constantly consume chemical energy (ATP) and convert it to work. In particular, actin filaments interact with myosin motors to generate contraction forces in the cell, which can drive cell motion and division [2–7].

Most of the research has focused, both experimentally and theoretically, on cells migration on a two-dimensional substrate (*crawling*) [8–11], mainly because such experimental systems are easily accessible hence this motion is more readily observable. These studies have stimulated the development of theories which now provide a detailed outline of some basic migration mechanisms, including the formation of *lamellipodia* arising from *actin* polymerization at the cell front, adhesion-mediated traction, and *actomyosin* contractility. The crawling motility mode requires actin cytoskeleton to be anchored to the substrate throughout *focal adhesions*, that are clusters of transmembrane proteins binding to the substrate [8].

However some cells, such as breast tumor cells, can also "swim" in a straight line inside a 3D tissue or a polymeric fluid [12]. Unlike cell crawling, in this case there is no solid surface present, and no cellular protrusion reminiscent of a lamellipodium (the cell shape instead remains roughly spherical). The lack of protrusions suggests that actin polymerisation may not be crucial for 3D cell swimming. Indeed, myosin motors contraction is believed to be the sole responsible for cell polarisation and motility [12]: together with some experiments on tumour cells [13], this observation suggests that cell swimming may be primarily driven by myosin activity.

Models of contraction-induced motility have been proposed in refs. [5–7,14]. All these considered the case of an active droplet moving inside a simple (Newtonian) and passive outer fluid. In some cases, the material inside the droplet was an active liquid crystal, in which case the onset of motility required rectifications of orientational splay fluctuations of an order parameter linked to

Soft Matter

PAPER

View Article Online
View Journal | View Issue

Cite this: *Soft Matter*, 2019, **15**, 8251

Rheology of active polar emulsions: from linear to unidirectional and inviscid flow, and intermittent viscosity†

G. Negro,[a] L. N. Carenza, *[a] A. Lamura,[b] A. Tiribocchi [cd] and G. Gonnella[a]

Received 28th June 2019,
Accepted 12th September 2019

DOI: 10.1039/c9sm01288e

rsc.li/soft-matter-journal

The rheological behaviour of an emulsion made of an active polar component and an isotropic passive fluid is studied by lattice Boltzmann methods. Different flow regimes are found by varying the values of the shear rate and extensile activity (occurring, *e.g.*, in microtubule-motor suspensions). By increasing the activity, a first transition occurs from the linear flow regime to spontaneous persistent unidirectional macro-scale flow, followed by another transition either to a (low shear) intermittent flow regime with the coexistence of states with positive, negative, and vanishing apparent viscosity, or to a (high shear) symmetric shear thinning regime. The different behaviours can be explained in terms of the dynamics of the polarization field close to the walls. A maximum entropy production principle selects the most likely states in the intermittent regime.

1 Introduction

Active gels[1–3] are a new class of complex fluids with striking physical properties and many possible innovative applications.[4–8] As other kinds of active systems,[9–17] they are maintained in their driven state – far from thermodynamic equilibrium – by energy supplied directly and independently at the level of individual constituents. Examples are suspensions of biological filaments, such as actomyosin and microtubule bundles, activated with motor proteins[18–21] and bacterial cultures.[22,23] The constituents of these systems have the natural tendency to assemble and align, thus developing structures with typical polar or nematic order. The combination of this property with self-motility capacity is at the origin of a wealth of interesting phenomena, not observable in the absence of activity,[24] including spontaneous flow,[1,25,26] active turbulence at low Reynolds numbers,[22,27,28] and unusual rheological properties.[3,29] Most of these behaviours were found in single component fluids, while mixtures of active and passive components have not been investigated too much so far.[30]

Complex rheological behaviours in active matter depend on the interplay between the external forcing and the circulating flow induced by active agents. For instance, the swimming mechanism of pusher microswimmers, like *E. Coli*, produces a far flow field characterized by quadrupolar symmetry, in which fluid is expelled along the fore–aft axes of the swimmer and drawn transversely, thus leading to *extensile* flow patterns. These enforce the applied flow, in the case of flow-aligning swimmers, causing shear thinning.[31] This may lead to the occurrence of a superfluidic regime with vanishing (apparent) shear viscosity, which was speculated in ref. 32 for the case of active liquid crystals close to the isotropic–nematic transition. Experiments[33,34] and further theories[35] confirmed that extensile active components are able to lower the viscosity of thin film suspensions. An effective inviscid flow was observed in ref. 36 and more recently in ref. 37, when the concentration and activity of *E. Coli* are sufficiently large to support coherent collective swimming. A related feature in extensile gels is the appearance of persistent uni-directional flows in experiments on bacterial suspensions[38] and ATP-driven gels.[39] Recently, numerical simulations in quasi-1d geometries and linear analysis of active polar liquid crystal models have shown the occurrence of vanishing and even negative viscosity states.[40] However, a complete characterization of the rheology of fully 2d active compounds has never been accomplished so far, despite being fundamental to unveil dynamical mechanisms leading to the complex properties presented. We also mention that puller swimmers – exerting a contractile force dipole on the surrounding fluid – still generate a quadrupolar far flow field, but this time the fluid is expelled transversely to their body. This explains the shear thickening behaviour observed in experiments performed on suspensions of *C. reinhardtii*[41] – a species of micro-alga that propels itself by means of two flagella producing contractile

[a] *Dipartimento di Fisica, Università degli Studi di Bari and INFN, Sezione di Bari, via Amendola 173, Bari, I-70126, Italy. E-mail: livio.carenza@ba.infn.it*
[b] *Istituto Applicazioni Calcolo, CNR, Via Amendola 122/D, I-70126 Bari, Italy*
[c] *Center for Life Nano Science@La Sapienza, Istituto Italiano di Tecnologia, 00161 Rome, Italy*
[d] *Istituto per le Applicazioni del Calcolo CNR, via dei Taurini 19, 00185 Rome, Italy*
† Electronic supplementary information (ESI) available. See DOI: 10.1039/c9sm01288e

International Journal of Modern Physics C
Vol. 30, No. 10 (2019) 1941002 (8 pages)

DOI: 10.1142/S012918311941002X

World Scientific
www.worldscientific.com

Dynamically asymmetric and bicontinuous morphologies in active emulsions

Livio Nicola Carenza* and Giuseppe Gonnella†

Dipartimento di Fisica
Università degli Studi di Bari and INFN
Sezione di Bari, via Amendola 173, 70126 Bari, Italy
**livio.carenza@ba.infn.it*
†*giuseppe.gonnella@ba.infn.it*

Antonio Lamura

Istituto Applicazioni Calcolo, CNR
via Amendola 122/D, 70126 Bari, Italy
antonio.lamura@cnr.it

Giuseppe Negro

Dipartimento di Fisica
Università degli Studi di Bari and INFN
Sezione di Bari, via Amendola 173, 70126 Bari, Italy
giuseppe.negro@ba.infn.it

Received 30 November 2018
Accepted 5 February 2019
Published 11 July 2019

The morphology of a mixture made of a polar active gel immersed in an isotropic passive fluid is studied numerically. Lattice Boltzmann method is adopted to solve the Navier–Stokes equation and coupled to a finite-difference scheme used to integrate the dynamic equations of the concentration and of the polarization of the active component. By varying the relative amounts of the mixture phases, different structures can be observed. In the contractile case, at moderate values of activity, elongated structures are formed when the active component is less abundant, while a dynamic emulsion of passive droplets in an active matrix is obtained for symmetric composition. When the active component is extensile, aster-like rotating droplets and a phase-separated pattern appear for asymmetric and symmetric mixtures, respectively. The relevance of space dimensions in the overall morphology is shown by studying the system in three dimensions in the case of extensile asymmetric mixtures where interconnected tube-like structures span the whole system.

Keywords: Polar active gels; emulsions; hybrid lattice Boltzmann method; morphological patterns.

PACS Nos.: 81.05.–t, 83.80.Hj, 82.70.Kj, 87.85.J–, 83.80.Xz.

*Corresponding author.

In Silico Characterization of Asymmetric Active Polar Emulsions

G. Negro[1,a)], L.N. Carenza[1,b)], P. Digregorio[1,c)], G. Gonnella[1,d)] and A. Lamura[2,e)]

[1]*Dipartimento di Fisica, Università degli studi di Bari and INFN, Sezione di Bari, Via Amendola 173, 70126 Bari, Italy.*
[2]*Istituto Applicazioni Calcolo, CNR, Via Amendola 122/D, 70126 Bari, Italy.*

[a)]Corresponding author: giuseppe.settimio.negro@gmail.com
[b)]livio.carenza@uniba.it
[c)]pasquale.digregorio@ba.infn.it
[d)]g.gonnella@ba.infn.it
[e)]a.lamura@iba.ac.cnr.it

Abstract. In this paper an in silico study of the behavior of an active polar emulsion is reported, focusing on the case of a highly off-symmetric ratio between the polar (active) and passive components, both for the extensile and contractile case. In absence of activity the system is characterized by an hexatic-ordered droplets phase. We find that small extensile activity is able to enhance the hexatic order in the array of droplets with respect to the passive case, while increasing activity aster-like rotating droplets appear. In contractile systems activity creates shear flows and elongated structures are formed.

INTRODUCTION

Active matter is a class of materials whose constituents are able to consume energy to move or to exercise stresses locally [1]. Research in this field has been mainly focused on single-component active systems and to a lesser extent on the behavior of solutions of active and passive components. Binary fluids with an active component have been considered in [2, 3] and very recently [4] a model has been introduced, where emulsification of the active component is favored by the presence of surfactant added to the mixture. This model generalizes the active gel theory to describe the behavior of a mixture of isotropic passive and polar active fluids, and, by numerical simulations, it was shown that activity strongly affects the behavior of the mixture, leading to a variety of morphologies whose formation strongly depends on the intensity and the kind of active doping. Indeed, polar active fluids are said to be either extensile (*e.g.* bacterial colonies and microtubules bundles) or contractile (*e.g.* actine and myosin filaments) according to the nature of the stress exerted by the active component on its neighborhood. Introducing a parameter that represents the strength of the active stress acting in the system (see Section MODEL AND METHODS), intensity of active doping can be tuned. This corresponds experimentally to keeping under control the amount of ATP in active gels of bundled microtubles [5] or the amount of oxygen available, the concentration of ingredients, or the temperature in bacterial suspensions.

In this work we complement previous analysis by considering a highly off-symmetric mixture with a 10 : 90 ratio between the active and passive components, both for extensile and contractile systems. In this case the equilibrium state of the system is characterized by an ordered array of droplets of the minority phase positioned at the vertices of a triangular lattice. We will show that, in spite of the strong unbalance between the two components, activity greatly affects the morphology of the system, leading to the development of a wide range of patterns both for the concentration and the velocity field. A small amount of extensile activity favors the elimination of defects in the system, as shown by measuring the number of defects in Voronoi tessellation. Increasing activity, isolated droplets tend to merge forming big rotating droplets with an aster-like shape. In the contractile case activity promotes the rupture of the hexagonal phase and the appearance of a matrix of the active component in the passive flowing background, differently from what happens in the symmetric case[4].

TIM 18 Physics Conference
AIP Conf. Proc. 2071, 020012-1–020012-8; https://doi.org/10.1063/1.5090059
Published by AIP Publishing. 978-0-7354-1799-1/$30.00

BIBLIOGRAPHY

[1] R. Adhikari, K. Stratford, M.E. Cates, and A.J. Wagner. Fluctuating lattice Boltzmann. *EPL*, 71(3):473–479, 2005. doi: 10.1209/epl/i2004-10542-5. URL https://doi.org/10.1209%2Fepl%2Fi2004-10542-5.

[2] K.I. Agladze, V.I. Krinsky, and A.M. Pertsov. Chaos in the non-stirred Belousov–Zhabotinsky reaction is induced by interaction of waves and stationary dissipative structures. *Nature*, 308:834, 1984.

[3] F.J. Alexander, H. Chen, S. Chen, and G.D. Doolen. Lattice Boltzmann model for compressible fluids. *Phys. Rev. A*, 46:1967–1970, 1992. doi: 10.1103/PhysRevA.46.1967. URL https://link.aps.org/doi/10.1103/PhysRevA.46.1967.

[4] M.G. Ancona. Fully-Lagrangian and Lattice-Boltzmann Methods for Solving Systems of Conservation Equations. *J. Comput. Phys.*, 115(1):107 – 120, 1994. ISSN 0021-9991. doi: https://doi.org/10.1006/jcph.1994.1181. URL http://www.sciencedirect.com/science/article/pii/S0021999184711818.

[5] Ichiro AOKI. A simulation study on the schooling mechanism in fish. *NIPPON SUISAN GAKKAISHI*, 48(8):1081–1088, 1982. doi: 10.2331/suisan.48.1081.

[6] A.D. Bates, S.B.S.A.D. Bates, A. Maxwell, and H.D.B.C.A. Maxwell. *DNA Topology*. Oxford bioscience. Oxford University Press, 2005. ISBN 9780198567097. URL https://books.google.it/books?id=WGBAGyzvQOUC.

[7] R. Benzi, S. Succi, and M. Vergassola. The lattice Boltzmann equation: theory and applications. *Phys. Rep.*, 222(3):145 – 197, 1992. ISSN 0370-1573. doi: https://doi.org/10.1016/0370-1573(92)90090-M. URL http://www.sciencedirect.com/science/article/pii/037015739290090M.

[8] A.N. Beris and B.J. Edwards. *Thermodynamics of Flowing Systems*. Oxford Engineering Science Series. Oxford University Press, 1994. ISBN 9780195344882. URL https://books.google.it/books?id=dqxFUy7_vhsC.

[9] P.L. Bhatnagar, E.P. Gross, and M. Krook. A Model for Collision Processes in Gases. I. Small Amplitude Processes in Charged and Neutral One-Component Systems. *Phys. Rev.*, 94:511–525, 1954. doi: 10.1103/PhysRev.94.511. URL https://link.aps.org/doi/10.1103/PhysRev.94.511.

[10] M.L Blow, S.P. Thampi, and J.M. Yeomans. Biphasic, Lyotropic, Active Nematics. *Phys. Rev. Lett.*, 113:248303, 2014.

[11] F. Bonelli, L.N. Carenza, G. Gonnella, D. Marenduzzo, E. Orlandini, and A. Tiribocchi. Lamellar ordering, droplet formation and phase inversion in exotic active emulsions. *Sci. Rep.*, 9:2801, 2019. doi: 10.1038/s41598-019-39190-6.

[12] F. Bonelli, L.N. Carenza, G. Gonnella, D. Marenduzzo, E. Orlandini, and A. Tiribocchi. Lamellar ordering, droplet formation and phase inversion in exotic active emulsions. *Sci. Rep.*, 9, 2019. doi: 10.1038/s41598-019-39190-6.

[13] Giovanni B. Brandani and Shoji Takada. Chromatin remodelers couple inchworm motion with twist-defect formation to slide nucleosomal dna. *PLOS Computational Biology*, 14(11):1–25, 11 2018. doi: 10.1371/journal.pcbi.1006512. URL https://doi.org/10.1371/journal.pcbi.1006512.

[14] A.J. Bray. Theory of phase ordering kinetics. *Physica A: Statistical Mechanics and its Applications*, 194(1):41 – 52, 1993. ISSN 0378-4371. doi: https://doi.org/10.1016/0378-4371(93)90338-5. URL http://www.sciencedirect.com/science/article/pii/0378437193903385.

[15] A.J. Bray. Theory of phase-ordering kinetics. *Advances in Physics*, 43(3):357–459, 1994. doi: 10.1080/00018739400101505. URL https://doi.org/10.1080/00018739400101505.

[16] D. Bray. *Cell Movements: From Molecules to Motility, 2nd Edition*. Garland Publishing, 2000.

[17] Robijn Bruinsma, Alexander Y. Grosberg, Yitzhak Rabin, and Alexandra Zidovska. Chromatin hydrodynamics. *Biophysical Journal*, 106(9):1871 – 1881, 2014. ISSN 0006-3495. doi: https://doi.org/10.1016/j.bpj.2014.03.038. URL http://www.sciencedirect.com/science/article/pii/S0006349514003403.

[18] J. Buhl, D. J. T. Sumpter, I. D. Couzin, J. J. Hale, E. Despland, E. R. Miller, and S. J. Simpson. From disorder to order in marching locusts. *Science*, 312(5778):1402–1406, 2006. ISSN 0036-8075. doi: 10.1126/science.1125142. URL https://science.sciencemag.org/content/312/5778/1402.

[19] J.M. Buick and C.A. Greated. Gravity in a lattice Boltzmann model. *Phys. Rev. E*, 61:5307–5320, 2000. doi: 10.1103/PhysRevE.61.5307. URL https://link.aps.org/doi/10.1103/PhysRevE.61.5307.

[20] S. Busuioc, V.E. Ambruş, T. Biciuşcă, and V. Sofonea. Two-dimensional off-lattice Boltzmann model for van der Waals fluids with variable temperature. *Computers & Mathematics with Applications*, 2019 *(accepted for publication)*.

[21] A.C. Callan-Jones, R.A. Pelcovits, V.A. Slavin, S. Zhang, D.H. Laidlaw, and G.B. Loriot. Simulation and visualization of topological defects in nematic liquid crystals. *Phys. Rev. E*, 74:061701, 2006. doi: 10.1103/PhysRevE.74.061701. URL https://link.aps.org/doi/10.1103/PhysRevE.74.061701.

[22] N. Cao, S. Chen, S. Jin, and D. Martínez. Physical symmetry and lattice symmetry in the lattice Boltzmann method. *Phys. Rev. E*, 55:R21–R24, 1997. doi: 10.1103/PhysRevE.55.R21.

[23] Livio Nicola Carenza, Giuseppe Gonnella, Antonio Lamura, Giuseppe Negro, and Adriano Tiribocchi. Lattice boltzmann methods and active fluids. *The European Physical Journal E*, 42(6):81, Jun 2019. ISSN 1292-895X. doi: 10.1140/epje/i2019-11843-6. URL https://doi.org/10.1140/epje/i2019-11843-6.

[24] L.N. Carenza, G. Gonnella, A. Lamura, and G. Negro. Dynamically asymmetric and bicontinuous morphologies in active emulsions. *Int. J. Mod. Phys. C*, 0(0): 1941002, 2019. doi: 10.1142/S012918311941002X. URL https://doi.org/10.1142/S012918311941002X.

[25] M. E. Cates, D. Marenduzzo, I. Pagonabarraga, and J. Tailleur. Arrested phase separation in reproducing bacteria creates a generic route to pattern formation. *Proceedings of the National Academy of Sciences*, 107(26):11715–11720, 2010. ISSN 0027-8424. doi: 10.1073/pnas.1001994107. URL https://www.pnas.org/content/107/26/11715.

[26] M.E. Cates and J. Tailleur. Motility-Induced Phase Separation. *Annu. Rev. Condens. Matter Phys.*, 6:219–244, 2015. doi: 10.1146/annurev-conmatphys-031214-014710.

[27] M.E. Cates, S.M. Fielding, D. Marenduzzo, E. Orlandini, and J.M. Yeomans. Shearing Active Gels Close to the Isotropic-Nematic Transition. *Phys. Rev. Lett.*, 101: 068102, 2008. doi: 10.1103/physrevlett.101.068102.

[28] M.E. Cates, O. Henrich, D. Marenduzzo, and K. Stratford. Lattice Boltzmann simulations of liquid crystalline fluids: active gels and blue phases. *Soft Matter*, 5: 3791–3800, 2009. doi: 10.1039/B908659P. URL http://dx.doi.org/10.1039/B908659P.

[29] P.M. Chaikin and T.C. Lubensky. *Principles of condensed matter physics*, volume 10.1017/CBO9780511813467. Cambridge University Press, 1995. ISBN 9780511813467. doi: 10.1017/CBO9780511813467.

[30] H. Chen, S. Chen, and W.H. Matthaeus. Recovery of the Navier-Stokes equations using a lattice-gas Boltzmann method. *Phys. Rev. A*, 45:R5339–R5342, 1992. doi: 10.1103/PhysRevA.45.R5339. URL https://link.aps.org/doi/10.1103/PhysRevA.45.R5339.

[31] H. Chen, I. Goldhirsch, and S.A. Orszag. Discrete Rotational Symmetry, Moment Isotropy, and Higher Order Lattice Boltzmann Models. *J. Sci. Comput.*, 34(1):87–112, 2008. ISSN 1573-7691. doi: 10.1007/s10915-007-9159-3. URL https://doi.org/10.1007/s10915-007-9159-3.

[32] B. Chopard and M. Droz. *Cellular Automata Modeling of Physical Systems*. Collection Alea-Saclay: Monographs and Texts in Statistical Physics. Cambridge University Press, 1998. doi: 10.1017/CBO9780511549755.

[33] A. Coclite, G. Gonnella, and A. Lamura. Pattern formation in liquid-vapor systems under periodic potential and shear. *Phys. Rev. E*, 89:063303, Jun 2014. doi: 10.1103/PhysRevE.89.063303. URL https://link.aps.org/doi/10.1103/PhysRevE.89.063303.

[34] A. Coclite, G. Gonnella, and A. Lamura. Pattern formation in liquid-vapor systems under periodic potential and shear. *Phys. Rev. E*, 89:063303, 2014. doi: 10.1103/PhysRevE.89.063303. URL https://link.aps.org/doi/10.1103/PhysRevE.89.063303.

[35] IAIN D. COUZIN, JENS KRAUSE, RICHARD JAMES, GRAEME D. RUXTON, and NIGEL R. FRANKS. Collective memory and spatial sorting in animal groups. *Journal of Theoretical Biology*, 218(1):1 – 11, 2002. ISSN 0022-5193. doi: https://doi.org/10.1006/jtbi.2002.3065. URL http://www.sciencedirect.com/science/article/pii/S0022519302930651.

[36] A. Cristea, G. Gonnella, A. Lamura, and V. Sofonea. A Lattice Boltzmann Study of Phase Separation in Liquid-Vapor Systems. *Commun. Comput. Phys.*, 7:350–361, 2010.

[37] L.F. Cugliandolo, G. Gonnella, and A. Suma. Rotational and translational diffusion in an interacting active dumbbell system. *Phys. Rev. E*, 91:062124, 2015. doi: 10.1103/PhysRevE.91.062124. URL https://link.aps.org/doi/10.1103/PhysRevE.91.062124.

[38] A. Czirók, Albert László Barabási, and T. Vicsek. Collective motion of self-propelled particles: Kinetic phase transition in one dimension. *Physical Review Letters*, 82(1):209–212, 1999. ISSN 0031-9007.

[39] P.G. de Gennes and J. Prost. *The physics of liquid crystals*. The International series of monographs on physics 83 Oxford science publications. Oxford University Press, 2nd ed edition, 1993. ISBN 0198520247,9780198520245. URL http://gen.lib.rus.ec/book/index.php?md5=F14F1C80040ED8BD61D087047E631765.

[40] S.R. de Groot and P. Mazur. *Non-Equilibrium Thermodynamics*. North-Holland and Publishing Company, 1962.

[41] G. De Magistris, A. Tiribocchi, C. A. Whitfield, R. J. Hawkins, M. E. Cates, and D. Marenduzzo. Spontaneous motility of passive emulsion droplets in polar active gels. *Soft Matter*, 10:7826–7837, 2014. doi: 10.1039/C4SM00937A. URL http://dx.doi.org/10.1039/C4SM00937A.

[42] S.J. DeCamp, G.S. Redner, A. Baskaran, M.F. Hagan, and Z. Dogic. Orientational order of motile defects in active nematics. *Nat. Mater.*, 14:11110, 2015.

[43] D. Dell'Arciprete, M.L. Blow, A.T. Brown, F. Farrell, J.S. Lintuvuori, A.F. McVey, D. Marenduzzo, and W.C. Poon. A growing bacterial colony in two dimensions as an active nematic. *Nat. Comm.*, 9:4190, 2018.

[44] C. Denniston, E. Orlandini, and J.M. Yeomans. Lattice Boltzmann simulations of liquid crystal hydrodynamics. *Phys. Rev. E*, 63:056702, 2001. doi: 10.1103/PhysRevE.63.056702. URL https://link.aps.org/doi/10.1103/PhysRevE.63.056702.

[45] R.H. Depue and R.V. Rice. F-actin is a right-handed helix. *J. Mol. Biol.*, 12:302, 1965.

[46] R.C. Dewar, C.H. Lineweaver, R.K. Niven, and K. Regenauer-Lieb. *Beyond the Second Law: Entropy Production and Non-equilibrium Systems*. Understanding Complex Systems. Springer Berlin Heidelberg, 2013. ISBN 9783642401541. URL https://books.google.it/books?id=xF65BQAAQBAJ.

[47] C. Dombrowski, L. Cisneros, S. Chatkaew, R.E. Goldstein, and J.O. Kessler. Self-Concentration and Large-Scale Coherence in Bacterial Dynamics. *Phys. Rev. Lett.*, 93:098103, 2004. doi: 10.1103/PhysRevLett.93.098103.

[48] A. Doostmohammadi, J. Ignés-Mullol, J.M. Yeomans, and F. Sagués. Active nematics. *Nat. Commun.*, 9:3246, 2018.

[49] G. Duclos, S. Garcia, H.G. Yevick, and P. Silberzan. Perfect nematic order in confined monolayers of spindle-shaped cells. *Soft Matter*, 10:2346, 2014. doi: 10.1039/C3SM52323C. URL http://dx.doi.org/10.1039/C3SM52323C.

[50] J. Dunkel, S. Heidenreich, K. Drescher, H. H. Wensink, M. Bär, and Raymond E. Goldstein. Fluid Dynamics of Bacterial Turbulence. *Phys. Rev. Lett.*, 110:228102, 2013. doi: 10.1103/PhysRevLett.110.228102. URL https://link.aps.org/doi/10.1103/PhysRevLett.110.228102.

[51] S.A. Edwards and J.M. Yeomans. Spontaneous flow states in active nematics: A unified picture. *EPL*, 85(1):18008, 2009. URL http://stacks.iop.org/0295-5075/85/i=1/a=18008.

[52] Murray Eisenberg and Robert Guy. A proof of the hairy ball theorem. *The American Mathematical Monthly*, 86(7):571–574, 1979. ISSN 00029890, 19300972. URL http://www.jstor.org/stable/2320587.

[53] J. Elgeti, M.E. Cates, and D. Marenduzzo. Defect hydrodynamics in 2D polar active fluids. *Soft Matter*, 7:3177–3185, 2011. doi: 10.1039/C0SM01097A. URL http://dx.doi.org/10.1039/C0SM01097A.

[54] R.G. Endres. Entropy production selects nonequilibrium states in multistable systems. *Scientific Reports*, 7(6):14437, 2017. URL https://doi.org/10.1038/s41598-017-14485-8.

[55] Martin Ester, Hans-Peter Kriegel, Jörg Sander, and Xiaowei Xu. A density-based algorithm for discovering clusters in large spatial databases with noise. pages 226–231. AAAI Press, 1996.

[56] G.A. Evans, J.M. Blackledge, and P.D. Yardley. *Finite Differences and Parabolic Equations*, pages 29–65. Springer London, London, 2000. ISBN 978-1-4471-0377-6. doi: 10.1007/978-1-4471-0377-6_2. URL https://doi.org/10.1007/978-1-4471-0377-6_2.

[57] F. Fadda, G. Gonnella, A. Lamura, and A. Tiribocchi. Lattice boltzmann study of chemically-driven self-propelled droplets. *Eur. Phys. J. E*, 40(12):112, 2017. ISSN 1292-895X. doi: 10.1140/epje/i2017-11603-8. URL https://doi.org/10.1140/epje/i2017-11603-8.

[58] S. M. Fielding and P. D. Olmsted. Spatiotemporal Oscillations and Rheochaos in a Simple Model of Shear Banding. *Phys. Rev. Lett.*, 92:084502, 2004. doi: 10.1103/PhysRevLett.92.084502. URL https://link.aps.org/doi/10.1103/PhysRevLett.92.084502.

[59] G. Foffano, J.S. Lintuvuori, A.N. Morozov, K. Stratford, M.E. Cates, and D. Marenduzzo. Bulk rheology and microrheology of active fluids. *Eur. Phys. J. E*, 35:98, 2012. doi: 10.1140/epje/i2012-12098-5.

[60] U. Frisch, B. Hasslacher, and Y. Pomeau. Lattice-Gas Automata for the Navier-Stokes Equation. *Phys. Rev. Lett.*, 56:1505–1508, 1986. doi: 10.1103/PhysRevLett.56.1505. URL https://link.aps.org/doi/10.1103/PhysRevLett.56.1505.

[61] S. Fürthauer, M. Strempel, S.W. Grill, and F. Jülicher. Active chiral fluids. *Eur. Phys. J. E*, 35(9):89, 2012. ISSN 1292-895X. doi: 10.1140/epje/i2012-12089-6. URL https://doi.org/10.1140/epje/i2012-12089-6.

[62] J. Gachelin, G. Mi no, H. Berthet, A. Lindner, A. Rousselet, and E. Clément. Non-Newtonian Viscosity of Escherichia coli Suspensions. *Phys. Rev. Lett.*, 110:268103, 2013. doi: 10.1103/PhysRevLett.110.268103. URL https://link.aps.org/doi/10.1103/PhysRevLett.110.268103.

[63] Y. Gan, A. Xu, G. Zhang, and Y. Li. Lattice Boltzmann study on Kelvin-Helmholtz instability: Roles of velocity and density gradients. *Phys. Rev. E*, 83:056704, 2011. doi: 10.1103/PhysRevE.83.056704.

[64] Yanbiao Gan, Aiguo Xu, Guangcai Zhang, Yingjun Li, and Hua Li. Phase separation in thermal systems: A lattice boltzmann study and morphological characterization. *Phys. Rev. E*, 84:046715, Oct 2011. doi: 10.1103/PhysRevE.84.046715. URL https://link.aps.org/doi/10.1103/PhysRevE.84.046715.

[65] Somdeb Ghose and R. Adhikari. Irreducible representations of oscillatory and swirling flows in active soft matter. *Phys. Rev. Lett.*, 112:118102, Mar 2014. doi: 10.1103/PhysRevLett.112.118102. URL https://link.aps.org/doi/10.1103/PhysRevLett.112.118102.

[66] L. Giomi and A. DeSimone. Spontaneous division and motility in active nematic droplets. *Phys. Rev. Lett.*, 112:147802, 2014. doi: 10.1103/PhysRevLett.112.147802. URL https://link.aps.org/doi/10.1103/PhysRevLett.112.147802.

[67] L. Giomi, M.C. Marchetti, and T.B. Liverpool. Complex Spontaneous Flows and Concentration Banding in Active Polar Films. *Phys. Rev. Lett.*, 101:198101, 2008. doi: 10.1103/PhysRevLett.101.198101. URL https://link.aps.org/doi/10.1103/PhysRevLett.101.198101.

[68] L. Giomi, T.B. Liverpool, and M.C. Marchetti. Sheared active fluids: Thickening, thinning, and vanishing viscosity. *Phys. Rev. E*, 81:051908, 2010. doi: 10.1103/PhysRevE.81.051908.

[69] L. Giomi, M.J. Bowick, X. Ma, and M.C. Marchetti. Defect Annihilation and Proliferation in Active Nematics. *Phys. Rev. Lett.*, 110:228101, 2013. doi: 10.1103/PhysRevLett.110.228101. URL https://link.aps.org/doi/10.1103/PhysRevLett.110.228101.

[70] L. Giomi, M.J. Bowick, P. Mishra, R. Sknepnek, and M.C. Marchetti. Defect dynamics in active nematics. *Philos. Trans. Royal Soc. A*, 372, 2014. doi: 10.1098/rsta.2013.0365.

[71] T. Le Goff, B. Liebchen, and D. Marenduzzo. Actomyosin contraction induces droplet motility. *arXiv:1712.03138*, 2003.

[72] G. Gonnella, A. Lamura, and V. Sofonea. Lattice Boltzmann simulation of thermal nonideal fluids. *Phys. Rev. E*, 76:036703, 2007. doi: 10.1103/PhysRevE.76.036703. URL https://link.aps.org/doi/10.1103/PhysRevE.76.036703.

[73] G. Gonnella, A. Lamura, A. Piscitelli, and A. Tiribocchi. Phase separation of binary fluids with dynamic temperature. *Phys. Rev. E*, 82:046302, 2010. doi: 10.1103/PhysRevE.82.046302. URL https://link.aps.org/doi/10.1103/PhysRevE.82.046302.

[74] G. Gonnella, A. Lamura, and A. Suma. Phase segregation in a system of active dumbbells. *Int. J. Mod. Phys. A*, 25(12):1441004, 2014. doi: 10.1142/S0129183114410046. URL https://doi.org/10.1142/S0129183114410046.

[75] S. Gottlieb and C.-W. Shu. Total variation diminishing Runge-Kutta schemes. *Math. Comp.*, 67:73–85, 1998. doi: 10.1090/S0025-5718-98-00913-2.

[76] Guillaume Grégoire and Hugues Chaté. Onset of collective and cohesive motion. *Phys. Rev. Lett.*, 92:025702, Jan 2004. doi: 10.1103/PhysRevLett.92.025702. URL https://link.aps.org/doi/10.1103/PhysRevLett.92.025702.

[77] S.R. De Groot and P. Mazur. *Non-Equilibrium Thermodynamics*. Dover Books on Physics. Dover Publications, 2013. ISBN 9780486153506. URL https://books.google.it/books?id=mfFyG9jfaMYC.

[78] A.Y. Grosberg and J.F. Joanny. Nonequilibrium statistical mechanics of mixtures of particles in contact with different thermostats. *Phys. Rev. E*, 92:032118, 2015. doi: 10.1103/PhysRevE.92.032118. URL https://link.aps.org/doi/10.1103/PhysRevE.92.032118.

[79] Y. Guangwu, C. Yaosong, and H. Shouxin. Simple lattice Boltzmann model for simulating flows with shock wave. *Phys. Rev. E*, 59:454–459, 1999. doi: 10.1103/PhysRevE.59.454. URL https://link.aps.org/doi/10.1103/PhysRevE.59.454.

[80] P. Guillamat, Z. Kos, J. Hardoüin, M. Ravnik, and R. Sagués. Active nematic emulsions. *Science Advances*, 4:4, 2018.

[81] Pau Guillamat, Žiga Kos, Jérôme Hardoüin, Jordi Ignés-Mullol, Miha Ravnik, and Francesc Sagués. Active nematic emulsions. *Science Advances*, 4(4), 2018. doi: 10.1126/sciadv.aao1470. URL https://advances.sciencemag.org/content/4/4/eaao1470.

[82] S. Guo, D. Samanta, Y. Peng, X. Xu, and X. Cheng. Symmetric shear banding and swarming vortices in bacterial superfluids. *Proc. Natl. Acad. Sci. USA*, 2018. ISSN 0027-8424. doi: 10.1073/pnas.1722505115. URL http://www.pnas.org/content/early/2018/06/20/1722505115.

[83] Z. Guo, C. Zheng, and B. Shi. Discrete lattice effects on the forcing term in the lattice Boltzmann method. *Phys. Rev. E*, 65:046308, 2002. doi: 10.1103/PhysRevE.65.046308. URL https://link.aps.org/doi/10.1103/PhysRevE.65.046308.

[84] O. Henrich, D. Marenduzzo, K. Stratford, and M.E. Cates. Domain growth in cholesteric blue phases: Hybrid lattice Boltzmann simulations. *Comput. Math. App.*, 59(7):2360 – 2369, 2010. ISSN 0898-1221. doi: https://doi.org/10.1016/j.camwa.2009.08.047. URL http://www.sciencedirect.com/science/article/pii/S0898122109006324. Mesoscopic Methods in Engineering and Science.

[85] O. Henrich, K. Stratford, D. Marenduzzo, P.V. Coveney, and M.E. Cates. Rheology of lamellar liquid crystals in two and three dimensions: a simulation study. *Soft Matter*, 8:3817–3831, 2012. doi: 10.1039/C2SM07374A. URL http://dx.doi.org/10.1039/C2SM07374A.

[86] A. K. Henrick, T. D. Aslam, and J. M. Powers. Mapped weighted essentially non-oscillatory schemes: Achieving optimal order near critical points. *J. Comput. Phys*, 207:542–567, 2005. doi: 10.1016/j.jcp.2005.01.023.

[87] S. Herminghaus, C. C. Maass, C. Krüger, S. Thutupalli, L. Goehring, and C. Bahr. Interfacial mechanisms in active emulsions. *Soft Matter*, 10:7008, 2014.

[88] P.C. Hohenberg and B.I. Halperin. Theory of dynamic critical phenomena. *Rev. Mod. Phys.*, 49:435, 1977. doi: 10.1103/RevModPhys.49.435. URL https://link.aps.org/doi/10.1103/RevModPhys.49.435.

[89] E. Ilseven and M. Mendoza. Lattice Boltzmann model for numerical relativity. *Phys. Rev. E*, 93:023303, 2016. doi: 10.1103/PhysRevE.93.023303. URL https://link.aps.org/doi/10.1103/PhysRevE.93.023303.

[90] S.J. Jaju and V. Kumaran. Structure-rheology relationship in a sheared lamellar fluid. *Phys. Rev. E*, 93:032609, 2016. doi: 10.1103/PhysRevE.93.032609. URL https://link.aps.org/doi/10.1103/PhysRevE.93.032609.

[91] G. S. Jiang and C. W. Shu. Efficient implementation of weighted ENO schemes. *J. Comput. Phys.*, 126:202–228, 1996. doi: 10.1006/jcph.1996.0130.

[92] J.F. Joanny and S. Ramaswamy. A drop of active matter. *J. Fluid Mech.*, 705:46, 2012. doi: https://doi.org/10.1017/jfm.2012.131.

[93] G. Kähler, F. Bonelli, G. Gonnella, and A. Lamura. Cavitation inception of a van der Waals fluid at a sack-wall obstacle. *Phys. Fluids*, 27, 2015. doi: 10.1063/1.4937595.

[94] T. Kataoka and M. Tsutahara. Lattice Boltzmann model for the compressible Navier-Stokes equations with flexible specific-heat ratio. *Phys. Rev. E*, 69:035701, 2004. doi: 10.1103/PhysRevE.69.035701. URL https://link.aps.org/doi/10.1103/PhysRevE.69.035701.

[95] T. Kataoka and M. Tsutahara. Lattice Boltzmann method for the compressible Euler equations. *Phys. Rev. E*, 69:056702, 2004. doi: 10.1103/PhysRevE.69.056702. URL https://link.aps.org/doi/10.1103/PhysRevE.69.056702.

[96] Felix C. Keber, Etienne Loiseau, Tim Sanchez, Stephen J. DeCamp, Luca Giomi, Mark J. Bowick, M. Cristina Marchetti, Zvonimir Dogic, and Andreas R. Bausch. Topology and dynamics of active nematic vesicles. *Science*, 345(6201):1135–1139, 2014. ISSN 0036-8075. doi: 10.1126/science.1254784. URL https://science.sciencemag.org/content/345/6201/1135.

[97] R. Kemkemer, D. Kling, D. Kaufmann, and H. Gruler. Elastic properties of nematoid arrangements formed by amoeboid cells. *Eur. Phys. J. E*, 1(2):215, 2000.

[98] T. Krüger, H. Kusumaatmaja, A. Kuzmin, O. Shardt, G. Silva, and E.M. Viggen. *The Lattice Boltzmann Method: Principles and Practice*. Graduate Texts in Physics. Springer International Publishing, 2016. ISBN 9783319446493. URL https://books.google.co.uk/books?id=S-d0DQAAQBAJ.

[99] K. Kruse, J.F. Joanny, F. Jülicher, J. Prost, and K. Sekimoto. Asters, Vortices, and Rotating Spirals in Active Gels of Polar Filaments. *Phys. Rev. Lett.*, 92:078101, 2004. doi: 10.1103/PhysRevLett.92.078101.

[100] K. Kruse, J.F. Joanny, F. Jülicher, J. Prost, and K. Sekimoto. Generic theory of active polar gels: a paradigm for cytoskeletal dynamics. *Eur. Phys. J. E*, 16(1):5–16, 2005. ISSN 1292-895X. doi: 10.1140/epje/e2005-00002-5. URL https://doi.org/10.1140/epje/e2005-00002-5.

[101] W. Kung, M.C. Marchetti, and K. Saunders. Hydrodynamics of polar liquid crystals. *Phys. Rev. E*, 73:031708, 2006. doi: 10.1103/PhysRevE.73.031708. URL https://link.aps.org/doi/10.1103/PhysRevE.73.031708.

[102] M. V. Kurik and O. D. Lavrentovich. Negative-positive monopole transitions in cholesteric liquid crystals. *Soviet Journal of Experimental and Theoretical Physics Letters*, 35:444, May 1982.

[103] Julia Kürner, Achilleas S. Frangakis, and Wolfgang Baumeister. Cryo-electron tomography reveals the cytoskeletal structure of spiroplasma melliferum. *Science*, 307(5708):436–438, 2005. ISSN 0036-8075. doi: 10.1126/science.1104031. URL https://science.sciencemag.org/content/307/5708/436.

[104] A.J.C. Ladd and R. Verberg. Lattice-Boltzmann Simulations of Particle-Fluid Suspensions. *J. Stat. Phys.*, 104(5):1191–1251, 2001. ISSN 1572-9613. doi: 10.1023/A:1010414013942. URL https://doi.org/10.1023/A:1010414013942.

[105] A. G. Lamorgese and R. Mauri. Diffuse-interface modeling of liquid-vapor phase separation in a van der waals fluid. *Physics of Fluids*, 21(4):044107, 2009. doi: 10.1063/1.3103826. URL https://doi.org/10.1063/1.3103826.

[106] A. Lamura and G. Gonnella. Lattice Boltzmann simulations of segregating binary fluid mixtures in shear flow. *Physica A*, 294(3):295 – 312, 2001. ISSN 0378-4371. doi: https://doi.org/10.1016/S0378-4371(01)00022-X. URL http://www.sciencedirect.com/science/article/pii/S037843710100022X.

[107] R.G. Larson. Fluid dynamics: Turbulence without inertia. *Nature*, 405, 2000. doi: 10.1038/35011172. URL http://gen.lib.rus.ec/scimag/index.php?s=10.1038/35011172.

[108] François A. Lavergne, Hugo Wendehenne, Tobias Bäuerle, and Clemens Bechinger. Group formation and cohesion of active particles with visual perception–dependent motility. *Science*, 364(6435):70–74, 2019. ISSN 0036-8075. doi: 10.1126/science.aau5347. URL https://science.sciencemag.org/content/364/6435/70.

[109] T. Lee and C.-L. Lin. A Characteristic Galerkin Method for Discrete Boltzmann Equation. *J. Comput. Phys.*, 171, 2001. doi: 10.1006/jcph.2001.6791.

[110] T. Leon and F. Nieves. Drops and shells of liquid crystal. *A. Colloid Polym Sci*, 289 (4):345–359, 2011. doi: https://doi.org/10.1007/s00396-010-2367-7.

[111] Jacqueline M. Leung, Mark A. Rould, Christoph Konradt, Christopher A. Hunter, and Gary E. Ward. Disruption of tgphil1 alters specific parameters of toxoplasma gondii motility measured in a quantitative, three-dimensional live motility assay. *PLOS ONE*, 9(1):1–10, 01 2014. doi: 10.1371/journal.pone.0085763. URL https://doi.org/10.1371/journal.pone.0085763.

[112] G. Li, J. Bensson, L. Nisimova, D. Munger, P. Mahautmr, J.X. Tang, M.R. Maxey, and Y.V. Brun. Accumulation of swimming bacteria near a solid surface. *Phys. Rev. E*, 84:041932, 2011. doi: 10.1103/PhysRevE.84.041932. URL https://link.aps.org/doi/10.1103/PhysRevE.84.041932.

[113] Q. Li and A.J. Wagner. Symmetric free-energy-based multicomponent lattice Boltzmann method. *Phys. Rev. E*, 76:036701, 2007. doi: 10.1103/PhysRevE.76.036701. URL https://link.aps.org/doi/10.1103/PhysRevE.76.036701.

[114] J. Lighthill. *Mathematical Biofluiddynamics*. CBMS-NSF Regional Conference Series in Applied Mathematics. Society for Industrial and Applied Mathematics, 1975. ISBN 9780898710144. URL https://books.google.it/books?id=iUFscfoRT08C.

[115] M. Linkmann, G. Boffetta, C.M. Marchetti, and B. Eckhardt. Phase transition to large scale coherent structures in 2d active matter turbulence. *arXiv*, 2018.

[116] F. Livolant. Cholesteric liquid crystalline phases given by three helical biological polymers: DNA, PBLG and xanthan. A comparative analysis of their textures. *J. Phys. France*, 47(1605):1605 – 1616, 1986.

[117] F. Livolant. Ordered phases of DNA in vivo and in vitro. *Physica A*, 176(117): 117 – 137, 1991. ISSN 0378-4371. doi: https://doi.org/10.1016/0378-4371(91)90436-G. URL http://www.sciencedirect.com/science/article/pii/037843719190436G.

[118] A. Loisy, J. Eggers, and T.B. Liverpool. Active Suspensions have Nonmonotonic Flow Curves and Multiple Mechanical Equilibria. *Phys. Rev. Lett.*, 121:018001, Jul 2018. doi: 10.1103/PhysRevLett.121.018001. URL https://link.aps.org/doi/10.1103/PhysRevLett.121.018001.

[119] H.M. López, J. Gachelin, C. Douarche, H. Auradou, and E. Clément. Turning Bacteria Suspensions into Superfluids. *Phys. Rev. Lett.*, 115:028301, 2015. doi: 10.1103/PhysRevLett.115.028301. URL https://link.aps.org/doi/10.1103/PhysRevLett.115.028301.

[120] H.M. López, J. Gachelin, C. Douarche, H. Auradou, and E. Clément. Turning Bacteria Suspensions into Superfluids. *Phys. Rev. Lett.*, 115:028301, 2015. doi: 10.1103/PhysRevLett.115.028301. URL https://link.aps.org/doi/10.1103/PhysRevLett.115.028301.

[121] V M. Kendon, Jean-Christophe Desplat, P Bladon, and M E. Cates. 3d spinodal decomposition in the inertial regime. 83, 02 1999.

[122] A. Maitra and M. Lenz. Spontaneous rotation can stabilise ordered chiral active fluids. *Nat. Commun.*, 10, 2019. doi: 10.1038/s41467-019-08914-7. URL http://gen.lib.rus.ec/scimag/index.php?s=10.1038/s41467-019-08914-7.

[123] M.C. Marchetti, J.F. Joanny, S. Ramaswamy, T.B. Liverpool, J.J. Prost, M. Rao, and R.A. Simha. Hydrodynamics of soft active matter. *Rev. Mod. Phys.*, 85:1143, 2013. doi: 10.1103/RevModPhys.85.1143.

[124] D. Marenduzzo, E. Orlandini, M.E. Cates, and J.M. Yeomans. Steady-state hydrodynamic instabilities of active liquid crystals: Hybrid lattice Boltzmann simulations. *Phys. Rev. E*, 76:031921, 2007. doi: 10.1103/PhysRevE.76.031921. URL https://link.aps.org/doi/10.1103/PhysRevE.76.031921.

[125] D. Marenduzzo, E. Orlandini, and J.M. Yeomans. Hydrodynamics and Rheology of Active Liquid Crystals: A Numerical Investigation. *Phys. Rev. Lett.*, 98:118102, 2007. doi: 10.1103/PhysRevLett.98.118102. URL https://link.aps.org/doi/10.1103/PhysRevLett.98.118102.

[126] D. Marenduzzo, E. Orlandini, M.E. Cates, and J.M. Yeomans. Lattice Boltzmann simulations of spontaneous flow in active liquid crystals: The role of boundary conditions. *J. Nonnewton. Fluid Mech.*, 149(1):56 – 62, 2008. ISSN 0377-0257. doi: https://doi.org/10.1016/j.jnnfm.2007.02.005. URL http://www.sciencedirect.com/science/article/pii/S037702570700047X. International Workshop on Mesoscale and Multiscale Description of Complex Fluids.

[127] K.C. Marshall and R.H. Cruickshank. Cell surface hydrophobicity and the orientation of certain bacteria at interfaces. *Arch. Microbiol.*, 91(1):29–40, 1973. ISSN 1432-072X. doi: 10.1007/BF00409536. URL https://doi.org/10.1007/BF00409536.

[128] P.C. Martin, O. Parodi, and P.S. Pershan. Unified Hydrodynamic Theory for Crystals, Liquid Crystals, and Normal Fluids. *Phys. Rev. A*, 6:2401, 1972. doi: 10.1103/PhysRevA.6.2401. URL https://link.aps.org/doi/10.1103/PhysRevA.6.2401.

[129] M. Mayer, M. Depken, J.S. Bois, F. Jülicher, and S. Grill. Anisotropies in cortical tension reveal the physical basis of polarizing cortical flows. *Nature*, 467:617, November 2010. doi: 10.1038/nature09376. URL https://www.nature.com/articles/nature09376#supplementary-information.

[130] G. Mazenko. *Nonequilibrium Statistical Mechanics*. Physics textbook. Wiley, 2006. ISBN 9783527406487. URL https://books.google.it/books?id=koMHQPyozBwC.

[131] S.R. McCandlish, A. Baskaran, and M.F. Hagan. Spontaneous segregation of self-propelled particles with different motilities. *Soft Matter*, 8(8):2527–2534, 2012.

[132] R. Mei and W. Shyy. On the Finite Difference-Based Lattice Boltzmann Method in Curvilinear Coordinates. *J. Comput. Phys.*, 143(2):426 – 448, 1998. ISSN 0021-9991. doi: https://doi.org/10.1006/jcph.1998.5984.

[133] K. Michielsen and H. De Raedt. Integral-geometry morphological image analysis. *Physics Reports*, 347(6):461 – 538, 2001. ISSN 0370-1573. doi: https://doi.org/10.1016/S0370-1573(00)00106-X. URL http://www.sciencedirect.com/science/article/pii/S037015730000106X.

[134] B.T. Nadiga. An Euler solver based on locally adaptive discrete velocities. *J. Stat. Phys.*, 81(1):129–146, 1995. ISSN 1572-9613. doi: 10.1007/BF02179972. URL https://doi.org/10.1007/BF02179972.

[135] S.R. Naganathan, S. Fürthauer, M. Nishikawa, F. Jülicher, and S.W. Grill. Active torque generation by the actomyosin cell cortex drives left–right symmetry breaking. *eLife*, 3:e04165, 2014. ISSN 2050-084X. doi: 10.7554/eLife.04165. URL https://doi.org/10.7554/eLife.04165.

[136] G. Negro, L.N. Carenza, P. Digregorio, G. Gonnella, and A. Lamura. Morphology and flow patterns in highly asymmetric active emulsions. *Physica A*, 503:464 – 475, 2018. ISSN 0378-4371. doi: https://doi.org/10.1016/j.physa.2018.03.011. URL http://www.sciencedirect.com/science/article/pii/S0378437118303194.

[137] G. Negro, S. Busuioc, V. E. Ambruş, G. Gonnella, A. Lamura, and V. Sofonea. Comparison between isothermal collision-streaming and finite-difference lattice boltzmann models. *International Journal of Modern Physics C*, 30(10):1941005, 2019. doi: 10.1142/S0129183119410055. URL https://doi.org/10.1142/S0129183119410055.

[138] M. Nobili and G. Durand. Disorientation-induced disordering at a nematic-liquid-crystal–solid interface. *Phys. Rev. A*, 46:R6174–R6177, Nov 1992. doi: 10.1103/PhysRevA.46.R6174. URL https://link.aps.org/doi/10.1103/PhysRevA.46.R6174.

[139] Melanie Norstrom and Margaret L. Gardel. Shear thickening of f-actin networks crosslinked with non-muscle myosin iib. *Soft Matter*, 7:3228–3233, 2011. doi: 10.1039/C0SM01157F. URL http://dx.doi.org/10.1039/C0SM01157F.

[140] R.R. Nourgaliev, T.N. Dinh, T.G. Theofanous, and D. Joseph. The lattice Boltzmann equation method: theoretical interpretation, numerics and implications. *Int. J. Multiph. Flow*, 29(1):117 – 169, 2003. ISSN 0301-9322. doi: https://doi.org/10.1016/S0301-9322(02)00108-8. URL http://www.sciencedirect.com/science/article/pii/S0301932202001088.

[141] E. Orlandini, M.E. Cates, D. Marenduzzo, L. Tubiana, and J.M. Yeomans. Hydrodynamic of Active Liquid Crystals: A Hybrid Lattice Boltzmann Approach. *Mol. Cryst. Liq. Cryst.*, 494(1):293–308, 2008. doi: 10.1080/15421400802430117. URL https://doi.org/10.1080/15421400802430117.

[142] E. Orlandini, M.E. Cates, D. Marenduzzo, L. Tubiana, and J.M. Yeomans. Hydrodynamic of Active Liquid Crystals: A Hybrid Lattice Boltzmann Approach. *Mol. Cryst. Liq. Cryst.*, 494:293, 2008. doi: 10.1080/15421400802430117.

[143] Daniel J. G. Pearce and Luca Giomi. Linear response to leadership, effective temperature, and decision making in flocks. *Phys. Rev. E*, 94:022612, Aug 2016. doi: 10.1103/PhysRevE.94.022612. URL https://link.aps.org/doi/10.1103/PhysRevE.94.022612.

[144] T.J. Pedley and J.O. Kessler. Hydrodynamic Phenomena in Suspensions of Swimming Microorganisms. *Annu. Rev. Fluid Mech.*, 24(1):313, 1992. doi: 10.1146/annurev.fl.24.010192.001525. URL https://doi.org/10.1146/annurev.fl.24.010192.001525.

[145] I. Petrelli, P. Digregorio, L.F. Cugliandolo, G. Gonnella, and A. Suma. Active dumbbells: dynamics and morphology in the coexisting region. *Eur. Phys. J. E*, 41(10):128, 2018. doi: 10.1140/epje/i2018-11739-y. URL https://doi.org/10.1140/epje/i2018-11739-y.

[146] R. Phillips, J. Kondev, J. Theriot, and H. Garcia. *Physical Biology of the Cell*. CRC Press, 2012. ISBN 9781134111589. URL https://books.google.it/books?id=5_MOBAAAQBAJ.

[147] R. Poincloux, O. Collin, F. Lizarraga, M. Romao, M. Debray, M. Piel, and P. Chavrier. Contractility of the cell rear drives invasion of breast tumor cells in 3d matrigel. 108:1943–8, 02 2011.

[148] E.M. Purcell. The efficiency of propulsion by a rotating flagellum. *Proc. Natl. Acad. Sci.*, 94(21):11307–11311, 1997. ISSN 0027-8424. doi: 10.1073/pnas.94.21.11307. URL https://www.pnas.org/content/94/21/11307.

[149] Y.H. Qian and S.A. Orszag. Lattice BGK Models for the Navier-Stokes Equation: Nonlinear Deviation in Compressible Regimes. *EPL*, 21(3):255, 1993. URL http://stacks.iop.org/0295-5075/21/i=3/a=001.

[150] Y.H. Qian, D. D'Humiéres, and P. Lallemand. Lattice BGK Models for Navier-Stokes Equation. *EPL*, 17(6):479, 1992. URL http://stacks.iop.org/0295-5075/17/i=6/a=001.

[151] S. Rafaï, L. Jibuti, and P. Peyla. Effective Viscosity of Microswimmer Suspensions. *Phys. Rev. Lett.*, 104:098102, 2010. doi: 10.1103/PhysRevLett.104.098102. URL https://link.aps.org/doi/10.1103/PhysRevLett.104.098102.

[152] S. Ramaswamy. The Mechanics and Statistics of Active Matter. *Annu. Rev. Condens. Matter Phys.*, 1:323, 2010. doi: 10.1146/annurev-conmatphys-070909-104101.

[153] S. Ramaswamy. Active matter. *J. Stat. Mech.*, 2017(5):054002, 2017. URL http://stacks.iop.org/1742-5468/2017/i=5/a=054002.

[154] S. Ramaswamy, R.A. Simha, and J. Toner. Active nematics on a substrate: Giant number fluctuations and long-time tails. *EPL*, 62:196, 2003. doi: 10.1209/epl/i2003-00346-7.

[155] P. Recho, T. Putelat, and L. Truskinovsky. Contraction-driven cell motility. *Phys. Rev. Lett.*, 111:108102, Sep 2013. doi: 10.1103/PhysRevLett.111.108102. URL https://link.aps.org/doi/10.1103/PhysRevLett.111.108102.

[156] Craig W. Reynolds. Flocks, herds and schools: A distributed behavioral model. *SIGGRAPH Comput. Graph.*, 21(4):25–34, August 1987. ISSN 0097-8930. doi: 10.1145/37402.37406. URL http://doi.acm.org/10.1145/37402.37406.

[157] I.H. Riedel, K. Kruse, and J. Howard. A Self-Organized Vortex Array of Hydrodynamically Entrained Sperm Cells. *Science*, 309(5732):300–303, 2005. ISSN 0036-8075. doi: 10.1126/science.1110329. URL https://science.sciencemag.org/content/309/5732/300.

[158] Jose A. Rodríguez, Miguel A. Lopez, Michelle C. Thayer, Yunzhe Zhao, Michael Oberholzer, Donald D. Chang, Neville K. Kisalu, Manuel L. Penichet, Gustavo Helguera, Robijn Bruinsma, Kent L. Hill, and Jianwei Miao. Propulsion of african trypanosomes is driven by bihelical waves with alternating chirality separated by kinks. *Proc. Natl. Acad. Sci.*, 106(46):19322–19327, 2009. ISSN 0027-8424. doi: 10.1073/pnas.0907001106. URL https://www.pnas.org/content/106/46/19322.

[159] D.H. Rothman and S. Zaleski. *Lattice-Gas Cellular Automata (Simple Models of Complex Hydrodynamics)*, volume 10.1017/CBO9780511524714. Cambridge University Press, 1997. ISBN 9780511524714,9780521552011,9780521607605. doi: 10.1017/CBO9780511524714.

[160] T. Sanchez, D.T.N. Chen, S.J. Decamp, M. Heymann, and Z. Dogic. Spontaneous motion in hierarchically assembled active matter. *Nature*, 491:431–434, 2012.

[161] S. Sankararaman and S. Ramaswamy. Instabilities and Waves in Thin Films of Living Fluids. *Phys. Rev. Lett.*, 102:118107, 2009. doi: 10.1103/PhysRevLett.102.118107. URL https://link.aps.org/doi/10.1103/PhysRevLett.102.118107.

[162] K. Schiele and S. Trimper. On the Elastic Constants of a Nematic Liquid Crystal. *Phys. Status Solidi B*, 118, 1983. doi: 10.1002/pssb.2221180132. URL http://gen.lib.rus.ec/scimag/index.php?s=10.1002/pssb.2221180132.

[163] F. Schlögl. Chemical reaction models for non-equilibrium phase transitions. *Zeitschrift für Physik*, 253(2):147–161, Apr 1972. ISSN 0044-3328. doi: 10.1007/BF01379769. URL https://doi.org/10.1007/BF01379769.

[164] David Seč, Tine Porenta, Miha Ravnik, and Slobodan Žumer. Geometrical frustration of chiral ordering in cholesteric droplets. *Soft Matter*, 8:11982–11988, 2012. doi: 10.1039/C2SM27048J. URL http://dx.doi.org/10.1039/C2SM27048J.

[165] X. Shan and H. Chen. Simulation of nonideal gases and liquid-gas phase transitions by the lattice Boltzmann equation. *Phys. Rev. E*, 49:2941–2948, 1994. doi: 10.1103/PhysRevE.49.2941. URL https://link.aps.org/doi/10.1103/PhysRevE.49.2941.

[166] X. Shan, Xue-Feng Yuan, and H. Chen. Kinetic theory representation of hydrodynamics: a way beyond the Navier–Stokes equation. *J. Fluid Mech.*, 550:413–441, 2006. doi: 10.1017/S0022112005008153.

[167] T.N. Shendruk, K. Thijssen, J.M. Yeomans, and A. Doostmohammadi. Twist-induced crossover from two-dimensional to three-dimensional turbulence in active nematics. *Phys. Rev. E*, 98:010601, 2018. doi: 10.1103/PhysRevE.98.010601. URL https://link.aps.org/doi/10.1103/PhysRevE.98.010601.

[168] C.-W. Shu and S. Osher. Efficient implementation of essentially non-oscillatory shock-capturing schemes. *J. Comput. Phys.*, 77:439–471, 1988. doi: 10.1016/0021-9991(88)90177-5.

[169] R.A. Simha and S. Ramaswamy. Hydrodynamic Fluctuations and Instabilities in Ordered Suspensions of Self-Propelled Particles. *Phys. Rev. Lett.*, 89:058101, 2002. doi: 10.1103/physrevlett.89.058101.

[170] V. Sofonea and R.F. Sekerka. Viscosity of finite difference lattice Boltzmann models. *J. Comput. Phys.*, 184, 2003. doi: 10.1016/s0021-9991(02)00026-8.

[171] V. Sofonea, A. Lamura, G. Gonnella, and A. Cristea. Finite-difference lattice boltzmann model with flux limiters for liquid-vapor systems. *Phys. Rev. E*, 70:046702, Oct 2004. doi: 10.1103/PhysRevE.70.046702. URL https://link.aps.org/doi/10.1103/PhysRevE.70.046702.

[172] V. Sofonea, A. Lamura, G. Gonnella, and A. Cristea. Finite-difference lattice Boltzmann model with flux limiters for liquid-vapor systems. *Phys. Rev. E*, 70, 2004. doi: 10.1103/PhysRevE.70.046702. URL http://gen.lib.rus.ec/scimag/index.php?s=10.1103/PhysRevE.70.046702.

[173] V. Sofonea, A. Lamura, G. Gonnella, and A. Cristea. Finite-difference lattice Boltzmann model with flux limiters for liquid-vapor systems. *Phys. Rev. E*, 70:046702, 2004. doi: 10.1103/PhysRevE.70.046702.

[174] V. Sofonea, T. Biciusca, S. Busuioc, V.E. Ambrus, G. Gonnella, and A. Lamura. Corner-transport-upwind lattice boltzmann model for bubble cavitation. *Phys. Rev. E*, 97:023309, 2018. doi: 10.1103/PhysRevE.97.023309. URL https://link.aps.org/doi/10.1103/PhysRevE.97.023309.

[175] H. Stark and T.C. Lubensky. Poisson-bracket approach to the dynamics of nematic liquid crystals. *Phys. Rev. E*, 67:061709, 2003. doi: 10.1103/PhysRevE.67.061709. URL https://link.aps.org/doi/10.1103/PhysRevE.67.061709.

[176] J. Stenhammar, R. Wittkowski, D. Marenduzzo, and M.E. Cates. Activity-Induced Phase Separation and Self-Assembly in Mixtures of Active and Passive Particles. *Phys. Rev. Lett.*, 114:018301, Jan 2015. doi: 10.1103/PhysRevLett.114.018301. URL https://link.aps.org/doi/10.1103/PhysRevLett.114.018301.

[177] S. Succi. *The Lattice Boltzmann Equation: For Fluid Dynamics and Beyond*. Numerical Mathematics and Scientific Computation. Clarendon Press, 2001. ISBN 9780198503989. URL https://books.google.it/books?id=0C0Sj_xgnhAC.

[178] S. Succi, R. Benzi, and F. Higuera. The lattice Boltzmann equation: A new tool for computational fluid-dynamics. *Phys. D: Nonlinear Phenomena*, 47(1): 219 – 230, 1991. ISSN 0167-2789. doi: https://doi.org/10.1016/0167-2789(91)90292-H. URL http://www.sciencedirect.com/science/article/pii/016727899190292H.

[179] A. Suma, G. Gonnella, G. Laghezza, A. Lamura, A. Mossa, and L.F. Cugliandolo. Dynamics of a homogeneous active dumbbell system. *Phys. Rev. E*, 90:052130, 2014. doi: 10.1103/PhysRevE.90.052130. URL https://link.aps.org/doi/10.1103/PhysRevE.90.052130.

[180] A. Suma, G. Gonnella, D. Marenduzzo, and E. Orlandini. Motility-induced phase separation in an active dumbbell fluid. *EPL*, 108(5):56004, 2014. URL http://stacks.iop.org/0295-5075/108/i=5/a=56004.

[181] C. Sun. Lattice-Boltzmann models for high speed flows. *Phys. Rev. E*, 58:7283–7287, 1998. doi: 10.1103/PhysRevE.58.7283. URL https://link.aps.org/doi/10.1103/PhysRevE.58.7283.

[182] T. Surrey, F. Nédélec, S. Leibler, and E. Karsenti. Physical Properties Determining Self-Organization of Motors and Microtubules. *Science*, 292:1167, 2001. doi: 10.1126/science.1059758.

[183] S.P. Thampi and J.M. Yeomans. Active turbulence in active nematics. *Eur. Phys. J. Spec. Top.*, 225(4):651–662, 2016.

[184] S.P. Thampi, R. Golestanian, and J.M. Yeomans. Instabilities and topological defects in active nematics. *EPL*, 105(1):18001, 2014. URL http://stacks.iop.org/0295-5075/105/i=1/a=18001.

[185] S.P. Thampi, R. Golestanian, and J.M. Yeomans. Vorticity, defects and correlations in active turbulence. *Philosophical Transactions of the Royal Society of London A: Mathematical, Physical and Engineering Sciences*, 372(2029), 2014. ISSN 1364-503X. doi: 10.1098/rsta.2013.0366. URL http://rsta.royalsocietypublishing.org/content/372/2029/20130366.

[186] A. Tiribocchi, N. Stella, G. Gonnella, and A. Lamura. Hybrid lattice Boltzmann model for binary fluid mixtures. *Phys. Rev. E*, 80:026701, 2009. doi: 10.1103/PhysRevE.80.026701.

[187] A. Tiribocchi, R. Wittkowski, D. Marenduzzo, and M.E. Cates. Active Model H: Scalar Active Matter in a Momentum-Conserving Fluid. *Phys. Rev. Lett.*, 115: 188302, 2015. doi: 10.1103/PhysRevLett.115.188302. URL https://link.aps.org/doi/10.1103/PhysRevLett.115.188302.

[188] E. Tjhung, M.E. Cates, and D. Marenduzzo. Nonequilibrium steady states in polar active fluids. *Soft Matter*, 7:7453–7464, 2011. doi: 10.1039/C1SM05396E. URL http://dx.doi.org/10.1039/C1SM05396E.

[189] E. Tjhung, M.E. Cates, and D. Marenduzzo. Nonequilibrium steady states in polar active fluids. *Soft Matter*, 7:7453–7464, 2011. doi: 10.1039/C1SM05396E. URL http://dx.doi.org/10.1039/C1SM05396E.

[190] E. Tjhung, D. Marenduzzo, and M. E. Cates. Spontaneous symmetry breaking in active droplets provides a generic route to motility. *Proc. Natl. Acad. Sci. U.S.A.*, 109(31):12381–12386, 2012. doi: 10.1073/pnas.1200843109. URL http://www.pnas.org/content/109/31/12381.abstract.

[191] E. Tjhung, D. Marenduzzo, and M.E. Cates. Spontaneous symmetry breaking in active droplets provides a generic route to motility. *Proc. Natl. Acad. Sci. U.S.A.*, 109(31):12381–12386, 2012. doi: 10.1073/pnas.1200843109. URL http://www.pnas.org/content/109/31/12381.abstract.

[192] E. Tjhung, A. Tiribocchi, D. Marenduzzo, and M.E. Cates. A minimal physical model captures the shapes of crawling cells. *Nat. Commun.*, 6:5420, 2015. doi: http://dx.doi.org/10.1038/ncomms6420. URL https://www.nature.com/articles/ncomms6420#supplementary-information.

[193] E. Tjhung, A. Tiribocchi, D. Marenduzzo, and M.E. Cates. A minimal physical model captures the shapes of crawling cells. *Nature Communications*, 6:5420, 2015. doi: http://dx.doi.org/10.1038/ncomms6420. URL https://www.nature.com/articles/ncomms6420#supplementary-information.

[194] E. Tjhung, A. Tiribocchi, D. Marenduzzo, and M.E. Cates. A minimal physical model captures the shapes of crawling cells. *Nat. Comm.*, 6:5420, 2015.

[195] E. Tjhung, M.E. Cates, and D. Marenduzzo. Contractile and chiral activities codetermine the helicity of swimming droplet trajectories. *Proc. Natl. Acad. Sci. USA*, 114(18):4631–4636, 2017. ISSN 0027-8424. doi: 10.1073/pnas.1619960114. URL http://www.pnas.org/content/114/18/4631.

[196] G. Tóth, C. Denniston, and J.M. Yeomans. Hydrodynamics of Topological Defects in Nematic Liquid Crystals. *Phys. Rev. Lett.*, 88:105504, 2002. doi: 10.1103/PhysRevLett.88.105504. URL https://link.aps.org/doi/10.1103/PhysRevLett.88.105504.

[197] J. A. Trangenstein. *Numerical solution of hyperbolic partial differential equations*. Cambridge University Press, New York, 2007.

[198] S. Čopar, J. Aplinc, Ž. Kos, S. Žumer, and M. Ravnik. Topology of three-dimensional active nematic turbulence confined to droplets. *arXiv:1908.00904v1*, 2019.

[199] T. Vicsek, A. Czirók, E. Ben-Jacob, I. Cohen, and O. Shochet. Novel Type of Phase Transition in a System of Self-Driven Particles. *Phys. Rev. Lett.*, 75:1226, 1995. doi: 10.1103/physrevlett.75.1226.

[200] Tamás Vicsek and Anna Zafeiris. Collective motion. *Physics Reports*, 517 (3):71 – 140, 2012. ISSN 0370-1573. doi: https://doi.org/10.1016/j.physrep.2012.03.004. URL http://www.sciencedirect.com/science/article/pii/S0370157312000968. Collective motion.

[201] Natalia Vladimirova, Andrea Malagoli, and Roberto Mauri. Two-dimensional model of phase segregation in liquid binary mixtures. *Phys. Rev. E*, 60:6968–6977, Dec 1999. doi: 10.1103/PhysRevE.60.6968. URL https://link.aps.org/doi/10.1103/PhysRevE.60.6968.

[202] R. Voituriez, J.F. Joanny, and J. Prost. Spontaneous flow transition in active polar gels. *EPL*, 70:404, 2005. doi: 10.1209/epl/i2004-10501-2.

[203] A. J. Wagner. The origin of spurious velocities in lattice boltzmann. *International Journal of Modern Physics B*, 17(01n02):193–196, 2003. doi: 10.1142/S0217979203017448. URL https://doi.org/10.1142/S0217979203017448.

[204] A. J. Wagner. Thermodynamic consistency of liquid-gas lattice boltzmann simulations. *Phys. Rev. E*, 74:056703, Nov 2006. doi: 10.1103/PhysRevE.74.056703. URL https://link.aps.org/doi/10.1103/PhysRevE.74.056703.

[205] A. J. Wagner and C. M. Pooley. Interface width and bulk stability: Requirements for the simulation of deeply quenched liquid-gas systems. *Phys. Rev. E*, 76:045702, Oct 2007. doi: 10.1103/PhysRevE.76.045702. URL https://link.aps.org/doi/10.1103/PhysRevE.76.045702.

[206] S. Wang and P.G. Wolynes. Active contractility in actomyosin networks. *Proc. Natl. Acad. Sci.*, 109(17):6446–6451, 2012. ISSN 0027-8424. doi: 10.1073/pnas.1204205109. URL https://www.pnas.org/content/109/17/6446.

[207] M. Watari and M. Tsutahara. Two-dimensional thermal model of the finite-difference lattice Boltzmann method with high spatial isotropy. *Phys. Rev. E*, 67:036306, 2003. doi: 10.1103/PhysRevE.67.036306. URL https://link.aps.org/doi/10.1103/PhysRevE.67.036306.

[208] H.H. Wensink, J. Dunkel, S. Heidenreich, K. Drescher, R.E. Goldstein, H. Lowen, and J.M. Yeomans. Meso-scale turbulence in living fluids. *Proc. Natl. Acad. Sci. USA*, 109, 2012. doi: 10.1073/pnas.1202032109. URL http://gen.lib.rus.ec/scimag/index.php?s=10.1073/pnas.1202032109.

[209] C.A. Whitfield and R.J. Hawkins. Instabilities, motion and deformation of active fluid droplets. *New J. Phys.*, 18(12):123016, 2016. URL http://stacks.iop.org/1367-2630/18/i=12/a=123016.

[210] R. Wittkowski, A. Tiribocchi, J. Stenhammar, R.J. Allen, D. Marenduzzo, and M.E. Cates. Scalar ϕ^4 field theory for active-particle phase separation. *Nat. Comm.*, 5, 2014.

[211] D.A Wolf-Gladrow. *Lattice Gas Cellular Automata and Lattice Boltzmann Models*, volume 10.1007/b72010. Springer-Verlag Berlin Heidelberg, 2000. ISBN 978-3-540-66973-9,978-3-540-46586-7. doi: 10.1007/978-3-540-46586-7_1.

[212] M.A. Wozniak, K. Modzelewska, L. Kwong, and P.J. Keely. Focal adhesion regulation of cell behavior. *Biochim. Biophys. Acta*, 1692(2):103 – 119, 2004. ISSN 0167-4889. doi: https://doi.org/10.1016/j.bbamcr.2004.04.007. URL http://www.sciencedirect.com/science/article/pii/S0167488904000990.

[213] D.C. Wright and N.D. Mermin. Crystalline liquids: the blue phases. *Rev. Mod. Phys.*, 61:385–432, 1989. doi: 10.1103/RevModPhys.61.385.

[214] A. Xu, G. Gonnella, and A. Lamura. Phase-separating binary fluids under oscillatory shear. *Phys. Rev. E*, 67:056105, 2003. doi: 10.1103/PhysRevE.67.056105. URL https://link.aps.org/doi/10.1103/PhysRevE.67.056105.

[215] A. Xu, G. Gonnella, and A. Lamura. Phase separation of incompressible binary fluids with lattice boltzmann methods. *Physica A*, 331(1):10 – 22, 2004. ISSN 0378-4371. doi: https://doi.org/10.1016/j.physa.2003.09.040. URL http://www.sciencedirect.com/science/article/pii/S0378437103008343.

[216] J.M. Yeomans. Mesoscale simulations: Lattice Boltzmann and particle algorithms. *Physica A: Statistical Mechanics and its Applications*, 369(1): 159 – 184, 2006. ISSN 0378-4371. doi: https://doi.org/10.1016/j.physa.2006.04.011. URL http://www.sciencedirect.com/science/article/pii/S0378437106004067.

[217] J.M. Yeomans and G. Gonnella. *Kinetics of Phase Transitions*, chapter 4 - Using the Lattice Boltzmann Algorithm to Explore Phase Ordering in Fluids. CRC Press, 2009. ISBN 978-0-8493-9065-4.

[218] J. Zhang, Y. Yao, L. Sheng, and J. Liu. Self-fueled biomimetic liquid metal mollusk. *Adv. Mater.*, 27:2648, 2015.

[219] R.Z. Zhang, M. Ye Rahimi, and J.J. de Pablo. Dynamic structure of active nematic shells. *Nature Communications*, 7:13483, 2016. doi: 10.1038/ncomms13483.

[220] S. Zhou, A. Sokolov, O. Lavrentovich, and I.S. Aranson. Living liquid crystals. *Proc. of the National Academy of Sciences*, 111(4):1265–1270, 2014. ISSN 0027-8424. doi: 10.1073/pnas.1321926111. URL http://www.pnas.org/content/111/4/1265.

[221] Shuang Zhou, Andrey Sokolov, Oleg D. Lavrentovich, and Igor S. Aranson. Living liquid crystals. *Proc. Natl. Acad. Sci.*, 111(4):1265–1270, 2014. ISSN 0027-8424. doi: 10.1073/pnas.1321926111. URL https://www.pnas.org/content/111/4/1265.

[222] Ye Zhou, Emre Bukusoglu, José A. Martínez-González, Mohammad Rahimi, Tyler F. Roberts, Rui Zhang, Xiaoguang Wang, Nicholas L. Abbott, and Juan J. de Pablo. Structural transitions in cholesteric liquid crystal droplets. *ACS Nano*, 10(7):6484–6490, 2016. doi: 10.1021/acsnano.6b01088. URL https://doi.org/10.1021/acsnano.6b01088. PMID: 27249186.

[223] Q. Zou and X. He. On pressure and velocity boundary conditions for the lattice Boltzmann BGK model. *Phys. Fluids*, 9(6):1591–1598, 1997. doi: 10.1063/1.869307. URL https://doi.org/10.1063/1.869307.

A

LIQUID-VAPOR PHASE SEPARATION

When a fluid, initially in a disordered state, is immediately cooled to a temperature below the spinodal line [1], in a region of coexistence between two phases, domains of the two different phases are formed and grow over time. In this case the phase separation takes the spinodal decomposition name. Typically the growth of such domains is a scale phenomenon, that is, there is a single length feature that tells the structure of the domains appears the same during the time evolution, when all lengths are rescaled with respect to l. The above is called the *dynamical scaling hypothesis*, and is supported by results of numerical simulations and experiments for the structure factor and correlation functions. Typically the average domains size $l(t)$ grows over time according to a power law, with an exponent α that depends on the presence of hydrodynamic effects and on the number of order parameter components and whether it is conserved or not. For binary mixtures we can distinguish three different regimes [14], each characterized by a specific physical growth mechanism, whose existence can be deduced by analysing the dynamics equations, Navier-Stokes equations and the order parameter evolution equation, and assuming that there is only one relevant characteristic length:

- *diffusive*
  Immediately following a quench, i.e. a sharp decrease in temperature, the growth mechanism of domains is the diffusion of molecules from smaller domains, larger curvature, to larger domains with lower curvature. It can be shown that the exponent with which the domains grow over time is in this case $\alpha = 1/3$

- *Hydrodynamic viscous*
  When, during the phase separation process, hydrodynamics begins to be relevant but the speeds are small and vary little over time, we can assume that the inertial term in the Navier-Stokes equations is negligible. Thus imposing viscous forces to be balanced by interface forces, it is possible to show that, in this regime, $\alpha = 1$ (as highlighted first by Siggia).

- *Hydrodynamic inertial*
  For higher velocities, the relevant physical phenomenon becomes the balance

[1] Curve in the temperature-density diagram, locus of points characterized by null second deirvatives of the Gibbs free energy.

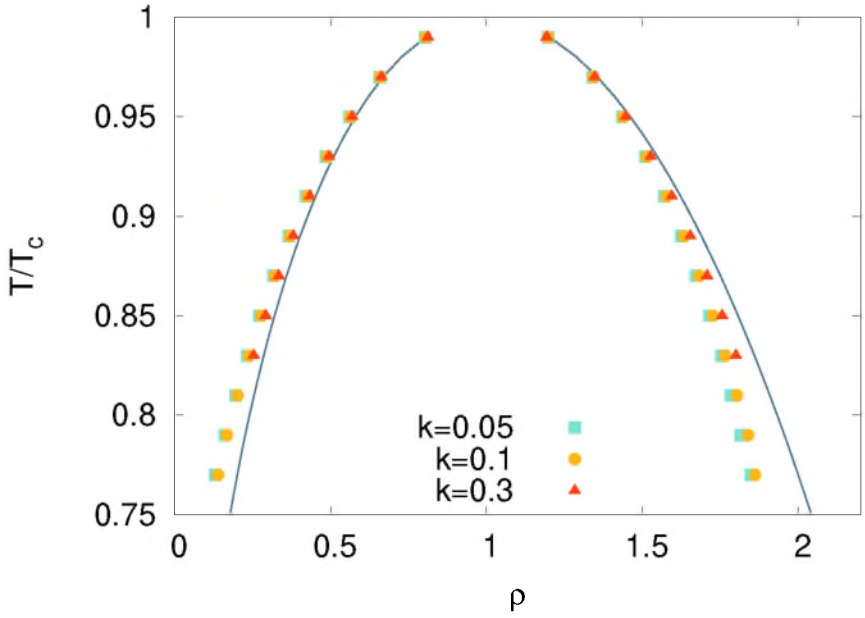

Figure A.1: *Numerical phase diagram.* Phase diagram, in the $(T/T_c, \rho)$ plane, of liquid-vapor phase separation. Squares and circles corresponds to numerical values, while continuum branches refer to theoretical prediction of the Maxwell construction.

between interface forces and inertial ones. Under this assumption one obtains $\alpha = 2/3$.

The inertial regime, for small viscosity values, and the viscous regime, for higher values of viscosity, have been observed numerically in an important work by Keadon et al. [121], for $3D$ binary mixtures. For single-component systems with Liquid-Vapor phase separation, where the order parameter is the density ρ, which is not locally conserved, only few results for 3D systems exist. Most of the work in past has been concerned with 2D systems [171], and reported evidence of an inertial regime with $\alpha = 2/3$, and of a regime characterized by a growth exponent $\alpha = 1/2$ for sufficiently high viscosities. The only work that considered Liquid-Vapor phase separation in $3D$ is [105], where authors report evidence of only the inertial ($\alpha = 2/3$) regime.

We performed $3D$ LB simulations of a van der Waals fluid as described in Chapter 3. In particular we used collision-streaming LB, where the only two relevant parameters are the relaxation time τ, that controls the viscosity, and the interface parameter k, directly related to the interface width and to the surface tension σ. First we reconstructed numerically the phase diagram in the temperature-density $(T/T_c, \rho)$[2] plane. Results are shown in Fig. A.1, with the theoretical curves, obtained from Maxwell construction, for comparison. Results corresponding to larger interface width and higher temperatures show a better match with theoretical predictions. Overall results are in good agreement with density values obtained from Maxwell construction, though deviations become larger reducing temperature.

We now discuss the results concerning the kinetics of phase separation on systems of size 512^3, summarizing them on a scaled plot. In the dynamical scaling hypothesis,

[2] T_c is the critical temperature.

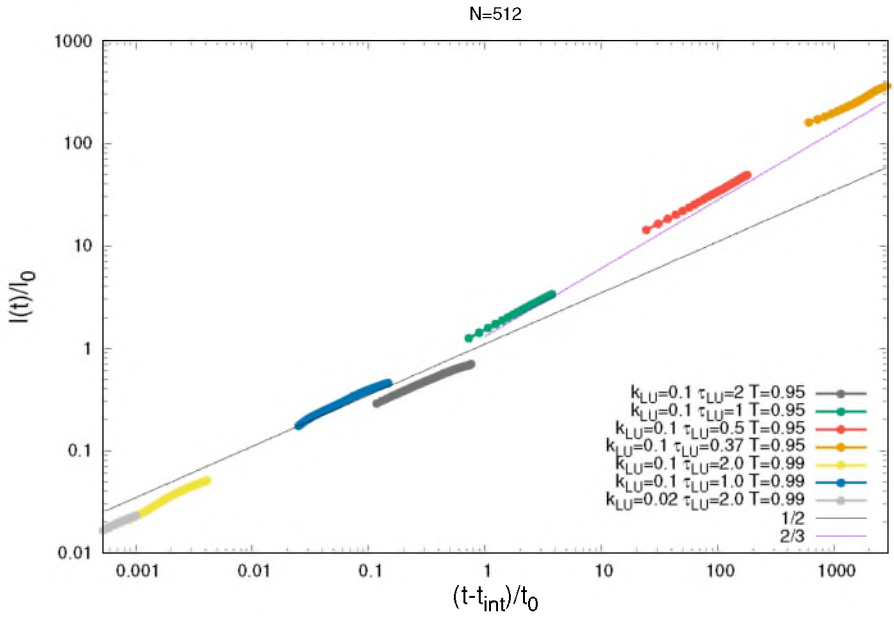

Figure A.2: *Domain size.* Scaling plot in the reduced variables $(l/l_0, t - t_{int}/t_0)$, for 512^3 LB simulations. Straight black and violet lines represent slopes 1/2 and 2/3 respectively.

one can define units of length and time by

$$l_0 = \eta^2/(\sigma\rho)\,, \quad t_0 = \eta^3/(\sigma^2\rho)\,, \tag{A.1}$$

which are the only such units derivable from η, σ, ρ. Data have been fitted, after the crossover region, with:

$$l(t) = (t - t_{int})^{\alpha}\,. \tag{A.2}$$

Results are displayed, in the reduced variables $(l/l_0, t - t_{int}/t_0)$, in Fig.A.2.

A.1. KINETICS AND MORPHOLOGY

We focus here on two cases with $\tau = \{0.5, 2\}$, for $T = 0.95$ and $k = 0.1$, which give exponents 2/3 and and 1/2. Domain growth is reported for both cases in Fig. A.3a. Growth for $\tau = 0.5$ (red curve) is clearly consistent with the slope 2/3. The grey curve on the same plot refers to the case $\tau = 2$. In this case, phase separation is ,as expected, delayed with respect to the previous case, and after a long crossover, 3/10 of a decade before the cut-off, growth with an exponent $\alpha \simeq 1/2$ starts. To better characterize the two different growth laws, we measured the separation depth $S(t)$. It is defined as

$$S = \langle \frac{\rho(x) - \rho_0}{\rho_{eq}(x) - \rho_0} \rangle\,, \tag{A.3}$$

where ρ_0 is the initial mean density, brackets indicate volume average, and

$$\rho_{eq}(x) = \begin{cases} \rho_{liquid}, & \text{if } \rho(x) > \rho_0 \\ \rho_{vapor}, & \text{if } \rho(x) < \rho_0. \end{cases} \tag{A.4}$$

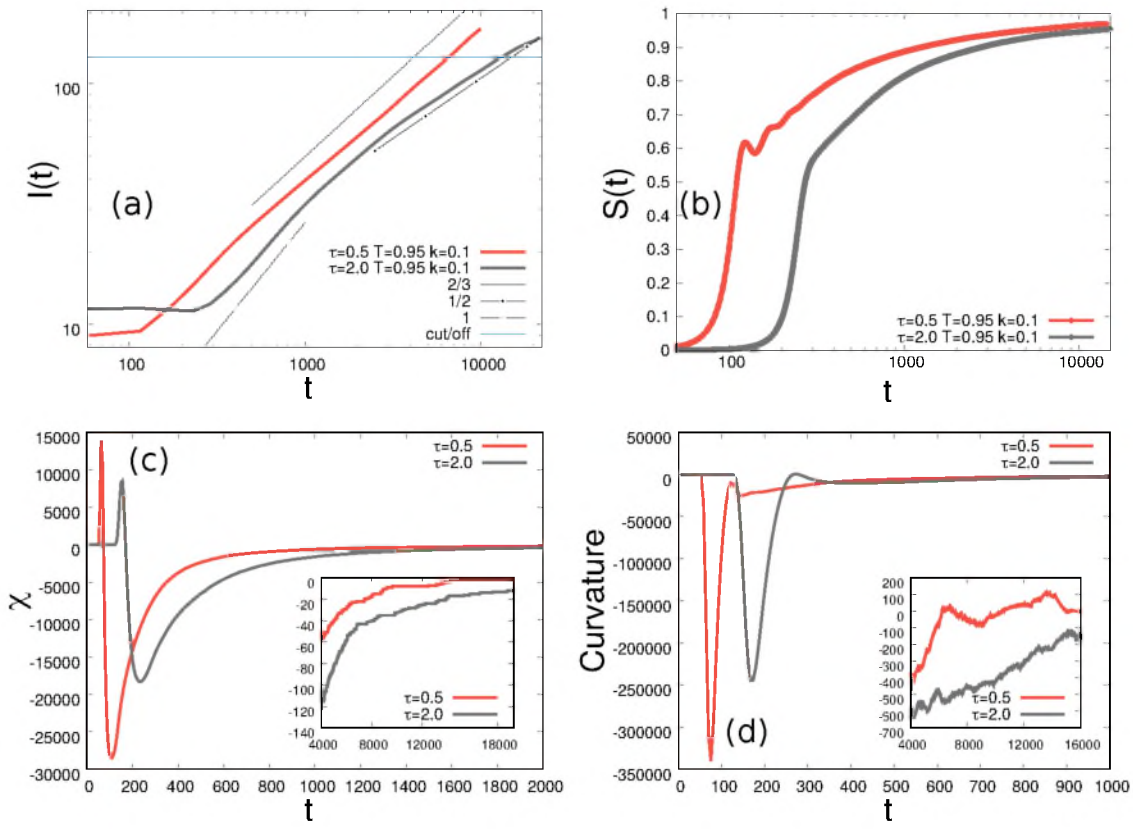

Figure A.3: *Kinetics and morphology.* (a) Domains length vs time. (b) Separation depth vs time. (c) Euler characteristic vs time. (d) Curvature vs time. All the plots refer to system sizes 512^3.

This quantity measures the "distance" of a single phase domains from their equilibrium state. Fig. A.3b shows the temporal evolution of the separation depth, for $\tau = 0.5$(red line) and $\tau = 2$ (gray line), for $T = 0.95$ and $k = 0.1$. For $\tau = 0.5$ phase separation takes place in three recognizable steps. First, there is a time delay, when no detectable phase separation takes place. Then, at the onset of phase separation, the process is very rapid and the separation depth “jumps” to a value greater than 0.6, meaning that the system reaches local equilibrium shortly after sharp interfaces are formed. Afterwards, in the third stage, phase separation proceeds much more slowly, as the density gradients within the single-phase domains are very small, while the densities of the two phases across any interface change only very slowly in time, asymptotically approaching equilibrium at $S = 1$. For $\tau = 2$, after the time delay, when the first spinodal decomposition pattern is formed, the separation depth jumps to a value close to 0.55, and then increases much faster (before $t = 1000$) than in the previous case. This indicates that during this crossover domains reach, in this case, an even better local equilibrium, resulting in an even slower growth(see grey curve in Fig. A.3a from $t = 4000$). The only remaining mechanism that can explain this slow growth is diffusion of interfaces, as one can also visually appreciate comparing snapshots of the system during the two regimes, presented in Fig.A.5.

The apparent impossibility to break the consecutiveness of domains reaching equilibrium and growth, seems at the basis of the absence of the viscous growth in Liquid vapor systems. In fact, in the viscous regime, one should observe a separation depth

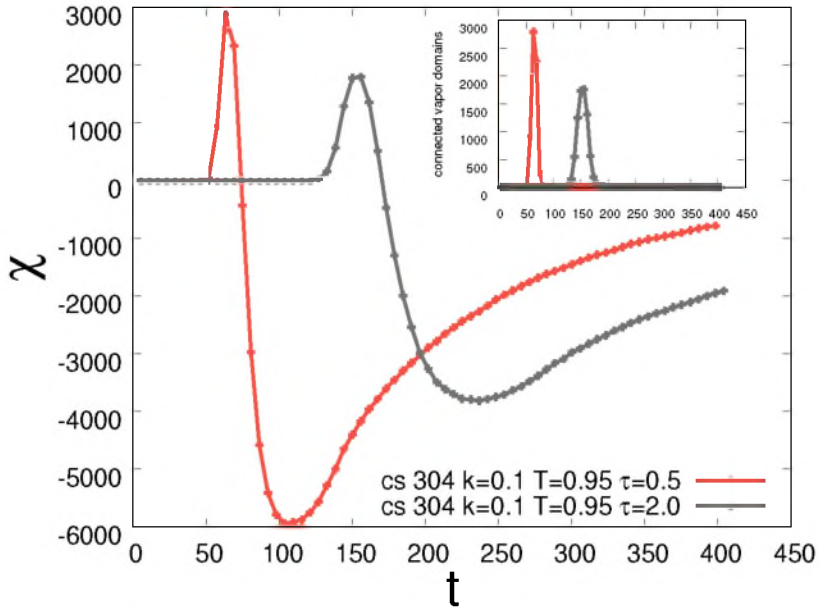

Figure A.4: *Comparison between Euler characteristic and db-scan results.* The db-scan measures directly the number of connected vapor domains. At the onset of phase separation both χ and the db-scan measure give the same results.

that growth more gradually after the time delay [201].

Going further in characterizing the different regimes we found, we measured the so called Minkowski functionals. the Euler characteristic χ (Fig. A.3c) and the mean domains curvature (Fig. A.3d). These have been measured following the procedure presented by Michielsen *et al.* [133]. The first step for the calculation of the so called Minkowski functionals is to transform the system at hand in a 3D cubic lattice filled with black and white pixels, with a suitable density cut-off.

For a 3d cubic lattice the four additive image functionals (Minkowski functionals) are the volume, the surface area, the mean breadth B (directly proportional to the mean curvature [133]), and the Euler characteristic χ. In 3D χ equals the number of regions of connected black voxels plus the number of completely enclosed regions of white voxels minus the number of tunnels, i.e. regions of white pixels piercing regions of connected black pixels. The calculation of these morphological measures relies on the preliminary determination of the total number of black voxels(cubes) n_c, black-white faces n_f, edges n_e and vertices n_v, so that:

$$V = n_c\,, \quad 2B = 3n_c - 2n_f + n_e\,, \quad \chi = -n_c + n_f - n_e + n_v\,. \tag{A.5}$$

The Euler characteristic χ can be directly related to the numbers of connected domains. This has been checked measuring the number of vapor connected domains through a dbscan algorithm[55]. The results obtained, for the two values of τ we are considering in this section, are displayed in Fig.A.4, for a smaller system with $L = 304$. Comparing the Euler characteristic(main plot), to the number of connected vapor domains(inset), one can appreciate how the results are very close. The fact that the latter goes to zero after the jump, which corresponds to the start of phase separation, allows us also to do some other considerations, inspired by the work of Xu [64]. It can be ar-

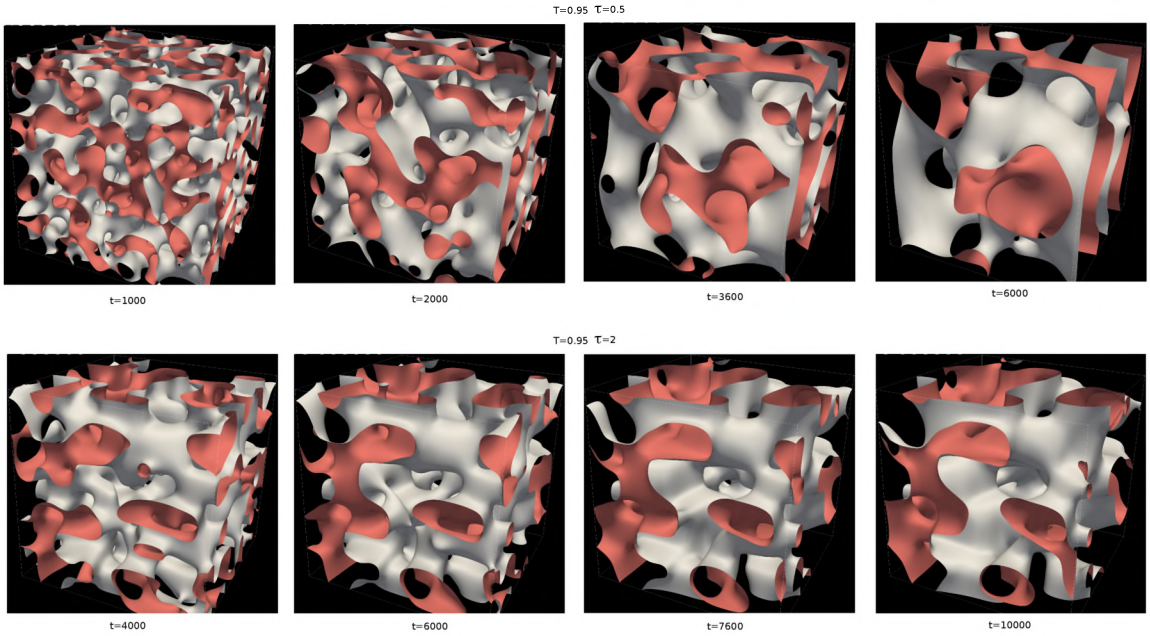

Figure A.5: *Snapshots.* Snapshots of the system during growth for the two cases considered in Fig.A.3. While during the inertial growth (first row) there is a change in domains shape, meaning that interfaces are still evolving in some ways, the diffusive growth (second row) it seems that interfaces are "frozen", and domains seem to grow with interface "diffusion".

gued that χ is negative (positive) if many disconnected black (white) regions dominate the system. Furthermore a vanishing Euler characteristic indicates a highly connected structure with equal numbers of black and white domains. Fig. A.3c shows the Euler characteristic for the two cases we are considering in this section. After a short time delay χ increases, indicating that the number of domains with $\rho > \rho_{threshold}$ increases. These results demonstrate that the phase separation process is in progress. Immediately after that, χ decreases to be less than zero, meaning that the number of domains with $\rho < \rho_{threshold}$ to increase. We have chosen $\rho_{threshold} = \rho_{average}$. For both cases, curves tend asymptotically to zero, showing a highly connected structure with equal numbers of black and white domains. Looking at the plot we can say that, on the onset of phase separation, for $\tau = 0.5$ we have more connected domains if compared to the case $\tau = 2$. This remains true also during domains growth (inset of Fig.A.3c). The mean domains curvature(Fig.A.3d) is more negative for $\tau = 0.5$ than for $\tau = 2$.

B

MAPPING WITH PHYSICAL UNITS

Here we present a possible mapping for the continuum model for active cholesteric liquid crystals used in Chapter 4. The same is also valid for active polar emulsions considered in Chapter 5.

By following previous studies [11], an approximate relation between simulation and physical units (for an active gel of cytoskeletal extracts) can be obtained using as length-scale, time-scale and force-scale respectively $L = 1\mu m$, $\tau = 10ms$ and $F = 1000nN$. These are the typical scales of cell extracts and actomyosin [139]. A mapping of some relevant quantities is reported in Table B.1.

Model parameters	Simulation units	Physical units
Shear viscosity, η	5/3	1.67 KPas
Elastic constant, K_Q	0.01	50 nN
Shape factor, ξ	0.7	dimensionless
Diffusion constant, $D = Ma$	0.007	0.06 $\mu m^2 s^{-1}$
Activity, ζ	$0 - 0.002$	$(0 - 20)$ KPa

Table B.1: Mapping of some relevant quantities between simulations units and physical units.

C

ADIMENSIONAL NUMBERS

In this Appendix we will furnish a derivation for the compression modulus B that we used to define the adimensional Ericksen number Er and the *active* Ericksen number Er_{act}.

In the following we consider the elastic coefficients for a binary mixture in the lamellar phase, in which one of the component is an isotropic fluid and the other is a polar liquid crystal. One of them, the compression modulus, is used to define the adimensional Ericksen number Er and its active counterpart Er_{act}, in terms of the model parameters. The analytical treatment generalizes that given in [90] for a simple lamellar fluid.

It is first convenient to rewrite the Landau-Brazovskii free-energy functional of Eq. (5.1) in a more symmetric form, in terms of the field $\psi = \phi - \phi_{cr}$, as

$$F[\psi,\mathbf{P}] = \int d\mathbf{r} \left| \frac{\tilde{a}}{2}\psi^2 + \frac{b}{2}\psi^4 + \frac{k_\phi}{2}\left|\nabla\psi\right|^2 + \frac{c}{2}(\nabla^2\psi)^2 - \frac{\alpha}{2}\psi\left|\mathbf{P}\right|^2 + \frac{\alpha}{4}\left|\mathbf{P}\right|^4 + \frac{k_P}{2}(\nabla\mathbf{P})^2 + \beta\mathbf{P}\cdot\nabla\psi \right| . \tag{C.1}$$

Eq. (5.1) of Chapter 5 can be obtained with $\tilde{a} = -a/\phi_{cr}^2$, $b = a/\phi_{cr}^4$ and $\phi_0 = 2\phi_{cr}$. At equilibrium, the chemical potential μ and the molecular field $\mathbf{h}$ must vanish:

$$\mu \equiv \frac{\delta F}{\delta\psi} = \tilde{a}\psi + b\psi^3 - k_\phi\nabla^2\psi + c\nabla^4\psi - \alpha\mathbf{P} - \beta\nabla\cdot\mathbf{P} = 0, \tag{C.2}$$

$$\mathbf{h} \equiv \frac{\delta \mathbf{F}}{\delta\mathbf{P}} = -\alpha\psi\mathbf{P} + \alpha\mathbf{P}^2\mathbf{P} - k_P\nabla^2\mathbf{P} + \beta\nabla\psi = 0. \tag{C.3}$$

We then take the single mode approximation [90], exact if considering only gradient terms in the above expressions,

$$\psi = \tilde{\psi}\sin(\kappa y), \tag{C.4}$$

where the amplitude $\tilde{\psi}$ and the wavenumber κ of the modulation have to be computed. Our simulations confirm that, as long as bulk parameters are small if compared to the elastic ones, the concentration field is modulated in a sinusoidal fashion. By substituting Eq. (C.4) into Eq. (C.3), and neglecting non linear contributions, we find that P_y must satisfy the equation

$$\partial_y^2 P_y = -\frac{\beta\kappa}{k_P}\tilde{\psi}\sin(\kappa y), \tag{C.5}$$

whose periodic solutions, with lamellar width $\lambda = 2\pi/\kappa$, are given by

$$P_y = C + \frac{\tilde{P}}{\kappa}\cos(\kappa y), \tag{C.6}$$

where C is a constant and

$$\tilde{P} = \beta\tilde{\psi}/k_P. \tag{C.7}$$

In order to find the coefficients C, $\tilde{\psi}$ and the wavenumber κ, we substitute profiles of ψ and P_y in Eq. (C.1), integrate over the lamellar wavelength λ and minimize with respect to κ, that is found to be $\sqrt{|k_\phi|/2c}$, the same as for the polarization-free case. Thus we rewrite the free-energy density as

$$f = \frac{1}{4}\left[(\tilde{a} - a_\phi - a_P)\tilde{\psi}^2 + \frac{3}{8}\left(b + \frac{4\alpha c^2\beta^4}{k_\phi^2 k_P^4}\right)\tilde{\psi}^4 + \alpha C^2\left(C^2 - \frac{6c\beta^2\tilde{\psi}^2}{k_\phi k_P^2}\right)\right], \tag{C.8}$$

where we defined $a_\phi = k_\phi^2/4c$ and $a_P = \beta^2/k_P$. Minimization of f with respect to C gives $C = 0$. Then, by further minimizing f with respect to $\tilde{\psi}$, we find

$$\tilde{\psi} = \pm 2|k_\phi|k_P^2\sqrt{\frac{a_\phi + a_P - \tilde{a}}{3(k_\phi^2 k_P^4 b + 4\alpha c^2\beta^4)}}. \tag{C.9}$$

This result shows that lamellar ordering occurs for $\tilde{a} < a_{cr} = a_\phi + a_P$. Thus, polarization enlarges the range of stability of the lamellar phase with respect to the Brazovskii theory, where lamellar ordering occurs if $\tilde{a} < a_\phi$.

We now introduce the elastic coefficients related to the free-energy cost of deviations from the harmonically modulated profile. We perturb equilibrium profiles by introducing a layer perturbation field $\vartheta(x, y)$, in terms of which the perturbated profiles become

$$\psi(x, y) = \tilde{\psi}\sin\left[\kappa(y - \vartheta(x, y))\right], \tag{C.10}$$

$$P(x, y) = \frac{\tilde{P}}{\kappa}\cos\left[\kappa(y - \vartheta(x, y))\right]. \tag{C.11}$$

The field ϑ is chosen so that its amplitude is much smaller than the lamellar width λ, but its typical variation lengthscale is much wider.

Because of the slowly-varying behaviour of ϑ, we flush out high-frequency modes to obtain a coarse-grained description of the model solely in terms of the layer displacement. This implies [90] that the following normalization condition holds:

$$\left|\frac{1}{L_x L_y}\int d\mathbf{r}\,\sin^2\left[\kappa(y - \vartheta(x, y))\right]\right|_{cg} = 1, \tag{C.12}$$

where L_x and L_y are the linear dimensions of the system and the boundary conditions are assumed to be periodic in both directions. By substituting Eqs. (C.10)-(C.11) and

their derivatives in Eq. (C.1) and by retaining only the elastic contributions, namely the gradient terms, we find the following coarse-grained free-energy functional:

$$F_{cg}[\vartheta] = \int d\mathbf{r}\, \frac{\tilde{\psi}^2}{2} \left[\left(k_\phi \kappa^2 + 2c\kappa^4 + \frac{\beta^2}{k_P} \right) (\partial_x \vartheta)^2 + \left(k_\phi \kappa^2 + 6c\kappa^4 + \frac{\beta^2}{k_P} \right) (\partial_y \vartheta)^2 + c\kappa^2 (\nabla^2 \vartheta)^2 \right] \equiv \int d\mathbf{r} \left[\frac{\Sigma}{2} (\partial_x \vartheta)^2 + \frac{B}{2} (\partial_y \vartheta)^2 + \frac{\Upsilon}{2} (\nabla^2 \vartheta)^2 \right] \quad \text{(C.13)}$$

where we have used Eq. (C.12), and Eq. (C.7) to get rid of $\tilde{P}$. In this expression we identify three contributions, combination of the three following effects: *(i)* stretching/shrinking of the lamellar surface in the layer direction (x in this Section) , *(ii)* compression/expansion of the lamellar layers in the gradient direction (y) and *(iii)* bending of the layers.

The coefficient of the derivative along the gradient direction is half of the compression modulus B and it gives the energy penalty per unit surface due to a change in the layer width. Its explicit expression is then given by

$$B = \left(\frac{\beta^2}{k_P} + \frac{k_\phi^2}{c} \right) \tilde{\psi}^2. \quad \text{(C.14)}$$

Analogously we can define the surface tension Σ as the energy penalty per unit surface due to the stretching of the layer as half of the coefficient in the layer direction

$$\Sigma = \left(\frac{\beta^2}{k_P} - \frac{k_\phi^2}{2c} \right) \tilde{\psi}^2. \quad \text{(C.15)}$$

It is worth noticing that, from one side, the liquid crystal network makes the lamellar structure stiffer, since the compression modulus is strengthened with respect to the polarization-free model, while on the other side, it counterbalances the negative surface tension of the lamellar phase. *In ultimis*, the coefficient of the laplacian term is half of the curvature modulus, which gives the energetic cost associated to an infinitesimal bending of a layer. It can be written as

$$\Upsilon = \frac{k_\phi}{2} \tilde{\psi}^2. \quad \text{(C.16)}$$

D

MOVIES DESCRIPTION

We give here a brief description of the movies cited in Chapter 4 (regarding the self propulsion and rotation of an active cholesteric droplet in 3d) and in Chapter 5 (regarding the rheological characterization of an active polar emulsion in 2d). Movies can be found at the following link: https://www.dropbox.com/sh/qs7fbvk8p2ttcst/AAC988O90RnPSYLhsX8sf13ua?dl=0.

D.1. SELF PROPELLED CHIRAL DROPLET

- Movie 1 Nematic Droplet in Rotational regime: The movie shows the dynamics of an active nematic droplet in the rotational regime ($\zeta = 0.001$). After an initial short transient the droplet sets into a stationary rotational motion around the axes joining the two boojums. Such motion is sustained by the energy injection due to the bending of the nematic field; this is more pronounced on the equatorial plane of the droplet where the resulting velocity field is stronger and exhibits a quadrupolar structure. The dynamic state stays stationary at long simulation times.

- Movie 2 Nematic Droplet in Chaotic regime: Since early simulation times, the droplet noticeably deforms under the effect of activity ($\zeta = 0.0015$). Energy injected is able to split each of the two boojums (+1 defects) at the poles into two +1/2 defects, for a total amount of 4 surface defects. These are connected in pairs by disclination lines inside the droplet (blue in the movie). Eventually, two defects of opposite topological charge may be created on the droplet surface, generating an extra disclination line in the bulk of the droplet. These move on the surface of the droplet until they find an oppositely charged defect and annihilate (a configuration of two annihilating defects is clearly visible at time $t = 1:20$). The droplet never sets into a stable or oscillatory steady state in the long term.

- Movie 3 Chiral Self-Propelling Droplet: If the LC droplet is chiral ($N = 2$ in the movie) the surface defect configuration rearranges to form a configuration reminiscent of the Frank-Pryce structure, characterized by two +1 defects close to each other. Once the droplet starts rotating under the effect of the activity ($\zeta =$

0.0010), the fan-like pattern of the LC on the droplet surface converts the rotational motion into propulsion. Thus the droplet moves with uniform rectilinear motion in the direction of the axis of rotation (y in the movie)

- Movie 4 Disclination Dance in a Chiral Droplet Fueled by Active Torques: The dynamics of a chiral droplet ($N = 1$ in the movie) activated by active torque dipoles ($\bar{\zeta} = -0.001$) is characterized by the formation of four $+1/2$ defects on its surface, connected in pairs by two disclination lines. Energy injected by the activity fuels to the mirror rotation of the surface defects. This leads to the dancing dynamics of the disclination lines in the interior of the droplet that, during rotation, first cross each other, then merge and rearrange in a helicoidal fashion.

D.2. MOVIES SHEARED ACTIVE EMULSIONS

- Movie 1: *Linear velocity profiles and lamellar phase.* The movie shows the dynamics of an active emulsion at $Er_{act} = 0.057, Er = 0.015$, in the red region of Fig. 5.17. The system first undergoes domains formation on the Brazovskii length-scale. Regions close to the walls are characterized by fast aligning dynamics due to the intense shear flow, resulting in a well aligned lamellar order at early times. Alignment in the bulk is much slower: first lamellar domains are tilted with respect to the imposed flow, then complete ordering is prevented by persistent disclinations. For instance we highlight the formation of a double buckle in the bulk at time t=0:51 that vanishes in the long term dynamics due to diffusion processes. Finally the system sets into an almost perfectly aligned state, except for some pearlification in the bulk.

- Movie 2: *Unidirectional motion.* Starting from a disordered isotropic configuration, the movie shows the dynamics of phase separation of the system at $Er_{act} = 0.344, Er = 0.022$. First an emulsion of active droplets develops in a passive background, while two active layers grow on both walls. The system soon sets in a $+-$ polarization configuration (t=0:16), thus leading to unidirectional flow since the very early dynamics, when the system is still symmetric. The layer on the bottom wall, the one found in the $-$ P_w state, progressively enlarges due to the merging with active domains that populate the bulk. On the contrary the top layer progressively narrows, as it behaves as a *reservoir* for the ϕ field. This leads to a top-bottom asymmetry in the concentration field. Eventually collisions of big domains on the top wall, as the one at time t=0:48, may momentarily arrest the narrowing of the top layer, but long-term dynamics is first characterized by instabilities that cancel out uniformity of the top layer (t=1:00), then by detachment of residual domains from the top wall. This, finally, leads to the formation of the stable $0-$ P_w state. Analogous dynamics occur for any case in the grey region of Fig.5.17.

- Movie 3: *Polarization flip.* The movie shows the dynamics of the flip of polarization at the boundary for the case at $Er_{act} = 0.57, Er = 0.003$, already discussed in Sec. 5.2.6. At time t=0:10 the two colliding domains, responsible for the polarization flip, have been highlighted with two black squares.

- Movie 4: *Active stress in polarization flip.* The movie shows the behavior of the active stress for the same case as in Movie 3. The colliding droplets have been highlighted with black squares. The scale of color is set as follows: beige for approximatively null values of the active shear stress, white and black respectively for positive and negative values. Thus, white layers close to the wall denote + polarization states and black ones characterize − configurations.

- Movie 5: *Activity quench.* The quenching dynamics from $Er_{act} = 0.57$ to $Er_{act} = 0.28$ at fixed $Er = 0.06$ is shown in this movie, corresponding to the case in panels (a)-(c) of Fig. 5.13. Starting from a symmetric configuration, typical of the cases in the green region of Fig. 5.17, and reducing the activity we find that active matter is progressively collected on one of the walls (the bottom one in the movie), thus ending up in an unidirectional asymmetric configuration (grey region of Fig.5.17).